© 2020 by Yubo “Paul” Yang. All rights reserved.

ELECTRON-ION CORRELATION AND FINITE-SIZE EFFECTS IN QUANTUM MONTE CARLO SIMULATIONS

BY

YUBO "PAUL" YANG

DISSERTATION

Submitted in partial fulfillment of the requirements
for the degree of Doctor of Philosophy in Physics
in the Graduate College of the
University of Illinois at Urbana-Champaign, 2020

Urbana, Illinois

Doctoral Committee:

Assistant Professor Bryan K. Clark, Chair
Professor David M. Ceperley, Director of Research
Professor James N. Eckstein
Professor Taylor L. Hughes

Abstract

This thesis explores properties of a mixture of electrons and ions using the quantum Monte Carlo method. In many electronic structure studies, purely electronic properties are calculated on a static potential energy surface generated by "clamped" ions. This can lead to quantitative errors, for example, in the prediction of diamond carbon band gap, as well as qualitatively wrong behavior, especially when light nuclei such as protons are involved. In this thesis, we explore different ways to include effects of dynamic ions and tackle challenges that arise in the process. We benchmarked the diffusion Monte Carlo (DMC) method on electron-ion simulations consisting of small atoms and molecules. We found the method to be nearly exact once sufficiently accurate trial wave functions have been constructed. The difference between the dynamic-ion and static-ion simulations can mostly be explained by the diagonal Born-Oppenheimer correction. We applied this method to solid hydrogen at megabar pressures and tackled additional problems involving geometry optimization and finite-size effects. The phase diagram produced by our electron-ion DMC simulations differ from previous DMC studies, showing 50 GPa higher molecular-molecular transition and 150 GPa higher molecular-to-atomic transition pressures. Both aforementioned studies forego the Born-Oppenheimer approximation (BOA) at hefty computational cost. Unfortunately, this makes it more difficult to compare our results with previous studies performed within the BOA. The remainder of the thesis tackle finite-size and ionic effects within the BOA. We calculated the Compton profile of solid and liquid lithium, achieving excellent agreement with experiment. Ionic effects of the liquid were included by averaging over disorder atomic configurations. Finite-size correction was crucial for the Compton profile near the Fermi surface. Finally, we tackled the finite-size error in the calculation of band gaps and devised a higher-order correction, which allowed thermodynamic values of the band gap to be obtained from small simulation cells. These advances mark important points along the path to the exact solution of the electron-ion problem. We expect that the better understanding of both the electron-ion wave function and its relation to finite-size effects obtained in this thesis can be crucial for future simulations of electron-ion systems.

To my friends and family.

Acknowledgments

First and foremost, I would like to thank my adviser, Prof. David Ceperley, for his unwavering support and guidance over the past six years. His rigor, honesty, curiosity, and openness deeply influenced the way I view and do science. I feel especially grateful for his fair treatment of students and collaborators. I was given much freedom to pursue my own interests and always felt like a valued member of the team. From these collaborations, I would like to thank Markus Holzmann and Carlo Pierleoni for many insightful discussions. I would like to thank the QMCPACK team, especially Raymond Clay III, who guided me through some initial hurtles getting to know the code and continue to be responsive and helpful. I look forward to continued collaborations, where I can learn from everyone and hopefully contribute more to our common interests.

I want to thank the CCMS program at LLNL, especially my mentor Miguel Morales. His enthusiasm of research is infectious. It was an invigorating summer interacting with Miguel and my fellow CCMS students Marnik Bercx, Ian Bakst, and Christopher Linderälv.

Of course, I would not be here without the loving care and support of my family and the wonderful company of my friends. I will not attempt to name everyone that was important for my life at Illinois, as I will invariably miss one of you even if I go on for pages. I do have to thank my officemate Brian Busemeyer for not only being a model colleague, who is always willing to answer stupid questions and entertain crazy ideas, but also for being a kind and wonderful friend. From our shared passion for coffee, badminton, swimming, and biking to our never-ending debates on Windows vs. Linux, Python 2 vs. 3, and functions vs. classes, I know we will remain colleagues and friends for years to come.

Thanks for funding from: U.S. Department of Energy (DOE) Grant No. DE-FG02-12ER46875 as part of the Scientific Discovery through Advanced Computing (SciDAC). DOE Grant No. NA DE-NA0001789. DOE Grant No. 0002911. The Blue Waters sustained-petascalecomputing project and the Illinois Campus Cluster, supported by the National Science Foundation (Awards No. OCI-0725070 and No. ACI-1238993), the state of Illinois, the University of Illinois at Urbana-Champaign, and its National Center for Supercomputing Applications and resources of the Oak Ridge Leadership Computing Facility (OLCF) at the Oak Ridge National Laboratory, which is supported by the Office of Science DOE Contract No. DE-AC05-00OR22725.

Table of Contents

List of Tables

List of Figures

List of Abbreviations

BOA	Born-Oppenheimer Approximation.
DBOC	Diagonal Born-Oppenheimer Correction.
EOS	Equation Of State.
DM	Density Matrix.
QMC	Quantum Monte Carlo.
RPIMC	Restricted Path Integral Monte Carlo.
VPI	Variational Path Integral.
RMC	Reptation Monte Carlo
FP-DMC	Fixed-Phase Diffusion Monte Carlo.
VMC	Variational Monte Carlo.
KW	Kolos and Wolniewicz.
RHF	Restricted Hartree Fock.
CISD	Configuration Interaction Singles Doubles.
CAS	Complete Active Space.
ANO	Atomic Natural Orbital.
ECG	Explicitly-Correlated Gaussian.
KS-DFT	Kohn-Sham Density Functional Theory.
HK	Hohenberg and Kohn.
LDA	Local Density Approximation.
PZ	Perdew and Zunger.
HOMO	Highest-Occupied Molecular Orbital.
LUMO	Lowest-Unoccupied Molecular Orbital.
PBE	Perdew, Burke, and Ernzerhof.
HSE	Heyd, Scuseria, and Ernzerhof.
SBJ	Slater-Backflow-Jastrow.

RPA	Random Phase Approximation.
RDM	Reduced Density Matrix.
LLT	Liquid-Liquid Transition.
DAC	Diamond Anvil Cell.
MD	Molecular Dynamics.
PES	Potential Energy Surface.
GPa	Giga-Pascal
LP	Low-pressure Phase.
BSP	Broken-Symmetry Phase.
IR	InfraRed.
EQQ	Electric Quadrupole-Quadrupole.
GCTABC	Grand-Canonical Twist Average Boundary Condition.
KZK	Kwee, Zhang, and Krakauer.
MSD	Mean-Squared Deviation.
FWHM	Full Width at Half Max.
SDF	Spectral Density Function.
BFD	Burkatzki, Filippi, and Dolg.
QE	Quantum Espresso.
PPC	PseudoPotential Correction.
FSC	Finite-Size Correction.
BF	Back Flow.
ZPE	Zero-Point Energy.

List of Symbols

h	Planck constant $\hbar = \dfrac{h}{2\pi}$.
Ψ	many-body electron-ion wave function.
ψ	many-body electron wave function.
ϕ	one-body electron wave function.
χ	one-body ion wave function.
$\boldsymbol{r}_i$	3D position of electron i.
$\boldsymbol{r}_I$	3D position of ion I.
$\boldsymbol{R}$	positions of all N electrons.
$\boldsymbol{R}_I$	positions of all N_I ions.
ρ	density matrix or electron density.
N	number of electrons.
N_I	number of ions.
Ω	total volume.
L	linear extent of the simulation cell.
r_s	Wigner-Seitz radius.
k_F	Fermi wave vector.
Γ	classical coulomb coupling parameter.
β	inverse temperature.
t	imaginary time unless otherwise specified.
τ	imaginary time step unless otherwise specified.
Z	canonical partition function.
$\hat{H}$	electron-ion hamiltonian.
$\hat{\mathcal{H}}$	electronic hamiltonian.
λ	quantumness $\lambda = \dfrac{\hbar^2}{2m}$.
Λ_{kj}	nonadiabatic coupling between electronic states k and j.

Λ	de Broglie wavelength.
P	pressure.
V	total potential energy.
T	total kinetic energy.
E	total energy.
E_T	trial total energy.
Ψ_T	trial wave function.
σ^2	variance of the local energy.
π	probability distribution.
Δ	band gap.
$g(r)$	pair correlation function.
$S(k)$	static structure factor.
U	negative exponent of the Jastrow wave function.
$u(r)$	pair contribution to U.
ω_p	plasmon frequency.
$\epsilon_{\boldsymbol{k}}$	dielectric function.
$n(\boldsymbol{k})$	momentum distribution.
$J(p)$	Compton profile.

Chapter 1

Introduction

1.1 The Electron-Ion Problem

The ultimate goal of this thesis is the accurate simulation of a many-body system of charged particles in the non-relativistic limit. This goal was not achieved, but some progress has been made. For the remainder of this thesis, the ground truth is assumed to be established by the exact solution of the Schrödinger equation (1.1) for the electron-ion wave function $\Psi(\boldsymbol{R}, \boldsymbol{R}_I)$ of N electrons and N_I ions

$$\hat{H}\Psi(\boldsymbol{R}, \boldsymbol{R}_I) = i\hbar\frac{d}{dt}\Psi(\boldsymbol{R}, \boldsymbol{R}_I), \tag{1.1}$$

where the electron-ion hamiltonian consists of non-relativistic kinetic energies and Coulomb interactions

$$\hat{H} = -\sum_{I=1}^{N_I}\frac{\hbar^2}{2m_I}\nabla_I^2 - \sum_{i=1}^{N}\frac{\hbar^2}{2m_i}\nabla_i^2 - \sum_{I=1}^{N_I}\sum_{i=1}^{N}\frac{Z_I k_e e^2}{|\boldsymbol{r}_I - \boldsymbol{r}_i|} + \frac{1}{2}\sum_{i=1}^{N}\sum_{j=1,j\neq i}^{N}\frac{k_e e^2}{|\boldsymbol{r}_i - \boldsymbol{r}_j|} + \frac{1}{2}\sum_{I=1}^{N_I}\sum_{J=1,J\neq I}^{N_I}\frac{k_e e^2}{|\boldsymbol{r}_I - \boldsymbol{r}_J|}. \tag{1.2}$$

The lower-case i, j and upper-case I, J refer to the electrons and ions, respectively. The lower-case $\boldsymbol{r}_i$ labels a single electron position, whereas the upper-case $\boldsymbol{R}$ denotes the positions of all electrons $\boldsymbol{R} \equiv \{\boldsymbol{r}_i\}$. $\boldsymbol{r}_I$ and $\boldsymbol{R}_I$ play analogous roles for the ions. Z_I is the atomic number of ion I. If any eigenstate of $\hat{H}$ can be constructed to arbitrary precision in a reasonable amount of time, which grows as a polynomial in the number of particles, then the many-body electron-ion problem can be declared solved. Unfortunately, even state-of-the-art methods struggle with just the ground state [1–3].

For equilibrium properties at high temperature, progress can be made by considering the Bloch equation (1.3) for the thermal density matrix $\rho \equiv \sum_i e^{-\beta E_i}\left|\Psi_i\right\rangle\left\langle\Psi_i\right|$

$$\hat{H}\rho = -\frac{d}{d\beta}\rho, \tag{1.3}$$

which results from the Schrödinger eq. (1.1) after a rotation from real to imaginary time $\tau = it$, which is

also the inverse temperature $\tau/\hbar = \beta \equiv 1/(k_B T)$. The partition function is a trace of the thermal density matrix and reduces to the classical Boltzmann distribution at high temperature

$$Z = \mathrm{Tr}\,(\rho) \underset{\beta\to 0}{\Rightarrow} Z \propto e^{-\beta V}. \tag{1.4}$$

Further, low-temperature properties of boltzmannons and bosons can be exactly and efficiently calculated using the path integral method (Sec.2.2.1). The exact method is no longer practical when fermions, e.g., electrons, are involved. Nevertheless, impressive results have been obtained for hydrogen when only the ground electronic state is considered [4, 5]. A complete treatment of the full electron-ion hamiltonian eq. (1.2) is rarely attempted [6, 7].

The solution of the electron-ion problem would be an important milestone in computational condensed matter, because it is considered a quantitatively accurate model for the vast majority of solids and liquids in condensed matter experiments. Further, theoretically, it is a natural extension of the jellium model to multi-component system and provides a firm foundation upon which relativistic effects can be included, for example via perturbation [8]. Finally, the laplacian in the non-relativistic kinetic energy operator can be interpreted as a generator of diffusion in imaginary time. This makes it more straightforward to develop intuitive understanding of the quantum kinetic energy as well as to deploy powerful computational techniques such as diffusion Monte Carlo (Sec. 2.2.3).

1.1.1 The Born-Oppenheimer Approximation

Suppose all eigenstates of the electronic hamiltonian $\{\psi_k\}$ are available at any ion configuration $\boldsymbol{R}_I$

$$\hat{\mathcal{H}}(\boldsymbol{R};\boldsymbol{R}_I)\psi_k(\boldsymbol{R};\boldsymbol{R}_I) = E_k(\boldsymbol{R}_I)\psi_k(\boldsymbol{R};\boldsymbol{R}_I). \tag{1.5}$$

Then, one can attempt to separate the electron and ion problems by expanding an eigenstate of the full hamiltonian $\hat{H}$ in the complete basis of electronic states

$$\Psi_l(\boldsymbol{R},\boldsymbol{R}_I) = \sum_{k=0}^{\infty} \chi_{lk}(\boldsymbol{R}_I)\psi_k(\boldsymbol{R};\boldsymbol{R}_I), \tag{1.6}$$

where $\chi_{lk}(\boldsymbol{R}_I)$ are expansion coefficients with no dependence on electron positions. This expansion results in a system of Schrödinger-like equations, each describing the ions moving on an electronic energy surface

E_j

$$\left(-\sum_I \frac{\hbar^2}{2M_I}\nabla_I^2 + E_j\right)\chi_j - \Lambda_{kj} = i\hbar\dot{\chi}_j, \tag{1.7}$$

and coupled by the so-called nonadiabatic operator Λ_{jk} [9]. Derivation and behavior of Λ_{jk} are discussed in Appendix A. While exact, eq. (1.7) is difficult to solve because all electronic states are coupled via Λ_{kj}. To fully separate the electron and ion problems, one must approximate Λ_{kj}.

There are two common approximations to Λ_{kj}, the first is to set the entire matrix to zero, the second is to set only the off-diagonal terms to zero. Both approximations decouple (1.7), allowing the complete separation of electronic and ionic motions. Many different and sometimes conflicting names have been given to these two approximations, including Born-Huang, Born-Oppenheimer and adiabatic approximation. To fix nomenclature, I will call the all-zero approximation, $\Lambda_{jk} = 0,\ \forall j,k$, the Born-Oppenheimer approximation (BOA). The diagonal terms Λ_{jj} are considered diagonal Born-Oppenheimer correction (DBOC). Non-zero off-diagonal elements are responsible for *nonadiabatic effects*.

1.2 Jellium

The jellium model eq. (1.8) brings the electronic problem into focus. It replaces the material-dependent ionic potential in the electronic hamiltonian with a rigid homogeneous background of positive charge and is an important stepping stone to the electron-ion problem. In Hartree atomic units

$$\hat{\mathcal{H}}_{HEG} = \sum_{i=1}^{N} -\frac{1}{2}\nabla_i^2 + \frac{1}{2}\sum_{i=1}^{N}\sum_{j=1,j\neq i}^{N}\frac{1}{|\boldsymbol{r}_i - \boldsymbol{r}_j|} + E_{e-b} + E_{b-b}, \tag{1.8}$$

where E_{e-b} and E_{b-b} are constants due to electron-background and background-background interactions. The isotropic background eliminates potential symmetry breaking interactions that can be introduced by a crystalline arrangement of the ions. The rigidity of the background also removes electron-ion coupling effects. This model was studied in great detail in the past century and its ground-state behavior was largely understood. Much progress has even been made regarding its excitations and finite-temperature properties.

There is only one length scale in the jellium model: the average electron-electron separation a. In units of bohr, this Wigner-Seitz radius $r_s = a/a_B$ determines the density of jellium.

$$\frac{1}{n} \equiv \frac{\Omega}{N} = \frac{4\pi}{3}(r_s a_B)^3 \tag{1.9}$$

in 3D, where a_B is the Bohr radius. The kinetic energy scales as r_s^{-2} (due to ∇^2) while the potential energies scales as r_s^{-1} (for $1/r$ potential), so r_s measures the relative strength of potential to kinetic energy. In this sense, r_s is the zero-temperature analogue of the classical coulomb coupling parameter

$$\Gamma \equiv \frac{e^2 n^{1/d}}{k_B T}. \tag{1.10}$$

The valence electron density in alkaline metals is $r_s \sim 2$, meaning the kinetic energy is important, so the electrons delocalize and form a liquid to minimize kinetic energy. At sufficiently large r_s (~ 100 in 3D and ~ 30 in 2D), the potential energy dominates, so the electrons localize to form a Wigner crystal.

1.3 Hydrogen

Hydrogen is a logical starting point for solving the electron-ion problem. It has the simplest atomic structure and no core electrons. The non-relativistic Schrödinger equation eq. (1.1) and (1.2) should work well for hydrogen. Further, the ground state of its electronic hamiltonian can be compactly and accurately represented [10]. Without core electrons, no essential modification needs to be made to the hamiltonian eq. (1.2) for a practical simulation, e.g., pseudopotential.

At sufficiently high temperatures, the hydrogen plasma, equal mixture of isotropic positive charges (protons) and negative charges (electrons), is a straightforward generalization of the jellium model to two components. However, at low temperatures, the two-component analogue of the Wigner crystal, solid hydrogen, is surprisingly complex. Since hydrogen is the lightest element, its zero-point motion has large amplitude. The ion wave function explores a sufficiently large space to invalidate the harmonic approximation for lattice vibrations. Further complicating matters, one can expect a metal-to-insulator transition as well as an atomic-to-molecular transition that may or may not coincide as temperature or pressure is decreased. On top of all that, naturally occurring isotopes, e.g., deuterium, and spin isomers, e.g., para- and ortho-H_2, allow the possibility of an intriguing blend of quantum effects at low temperatures.

Hydrogen is also interesting due to its practical relevance. Being the most abundant element in the observable universe, hydrogen and its isotopes are crucial for the understanding of stars and gas giants. Consider Jupiter, which contains insulating gaseous H_2 in the outer envelope and liquid metallic hydrogen deep inside. If there was a first-order liquid-liquid transition between the two phases, then there would be an interface across which density changes discontinuously. Depending on the solubility of helium in the two phases, there is the possibility of helium rain across the interface and extra heat radiation due to this condensation [11]. Further, interior models of stars and gas giants rely on numerically accurate equation-

of-state (EOS) of various chemical species involving hydrogen (H^+, H, H_2). A few percent change to the hydrogen EOS is enough to eliminate/create a rocky core for Jupiter [12].

In addition to its relevance in astrophysics, hydrogen is also important in energy applications. Accurate understanding of hydrogen EOS at high temperatures and pressures has obvious benefits to fusion experimental design. Even at low temperatures, hydrogen-rich compounds, at sufficiently high pressures, have recently smashed the superconducting transition temperature records held by the so-called "high-temperature" superconductors [13, 14].

Finally, the 85-year-old prediction for a low-temperature insulating-to-metallic transition of solid hydrogen, the Wigner-Huntington transition, is close to being established [15–17]. Experimental observations [16, 17] and theoretical calculations [2, 18] are converging, although more experimental and theoretical characterizations are needed to settle current debates.

1.4 Lithium, Diamond, and Silicon

Despite complications introduced by core electrons, the jellium model is arguably better realized in the valence of alkaline metals, e.g., lithium and sodium, than it is in hydrogen. The heavier nuclei are less quantum and the core electrons screen their interaction with the valence electrons. This allows the harmonic approximation to be more widely applicable. More importantly, they are easier to handle in experiments than hydrogen and scatter X-rays more strongly, which facilitates precise experimental determination of lattice structure along with other properties. These advantages allowed us to obtain excellent agreement with experiment using an electron-ion QMC simulation performed within the BOA in chapter 7.

In addition to alkaline metals, elemental insulators, e.g., diamond carbon and silicon, remain important testing grounds for electronic QMC methods. Accurate and practical prediction of excitation energies using QMC is still an active area of research. We make some progress in chapter 8 by reducing finite-size error in bandgap calculations.

1.5 Thesis Outline

The remainder of this thesis is organized as follows. In chapter 2, I start by introducing the Monte Carlo methods that we use to accurately treat electron correlation in the electronic problem as well as to solve the full electron-ion problem at times. I then introduce the effective one-particle electronic structure methods used to generate trial wave functions for the aforementioned QMC methods. Chapter 3 displays the form and properties of the Slater-Jastrow wave function in detail, while chapter 4 discusses many-body finite-size

correction, sometimes based on the properties of the many-body wave function. Both wave function form and finite-size correction are crucial for accurate and practical QMC simulations. The next four chapters display QMC results for a few simple electron-ion systems. Chapter 5 benchmarks the QMC method as a complete solver for the electron-ion problem without invoking the BOA on small atoms and molecules. Chapter 6 applies this dynamic-ion QMC method to solve for the ground state of solid hydrogen. Chapter 7 considers the effect of the ions on the momentum distribution of the valence electrons in lithium within the BOA. Finally, chapter 8 presents an improved finite-size correction to the (purely electronic) bandgap calculated in QMC.

Chapter 2

Methods

The main method used throughout this thesis is ground-state quantum Monte Carlo (QMC). This chapter provides a physically motivated introduction to this method. In the first part, I start from the familiar finite-temperature classical Monte Carlo method, then describe its generalization to a quantum system, finally take the zero-temperature limit. The second part of this chapter describes practical methods for constructing a many-body trial wave function, which is a crucial ingredient in many QMC methods.

2.1 Classical Monte Carlo

The Monte Carlo methods mentioned in this thesis perform high-dimensional integrals by using random numbers to sample probability distributions. These distributions must be non-negative in the entire domain of "states" over which they are defined. In classical mechanics, a "state" of N particles in 3 dimensions is labeled by the positions $\boldsymbol{R} \equiv \{\boldsymbol{r}_i\}$ and momenta $\boldsymbol{P} \equiv \{\boldsymbol{p}_i\}$ of the particles $i = 1, \ldots, N$. The classical partition function for the canonical ensemble

$$Z \equiv \mathrm{Tr}(e^{-H/k_B T}) = \frac{1}{N! h^{3N}} \int d^{3N}\boldsymbol{R} d^{3N}\boldsymbol{p}\; e^{-H(\boldsymbol{R},\boldsymbol{P})/k_B T}, \tag{2.1}$$

where $H(\boldsymbol{R}, \boldsymbol{P})$ is the hamiltonian, k_B is the Boltzmann constant, h is the Planck constant, and T is temperature. For N distinguishable non-relativistic particles with mass m, the kinetic contribution $\dfrac{p^2}{2m}$ to eq. (2.1) can be integrated analytically, giving

$$Z = \frac{1}{N! \Lambda^3} \int d^{3N}\boldsymbol{R} e^{-\beta V(\boldsymbol{R})}, \tag{2.2}$$

where $V(\boldsymbol{R})$ is the potential energy of the N-particle system, $\beta \equiv k_B T$, and Λ the de Broglie wavelength

$$\Lambda = \left(\frac{h^2}{2\pi m k_B T} \right)^{1/2}. \tag{2.3}$$

All equilibrium statistical mechanics properties can be calculated from the partition function, so the entirety of classical equilibrium statistical mechanics reduces to the problem of evaluating the 3N-dimensional integral in eq. (2.2) and its derivatives. Monte Carlo methods are ideally suited to evaluating high-dimensional integrals, because the amount of computation does not increase as an exponential in the number of dimensions as in a brute-force quadrature approach.

To calculate a property in the canonical ensemble, ones takes the trace

$$\langle O \rangle = \frac{\mathrm{Tr}\left(Oe^{-\beta H}\right)}{\mathrm{Tr}\left(e^{-\beta H}\right)}, \tag{2.4}$$

where $\langle\rangle$ denotes ensemble average. Limiting to local observables that can be evaluated on the particle coordinates, e.g., total potential energy $V(\boldsymbol{r})$ and pair correlation function $g(r)$

$$\langle O \rangle = \int d^{3N}\boldsymbol{R} \frac{e^{-\beta V(\boldsymbol{R})}}{\int d^{3N}\boldsymbol{R}' e^{-\beta V(\boldsymbol{R}')}} O(\boldsymbol{R}) = \int d^{3N}\boldsymbol{R} \pi(\boldsymbol{R}) O(\boldsymbol{R}), \tag{2.5}$$

where $\pi(\boldsymbol{R})$ is the *Bolzmann distribution*

$$\pi(\boldsymbol{R}) \equiv \frac{e^{-\beta V(\boldsymbol{r})}}{\int d^{3N}\boldsymbol{R}' e^{-\beta V(\boldsymbol{R}')}} \propto e^{-\beta V(\boldsymbol{R})}. \tag{2.6}$$

Monte Carlo estimation of $\langle O \rangle$ works by sampling particle configurations from the Bolzmann distribution $\pi(\boldsymbol{R})$ and accumulating the average $O(\boldsymbol{R})$

$$\langle O \rangle = \lim_{N_s \to \infty} \frac{1}{N_s} \sum_{i=1}^{N_s} O(\boldsymbol{R}_i). \tag{2.7}$$

How does one sample a generic multi-dimensional probability distribution such as $\pi(\boldsymbol{R})$? An excellent answer was given a 1953 paper authored by Metropolis *et al.* [19]. The Metropolis algorithm, designed by the Rosenbluths supervised by the Tellers, works by constructing a Markov chain having $\pi(\boldsymbol{R})$ as its stationary state. This is achieved by a rejection method that maintains detailed balance

$$\pi(\boldsymbol{R}) P(\boldsymbol{R} \to \boldsymbol{R}') = \pi(\boldsymbol{R}') P(\boldsymbol{R}' \to \boldsymbol{R}), \tag{2.8}$$

where $P(\boldsymbol{R} \to \boldsymbol{R}')$ is the Markov chain transition probability from state $\boldsymbol{R}$ to $\boldsymbol{R}'$. The Metropolis algorithm breaks P into two steps: proposal and acceptance

$$P(\boldsymbol{R} \to \boldsymbol{R}') = T(\boldsymbol{R} \to \boldsymbol{R}') A(\boldsymbol{R} \to \boldsymbol{R}'), \tag{2.9}$$

with the following accept/reject criteria: For any transition probability used to propose the state change $T(\boldsymbol{R} \to \boldsymbol{R}')$, accept the change with probability

$$A(\boldsymbol{R} \to \boldsymbol{R}') = \min\left(1, \frac{\pi(\boldsymbol{R}')T(\boldsymbol{R}' \to \boldsymbol{R})}{\pi(\boldsymbol{R})T(\boldsymbol{R} \to \boldsymbol{R}')}\right). \tag{2.10}$$

Using eq. (2.9) and (2.10) to prove eq. (2.8) is a good way to appreciate the design of this acceptance probability.

Mathematically, $\pi(\boldsymbol{R})$ is the unique stationary state of the Markov chain constructed by the Metropolis method so long as $P(\boldsymbol{R} \to \boldsymbol{R}')$ is ergodic. That is, there is finite probability of reaching any state $\boldsymbol{R}'$ starting from any state $\boldsymbol{R}$ using the transition rule P. In practice, however, a simulation can be stuck in a meta-stable state for its entire duration, for example, due to a bad initial condition. Careful monitoring and checking of convergence is a must in any serious Monte Carlo simulation.

2.2 Quantum Monte Carlo

I will start with the general, albeit somewhat complicated, path integral Monte Carlo (PIMC) method, because it rigorously takes temperature into account and connects well with classical Monte Carlo. Then, I will describe ground-state methods as limits and efficiency tricks to specialize the path integral method to the ground state. While contrary to the historic progression of these methods, I find this perspective helpful for relating the methods and visualizing them in their respective niches.

2.2.1 Path Integral Monte Carlo

The quantum partition function for the canonical ensemble needs to trace over discrete N-particle eigenstates, rather than 2N 3-dimensional variables as in eq. (2.1)

$$Z \equiv \mathrm{Tr}(e^{-\hat{H}/k_BT}) = \mathrm{Tr}\left(\sum_{i=1}^{\infty} e^{-E_i/k_BT} \left|\Psi_i\right\rangle \left\langle\Psi_i\right|\right), \tag{2.11}$$

where E_i and $|\Psi_i\rangle$ are the eigenvalues and eigenstates of the hamiltonian H. To make contact with classical mechanics, we put the density matrix (DM) for distinguishable particles in position basis (first quantization)

$$\rho_D(\boldsymbol{R}, \boldsymbol{R}'; \beta) \equiv \langle \boldsymbol{R}|e^{-\beta H}|\boldsymbol{R}'\rangle, \tag{2.12}$$

where $\beta \equiv \frac{1}{k_B T}$. Then the partition function becomes

$$Z(\beta) = \int d^{3N}\boldsymbol{R}\rho_D(\boldsymbol{R}, \boldsymbol{R}; \beta), \tag{2.13}$$

which can be exactly factorized into two pieces

$$Z(\beta) = \int d^{3N}\boldsymbol{R}d^{3N}\boldsymbol{R}'\rho_D(\boldsymbol{R}, \boldsymbol{R}'; \tau)\rho_D(\boldsymbol{R}', \boldsymbol{R}; \beta - \tau). \tag{2.14}$$

This factorization can be repeated until the temperature becomes high enough ($\tau \to 0$) that a semi-classical approximation to $\rho_D(\boldsymbol{R}, \boldsymbol{R}'; \tau)$ is accurate. Given translation symmetry along imaginary time, β is typically broken down into M equal-length pieces, i.e., $\tau = \beta/M$. For N non-relativistic particles each having mass m, ρ_D can be calculated as an integral over a discretized *path* of particle coordinates $\{\boldsymbol{R}_m\}$

$$\rho_D(\boldsymbol{R}_0, \boldsymbol{R}_M; \beta) = \lim_{M\to\infty} \int d\boldsymbol{R}_1 \dots d\boldsymbol{R}_{M-1} \exp\left(\sum_{m=1}^{M} \ln \rho_D^p(\boldsymbol{R}_{m-1}, \boldsymbol{R}_m)\right). \tag{2.15}$$

The *primitive approximation* for the high-temperature density matrix ρ_D^p satisfies

$$\frac{dN}{2}\ln(4\pi\lambda\tau) - \ln \rho_D^p(\boldsymbol{R}_m - 1, \boldsymbol{R}_m) = \frac{(\boldsymbol{R}_{m-1} - \boldsymbol{R}_m)^2}{4\lambda\tau} + \tau V(\boldsymbol{R}_m), \tag{2.16}$$

where $\lambda \equiv \dfrac{\hbar^2}{2m}$ is the *quantumness* of the particle and d is the number of spatial dimensions. Thus,

$$\rho_D(\boldsymbol{R}_0, \boldsymbol{R}_M; \beta) = \lim_{M\to\infty} (4\pi\lambda\tau)^{-dNM/2} \exp\left(-\sum_{m=1}^{M}\left[\frac{(\boldsymbol{R}_{m-1} - \boldsymbol{R}_m)^2}{4\lambda\tau} + \tau V(\boldsymbol{R}_m)\right]\right). \tag{2.17}$$

The main advantage of eq. (2.15) is that it turns the partition function eq. (2.13) into an integral of a product of high-temperature DMs over all closed paths

$$Z = \lim_{M\to\infty} \int d\boldsymbol{R}d\boldsymbol{R}_1 \dots d\boldsymbol{R}_{M-1}\rho_D(\boldsymbol{R}, \boldsymbol{R}_1; \tau)\rho_D(\boldsymbol{R}_1, \boldsymbol{R}_2; \tau) \dots \rho_D(\boldsymbol{R}_{M-1}, \boldsymbol{R}; \tau). \tag{2.18}$$

Each closed path can be visualized as a collection of ring polymers, one for each particle. The linear extension of a ring polymer is proportional to the particle's de Broglie wavelength $\Lambda = \sqrt{4\pi\lambda\beta}$ eq. (2.3). For distinguishable particles, the integral needed to evaluate the quantum partition function eq. (2.18) poses no essential difficulty to a Monte Carlo method when compared with its classical counterpart eq. (2.2). One simply has to integrate M classical systems, which are coupled by the spring-like kinetic energy term in

eq. (2.16). Each classical system is typically referred to as a *slice* of imaginary time or a *bead* on the ring polymer. Converged results is obtained in the zero time step $\tau \to 0$, equivalently the infinite slice $M \to \infty$ limit. The the primitive approximation eq. (2.16) to the exact density matrix is correct only to $O(\tau)$, so a large number of beads is needed, resulting in slow simulations. Better approximations can be constructed to be correct to $O(\tau^2)$, for example the pair-product form in Ref. [20]. However, if the particles are identical bosons, then one has to consider particle permutations along the path (fermions pose an additional essential problem, see Sec. 2.2.5)

$$\rho_B(\boldsymbol{R}_0, \boldsymbol{R}_M; \beta) = \frac{1}{N!} \sum_{\mathcal{P}} \rho_D(\boldsymbol{R}_0, \mathcal{P}\boldsymbol{R}_M; \beta), \tag{2.19}$$

where $\mathcal{P}\boldsymbol{R}_M$ contains the same N coordinates as $\boldsymbol{R}_M$, but with the particles relabeled. This permutation can happen via any number of 1-, 2-, and up to N-particle exchanges between adjacent time slices along the path. Thus, the state space of bosonic path integral is much larger than that of boltzmannic path integral. Efficient sampling of permuting paths is a significant technical challenge. Fortunately, no uncontrolled approximation has been introduced and exact simulations are possible for both bolzmannons and bosons via the Monte Carlo method [20, 21].

2.2.2 Variation Path Integral a.k.a. Reptation Monte Carlo

Even with accurate approximation to the high-temperature density matrix, the ground state is still costly to study using the path integral formalism presented so far, because a large number of time slices have to be included to approximate $\beta \to \infty$. Fortunately, one can still efficiently study this zero-temperature limit with the help of a trial wave function $|\Psi_T\rangle$, so long as it is non-negative. The ground-state "partition" function has only one term

$$Z_0 = \lim_{\beta\to\infty} \langle \Psi_0 | e^{-\beta H} | \Psi_0 \rangle \,, \tag{2.20}$$

where $|\Psi_0\rangle$ is the ground state of the hamiltonian H. For sufficiently large β, any trial wave function not orthogonal to the ground state $\langle \Psi_T | \Psi_0 \rangle \neq 0$ will be projected to the ground state by $e^{-\beta H}$, so

$$Z_0 = \lim_{\beta\to\infty} \langle \Psi_T | e^{-\frac{\beta}{2}H} e^{-\frac{\beta}{2}H} | \Psi_T \rangle \approx \langle \Psi_T | e^{-\beta_e H} e^{-\beta_e H} | \Psi_T \rangle \,, \tag{2.21}$$

for some β_e large enough to be considered "equilibrated". Performing path discretization as before

$$Z_0 = \lim_{M\to\infty} \int d\boldsymbol{R}_{-M} \dots d\boldsymbol{R}_0 \dots d\boldsymbol{R}_M \Psi_T^*(\boldsymbol{R}_{-M}) \rho(\boldsymbol{R}_{-M}, \boldsymbol{R}_{-M+1}; \tau) \dots \rho(\boldsymbol{R}_{M-1}, \boldsymbol{R}_M; \tau) \Psi_T(\boldsymbol{R}_M), \quad (2.22)$$

where $\tau = \beta_e/M$. β_e can be small if $|\Psi_T\rangle$ is a good approximate to the ground state $|\Psi_0\rangle$. In this sense, $|\Psi_T\rangle\langle\Psi_T|$ plays the role of a low-temperature density matrix to quickly close a long path, although its temperature is ill-defined. No permutation needs to be sampled because quantum statistics are encoded in the trial wave function. However, translation symmetry along imaginary time is broken. The $2M+1$ time slices each sample a different probability distribution. Observables that do not commute with the hamiltonian are unbiased only when evaluated in the middle section $\boldsymbol{R}_m$, where $|m|$ is small. This is because $\boldsymbol{R}_m$ needs to be sufficiently separated from the trail wave function slices $\boldsymbol{R}_{-M}$ and $\boldsymbol{R}_M$ to be considered the zero-temperature limit. The trial wave functions at the ends and the DMs in the middle of eq. (2.22) must all be non-negative for the integrand to be interpreted as a probability distribution for the path $\{\boldsymbol{R}_{-M}, \dots, \boldsymbol{R}_M\}$. This path is open in general ($\boldsymbol{R}_{-M} \neq \boldsymbol{R}_M$) and can be visualized as a "reptile". This method was first mentioned as variational path integral (VPI) [20], but later popularized as reptation Monte Carlo (RMC) [22]. While the RMC method can be efficient, it still requires all M classical systems to be stored in memory at one time and intelligent Monte Carlo moves to change the reptile without ergodicity problems. This makes RMC more troublesome to implement than classical Monte Carlo or molecular dynamics, because the entire reptile, containing $O(M)$ classical systems have to be updated to generate $O(1)$ new decorrelated sample for the pure estimator eq. (2.23).

2.2.3 Diffusion Monte Carlo

The diffusion Monte Carlo (DMC) method can be viewed as a simplification of RMC. When calculating a ground-state observable using eq. (2.21), the *pure estimator*

$$\langle \hat{O} \rangle_p \equiv \langle \Psi_T | e^{-\beta_e H} \hat{O} e^{-\beta_e H} | \Psi_T \rangle \approx \langle \Psi_0 | \hat{O} | \Psi_0 \rangle \quad (2.23)$$

is an unbiased ground-state estimate of $\hat{O}$ whether it commutes with the hamiltonian or not. We can forgo the pure estimator for a simpler algorithm. Consider the *mixed estimator*

$$\langle \hat{O} \rangle_m \equiv \langle \Psi_T | \hat{O} e^{-\beta_e H} | \Psi_T \rangle \approx \langle \Psi_T | \hat{O} | \Psi_0 \rangle \,. \quad (2.24)$$

Equation (2.24) has the advantage that the operator can be immediately applied to a trial wave function, which is known at the beginning of the calculation. Further, the Ψ_0 on the r.h.s. can be interpreted as being propagated from Ψ_T using the *imaginary-time propagator*

$$\hat{U}(t) = e^{-tH}. \tag{2.25}$$

For any $t > \beta_e$, the mean of the observable eq. (2.24) should be stationary. The algorithm as described so far is similar to classical molecular dynamics. One starts with a trial wave function at $t = 0$ and propagates it along imaginary time. After some initial equilibration period, the mixed estimator fluctuates around some stationary mean. One then runs for "longer" and accumulate statistics.

For identical non-relativistic particles having mass m, $\hat{U}$ in coordinate basis is the Green function for imaginary-time Schrödinger equation

$$\begin{aligned} G(\boldsymbol{R}' \leftarrow \boldsymbol{R}; t) &= \langle \boldsymbol{R}' | \hat{U}(t) | \boldsymbol{R} \rangle = \langle \boldsymbol{R}' | e^{-t(\lambda \nabla^2 + V)} | \boldsymbol{R} \rangle \\ \lim_{\tau \to 0} G(\boldsymbol{R}' \leftarrow \boldsymbol{R}; \tau) &= \left((4\pi\lambda\tau)^{-dN/2} e^{-\frac{(\boldsymbol{R} - \boldsymbol{R}')^2}{4\lambda\tau}} \right) \left(e^{-\tau V(\boldsymbol{R})} \right). \end{aligned} \tag{2.26}$$

The two terms in eq. (2.26) are the Green function for diffusion and weight accumulation. The quantumness $\lambda = \frac{\hbar^2}{2m}$ of the particle determines its diffusion constant in imaginary time. Lighter particles diffuse "faster". One can, in principle, start with any classical system $\boldsymbol{R}$, apply the Green functions repeatedly to update $\boldsymbol{R}$, and eventually end up sampling the mixed distribution $\langle \Psi_T | \Psi_0 \rangle$.

While eq. (2.24)-(2.26) contain the main idea behind the DMC method, they do not result in a practical algorithm. The weight of the classical system due to the potential term goes to zero or infinity exponentially fast, especially when two charged particles coalesce. For a stable algorithm, one can modify the Green function eq. (2.26) to more directly sample the mixed distribution

$$f(\boldsymbol{R}, t) \equiv \Psi_T^*(\boldsymbol{R}) e^{-t(H - E_T)} \Psi_T(\boldsymbol{R}) \underset{t \to \infty}{=} \Psi_T^*(\boldsymbol{R}) \Psi_0(\boldsymbol{R}), \tag{2.27}$$

where a trial energy E_T is introduced to stablize the potential term. Substitute $\Psi_T^{-1} f$ in place of Ψ into the imaginary-time Schrödinger equation $-\partial_t \Psi = H\Psi$, where $H = -\lambda\nabla^2 + V$, we obtain

$$-\partial_t f = \Psi_T H \Psi_T^{-1} f \Rightarrow -\partial_t f = -\lambda \boldsymbol{\nabla} \cdot (\boldsymbol{\nabla} - \boldsymbol{v}) f + (E_L - E_T) f, \tag{2.28}$$

where the local energy $E_L \equiv \dfrac{H\Psi_T}{\Psi_T}$ and the drift vector

$$\boldsymbol{v} \equiv 2\Psi_T^{-1}\boldsymbol{\nabla}\Psi_T = \boldsymbol{\nabla}\ln\Psi_T^2. \tag{2.29}$$

After this *importance-sampling transformation*, the Green function eq. (2.26) is now modified to have three contributing processes: diffusion, drift, and weighting. The pure diffusion process becomes a drift-diffusion process guided by the trial wave function. Further, the weighting by the bare potential energy becomes weighting by the local energy. Given suitably designed trial wave function, E_L can be made continuous even if the original potential V contains divergences, e.g., in the coulomb interaction. In practice, the mixed distribution is approximated by an ensemble of walkers

$$f(\boldsymbol{R}, t) \approx \sum_{m=1}^{N_w} \delta(\boldsymbol{R} - \boldsymbol{R}_m), \tag{2.30}$$

and the trial energy E_T is adjusted every so often to keep the population of walkers N_w from explosion and extinction. Equation (2.28) defines the DMC algorithm. While not strictly necessary, one typically adds a Metropolis rejection step using the Green function G as transition probability T in eq. (2.10). This ensures that the algorithm samples the desired probability distribution at any finite time step, where the Green function is approximate [23].

For bosons and Bolzmannons, DMC gives the exact ground-state energy of H in the limit of infinitesimal time step and uncontrolled walker population. Observables that do not commute with the hamiltonian will suffer a mixed-estimator error, which vanishes as the trial wave function approaches the ground state.

2.2.4 Variational Monte Carlo

Variational Monte Carlo (VMC) can be viewed as a limit of DMC at zero projection time, i.e., no branching. I define VMC as a Monte Carlo algorithm that calculates the expectation value of an operator using a fixed trial wave function Ψ_T

$$\langle \hat{O} \rangle = \langle \Psi_T | \hat{O} | \Psi_T \rangle \,. \tag{2.31}$$

When VMC is used to calculate the expectation value of the hamiltonian ($\hat{O} = \hat{\hat{\mathcal{H}}}$), the resultant energy is an upper bound to the true ground-state energy by the variational principle

$$E_V \equiv \langle \Psi_T | \hat{\hat{\mathcal{H}}} | \Psi_T \rangle = \langle \Psi_T | E_L(\boldsymbol{R}; \Psi_T) | \Psi_T \rangle \geq E_0, \tag{2.32}$$

where the local energy serves as a local estimator for the total energy

$$E_L(\boldsymbol{R}; \Psi_T) \equiv \frac{\hat{\mathcal{H}} \Psi_T}{\Psi_T}(\boldsymbol{R}). \tag{2.33}$$

The variational energy E_V is often taken as a measure of the quality of the trial wave function. In *variational optimization*, one changes parameters in Ψ_T to lower E_V. However, E_V is only one number and is far from a complete descriptor of the 3N-dimensional many-body wave function. Another, arguably more powerful, measure of the quality of Ψ_T is the variance of the local energy eq. (2.33)

$$\sigma^2[\Psi_T] \equiv \langle \Psi_T | (E_L(\boldsymbol{R}; \Psi_T) - E_V)^2 | \Psi_T \rangle \geq 0. \tag{2.34}$$

This variance will be zero if Ψ_T is any eigenstate of $\hat{\mathcal{H}}$. Further, for systems with a gap E_g, σ^2 and E_V also provide a lower bound for the ground-state energy by eq. (6.16) in Ref. [24]

$$E_V - \sigma^2 / E_g \leq E_0 \leq E_T. \tag{2.35}$$

The VMC algorithm is particularly simple for a local observable. In this case, eq. (2.31) becomes an integral over the $3N$-dimensional particle coordinates

$$\langle O \rangle = \int d\boldsymbol{r} \frac{O(\boldsymbol{r}) |\Psi_T(\boldsymbol{r})|^2}{\langle \Psi_T | \Psi_T \rangle}, \tag{2.36}$$

which is easily evaluated by sampling $\boldsymbol{r}$ from the probability distribution

$$P(\boldsymbol{r}) = \frac{|\Psi_T(\boldsymbol{r})|^2}{\langle \Psi_T | \Psi_T \rangle}, \tag{2.37}$$

and accumulating $O(\boldsymbol{r})$. How does one sample a generic probability distribution like $P(\boldsymbol{r})$? One can use the Metropolis algorithm to devise a Markov chain with $P(\boldsymbol{r})$ being the stationary distribution. Alternatively, $P(\boldsymbol{r})$ can be set to be the stationary distribution of a dynamical process, e.g., Fokker-Planck dynamics [25].

Suppose we wish a drift-diffusion process governed by

$$\frac{\partial f}{\partial t} = \sum_{i=1}^{N} \lambda \frac{\partial}{\partial \boldsymbol{x}_i} \left(\frac{\partial}{\partial \boldsymbol{x}_i} - \boldsymbol{v}_i(\boldsymbol{r}) \right) f \tag{2.38}$$

to have $P(\boldsymbol{r})$ as its stationary distribution

$$\lim_{t \to \infty} f(\boldsymbol{r}, t) = P(\boldsymbol{r}) \propto |\Psi_T|^2. \tag{2.39}$$

We can set each term in sum of the r.h.s. of eq. (2.38) to vanish

$$\nabla_i^2 P = P \boldsymbol{\nabla}_i \cdot \boldsymbol{v}_i + \boldsymbol{v}_i \cdot \boldsymbol{\nabla}_i P, \tag{2.40}$$

which gives the drift vector

$$\boldsymbol{v}_i = \frac{\boldsymbol{\nabla}_i f}{f} = 2 \frac{\boldsymbol{\nabla}_i \Psi_T}{\Psi_T}. \tag{2.41}$$

$\boldsymbol{v}$ pushes a walker towards peaks of $P(\boldsymbol{r})$, making the sampling process more efficient than a random move. In fact, no accept/reject procedure is necessary. The correct stationary distribution $P(\boldsymbol{r})$ will be reached so long as the time step is small enough to accurately approximate the Green function for each step. The Langevin equation needed to solve eq. (2.38) is

$$\frac{\partial \boldsymbol{r}(t)}{\partial t} = \lambda \boldsymbol{v}(\boldsymbol{r}(t)) + \boldsymbol{\eta}, \tag{2.42}$$

where $\boldsymbol{\eta}$ is a multidimensional Gaussian with a mean of zero and a variance of 2λ. In this light, the VMC algorithm is more akin to stochastic classical molecular dynamics than Monte Carlo. However, the most efficient algorithm is obtained when the Fokker-Planck formulation is combined with Metropolis Monte Carlo. By introducing a metropolis accept/reject procedure at each step of the Fokker-Planck dynamics, we eliminate the time step bias because detailed balance is enforced to sample $|\Psi_T|^2$. Another way to view this is that Fokker-Planck dynamics provides efficient drift-diffusion moves for an exact Monte Carlo method.

Equation (2.38) defines an efficient implementation of the VMC algorithm. Interestingly, the governing equation of DMC eq. (2.28) without the branching term is identical to that of VMC eq. (2.38) when the same trial wave function is used for drift eq. (2.41). This implies that the drift-diffusion term in the DMC Green function performs sampling of the trial wave function only. The local energy term in eq. (2.28), when accumulated over the drift-diffusion process, is responsible for imaginary-time projection.

2.2.5 Fermion Sign Problem

An essential difficult arises when one applies the path integral formalism to fermions. Even- and odd-permutations contribute to the fermion DM with opposite signs

$$\rho_F(\boldsymbol{r}_0, \boldsymbol{r}_M; \beta) = \frac{1}{N!} \sum_{\mathcal{P}} (-1)^{\mathcal{P}} \rho_D(\boldsymbol{r}_0, \mathcal{P}\boldsymbol{r}_M; \beta). \tag{2.43}$$

ρ_F is no longer positive definite and cannot be interpreted as a probability distribution to be sampled by Monte Carlo. The canonical workaround is to sample the absolute value of the fermionic DM, which is the bosonic DM, and keep the sign as an observable. In this way, a fermionic observable is calculated as the ratio between a signful bosonic observable and the bosonic average of the permutation sign

$$\langle \hat{O} \rangle_F \equiv \frac{\mathrm{Tr}\left(\hat{O}e^{-\beta H}\right)_F}{\mathrm{Tr}\left(e^{-\beta H}\right)_F} = \frac{\mathrm{Tr}\left(\hat{O}\hat{\sigma}e^{-\beta H}\right)_B}{\mathrm{Tr}\left(\hat{\sigma}e^{-\beta H}\right)_B} = \frac{\mathrm{Tr}\left(\hat{O}\hat{\sigma}e^{-\beta H}\right)_B / Z_B}{\mathrm{Tr}\left(\hat{\sigma}e^{-\beta H}\right)_B / Z_B} = \frac{\langle \hat{O}\hat{\sigma} \rangle_B}{\langle \hat{\sigma} \rangle_B}. \tag{2.44}$$

While mathematically exact, this leads to the well-known *fermion sign problem*, where the denominator in eq. (2.44), the average sign, goes to zero exponentially fast as system size N and inverse temperature β increase. To see this, consider the total free energies of N bosons vs. N fermions governed by the same hamiltonian H. The average sign can be written as an exponential of the free energy difference

$$\langle \hat{\sigma} \rangle_B = \frac{Z_F}{Z_B} = \frac{e^{-\beta F_F}}{e^{-\beta F_B}} = e^{-\beta(F_F - F_B)}. \tag{2.45}$$

Since the total free energy is extensive, the exponent in eq. (2.45) is proportional to βN. At zero Kelvin, all permutations are equally likely and the average sign is exactly zero. At the degeneracy temperature and above, *signful* PIMC is often possible, but comes at a hefty computational cost even for very small systems, e.g., $O(10)$ particles. A practical workaround for the sign problem in path integral is the restricted path approximation [26–28]. This approximation uses a trial density matrix to restrict the space of paths that can be sampled. Any Monte Carlo move that constructs a path which crosses the node of the trial density matrix is rejected. This restricted path integral Monte Carlo (RPIMC) method was proved to be exact if the node of the trial density matrix is exact [27].

The sign problem manifests rather differently in DMC than it does in PIMC. If one runs the bosonic DMC algorithm eq. (2.28) using the absolute value of a fermionic trial wave function $|\Psi_T|$ as guiding function, then the drift vector eq. (2.29) will diverge as a walker approaches the node of Ψ_T, pushing the walker away. This trapping effect greatly diminishes the chance that a walker can cross the node. Thus, the walker distribution will approach the bosonic solution in this positive nodal pocket. However, once a walker does cross the

node, it quickly gets pushed to regions with high $|\Psi_T|^2$ and branches to solve a similar bosonic problem in the newly found negative nodal pocket. Walkers in the positive nodal pocket contribute to estimators with a positive sign, whereas walkers in the negative pocket contribute with a negative sign. While the final average is the exact fermionic estimator, it is the difference between two large values and its noise diverges exponentially fast with system size and projection time. Exact fermionic simulation is possible using the release-node method [29], but a highly-accurate trial wavefunction is required and much care must be taken to efficiently converge the calculation before noise takes over.

The practical workaround for the sign problem in DMC is the *fixed-node approximation* (for real-valued wave functions). In this approximation, no walker is allowed to cross the node of the trial wave function. This effectively adds to the hamiltonian an infinite potential barrier at the node of Ψ_T. The bosonic problem is exactly solved in the nodal pocket within this barrier, while the rest of Hilbert space is constructed via antisymmetry of the wave function. This restricted random walk effectively constructs a *fixed-node wave function* Ψ_{FN} as an approximation to the true ground state, so the fixed-node DMC (FN-DMC) total energy is variational $E_{FN} \geq E_0$. The exact ground-state energy can be obtained if the node of the trial wave function is exact. When generalized to systems with complex-valued trial wave function, an analogous work around is the fixed-phase DMC method (FP-DMC), which forbids walkers to move past phase-change boundaries of the trial wave function. FP-DMC is so similar to FN-DMC that they are often not distinguished as different methods in the literature.

For a general fermionic system, the sign problem is present in all known QMC methods in some form. However, the sign problem can be absent in a particular system, for example due to particle-hole symmetry in a half-filled Hubbard model, and can be alleviated at finite-temperature. Unfortunately, no known polynomial-scaling algorithm can solve the sign problem in all cases.

2.3 Effective One-Particle Theories

The most widely used ground-state QMC method, FN-DMC, requires a trial wave function Ψ_T to start the imaginary time projection process. The node of Ψ_T directly controls the one uncontrolled error, the fixed-node error, in the DMC total energy. Even bosonic details of Ψ_T can matter to observables that do not commute with the hamiltonian due to the mixed-estimator error. Further, the complexity of Ψ_T affects the efficiency of a DMC run, because Ψ_T and many its derivatives need to be evaluated at every step of the algorithm. Therefore, accurate and compact trial wave functions are crucial for practical high-accuracy DMC simulations.

While it is possible to construct such trial wave functions analytically [10, 30, 31], the process is rather involved and requires deep understanding of the particular system being simulated. For a generic material, it is much easier to base the many-body trial wave function on existing mean-field theory or effective one-electron theory that approximately include some effects of electron correlation. This chapter introduces one theory in each of these two categories.

2.3.1 Hartree-Fock

2.3.1.1 The Hartree-Fock Equations

The Hartree-Fock (HF) equations are a set of equations that couple spin orbitals in a determinant wave function. They can be obtained by minimizing the energy of a Slater determinant with the constraint that spin orbitals remain orthonormal. If each molecular orbital a is written as a linear combination of a set of basis functions $\{\phi_\mu\}$

$$\psi_a = \sum_{\mu=1}^{K} C_{\mu a}\phi_\mu, \tag{2.46}$$

then the constraint optimization problem can be converted to a set of linear equations, resulting in an eigenvalue problem. However, the eigenvectors of this linear problem are needed to construct the problem to be solved. This self-consistency requirement makes the HF equations non-linear, thus requiring an iterative solver. Once an initial guess for the eigenvectors $C_{\mu a}$ have been chosen, one can construct the linear problem to be solved via a *Fock matrix*. For a spin-unpolarized system $N_\uparrow = N_\downarrow = N/2$, the restricted Hartree-Fock (RHF) solution is defined by the first $N/2$ eigenvectors of the Fock matrix

$$F_{\mu\nu} = H^{\text{core}}_{\mu\nu} + \sum_{\lambda\sigma} P_{\lambda\sigma}\left[(\mu\nu|\sigma\lambda) - \frac{1}{2}(\mu\lambda|\sigma\nu)\right], \tag{2.47}$$

where $P_{\lambda\sigma} = 2\sum_{a=1}^{N/2} C_{\lambda a}C^*_{\sigma a}$ is the density matrix of the trial states. The *Coulomb integral* notation

$$(\mu\nu|\lambda\sigma) = \iint d\boldsymbol{r}_1 d\boldsymbol{r}_2 \psi^*_\mu(\boldsymbol{r}_1)\psi_\nu(\boldsymbol{r}_1)\frac{1}{|\boldsymbol{r}_1 - \boldsymbol{r}_2|}\psi^*_\lambda(\boldsymbol{r}_2)\psi_\sigma(\boldsymbol{r}_2). \tag{2.48}$$

$H^{\text{core}}_{\mu\nu}$ is the one-electron part of the Hamiltonian expressed in the given basis

$$H^{\text{core}}_{\mu\nu} = \int d\boldsymbol{r}_1 \phi^*_\mu(\boldsymbol{r}_1)\left(-\frac{1}{2}\nabla_1^2 - \sum_A \frac{Z_A}{|\boldsymbol{r}_1 - \boldsymbol{R}_A|}\right)\phi_\nu(\boldsymbol{r}_1). \tag{2.49}$$

The RHF total energy is the expectation of the electronic hamiltonian in the determinant wave function

$$\Psi_{RHF} = D_{\uparrow}(\{\psi_a\})D_{\downarrow}(\{\psi_a\}), \tag{2.50}$$

$$E_0^{RHF} \equiv \langle \Psi_{RHF}|\hat{\mathcal{H}}|\Psi_{RHF}\rangle = 2\sum \langle \psi_a|H_{\mu\nu}^{\text{core}}|\psi_a\rangle + \sum_{a=1}^{N/2}\sum_{b=1}^{N/2}\langle ab||ab\rangle\,, \tag{2.51}$$

where the *exchange integral* is defined as

$$\langle ab||ab\rangle \equiv \int d\boldsymbol{r}_1 d\boldsymbol{r}_2 \psi_a^*(\boldsymbol{r}_1)\psi_b^*(\boldsymbol{r}_2)r_{12}^{-1}(1-\mathcal{P}_{12})\psi_c(\boldsymbol{r}_1)\psi_d(\boldsymbol{r}_2). \tag{2.52}$$

Importantly, E_0^{RHF} is not the sum of the eigenvalues of the Fock operator

$$2\sum_{a=1}^{N/2}\epsilon_a = 2\sum \langle \psi_a|H_{\mu\nu}^{\text{core}}|\psi_a\rangle + 2\sum_{a=1}^{N/2}\sum_{b=1}^{N/2}\langle ab||ab\rangle = E_0^{RHF} - \sum_{a=1}^{N/2}\sum_{b=1}^{N/2}\langle ab||ab\rangle\,, \tag{2.53}$$

because it double counts Coulomb interaction. The root cause if that both ϵ_a and ϵ_b include the Coulomb interaction energy between orbitals a and b. Not being able to sum the eigenvalues to obtain the total energy is a minor inconvenience for the fact that these eigenvalues have the physical meaning of electron/hole excitation energies. Since the HF method constructs a determinant as trial wave function for the exact electronic hamiltonian, the HF energy is variational $E_0^{RHF} \geq E_0$.

The RHF equations can be generalized to treat open-shell systems. If $N_\uparrow \neq N_\downarrow$, but the spatial part of each occupied orbital is required to be identical for the $\uparrow$ and $\downarrow$ electrons. Then, the method is known as restricted open-shell HF (ROHF). If the occupied orbitals are further allowed to differ, then the method is unrestricted (UHF). An application of RHF to the isolated H_2 molecule is detailed in Appendix B.

2.3.1.2 Koopmans Theorem

HF theory can be used to study excitations from the ground state. Consider removing an electron from orbital $\delta \leq N$, thus creating a hole (h). The wave function for the $(N-1)$-electron system is [32]

$$|\Psi_{HF}^{(h,\delta)}\rangle = \hat{a}_\delta\,|\Psi_{HF}\rangle\,. \tag{2.54}$$

In the frozen orbital approximation, where the orbitals of the remaining electrons cannot respond to the removed one, the energy of this wave function can be shown to differ from the ground state by ϵ_δ, the HF

eigenvalue of the orbital being emptied

$$E_{HF}^{(h,\delta)} \equiv \langle |\Psi_{HF}^{(h,\delta)}\rangle \, |\hat{\mathcal{H}}| \, |\Psi_{HF}^{(h,\delta)}\rangle \rangle = E_{HF} - \epsilon_\delta. \tag{2.55}$$

T. Koopmans [33] first proved this for the highest occupied molecular orbital (HOMO) as an approximation to the ionization energy, although the above derivation is general for any orbital. Following Chapter 2.2.3 in Ref. [32], one can similarly calculate the energy of an N-electron system that differs from the HF ground state by an electron-hole excitation

$$|\Psi_{HF}^{(e,\gamma;h,\delta)}\rangle = \hat{a}_\gamma^\dagger \hat{a}_\delta \, |\Psi_{HF}\rangle \, , \; \gamma > N, \; \delta \leq N. \tag{2.56}$$

$$E_{HF}^{(e,\gamma;h,\delta)} = E_{HF} + \epsilon_\gamma - \epsilon_\delta - \Delta_{\gamma\delta}, \tag{2.57}$$

where $\Delta_{\gamma\delta} > 0$. For a stable HF solution, eq. (2.57) leads to a *coulomb gap* in the HF density of states

$$N(e) < 2^{d-1} d \left(\frac{\epsilon}{e^2}\right)^d (e - e_F)^{d-1}, \tag{2.58}$$

where d is the number of spatial dimensions, and ϵ is the dielectric constant of the insulator. That is, the HF density of states must vanish at least as fast as $(e - e_F)^{d-1}$ around the Fermi energy e_F.

Koopmans theorem is only applicable relative to the HF ground state. For example, one cannot repeatedly apply Koopmans theorem to reconstruct the total energy of the system by stripping one electron at a time. As shown in eq. (2.53), the sum of HF eigenvalues double counts the Coulomb interaction energy.

2.3.1.3 Basis Set Error

To obtain a converged HF solution, the basis set used to represent the spin orbitals, i.e. $\{\phi_\mu\}$ in eq. (2.46), must be complete. In practice, one can approach this *complete basis set limit* by using a sequence of basis sets increasing in size. The correlation-consistent (cc) basis sets are a widely used standard for this purpose. The convergence of the total energy of an H_2 molecule is shown in Fig. 2.1 and compared to the exact references obtained by Kolos and Wolniewicz (KW) [34]. The total energy is converged on the scale of the plot using a triple-zeta (TZ) basis, which contains three basis functions per atom, and above. All RHF energy curves are at least 40 mha above the exact solution of the Schrödinger equation including electron-electron correlation, in accordance with the variational principle. Further, even after basis-set convergence, the RHF energy is still quite different from the exact values. Remarkably, besides an overall shift, the HF curve agrees well with the KW curve at equilibrium bond length 1.4 bohr and below. However, at larger bond lengths the

HF energy increases faster than the KW curve and is above the exact total energy at infinite separation. This is because the two electrons are forced into the same orbital, when they should each reside close to a different proton. This correlation between unlike-spin electrons is completely absent from the HF method. The difference between the exact and the RHF energies defines the *correlation energy*.

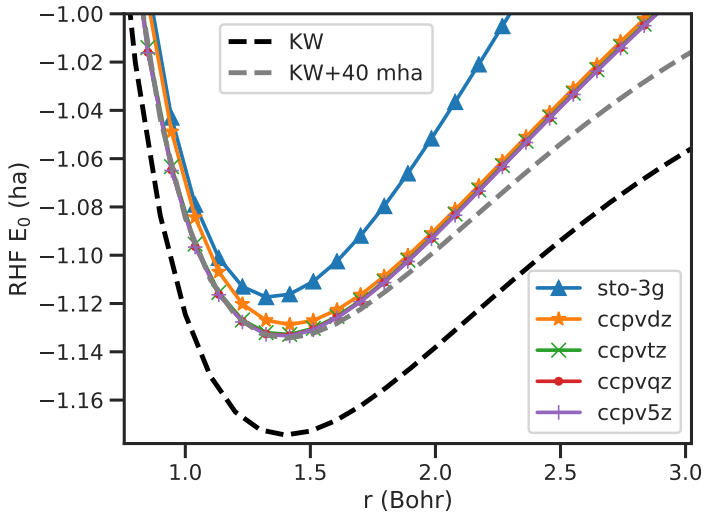

Figure 2.1: RHF electronic ground-state energy of H_2 in STO-3G and correlation consistent (cc) basis sets as compared to the exact values calculated by Kolos and Wolniewicz (KW) [34]

2.3.1.4 Beyond Hartree-Fock

Even when the complete basis set limit is reached, the HF solution is still not the exact electronic ground state due to its neglect of electron correlation. One way to account for correlation effects is to perform a determinant expansion eq. (2.59). The unoccupied *virtual* orbitals can be used to construct N-electron determinants that differ from the HF ground state by changing orbital occupation. These determinants form a many-body basis, in which any wave function can be expressed as a linear combination. This leads to the configuration interaction (CI) expansion, where the exact electronic ground state is expanded as a sum of determinants

$$\psi_0 = \lim_{M\to\infty} \sum_{i=0}^{M} c_i \left|D_i\right\rangle . \tag{2.59}$$

If all determinants that differ by one particle-hole excitation from reference are considered, then we obtain a CI singles (CIS) expansion. If these and all determinants with two particle-hole excitations are considered, then the expansion is CI singles and doubles (CISD), etc.. If all excitations among a set of "active" orbitals

are considered, then the expansion is said to involve the complete active space (CAS).

2.3.1.5 Static and Dynamic Correlation

The ground state is said to have *static correlation* if one or more determinants in the exact expansion eq. (2.59) are nearly degenerate with the reference determinant. This will happen if there are virtual orbitals nearly degenerate with the highest occupied molecular orbital. In contrast, the system has *dynamic correlation* if the c_i coefficients are small but non-zero for many determinants with high levels of excitation. Dynamic correlation is often attributed to strong local correlation such as the electron-electron cusp condition. The current definition of static and dynamic correlations is not precise [35]. I introduce the above working definitions, because static correlation can be interpreted as a delocalization error due to fractional electron [36], and is related to the self-interaction error in density functional theory (DFT). This bridges the languages used in quantum chemistry and condensed matter as well as points to a solution of the infamous "bandgap problem", to be introduced in Sec. 2.3.2.3.

While the HF method enjoys much success in the study of atoms, its complete neglect of (Coulomb) electron correlation is woefully inadequate for many solids. The HF total energy is dominated by inner shell contributions, which overshadows the valence contributions important for correlated excitations in solids. The HF energy eigenvalues show vanishing density of states at the Fermi level in metals and unphysically large band gaps in insulators [37].

2.3.2 Kohn-Sham Density Functional Theory

Using a mapping from electron density to total energy, density functional theory (DFT) is a method that can, in principle, exactly include electron correlation effects. Though the exact density functional is unknown, even approximate functionals can lead to useful results. DFT uses the three-dimensional total electron density $n(\boldsymbol{r})$ as the basic variable rather than the 3N-dimensional many-body wave function $\Psi(\boldsymbol{r}_1, \ldots, \boldsymbol{r}_N)$. This is a dramatic simplification that likely lead to its dominance in modern electronic structure theory of solids and material science.

2.3.2.1 The Hohenberg-Kohn theorems

While having roots in Thomas-Fermi theory [38], DFT was put on firm theoretical foundation by P. Hohenberg and W. Kohn (HK) in 1964 [39], where they calculate the total electronic energy E from an external

potential $v(\boldsymbol{r})$ and a functional of the ground-state electron density

$$E \equiv \int d\boldsymbol{r} n(\boldsymbol{r}) v(\boldsymbol{r}) + F[n(\boldsymbol{r})]. \tag{2.60}$$

Two theorems are often attributed to this work:

Definition 2.1. *V-representable density* A density $n(\boldsymbol{r})$ is V-representable if it is the ground-state density of some Hamiltonian H in an external potential $v(\boldsymbol{r})$.

Theorem 2.1. Assuming non-degenerate ground state, any V-representable ground-state density $n(\boldsymbol{r})$ uniquely determines its external potential $v(\boldsymbol{r})$.

Proof. by contradiction: Suppose there are two distinct external potentials v and v' that give rise to the same density n via different hamiltonians H, H' and wave functions Ψ and Ψ', respectively. By the variational principle $\langle\Psi'|H'|\Psi'\rangle + \langle\Psi'|v'-v|\Psi'\rangle = \boxed{\langle\Psi'|H|\Psi'\rangle > \langle\Psi|H|\Psi\rangle} = \langle\Psi|H'|\Psi\rangle + \langle\Psi|v'-v|\Psi\rangle > \langle\Psi'|H'|\Psi'\rangle + \langle\Psi|v'-v|\Psi\rangle$. Since Ψ and Ψ' give the same density, the local term $\langle v'-v\rangle$ cancels to give $\langle\Psi'|H'|\Psi'\rangle > \langle\Psi'|H'|\Psi'\rangle$, which is a contradiction. □

Theorem 2.2. Assuming number-conserving density variations that retain V-representability, the energy functional has a unique minimum at the ground-state density.

Proof. Consider an external potential v, its hamiltonian H, and its unique ground state Ψ and density n. After a number-conserving variation, the new wave function Ψ' can be used with the original hamiltonian and $\langle\Psi'|H|\Psi'\rangle > \langle\Psi|H|\Psi\rangle$ by the variational principle. □

These initial proofs by HK have two important assumptions: 1. the ground-state is non-degenerate and 2. the electron density $n(\boldsymbol{r})$ is V-representable. The latter is especially sever because reasonable densities were shown not to be V-representable [40, 41]. Fortunately, M. Levy proved that both assumptions can be weakened [42]. The HK theorems hold for N-representable densities regardless of ground-state degeneracy.

Definition 2.2. *N representable density* A density $n(\boldsymbol{r})$ is N-representable if it can be obtained from some many-body wave function of N particles.

While less publicized, HK also pointed out that the exact density functional less the direct/Column contribution can be calculated from a local energy-density functional $g_{\boldsymbol{r}}[n]$

$$G[n] \equiv F[n] - \frac{1}{2}\int d\boldsymbol{r} d\boldsymbol{r}' \frac{n(\boldsymbol{r})n(\boldsymbol{r}')}{|\boldsymbol{r}-\boldsymbol{r}'|} = \int \boldsymbol{r} g_{\boldsymbol{r}}[n], \tag{2.61}$$

$$g_{\boldsymbol{r}}[n] \equiv \frac{1}{2}\nabla_{\boldsymbol{r}}\nabla_{\boldsymbol{r}'} n_1(\boldsymbol{r},\boldsymbol{r}')|_{\boldsymbol{r}=\boldsymbol{r}'} + \frac{1}{2}\int d\boldsymbol{r}' \frac{C_2(\boldsymbol{r}-\boldsymbol{r}'/2;\boldsymbol{r}+\boldsymbol{r}'/2)}{|\boldsymbol{r}'|}, \tag{2.62}$$

which is constructed from one- and two-body reduced density matrices n_1 and C_2. They even went as far as to relate the leading-order behavior of the density functional to polarizability

$$G[n] = G[n_0] + \int d\boldsymbol{r} d\boldsymbol{r}' K(\boldsymbol{r} - \boldsymbol{r}')\tilde{n}(\boldsymbol{r})\tilde{n}(\boldsymbol{r}') + h.o., \tag{2.63}$$

where $\tilde{n}$ is a small number-conserving density variation and the kernel K is related to the polarizability in reciprocal space

$$K(\boldsymbol{r} - \boldsymbol{r}') = \frac{1}{\Omega}\sum_{\boldsymbol{q}} K(\boldsymbol{q}) e^{-i\boldsymbol{q}\cdot(\boldsymbol{r}-\boldsymbol{r}')}, \tag{2.64}$$

$$K(\boldsymbol{q}) = \frac{2\pi}{q^2}\left[\frac{1}{\alpha(\boldsymbol{q})} - 1\right] = \frac{2\pi}{q^2}\frac{1}{\epsilon(\boldsymbol{q})}, \tag{2.65}$$

where $\alpha(\boldsymbol{q})$ and $\epsilon(\boldsymbol{q})$ are the polarizability and dielectric constant, respectively. The HK theorems and limits provide some checks for practical parametrization of the exact density functional. Unfortunately, they provide no guidance on how one might start to construct numerical approximations to the exact functional.

2.3.2.2 The Kohn-Sham equations

One year after HK, W. Kohn and L. J. Sham (KS) [43] worked out practical guidelines for constructing approximations to the exact density functional. KS first partitioned the total energy to highlight the least-understood "exchange-correlation" term $E_{xc}[n]$.

$$E = \int d\boldsymbol{r} n(\boldsymbol{r}) v(\boldsymbol{r}) + \frac{1}{2}\int d\boldsymbol{r} d\boldsymbol{r}' \frac{n(\boldsymbol{r})n(\boldsymbol{r}')}{|\boldsymbol{r} - \boldsymbol{r}'|} + T[n] + E_{\mathrm{xc}}[n], \tag{2.66}$$

where T is a kinetic energy functional. KS then approximated E_{xc} by the corresponding contribution in the homogeneous electron gas, the local density approximation (LDA)

$$E_{\mathrm{xc}}[n] = \int d\boldsymbol{r} n(\boldsymbol{r}) \epsilon_{\mathrm{xc}}(n(\boldsymbol{r})). \tag{2.67}$$

Next, by minimizing eq. (2.66) with respect to number-conserving density variation, they obtained the stationary condition for the ground-state density

$$\int \delta n \left[\frac{\delta T[n]}{\delta n} + v(\boldsymbol{r}) + \int d\boldsymbol{r}' \frac{n(\boldsymbol{r}')}{|\boldsymbol{r} - \boldsymbol{r}'|} + \frac{d(n\epsilon_{\mathrm{xc}}(n))}{dn}\right] = 0. \tag{2.68}$$

To solve eq. (2.68), KS *assumed* that the ground-state density n came from an auxiliary system of non-interacting electrons, i.e., a Slater determinant. This KS *ansatz* turns eq. (2.68) into a system of one-particle equations of non-interacting particles in some effective potential v_{KS}^{eff} determined by the density $n(\boldsymbol{r})$. Most practical implementations of DFT use the KS auxiliary-system formulation.

Practical success of the DFT LDA method was not realized until 1981, when J. P. Perdew and A. Zunger (PZ) [37] parametrized exact quantum Monte Carlo data of the homogeneous electron gas, obtained by D. M. Ceperley and B. J. Alder [44] the year prior. PZ's eq. (13-17) define the KS-DFT method and the LDA we use today. The electron density for spin σ is a sum of occupied spin orbitals squared

$$n_\sigma = \sum_\sigma \sum_{a=1}^{N_\sigma} f_{a\sigma} |\psi_{a\sigma}(\boldsymbol{r})|^2, \tag{2.69}$$

where the occupation numbers $f_{a\sigma} \in [0, 1]$, and the kinetic energy is the sum of contributions from all occupied spin orbitals of the non-interacting system

$$T_s[n] = \sum_\sigma \sum_{a=1}^{N_\sigma} f_{a\sigma} \left\langle \psi_{a\sigma} \right| -\frac{1}{2}\nabla^2 \left| \psi_{a\sigma} \right\rangle . \tag{2.70}$$

Minimizing eq. (2.66) with the constraint that the spin orbitals remain orthonormal, PZ obtains

$$\frac{\delta}{\delta\psi_{a\sigma}} \left[T_s[n] + \int d\boldsymbol{r} v(\boldsymbol{r}) + \int d\boldsymbol{r} \int d\boldsymbol{r}' \frac{n(\boldsymbol{r}')}{|\boldsymbol{r} - \boldsymbol{r}'|} + \frac{\delta}{\delta n_\sigma} E_{xc}(n_\uparrow, n_\downarrow) \right] . \tag{2.71}$$

2.3.2.3 The Band Gap Problem

The Kohn-Sham eigenvalues do not have the same physical meaning as the Hartree-Fock eigenvalues as given by Koopmans theorem. Thus, a band gap "problem" arises when one compares the HOMO-LUMO gap from KS-DFT to experimental measurements of the fundamental gap E_g. The eigenvalue of the Kohn-Sham HOMO can be identified with the ionization energy of an isolated molecule if the exchange-correlation potential vanish at infinity. This is a special case, because the ionization energy is dominated by the long-range asymptotic behavior of the 1RDM, which is determined by the long-range tail of the electronic density with no contribution from the short-sighted exchange correlation potential.

When extended to handle systems with fractional electron number, the derivative discontinuity of the exact density functional is E_g. It has contribution from both the non-interacting kinetic functional $T_s[n]$ and the exact exchange-correlation functional $E_{xc}[n]$. The KS HOMO-LUMO gap measures the derivative discontinuity in $T_s[n]$. However, as shown in Fig. 2.2, the $E_{xc}[n]$ under LDA is smooth, so its contribution to the gap is missing. As a result, the LDA gap is $\sim 50\%$ that of experiment, showing that the derivative

discontinuity in $E_{xc}[n]$ can be of similar magnitude as the gap and cannot be ignored.

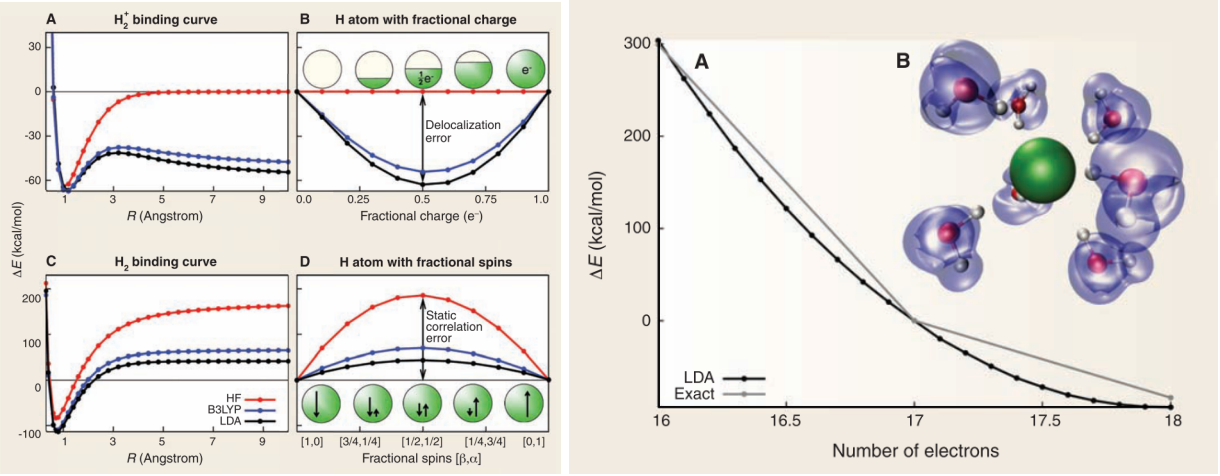

Figure 2.2: A. J. Cohen, P. Mori-Sánchez, and W. Yang [36] explains that the self-interaction error in H_2^+ binding curve (left panel A) is due to the presence of fractional electron (left panel B), which leads to a delocalization error when LDA is used.

2.3.2.4 Beyond Local Density Approximation

While extremely successful, the LDA has well-documented deficiencies. As discussed in Sec. 2.3.2.3, LDA underestimates the band gap due to a lack of derivative discontinuity. Further, it tends to overestimate the binding energy of molecular systems. This is attributed to the logarithmic divergence of the LDA correlation functional as density tends to infinity (see eq. (7.55) in Ref. [32]).

The logarithmic divergence of the LDA is largely corrected by the generalized gradient approximation (GGA). This modification is not as straight-forward as adding an extra term that depends on the gradient of the electron density $\boldsymbol{\nabla} n$ to the exchange-correlation function. An arbitrary choice of the gradient term can distort the xc hole and break the sum rule that controls its global strength

$$\int \boldsymbol{r}' n(\boldsymbol{r}')[g(\boldsymbol{r}, \boldsymbol{r}') - 1] = -1. \tag{2.72}$$

J. Perdew and co-workers overcame this difficulty by introducing a real-space cutoff to the exchange hole. While the details are technical, the final form of the GGA exchange functional is elegant

$$E_x^{GGA}[n] = \int d\boldsymbol{r} n(\boldsymbol{r}) \epsilon_x(n(\boldsymbol{r})) F_x(\boldsymbol{s}(\boldsymbol{r})), \tag{2.73}$$

where ϵ_x is the LDA exchange function and the scaled gradient

$$\boldsymbol{s}(\boldsymbol{r}) = \frac{\boldsymbol{\nabla} n(\boldsymbol{r})}{2k_F(\boldsymbol{r})n(\boldsymbol{r})}. \tag{2.74}$$

A simple form for the *exchange enhancement factor* F_x was given by J. Perdew, K. Burke, and E. Ernzerhof [45] in 1996. After another careful cutoff on the correlation functional, the immensely popular PBE functional was constructed. The PBE xc functional takes the same form as eq. (2.73), but with a different enhancement factor: F_{xc} instead of F_x. PBE softens molecular bonds relative to the LDA and predicts an order of magnitude more accurate dissociation energies of many molecules [45].

Unfortunately, both LDA and PBE suffer from a well-known failure of any local and semi-local density functional theory: the absence of Van der Waals interaction. This interaction is entirely due to the correlation of density fluctuations and is dominant for two neutral objects with non-overlapping electron densities. When fluctuation creates an instantaneous dipole moment in one electron distribution, it induces an anti-aligned dipole moment in the other. The van der Waals interaction is thus attractive and decays as dipole-dipole interaction strength, $\frac{1}{r^6}$, in the separation distance r between the centers of the two distributions. While KS-DFT relies on the average electron density of a non-interacting system, it is still possible to include the contribution of Van der Waals interaction in the density functional. Consider the Coulomb interaction as a perturbation to two widely separated atoms, one can show that the interaction energy is proportional to a convolution of the density-density response functions of the isolated atoms

$$\begin{aligned}\langle \hat{H}_{12} \rangle = -\frac{\hbar}{2\pi} \int d\boldsymbol{r}_1 d\boldsymbol{r}_1' \int d\boldsymbol{r}_2 d\boldsymbol{r}_2' \frac{e^2}{|\boldsymbol{r}_1 - \boldsymbol{r}_2|} \frac{e^2}{|\boldsymbol{r}_1' - \boldsymbol{r}_2'|} \\ \times \int \lim_0^\infty \chi_1(\boldsymbol{r}_1, \boldsymbol{r}_1') \chi_2(\boldsymbol{r}_2, \boldsymbol{r}_2') + h.o.,\end{aligned} \tag{2.75}$$

as written in eq. (7.116) in Ref. [32]. One can then proceed to approximate the density-density response function using the static electron density, e.g. using the polarizability of the homogeneous electron gas.

Finally, exact-exchange functionals such as PBE0 and HSE [46] have been developed for atoms having localized valence electrons, e.g., with d or f angular momentum. These functionals are crucial in the study of magnetism, as the PBE functional overly favor delocalized electrons and often predict qualitatively wrong magnetic momentum and spin orderings of transition metals. However, these exact-exchange functionals were never a focus throughout this thesis, so I will not go into details here.

Chapter 3

Slater-Jastrow wave function

In the previous chapter, I introduced the FN-DMC method, which calculates ground-state properties of a many-body system starting from a trial wave function Ψ_T. The accuracy and efficiency of the method depend on the choice of Ψ_T. Understanding of the many-body wave function and its connection to physical properties of particular systems can help us make educated guesses at high-quality trial wave function and perform accurate simulations. In this chapter, I will describe the most well-understood many-body wave function for electronic structure, the Slater-Jastrow wave function, and discuss what behavior of electrons we can learn from it.

The many-body wave function is also interesting in its own right. One goal of studying the many-body wave function is to understand electron correlation [47]. As P.A.M. Dirac pointed out, knowing the Dirac/Schrödinger equation and the hamiltonian of the system does not constitute an understanding, because it "leads to equations much too complicated to be soluble" [48]. Even a simple hamiltonian that contains only pair interactions, e.g., the Coulomb hamiltonian, can create complex many-body correlations and phase diagrams. Thus, direct studies of experimental observables, the many-body wave function, and perhaps properties the exact density functional will be more informative.

3.1 Historic Overview

In condensed matter, the development of many-body wave function took off in the study of homogeneous quantum liquids, e.g., liquid helium and the homogeneous electron gas, a.k.a. jellium. Most studies made use of the variational principle eq. (2.32), which states that given a Hamiltonian $\hat{\mathcal{H}}$, any normalized trial wave function Ψ_T will have an energy value no less than that of the true ground state $\langle\Psi_T|\hat{\mathcal{H}}|\Psi_T\rangle \geq \langle\Psi_0|\hat{\mathcal{H}}|\Psi_0\rangle$. This principle allowed the pioneers to make educated guesses, then check their quality using the expectation value of $\hat{\mathcal{H}}$.

As early as 1934, E. Wigner [49] noted that by introducing a "hole" in the correlation function of opposite-spin elections, one can improve the Slater determinant and lower its energy value in the homogeneous electron

gas. Although, this hint was not acted on until much later. In 1940, A. Bijl [50] found that the logarithm of the wave function of many-interacting particles is size-extensive. This logarithm can be expressed as a perturbation expansion involving one- and two-electron terms and is convergent in the thermodynamic limit. Unfortunately, this work went unnoticed for 30 years while others independently developed similar ideas. Expanding the logarithm of the wave function is a general idea that later became known as the Bijl-Dingle-Jastrow-Feenberg expansion [51] for historical reasons, which I will now describe.

In 1949, R. B. Dingle [52], while estimating the zero-point energy of hard spheres, came up with a product of exponential functions as a variational wave function by considering symmetries and limits. In 1955, R. Jastrow [53] generalized the Dingle pair-product wave functions to indistinguishable particles with Bose and Fermi statistics. To generalize to fermions, he multiplied by a Slater determinant to enforce antisymmetric permutation symmetry. Thus, the Slater-Jastrow wave function was born. While this thesis is mostly focused on the Slater-Jastrow wave function for electronic matter, the idea of separating particle statistics from correlation is general. The Slater-Jastrow wave function is the fermion variant of eq. (3.1)

$$\Psi = \begin{cases} I(\{\phi_i\})\exp(-U) & \text{distinguishabe} \\ P(\{\phi_i\})\exp(-U) & \text{bosons} \\ D(\{\phi_i\})\exp(-U) & \text{fermions} \end{cases}, \tag{3.1}$$

where I, P, D are identity, permanent, and determinant, respectively. $\{\phi_i\}$ is a set of single-particle wave functions and U consists of pair terms only

$$U = \sum_{i<j} u(r_i j). \tag{3.2}$$

The minus sign in the definition of eq. (3.1) is intentional. At high temperature, $|\Psi|^2$ for distinguishable particles becomes the Bolzmann distribution eq. (2.6). When only pair interaction is present, the pair contribution to U has the same sign as the potential (see Chapter 6.6 in Ref. [24])

$$\lim_{\beta\to 0} u(r_i j) = \frac{1}{2}\beta v(r_i j). \tag{3.3}$$

Some important improvements to eq. (3.1) came from the study of bosons rather than fermions.

In 1956, R.P. Feynman and M. Cohen [54] found it crucial to include the effect of back flow to accurately describe rotons in liquid helium. A roton is the quantum analog of a microscopic vortex ring. When an atom moves through the ring, it triggers a returning flow far from the ring, a.k.a. back flow. R.P. Feynman

first estimated the energy-momentum curve of liquid helium using a permanent of plane wave orbitals in 1954, but found the roton energies severely over-estimated [55]. It is only after the introduction of back flow into the trial wave function did the roton energy reduce to a reasonable value, in qualitative agreement with the phenomenological theory of Landau and with experiment [54]. In 1961, F.Y. Wu and E. Feenberg [56] related the Jastrow pair function, $u(r)$ in eq. (3.2), to the pair correlation function of liquid helium

$$u(r) = g(r) - \frac{1}{8\pi^3\rho}\int d\boldsymbol{k} e^{-i\boldsymbol{k}\cdot\boldsymbol{r}} \frac{[S(k)-1]^2}{1+\xi[S(k)-1]}, \tag{3.4}$$

where $\xi \approx 0.97$ gave accurate results under the superposition approximation. Direct relation between experimentally measurable correlation functions and the wave function is an important avenue to glean understanding from the many-body wave function. Similar ideas arose in the study of fermions in the same year.

Also in 1961, T. Gaskell [57] derived a Jastrow pair function for homogeneous electron gas from perturbation calculation of its pair correlation function. He expressed the Jastrow pair function in collective coordinates and derived an analytical formula using the random phase approximation (RPA). By minimizing the total energy in the long wavelength limit, Gaskell found an accurate Jastrow pair function, having correct limits at both short and long wavelengths. This Gaskell RPA wave function proved particularly useful in the study of the homogeneous electron gas and will be discussed in Sec. 3.4, then extended in Sec. 3.5. Remarkably, this wave function is accurate in both 2D and 3D. Using the Gaskell RPA wave function as trial function, in 1980, D. M. Ceperley and B. J. Alder [44] found the ground state of the homogeneous electron gas in 3D using exact QMC simulations.

A common theme of these early successes is guessing and checking of correlation. One guesses that a many-body correlation is important, incorporates said correlation into the wave function, then checks if the energy value is lowered and/or correlation functions get closer to experiment. In contrast, recent improvements to the many-body wave function rely heavily on numerical optimization of general wave function forms with many parameters. Examples include orbital rotation in a single determinant, multi-determinant expansion, iterative back flow [58], and neural network. As we move towards these complicated wave functions, it will likely become increasingly difficult to extract physical understanding directly from the wave function. This chapter will serve as a summary of some physical insights we have been able to grasp from the Slater-Jastrow wave function. I hope some of these will remain useful for more complex wave function forms. After some definitions, I will first discuss the short-range asymptotic behavior of the two-body contribution, i.e., the cusp condition in Sec. 3.3. Second, I discuss the two-body long wavelength

behavior by studying the Gaskell RPA Jastrow in Sec. 3.4 for one-component system, then extend it to multi-component system in Sec. 3.5. Third, in Sec. 3.6, I show observables that can be calculated from the Slater determinant in plane wave basis, namely the momentum distribution from one-particle reduced density matrix (1RDM) in Sec. 3.6.1 and the static structure factor from two-particle reduced density matrix (2RDM) in Sec. 3.6.2.

3.2 Definitions

Definition 3.1. The *Fourier Transform* of a 3D function in coordinate space is defined as

$$f(\boldsymbol{k}) = \int d^3\boldsymbol{r} e^{i\boldsymbol{k}\cdot\boldsymbol{r}} f(\boldsymbol{r}). \tag{3.5}$$

The above Fourier transform convention eq. (3.5) defines its inverse

$$f(\boldsymbol{r}) = \int \frac{d^3\boldsymbol{k}}{(2\pi)^3} e^{-i\boldsymbol{k}\cdot\boldsymbol{r}} f(\boldsymbol{k}). \tag{3.6}$$

The consistency of eq. (3.5) and (3.6) can be checked using the Coulomb potential $v(\boldsymbol{r}) = \frac{1}{r}$ and $v(\boldsymbol{k}) = \frac{4\pi}{k^2}$.

In a finite cell of volume Ω, momentum states are discretized. Each state takes up $\frac{(2\pi)^3}{\Omega}$ in reciprocal space. Therefore the inverse Fourier transform (3.6) becomes

$$f(\boldsymbol{r}) = \frac{1}{\Omega} \sum_{\boldsymbol{k}} e^{-i\boldsymbol{k}\cdot\boldsymbol{r}} f_{\boldsymbol{k}}. \tag{3.7}$$

Definition 3.2. The *collective coordinates* of N particles of species α is the Fourier transform of their instantaneous number density

$$\rho^\alpha(\boldsymbol{k}) = \int d^3\boldsymbol{r} e^{i\boldsymbol{k}\cdot\boldsymbol{r}} \rho^\alpha(\boldsymbol{r}) = \int d^3\boldsymbol{r} e^{i\boldsymbol{k}\cdot\boldsymbol{r}} \sum_{j=1}^{N_\alpha} \delta(\boldsymbol{r} - \boldsymbol{r}_j^\alpha) = \sum_{j=1}^{N_\alpha} e^{i\boldsymbol{k}\cdot\boldsymbol{r}_j^\alpha}. \tag{3.8}$$

The collective coordinates provide a fixed basis for many-body functions in reciprocal space. Consider N

particles in a cell of volume Ω interacting via an isotropic pair potential $v(r)$. The potential energy

$$\begin{aligned} V =& \sum_{i<j} v(r_{ij}) = \frac{1}{2}\sum_{i\neq j} v(r_{ij}) \\ =& \frac{1}{2\Omega}\sum_{\boldsymbol{k}} v_{\boldsymbol{k}} \sum_{i\neq j} e^{-i\boldsymbol{k}\cdot(\boldsymbol{r}_i-\boldsymbol{r}_j)} \\ =& \frac{1}{2\Omega}\sum_{\boldsymbol{k}} v_{\boldsymbol{k}} \left(\rho_{\boldsymbol{k}}\rho_{-\boldsymbol{k}} - N\right). \end{aligned} \tag{3.9}$$

When generalized to multiple species, eq. (3.9) becomes

$$\begin{aligned} V =& \frac{1}{2}\sum_{\alpha,\beta}\sum_{i=1}^{N_\alpha}\sum_{j=1}^{N_\beta,(j,\beta)\neq(i,\alpha)} v^{\alpha\beta}(|\boldsymbol{r}_i^\alpha - \boldsymbol{r}_j^\beta|) \\ =& \frac{1}{2\Omega}\sum_{\boldsymbol{k}} v_{\boldsymbol{k}}^{\alpha\beta}\left(\rho_{\boldsymbol{k}\alpha\beta}^{\beta}\rho_{-\boldsymbol{k}}^{\alpha} - \delta_{\alpha\beta}N_\alpha\right). \end{aligned} \tag{3.10}$$

For particles interacting via the Coulomb pair potential

$$v^{\alpha\beta}(\boldsymbol{r}) = \frac{Q_\alpha Q_\beta}{r}, \tag{3.11}$$

where Q_α and Q_β are the charges of species α and β, respectively.

Definition 3.3. *Jastrow Pair Function*: The general form of a Jastrow wavefunction containing two-body terms is

$$\Psi = \exp\left(-U\right), \tag{3.12}$$

where

$$\begin{aligned} U =& \frac{1}{2}\sum_{\alpha,\beta}\sum_{i=1}^{N_\alpha}\sum_{j=1}^{N_\beta,(j,\beta)\neq(i,\alpha)} u^{\alpha\beta}(|\boldsymbol{r}_i^\alpha - \boldsymbol{r}_j^\beta|) \\ =& \frac{1}{2\Omega}\sum_{\boldsymbol{k}\alpha\beta} u_{\boldsymbol{k}}^{\alpha\beta}\left(\rho_{\boldsymbol{k}}^{\beta}\rho_{-\boldsymbol{k}}^{\alpha} - \delta_{\alpha\beta}N_\alpha\right). \end{aligned} \tag{3.13}$$

$u^{\alpha\beta}(\boldsymbol{r})$ is the *Jastrow pair function*. In the high temperature limit, $u^{\alpha\beta}(\boldsymbol{r}) = \frac{v^{\alpha\beta}(\boldsymbol{r})}{2k_BT}$. $u_{\boldsymbol{k}}^{\alpha\beta}$ is the Fourier transform of $u^{\alpha\beta}(\boldsymbol{r})$ in the unit cell having volume Ω as defined by eq. (3.7).

Definition 3.4. A *Slater determinant* is a many-body wavefunction ansatz for the ground state of a collection of same-spin fermions. It is the anti-symmetrized version of a product wavefunction ansatz for

distinguishable particles.

$$\Psi = \frac{1}{\sqrt{N!}} \sum_{\mathcal{P}} (-1)^{\mathcal{P}} \left(\prod_{i=1}^{N} \phi_{\mathcal{P}_i}(\boldsymbol{r}_i) \right), \tag{3.14}$$

where N is the number of fermions, $\boldsymbol{r}_1, \boldsymbol{r}_2, \ldots, \boldsymbol{r}_N$ are their spatial coordinates. $\mathcal{P}$ is a permutation of the particle indices $1, 2, \ldots, N$. $\phi_1, \phi_2, \ldots, \phi_N$ are a set of one-body wave functions (a.k.a. orbitals).

3.3 Cusp Conditions

Derivation guided by Ex. 6.6 in Ref. [24]

Consider two non-relativistic distinguishable particles having masses m_1 and m_2 interacting via a pair potential $v(r)$. The Schrödinger equation in the center-of-mass coordinate is

$$\left[-\lambda \nabla^2 + v(r) \right] \psi = E\psi, \tag{3.15}$$

where $\lambda = \frac{\hbar^2}{2\mu}$, and $\mu = (m_1^{-1} + m_2^{-1})^{-1}$. The ground-state wave function

$$\psi = \exp(-u(r)) \tag{3.16}$$

should have a stationary local energy

$$\begin{aligned} E_L \equiv \frac{\hat{\mathcal{H}}\psi}{\psi} &= v(r) + \lambda \nabla^2 u(r) - (\boldsymbol{\nabla} u(r))^2 \\ &= v(r) + \lambda(u'' + \frac{(d-1)u'}{r}) - \lambda u'^2 = \text{const.}, \end{aligned} \tag{3.17}$$

where d is the number of spatial dimensions. We see that the laplacian term in the kinetic energy has a potentially divergent term at $r = 0$. This term can respond to the potential and keep E_L stationary, even if $v(r)$ has a divergence at $r = 0$, e.g., the Coulomb potential. Suppose the two particles have charges q_1, q_2, and $v(r) = q_1 q_2 / r$, the condition for stationary E_L is

$$\lim_{r \to 0} \frac{1}{r}(q_1 q_2 + \lambda(d-1)u') = 0 \Rightarrow u'(0) = -\frac{q_1 q_2}{\lambda(d-1)} \tag{3.18}$$

For electron-electron interaction in Hartree atomic units $m_1 = m_2 = 1$, so $\lambda = 1$ and $u'(0) = -\frac{1}{2}$ in 3D. This is the cusp condition for unlike-spin electron pair. For same-spin pair, the two particles are indistinguishable and the laplacian for each particle contributes a copy of the divergent term, thus $u'(0) = -\frac{1}{4}$. For an

electron-ion pair in the clamped-ion approximation ($m_2 \to \infty$)

$$u'(0) = \frac{2Z}{d-1}, \tag{3.19}$$

where Z is the atomic number of the ion. Imposing the cusp conditions on a trial wave function greatly reduces the variance of the local energy and improves the efficiency of a QMC calculation. The electron-ion cusp eq. (3.19) is the most important one to maintain, because the wave function amplitude around an ion is high and many samples from the MC algorithm will have some electron close to an ion. In contrast, one rarely samples a configuration with two electrons close together due to strong electron-electron repulsion at density relevant for materials science, e.g., bulk silicon. However, at high density, electron-electron correlation is weak relative to kinetic energy, so the electron-electron cusp condition is important to maintain. Nevertheless, the effect of imposing the electron-electron cusp condition is typically less pronounced than that of the electron-ion one.

3.4 Gaskell RPA Jastrow

The RPA Jastrow potential electron gas in 3D given by T. Gaskell [29, 57, 59, 60] is

$$2\rho u_k^{RPA} = \left[\left(S_0(k)^{-2} + 2\rho v_k/\epsilon_k\right)^{-1/2}\right]^{-1} - S_0(k)^{-1}, \tag{3.20}$$

where the ν_k is the Coulomb potential in reciprocal space and ϵ_k is the energy-momentum dispersion relation. For non-relativistic electrons in 3D, $\nu_k = \frac{4\pi}{k^2}$ and $\epsilon_k = \frac{k^2}{2}$ using Hartree atomic units. $S_0(k)$ is the static structure factor of the free Fermi gas [61]

$$S_0(k) = \left\{\frac{3}{4}\left(\frac{k}{k_F}\right) - \frac{1}{16}\left(\frac{k}{k_F}\right)^3\right\}\Theta(2k_F - k) + \Theta(k - 2k_F). \tag{3.21}$$

Gaskell [57] used an integral identity to obtain an approximate relation between the Jastrow potential and the static structure factor

$$2\rho u_{\boldsymbol{k}} \approx S^{-1}(\boldsymbol{k}) - S_0^{-1}(\boldsymbol{k}). \tag{3.22}$$

Therefore, the RPA structure factor can be read off of u_k^{RPA} in eq. (3.20) via eq. (3.22)

$$S^{RPA}(k) = \left(S_0^{-2}(k) + 2\rho v_k/\epsilon_k\right)^{-1/2}, \tag{3.23}$$

where k_F is the Fermi k-vector. For unpolarized electrons $k_F = 3\pi^2\rho = \left(\frac{9\pi}{4r_s^3}\right)^{1/3}$.

Equation (3.23) is exact in the long wavelength $k \to 0$ limit. Taylor expanding eq. (3.23) around $k = 0$

$$S(k) = \frac{k^2}{2\omega_p} - \frac{k_F^2 k^4}{9\omega_p^3} + O\left(k^6\right), \tag{3.24}$$

where the plasmon frequency $\omega_p = \sqrt{4\pi\rho} = \sqrt{3/r_s^3}$.

While Gaskell originally derived eq. (3.20) using perturbation theory, one can derive the same form by minimizing the variance of the local energy in the long wavelength limit, as shown in the next Sec. 3.5.

3.5 Multi-Component RPA Jastrow

Based on notes from D. M. Ceperley dated Sep. 1980

Given Jastrow wavefunction $\Psi = \exp(-U)$, where

$$U = \sum_{i<j} u(r_{ij}) = \frac{1}{2}\sum_{\alpha,\beta}\sum_{i=1}^{N_\alpha}\sum_{j=1}^{N_\beta,(j,\beta)\neq(i,\alpha)} u^{\alpha\beta}(|\boldsymbol{r}_i^\alpha - \boldsymbol{r}_j^\beta|), \tag{3.25}$$

and non-relativistic Coulomb hamiltonian

$$H = \hat{T} + V = \sum_{\alpha}\sum_{j=1}^{N_\alpha} -\lambda_\alpha \nabla_j^{\alpha 2} + \frac{1}{2}\sum_{\alpha,\beta}\sum_{i=1}^{N_\alpha}\sum_{j=1}^{N_\beta,(j,\beta)\neq(i,\alpha)} v^{\alpha\beta}(|\boldsymbol{r}_i^\alpha - \boldsymbol{r}_j^\beta|), \tag{3.26}$$

where α, β label particle species, i, j label particle positions. $\lambda_\alpha = \frac{\hbar^2}{2m_\alpha}$, $v^{\alpha\beta}(\boldsymbol{r}) = \frac{Q_\alpha Q_\beta}{r}$. In terms of pair potentials and collective coordinates (see Fourier convention eq. (3.5) and its corollaries eq. (3.6-3.8))

$$U = \frac{1}{2\Omega}\sum_{\boldsymbol{k}\alpha\beta} u_{\boldsymbol{k}}^{\alpha\beta}\left(\rho_{\boldsymbol{k}}^\beta \rho_{-\boldsymbol{k}}^\alpha - \delta_{\alpha\beta}N_\alpha\right), \tag{3.27}$$

$$V = \frac{1}{2\Omega}\sum_{\boldsymbol{k}\alpha\beta} v_{\boldsymbol{k}}^{\alpha\beta}\left(\rho_{\boldsymbol{k}}^\beta \rho_{-\boldsymbol{k}}^\alpha - \delta_{\alpha\beta}N_\alpha\right). \tag{3.28}$$

The **goal** of this section is to obtain good Jastrow pair potentials $u_{\boldsymbol{k}}^{\alpha\beta}$. The *strategy* is to minimize the variance the local energy $E_L \equiv \Psi^{-1}H\Psi = T + V$, where

$$T = \sum_{\gamma} -\lambda_\gamma \sum_{l=1}^{N_\gamma}\left(\boldsymbol{\nabla}_l^\gamma U \cdot \boldsymbol{\nabla}_l^\gamma U - \nabla_l^{\gamma 2} U\right). \tag{3.29}$$

In the following, I will detail the few steps needed to obtain the RPA Jastrow potentials. First, we

express the local energy in terms of the collective coordinates eq. (3.8). Second, we find the equations that make the local energy invariant to changes in the collective coordinates. Third and finally, we solve these equations for one and two component systems. Assume $u^{\alpha\beta} = u^{\beta\alpha}$ and $u_{\boldsymbol{k}} = u_{-\boldsymbol{k}}$.

3.5.1 Local Energy of Jastrow Wavefunction

The gradient, laplacian, and gradient squared of eq. (3.27) are

$$\boldsymbol{\nabla}_l^\gamma U = \frac{1}{2\Omega}\sum_{\boldsymbol{k}\alpha}(i\boldsymbol{k})u_{\boldsymbol{k}}^{\gamma\alpha}\left(e^{i\boldsymbol{k}\cdot\boldsymbol{r}_l^\gamma}\rho_{-\boldsymbol{k}}^\alpha - \rho_{\boldsymbol{k}}^\alpha e^{-ik\cdot\boldsymbol{r}_l^\gamma}\right) \tag{3.30}$$

$$\boldsymbol{\nabla}_l^\gamma \cdot \boldsymbol{\nabla}_l^\gamma U = -\frac{1}{2\Omega}\sum_{\boldsymbol{k}\alpha}k^2 u_{\boldsymbol{k}}^{\gamma\alpha}\left(e^{i\boldsymbol{k}\cdot\boldsymbol{r}_l^\gamma}\rho_{-\boldsymbol{k}}^\alpha + \rho_{\boldsymbol{k}}^\alpha e^{-\boldsymbol{k}\cdot\boldsymbol{r}_l^\gamma} - 2\delta_{\alpha\gamma}\right) \tag{3.31}$$

$$\begin{aligned}\boldsymbol{\nabla}_l^\gamma U \cdot \boldsymbol{\nabla}_l^\gamma U = &-\frac{1}{4\Omega^2}\sum_{\boldsymbol{k}\boldsymbol{q}\alpha\beta}\boldsymbol{k}\cdot\boldsymbol{q}u_{\boldsymbol{k}}^{\gamma\alpha}u_{\boldsymbol{q}}^{\gamma\beta}\times(\\ &e^{i(\boldsymbol{k}+\boldsymbol{q})\cdot\boldsymbol{r}}\rho_{-\boldsymbol{k}}^\alpha\rho_{-\boldsymbol{q}}^\beta - e^{i(\boldsymbol{k}-\boldsymbol{q})\cdot\boldsymbol{r}}\rho_{-\boldsymbol{k}}^\alpha\rho_{\boldsymbol{q}}^\beta - e^{i(\boldsymbol{q}-\boldsymbol{k})\cdot\boldsymbol{r}}\rho_{\boldsymbol{k}}^\alpha\rho_{-\boldsymbol{q}}^\beta + e^{-i(\boldsymbol{k}+\boldsymbol{q})\cdot\boldsymbol{r}}\rho_{\boldsymbol{k}}^\alpha\rho_{\boldsymbol{q}}^\beta\\ &)\,.\end{aligned} \tag{3.32}$$

Summing over l turns $e^{i\boldsymbol{k}\cdot\boldsymbol{r}_l^\gamma}$ into $\rho_{\boldsymbol{k}}^\gamma$ in eq. (3.31) and (3.32). Thus

$$\sum_{l=1}^{N_\gamma}\boldsymbol{\nabla}_l^\gamma \cdot \boldsymbol{\nabla}_l^\gamma U = -\frac{1}{2\Omega}\sum_{\boldsymbol{k}\alpha}k^2 u_{\boldsymbol{k}}^{\gamma\alpha}\left(\rho_{\boldsymbol{k}}^\gamma\rho_{-\boldsymbol{k}}^\alpha + \rho_{\boldsymbol{k}}^\alpha\rho_{-\boldsymbol{k}}^\gamma - 2N_\gamma\delta_{\alpha\gamma}\right) \tag{3.33}$$

$$\begin{aligned}\sum_{l=1}^{N_\gamma}\boldsymbol{\nabla}_l^\gamma U \cdot \boldsymbol{\nabla}_l^\gamma U = &-\frac{1}{4\Omega^2}\sum_{\boldsymbol{k}\boldsymbol{q}\alpha\beta}\boldsymbol{k}\cdot\boldsymbol{q}u_{\boldsymbol{k}}^{\gamma\alpha}u_{\boldsymbol{q}}^{\gamma\beta}\times(\\ &\rho_{\boldsymbol{k}+\boldsymbol{q}}^\gamma\rho_{-\boldsymbol{k}}^\alpha\rho_{-\boldsymbol{q}}^\beta - \rho_{\boldsymbol{k}-\boldsymbol{q}}^\gamma\rho_{-\boldsymbol{k}}^\alpha\rho_{\boldsymbol{q}}^\beta - \rho_{\boldsymbol{q}-\boldsymbol{k}}^\gamma\rho_{\boldsymbol{k}}^\alpha\rho_{-\boldsymbol{q}}^\beta + \rho_{-(\boldsymbol{k}+\boldsymbol{q})}^\gamma\rho_{\boldsymbol{k}}^\alpha\rho_{\boldsymbol{q}}^\beta\\ &)\,.\end{aligned} \tag{3.34}$$

Equation (3.34) contains terms that couple three wave vectors, i.e. $O(\rho^3)$. In the spirit of RPA, we will drop all such *mode coupling* terms. Note $\rho_{\boldsymbol{0}}^\gamma = N_\gamma$, and use $u_{\boldsymbol{k}} = u_{-\boldsymbol{k}}$

$$\sum_{l=1}^{N_\gamma}\boldsymbol{\nabla}_l^\gamma U \cdot \boldsymbol{\nabla}_l^\gamma U = \frac{N_\gamma}{2\Omega^2}\sum_{\boldsymbol{k}\alpha\beta}k^2 u_{\boldsymbol{k}}^{\gamma\alpha}u_{\boldsymbol{k}}^{\gamma\beta}\left(\rho_{-\boldsymbol{k}}^\alpha\rho_{\boldsymbol{k}}^\beta + \rho_{\boldsymbol{k}}^\alpha\rho_{-\boldsymbol{k}}^\beta\right). \tag{3.35}$$

Finally, sum over γ with $-\lambda_\gamma$ to obtain terms in the kinetic energy. To simplify later assembly of the local energy, rename dummy variables α, β, γ such that every $O(\rho^2)$ term contains $\rho^\alpha_{\boldsymbol{k}}\rho^\beta_{-\boldsymbol{k}}$ (use $u^{\alpha\beta} = u^{\beta\alpha}$)

$$\sum_\gamma -\lambda_\gamma \sum_{l=1}^{N_\gamma} \boldsymbol{\nabla}_l^\gamma U \cdot \boldsymbol{\nabla}_l^\gamma U = -\frac{1}{\Omega}\sum_{\boldsymbol{k}\alpha\beta\gamma} \lambda_\gamma \frac{N_\gamma}{\Omega} k^2 u^{\gamma\alpha}_{\boldsymbol{k}} u^{\gamma\beta}_{\boldsymbol{k}} \rho^\alpha_{\boldsymbol{k}}\rho^\beta_{-\boldsymbol{k}}, \tag{3.36}$$

$$\sum_\gamma -\lambda_\gamma \sum_{l=1}^{N_\gamma} \boldsymbol{\nabla}_l^\gamma \cdot \boldsymbol{\nabla}_l^\gamma U = -\frac{1}{\Omega}\left(\sum_{\boldsymbol{k}\alpha\beta} \frac{\lambda_\alpha + \lambda_\beta}{2} u^{\alpha\beta}_{\boldsymbol{k}} \rho^\alpha_{\boldsymbol{k}}\rho^\beta_{-\boldsymbol{k}} - N_\alpha \lambda_\alpha \delta_{\alpha,\beta}\right). \tag{3.37}$$

Finally, the local energy can be assembled

$$E_L = \sum_{\boldsymbol{k}} \left[\frac{v^{\alpha\beta}_{\boldsymbol{k}}}{2\Omega} - \frac{\frac{\lambda_\alpha+\lambda_\beta}{2}k^2 u^{\alpha\beta}_{\boldsymbol{k}}}{\Omega} - \sum_\gamma \frac{(N_\gamma/\Omega)\lambda_\gamma k^2 u^{\alpha\gamma}_{\boldsymbol{k}} u^{\beta\gamma}_{\boldsymbol{k}}}{\Omega}\right]\rho^\alpha_{\boldsymbol{k}}\rho^\beta_{-\boldsymbol{k}} + \frac{N_\alpha^2(\lambda_\alpha + \frac{1}{2})}{\Omega}. \tag{3.38}$$

3.5.2 Equations that define the RPA Jastrow Pair Potentials

Variance of E_L can be minimized by setting the $\rho^\alpha_{\boldsymbol{k}}\rho^\beta_{-\boldsymbol{k}}$ term to zero. Define $\epsilon^\alpha_{\boldsymbol{k}} \equiv \lambda_\alpha k^2$

$$\frac{v^{\alpha\beta}_{\boldsymbol{k}}}{2} - \frac{\epsilon^\alpha_{\boldsymbol{k}} + \epsilon^\beta_{\boldsymbol{k}}}{2} u^{\alpha\beta}_{\boldsymbol{k}} - \sum_\gamma \frac{N_\gamma}{\Omega}\epsilon^\gamma_{\boldsymbol{k}} u^{\alpha\gamma}_{\boldsymbol{k}} u^{\beta\gamma}_{\boldsymbol{k}} = 0. \tag{3.39}$$

Equation (3.39) can be solved for each $\boldsymbol{k}$ independently. We no longer need the collective coordinates or the label $\boldsymbol{k}$. It is now safe to recycle the symbol $\rho_\gamma \equiv \frac{N_\gamma}{\Omega}$ to mean the number density of species γ. Simplify eq. (3.39) to

$$\frac{v_{\alpha\beta}}{2} - \frac{1}{2}(\epsilon_\alpha + \epsilon_\beta)u_{\alpha\beta} - \sum_\gamma \rho_\gamma \epsilon_\gamma u_{\alpha\gamma} u_{\beta\gamma} = 0. \tag{3.40}$$

3.5.3 Solving for the RPA Jastrow Pair Function

One Component

For a one-component system, eq. (3.40) becomes a quadratic equation of one variable u_{11}

$$\frac{v_{11}}{2} - \epsilon_1 u_{11} - \rho_1 \epsilon_1 u_{11}^2 = 0. \tag{3.41}$$

The solution is

$$2\rho_1 u_{11} = -1 + \sqrt{1 + 2\rho_1 v_{11}/\epsilon_1}, \tag{3.42}$$

which agrees with Gaskell's solution eq. (3.20), except $S_0(k)$ is replaced by 1. Notice, if one uses a different

Fourier convention, replacing volume Ω with number of particles N in eq. (3.27)

$$U = \frac{1}{2N} \sum_{\boldsymbol{k}\alpha\beta} \tilde{u}_{\boldsymbol{k}}^{\alpha\beta} \left(\rho_{\boldsymbol{k}}^{\beta} \rho_{-\boldsymbol{k}}^{\alpha} - \delta_{\alpha\beta} N_{\alpha} \right), \tag{3.43}$$

then the density ρ drops from the expression for $\tilde{u}$, e.g., eq. (8) in Ref. [29] and eq. (3) in Ref. [6]

$$2\tilde{u} = -1 + (1 + 2v_k/e_k). \tag{3.44}$$

Two Components

For two-component system, eq. (3.40) becomes a set of 3 coupled quadratic equations

$$\begin{cases} \frac{v_{11}}{2} - \epsilon_1 u_{11} - \rho_1 \epsilon_1 u_{11}^2 - \rho_2 \epsilon_2 u_{12}^2 = 0 \\ \frac{v_{12}}{2} - \frac{1}{2}(\epsilon_1 + \epsilon_2) u_{12} - \rho_1 \epsilon_1 u_{11} u_{12} - \rho_2 \epsilon_2 u_{12} u_{22} = 0 \\ \frac{v_{22}}{2} - \epsilon_2 u_{22} - \rho_1 \epsilon_1 u_{12}^2 - \rho_2 \epsilon_2 u_{22}^2 = 0. \end{cases} \tag{3.45}$$

Suppose species 2 has infinite mass $\lambda_2 \to 0$, thus no dispersion $\epsilon_2 = 0$. Then we should ignore the last equation ($\alpha = \beta = 2$), which determines u_{22} (when $u_{12} = 0$). The remaining equations allow us to solve for the Jastrow pair potentials u_{11} and u_{12}

$$\begin{cases} \frac{v_{11}}{2} - \epsilon_1 u_{11} - \rho_1 \epsilon_1 u_{11}^2 = 0 \\ \frac{v_{12}}{2} - \frac{\epsilon_1}{2} u_{12} - \rho_1 \epsilon_1 u_{11} u_{12} = 0 \end{cases}. \tag{3.46}$$

The first equation provides the same Jastrow potential as in the one-component case eq. (3.42). The second equation can be used to solve for u_{12}

$$\begin{aligned} (1 + 2\rho u_{11}) \epsilon_1 u_{12} &= v_{12} \\ \Rightarrow u_{12} &= \frac{v_{12}/\epsilon_1}{\sqrt{1 + 2\rho_1 v_{11}/\epsilon_1}}. \end{aligned} \tag{3.47}$$

For completeness, the exact solutions are (by Mathematica)

$$2\rho_1 u_{11} = -1 + \frac{\epsilon_1(1 + a_{11}) \pm \epsilon_2 \sqrt{A}}{\sqrt{\epsilon_1 \epsilon_2} \sqrt{B}}, \tag{3.48}$$

$$u_{12} = \frac{\pm v_{12}}{\sqrt{\epsilon_1 \epsilon_2} \sqrt{B}}, \tag{3.49}$$

$$2\rho_2 u_{22} = -1 + \frac{\epsilon_2(1 + a_{22}) \pm \epsilon_1 \sqrt{A}}{\sqrt{\epsilon_1 \epsilon_2} \sqrt{B}}, \tag{3.50}$$

where

$$A = (1+a_{11})(1+a_{22}) - a_{12}^2, \tag{3.51}$$

$$B = \frac{\epsilon_2}{\epsilon_1}(1+a_{22}) + \frac{\epsilon_1}{\epsilon_2}(1+a_{11}) \pm 2\sqrt{A}, \tag{3.52}$$

with

$$\begin{cases} a_{11} = \frac{2\rho_1 v_{11}}{\epsilon_1} \\ a_{12} = \frac{2\sqrt{\rho_1\rho_2}v_{11}}{\sqrt{\epsilon_1\epsilon_2}} \\ a_{22} = \frac{2\rho_2 v_{22}}{\epsilon_2} \end{cases} . \tag{3.53}$$

3.6 Slater Determinant in Plane Wave Basis

Based on notes from D. M. Ceperley dated Aug. 1 2018

When the orbitals are expressed in plane wave basis

$$\phi_i(\boldsymbol{r}) = \sum_{\boldsymbol{k}} c_{i\boldsymbol{k}} e^{i\boldsymbol{k}\cdot\boldsymbol{r}}. \tag{3.54}$$

We require the orbitals to be orthonormal

$$\int_\Omega d\boldsymbol{r}\phi_i(\boldsymbol{r})^*\phi_j(\boldsymbol{r}) = \delta_{ij} \Rightarrow \Omega\sum_{\boldsymbol{k}} c^*_{i\boldsymbol{k}}c_{j\boldsymbol{k}} = \delta_{ij}. \tag{3.55}$$

We can verify that the determinant written in eq (3.14) is normalized

$$\begin{aligned} \langle\rangle \equiv & \int d\boldsymbol{r}_1 \dots d\boldsymbol{r}_N \Psi^* \ \Psi \\ = & \frac{1}{N!}\sum_{\mathcal{P},\mathcal{P}'}(-1)^{\mathcal{P}}(-1)^{\mathcal{P}'}\left(\prod_{l=1}^N \int d\boldsymbol{r}_l \phi^*_{\mathcal{P}_l}(\boldsymbol{r}_l)\phi_{\mathcal{P}'_l}(\boldsymbol{r}_l)\right) \\ = & \frac{1}{N!}\sum_{\mathcal{P},\mathcal{P}'}(-1)^{\mathcal{P}}(-1)^{\mathcal{P}'}\left(\prod_{l=1}^N \delta_{\mathcal{P}_l,\mathcal{P}'_l}\right) \\ = & \frac{1}{N!}\sum_{\mathcal{P}} = 1. \end{aligned} \tag{3.56}$$

The key step in eq (3.56) is to separate and distribute the many-body integrals into the product.

Many properties of the slater determinant can be evaluated analytically. Here we focus on reciprocal-space properties accessible by scattering experiments: the momentum distribution $n(\boldsymbol{k})$ and the static structure

factor $S(\boldsymbol{k})$.

3.6.1 Momentum Distribution

The momentum distribution is the Fourier transform of the 1RDM (eq. (5.9) in Ref. [24]). The 1RDM can be calculated from the many-body wavefunction

$$\rho(\boldsymbol{x},\boldsymbol{x}') = N\int d\boldsymbol{r}_2\dots\boldsymbol{r}_N \Psi^*(\boldsymbol{x},\boldsymbol{r}_2,\dots)\Psi(\boldsymbol{x}',\boldsymbol{r}_2,\dots). \tag{3.57}$$

Given a Slater determinant wavefunction eq (3.14), all the $d\boldsymbol{r}$ integrals can be done analytically

$$\begin{aligned}
\rho(\boldsymbol{x},\boldsymbol{x}') =& N\int d\boldsymbol{r}_2\dots d\boldsymbol{r}_N \left(\frac{1}{N!}\sum_{\mathcal{P},\mathcal{P}'}(-1)^{\mathcal{P}}(-1)^{\mathcal{P}'}\phi^*_{\mathcal{P}_1}(\boldsymbol{x})\phi_{\mathcal{P}'_1}(\boldsymbol{x}')\prod_{l=2}^{N}\phi_{\mathcal{P}_l^*}(\boldsymbol{r}_l)\phi_{\mathcal{P}'_l}(\boldsymbol{r}_l)\right)\\
=&\frac{N}{N!}\sum_{\mathcal{P},\mathcal{P}'}(-1)^{\mathcal{P}}(-1)^{\mathcal{P}'}\left(\phi^*_{\mathcal{P}_1}(\boldsymbol{x})\phi_{\mathcal{P}'_1}(\boldsymbol{x}')\prod_{l=2}^{N}\delta_{\mathcal{P}_l,\mathcal{P}'_l}\right)\\
=&\frac{N}{N!}\sum_{\mathcal{P}}\phi^*_{\mathcal{P}_1}(\boldsymbol{x})\phi_{\mathcal{P}_1}(\boldsymbol{x}')\\
=&\sum_{\mathcal{P}_1=1}^{N}\phi^*_{\mathcal{P}_1}(\boldsymbol{x})\phi_{\mathcal{P}_1}(\boldsymbol{x}').
\end{aligned} \tag{3.58}$$

Notice that the diagonal ($\boldsymbol{x}=\boldsymbol{x}'$) of the 1RDM is particle density. Given PW orbitals eq (3.54)

$$\begin{aligned}
n(\boldsymbol{k}) =&\frac{1}{(2\pi)^3 N}\int d\boldsymbol{r}d\boldsymbol{r}'' e^{-i\boldsymbol{k}\cdot\boldsymbol{r}''}\rho(\boldsymbol{r},\boldsymbol{r}-\boldsymbol{r}'')\\
=&\frac{1}{(2\pi)^3 N}\sum_{i,\boldsymbol{g},\boldsymbol{g}'}c^*_{i\boldsymbol{g}}c_{i\boldsymbol{g}'}\int d\boldsymbol{r}d\boldsymbol{r}'' e^{-i\boldsymbol{g}\cdot\boldsymbol{r}}e^{i\boldsymbol{g}'\cdot(\boldsymbol{r}-\boldsymbol{r}'')}\\
=&\frac{1}{(2\pi)^3 N}\sum_{i,\boldsymbol{g},\boldsymbol{g}'}c^*_{i\boldsymbol{g}}c_{i\boldsymbol{g}'}\Omega\delta_{\boldsymbol{g},\boldsymbol{g}'}\Omega\delta_{\boldsymbol{g}',-\boldsymbol{k}}\\
=&\frac{\Omega}{(2\pi)^3}\frac{\Omega}{N}\sum_{i=1}^{N}|c_{i,-\boldsymbol{k}}|^2.
\end{aligned} \tag{3.59}$$

Given the current definitions, $\int d\boldsymbol{k}n(\boldsymbol{k}) = 1$ for an infinite system. In practice, one bins the Fourier coefficient squared of all occupied orbitals at allowed momenta of the supercell.

3.6.2 Static Structure Factor

The static structure factor is the density-density correlation function in reciprocal space

$$\begin{aligned} S_{\boldsymbol{q}} \equiv & \frac{1}{N}\left\langle \rho_{\boldsymbol{q}}\rho_{-\boldsymbol{q}}\right\rangle \equiv \frac{1}{N}\left\langle (\sum_{i=1}^{N} e^{i\boldsymbol{q}\cdot\boldsymbol{r}_i})(\sum_{j=1}^{N} e^{-i\boldsymbol{q}\cdot\boldsymbol{r}_j})\right\rangle \\ = & \frac{1}{N}\sum_{ij}\left\langle e^{i\boldsymbol{q}\cdot(\boldsymbol{r}_i-\boldsymbol{r}_j)}\right\rangle = 1+\frac{1}{N}\sum_{i\neq j}\left\langle e^{i\boldsymbol{q}\cdot(\boldsymbol{r}_i-\boldsymbol{r}_j)}\right\rangle \\ = & 1+(N-1)\left\langle e^{i\boldsymbol{q}\cdot(\boldsymbol{r}_1-\boldsymbol{r}_2)}\right\rangle . \end{aligned} \tag{3.60}$$

Focus on the many-body integral

$$\left\langle e^{i\boldsymbol{q}\cdot(\boldsymbol{r}_1-\boldsymbol{r}_2)}\right\rangle = \frac{1}{N!}\sum_{\mathcal{P},\mathcal{P}'}(-1)^{\mathcal{P}}(-1)^{\mathcal{P}'}\int d\boldsymbol{r}_1\ldots d\boldsymbol{r}_N e^{i\boldsymbol{q}\cdot(\boldsymbol{r}_1-\boldsymbol{r}_2)}\prod_{l=1}^{N}\phi^*_{\mathcal{P}_l}(\boldsymbol{r}_l)\phi_{\mathcal{P}'_l}(\boldsymbol{r}_l). \tag{3.61}$$

Similar to eq (3.56) and eq (3.59), $\mathcal{P}_l=\mathcal{P}'_l,\forall l\neq 1,2$. Define $\mathcal{P}_1=i$, $\mathcal{P}_2=j$, then $\mathcal{P}'_{1,2}=i,j$ contributes a positive term, and $\mathcal{P}'_{1,2}=j,i$ contributes a negative term. Thus eq (3.61) simplifies

$$\begin{aligned} \left\langle e^{i\boldsymbol{q}\cdot(\boldsymbol{r}_1-\boldsymbol{r}_2)}\right\rangle = & \frac{1}{N(N-1)}\sum_{i,j}\int d\boldsymbol{r}_1 d\boldsymbol{r}_2 e^{i\boldsymbol{q}\cdot(\boldsymbol{r}_1-\boldsymbol{r}_2)}\times \\ & \left[\phi^*_i(\boldsymbol{r}_1)\phi_i(\boldsymbol{r}_1)\phi^*_j(\boldsymbol{r}_2)\phi_j(\boldsymbol{r}_2)-\phi^*_i(\boldsymbol{r}_1)\phi_j(\boldsymbol{r}_1)\phi^*_j(\boldsymbol{r}_2)\phi_i(\boldsymbol{r}_2)\right] \\ = & \frac{1}{N(N-1)}\sum_{i\neq j}\left[\int d\boldsymbol{r}_1 e^{i\boldsymbol{q}\cdot\boldsymbol{r}_1}\phi^*_i(\boldsymbol{r}_1)\phi_i(\boldsymbol{r}_1)\int d\boldsymbol{r}_1 e^{-i\boldsymbol{q}\cdot\boldsymbol{r}_2}\phi^*_j(\boldsymbol{r}_2)\phi_j(\boldsymbol{r}_2)\right. \\ & \left.-\int d\boldsymbol{r}_1 e^{i\boldsymbol{q}\cdot\boldsymbol{r}_1}\phi^*_i(\boldsymbol{r}_1)\phi_j(\boldsymbol{r}_1)\int d\boldsymbol{r}_1 e^{-i\boldsymbol{q}\cdot\boldsymbol{r}_2}\phi^*_j(\boldsymbol{r}_2)\phi_i(\boldsymbol{r}_2)\right] \\ = & \frac{1}{N(N-1)}\sum_{i\neq j}\left[m_{ii}(\boldsymbol{q})m_{jj}(-\boldsymbol{q})-m_{ij}(\boldsymbol{q})m_{ji}(-\boldsymbol{q})\right], \end{aligned} \tag{3.62}$$

where we have defined the matrix of integrals

$$m_{ij}(\boldsymbol{q}) \equiv \int d\boldsymbol{r}\phi^*_i(\boldsymbol{r})\phi_j(\boldsymbol{r})e^{i\boldsymbol{q}\cdot\boldsymbol{r}}. \tag{3.63}$$

Notice $m^*_{ij}(\boldsymbol{q})=m_{ji}(-\boldsymbol{q})$, thus

$$\begin{aligned} S_{\boldsymbol{q}} = & 1+\frac{1}{N}\sum_{i\neq j}\left[m_{ii}(\boldsymbol{q})m^*_{jj}(\boldsymbol{q})-m_{ij}(\boldsymbol{q})m^*_{ij}(\boldsymbol{q})\right] \\ = & 1+\frac{1}{N}\left[|\sum_i m_{ii}(\boldsymbol{q})|^2-\sum_{i,j}|m_{ij}(\boldsymbol{q})|^2\right]. \end{aligned} \tag{3.64}$$

3.6.3 Example: Free Fermions

The ground-state wavefunction of non-interacting fermions is a determinant of plane waves. The first N plane-wave orbitals with the lowest momenta are filled. In case of degeneracy, the wavefunction will have a non-zero net momentum.

Simply stated, the free fermion wavefunction is a determinant eq (3.14) whose orbitals each have a single Fourier component

$$c_{i\boldsymbol{k}} = \frac{1}{\sqrt{\Omega}}\delta_{\boldsymbol{k},\boldsymbol{k}_i}. \tag{3.65}$$

We see from eq (3.59) that the momentum distribution $n(\boldsymbol{k})$ of the free fermions is a step function, which is constant within the Fermi surface and zero outside. As for the static structure factor $S(\boldsymbol{k})$, first note that the matrix of integrals $m_{ij}(\boldsymbol{q})$ eq (3.63) is sparse

$$m_{ij}(\boldsymbol{q}) = c^*_{i\boldsymbol{k}_i} c_{j\boldsymbol{k}_j} \Omega \delta_{\boldsymbol{q},\boldsymbol{k}_i-\boldsymbol{k}_j} = \delta_{\boldsymbol{q},\boldsymbol{k}_i-\boldsymbol{k}_j}. \tag{3.66}$$

Plug (3.66) into (3.64) and

$$S_{\boldsymbol{q}} = \begin{cases} N & \boldsymbol{q} = \boldsymbol{0} \\ 1 - \frac{1}{N}\sum\limits_{i,j} |\delta_{\boldsymbol{q},\boldsymbol{k}_i-\boldsymbol{k}_j}|^2 & \boldsymbol{q} \neq \boldsymbol{0} \end{cases}. \tag{3.67}$$

Eq (3.66) has a simple geometric interpretation. Namely, $m_{ij}(\boldsymbol{q})$ is non-zero only if $\boldsymbol{q}$ connects two occupied plane wave orbitals. In the thermodynamic limit, the geometric interpretation allows $S(\boldsymbol{k})$ to be calculated from a simple integral for the overlapping volume of two spheres

$$\begin{aligned} S(\boldsymbol{k} \neq \boldsymbol{0}) =& 1 - \left(\frac{4\pi k_F^3}{3}\right)^{-1} 2\int_{q/2}^{k_F} dk\pi(k_F^2 - k^2) \\ =& \begin{cases} \frac{3}{4}\left(\frac{q}{k_F}\right) - \frac{1}{16}\left(\frac{q}{k_F}\right)^3 & q < 2k_F \\ 1 & q \geq 2k_F \end{cases}. \end{aligned} \tag{3.68}$$

3.7 Beyond Slater-Jastrow

One way to systematically obtain more accurate wave functions than Slater-Jastrow is to expand the many-body wave function in a basis of determinants. This configuration interaction (CI) method is routinely used in quantum chemistry to study molecules. The CI method is especially effective when the correlation in the

ground state is mostly static in nature, e.g., in benzene molecule where the ground-state wave function is approximately the equal superposition of six non-interacting determinants. This method is less successful in bulk calculations due to difficulties in performing finite-size extrapolation. Specifically, a fixed-length determinant expansion is more accurate for a small system than a large one. Thus, properties such as the total energy are not size-extensive and cannot be extrapolated to the thermodynamic limit using known asymptotic formula.

Another method for systematically improving the many-body wave function is to use the generalized Feynman-Kac formula (eq. (6.12) in Ref. [24]), which is intimately related to the DMC method (eq. (24.23) in Ref. [24])

$$\Psi_0 = \frac{\Psi_T}{\langle \Psi_T | \Psi_0 \rangle} \left\langle \exp\left(- \int_0^\infty dt [E_L(\boldsymbol{R}_t; \Psi_T) - E_0] \right) \right\rangle_{\Psi_T^2}, \tag{3.69}$$

where $\langle \rangle_{\Psi_T^2}$ denotes average over drift-diffusion random walks guided by Ψ_T eq. (2.28). $E_L(\boldsymbol{R}_t; \Psi_T)$ is the local energy of the trial wave function at walker position $\boldsymbol{R}_t$ during the random walk. If Ψ_T is a good approximation for the ground state Ψ_0, then imaginary time propagation can be cut off at a small equilibrium "time" τ and eq. (3.69) has a compelling physical interpretation eq. (6.13) in Ref. [24]

$$\ln \Psi_0(\boldsymbol{R}_0) \approx \ln \Psi_T(\boldsymbol{R}_0) - \tau [\langle E_L \rangle_{\Psi_T^2}(\boldsymbol{R}_0) - E_0]. \tag{3.70}$$

Equation (3.70) says the correction to the exponent of Ψ_T at $\boldsymbol{R}_0$ is proportional to the average of its local energy over a small region around $\boldsymbol{R}_0$ having size $O(\sqrt{d\lambda\tau})$ in dN-dimensional space. This observation is quite useful for practitioners of the DMC method, because it implies longer projection time is needed for:

1. *larger system*, because the space over which E_L needs to be averaged increase with N.
2. *heavier particles*, because they have smaller quantumness λ, thus smaller diffusion constant.
3. *long-range properties*, because the effect of projection is local and expands slowly with projection time.

Finally, the Feynman-Kac formula was shown to be capable of suggesting compact wave function that accurately capture electron correlation starting from a simple initial guess [10].

Chapter 4

Finite-size Effects

In the previous two chapters, I introduced the ground-state QMC method and the trial wave function needed to make it accurate for a well-defined electron-ion Hamiltonian. However, practical QMC simulations cannot handle the hamiltonian governing $O(10^{23})$ particles found in typical condensed matter experiments. While we use periodic boundary condition to eliminate surfaces from our simulations, there is significant remaining difference between the properties of this model system and those from experiment.

In this chapter, I will describe common types of finite size effects encountered in electronic structure simulations and a few correction schemes. I will begin discussion from the most general correction that works for quantum and classical systems at zero and finite temperature: the static structure factor correction to the potential energy. From there, the method is extended to correct kinetic energy using the momentum distribution, and in the quantum case, using the Jastrow pair function.

4.1 Correction to the potential energy

4.1.1 General Theory

Given a simulation using periodic boundary conditions, the accessible momenta are quantized. As the simulation cell is enlarged, the grid of accessible momenta becomes finer until it grants access to the full continuum of momentum space in the thermodynamic limit. By considering the difference between this infinite system and the finite simulation cell, we can understand finite-size effects and attempt to correct them. Consider an orthorhombic box with side length L_x along the x direction. The momentum along the x direction must take discrete values $k_x = \frac{2\pi}{L_x} n_x$, where $n_x \in \mathbb{N}$. Similarly discretization exist along the other directions. In a simulation where particles interact via the Coulomb pair potential $v(r) = \frac{1}{r}$, the total potential energy of the system

$$V \equiv V_{\text{background}} + \frac{1}{2} \sum_{i=1}^{N} \sum_{\boldsymbol{L}} \sum_{j=1}^{N} v(|\boldsymbol{x}_i - \boldsymbol{x}_j - \boldsymbol{L}|), \tag{4.1}$$

where $\boldsymbol{L}$ loop over the supercell lattice. The sums loop over all pairs of particles in the infinite system. This equation can be equivalently written in reciprocal space as

$$V_N \equiv V/N = v_M + \frac{1}{2\Omega} \sum_{\boldsymbol{k} \neq \boldsymbol{0}} v_{\boldsymbol{k}} S(\boldsymbol{k}), \tag{4.2}$$

where $v_{\boldsymbol{k}} = \frac{2\pi(d-1)}{k^{d-1}}$ is the Fourier transform of the Coulomb pair potential in d spatial dimensions. v_M is the Madelung constant, which combines the electrostatic energy of an infinite periodic array of charges on $\boldsymbol{L}$ with a neutralizing background. Equation (4.2) looks different than its original proposal in Ref. [62] due to a difference in Fourier transform convention. Here, I follow the definitions eq. (6) and (7) in Ref. [60], which are reiterated in Sec. 3.1.

Suppose $S(\boldsymbol{k})$ is converged, i.e., does not change with system size, then the only difference between the infinite-system and the finite-size potential energies is the replacement of the sum in eq. (4.2) by an integral

$$\Delta V_N \equiv V_\infty - V_N = \left[\int \frac{d^d \boldsymbol{k}}{(2\pi)^d} - \frac{1}{\Omega} \sum_{\boldsymbol{k}} \right] \frac{v_k}{2} S(\boldsymbol{k}). \tag{4.3}$$

Equation (4.3) is not practical, because $\lim_{k \to \infty} S(k) = 1$ and both the sum and the integral diverge. Fortunately, large k corresponds to short-range interaction, so its contribution to finite-size error vanish rapidly with system size. Thus, we can truncate the large-k part of eq. (4.3) with little effect on its value. This can be achieved either using an explicit suppression factor $e^{-\epsilon k^2}$ as done in eq. (24) of Ref. [63] by Drummond *et al.*, or splitting out the long-range part of the Coulomb potential as done in eq. (30) of Ref. [60] by Holzmann *et al.*.

While the Madelung term in eq. (4.2) is specific to charged systems, the idea of finite-size error as a quadrature error eq. (4.3) applies to any pair potential $v(\boldsymbol{r})$. This error can be accurately corrected given converged pair correlation functions in real $g(\boldsymbol{r})$ and reciprocal $S(\boldsymbol{k})$ spaces.

4.1.2 Homogeneous electron gas

In the case of the electron gas, more progress can be made due to known long-wavelength behavior of the wave function. The dominant contribution to eq. (4.3) comes from the volume element around $\boldsymbol{k} = \boldsymbol{0}$, because v_k diverges there.

$$\Delta V_N \approx \int_{\frac{(2\pi)^d}{\Omega}} \frac{d^d \boldsymbol{k}}{(2\pi)^d} \frac{v_k}{2} S(\boldsymbol{k}). \tag{4.4}$$

Bohm and Pines [64] discovered that the many-body wave function of the electron gas can be factored into short-range and long-range contributions, where the long-range part describes weakly coupled collective modes (plasmons) [60, 65]

$$\Psi = \Psi_{s.r.} \exp\left(-\frac{1}{2\Omega} \sum_{\boldsymbol{k}} u_{\boldsymbol{k}} \rho_{\boldsymbol{k}} \rho_{-\boldsymbol{k}} + \frac{1}{\Omega^2} \sum_{\boldsymbol{k},\boldsymbol{q}} w(\boldsymbol{k},\boldsymbol{q}) \rho_{\boldsymbol{k}+\boldsymbol{q}} \rho_{-\boldsymbol{k}} \rho_{-\boldsymbol{q}} + \dots \right). \tag{4.5}$$

In the random phase approximation (RPA), we ignore the mode coupling terms, such as $w(\boldsymbol{k},\boldsymbol{q})$, and find the Gaskell RPA static structure factor eq. (3.23). Using the leading-order approximation of $S(\boldsymbol{k})$ eq. (3.24) in the finite-size correction formula eq. (4.4), we obtain the main correction to the potential energy

$$\Delta V_N^{l.o.} = \frac{\omega_p}{4}. \tag{4.6}$$

Similarly, in 2D [66]

$$S_0(k) = \left\{ \frac{2}{\pi} \left[\arcsin\left(\frac{k}{2k_F} + \frac{k}{2k_F} \sqrt{1 - \left(\frac{k}{2k_F} \right)^2} \right) \right] \right\} \Theta(2k_F - k) + \Theta(k - 2k_F), \tag{4.7}$$

$$S(k) = \frac{(k/k_F)^{3/2}}{2^{3/4} r_s^{1/2}} + O(k^2), \tag{4.8}$$

$$\Delta V_N^{l.o.} = \frac{C_{2D}}{\pi^{5/4} (2r_s)^{3/2}} \frac{1}{N^{5/4}} + O(N^{-3/2}), \tag{4.9}$$

where $k_F \equiv \sqrt{2}/r_s$, $C_{2D} = 3.9852$ and 3.9590 for square and hexagonal cells, respectively [63]. Equation (4.9) differs from eq. (60) in Ref. [63], because Ref. [63] erroneously used the dimensionless form of the RPA structure factor rather than its Hartree atomic unit form eq. (4.8).

4.1.3 Inhomogeneous system

In a real crystal, valence electrons interact with a periodic arrangement of localized ionic cores rather than a homogeneous neutralizing background of positive charge. In such inhomogeneous systems, it is instructive to separate the static and fluctuating contributions to the static structure factor

$$S(\boldsymbol{k}) \equiv \frac{1}{N} \langle \rho_{\boldsymbol{k}} \rho_{-\boldsymbol{k}} \rangle = \frac{1}{N} \langle (\rho_{\boldsymbol{k}} - \langle \rho_{\boldsymbol{k}} \rangle)(\rho_{\boldsymbol{k}} - \langle \rho_{\boldsymbol{k}} \rangle) \rangle + \frac{1}{N} \langle \rho_{\boldsymbol{k}} \rangle \langle \rho_{-\boldsymbol{k}} \rangle. \tag{4.10}$$

As shown in Fig. 4.1, the static part due to charge density $\rho_{\boldsymbol{k}}$ is non-zero only at reciprocal lattice of the primitive cell of the underlying crystal structure, whereas the fluctuating part varies smoothly from 0 to 1. Its value within the missing $\boldsymbol{k} = \boldsymbol{0}$ region (red area in Fig. 4.1) can be used to correct the potential energy to

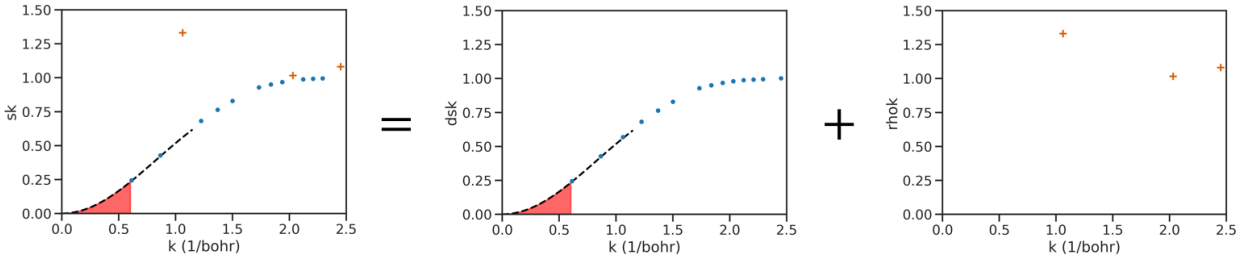

Figure 4.1: Fluctuating and static contributions from valence electrons in the conventional cell of bulk silicon.

leading order following eq. (4.4). Changes in the charge density with system size is a higher-order effect and is small compared to the total potential energy [67]. However, as shown in Ref. [68], this static contribution becomes important when energy differences are taken, such as in the calculation of the fundamental gap.

Even in an insulator, eq. (3.23) still works well at $k \ll k_F$, but the short-range contribution $S_0(k)$ no longer comes from a simple determinant of plane waves. Dielectric screening suppresses long-range fluctuation and changes the leading-order behavior of $S(k)$ from eq. (3.24) to eq. (7) in Ref. [68]

$$S(k) \approx \frac{k^2}{2\omega_p}(1-\epsilon_k^{-1})^{1/2}, \tag{4.11}$$

so long as only one excitation dominates the dynamic structure factor.

4.2 Correction to the kinetic energy

4.2.1 From momentum distribution

The kinetic energy can be calculated as the second moment of the momentum distribution

$$T_N \equiv T/N = \frac{1}{\rho}\int \frac{d^d\boldsymbol{k}}{(2\pi)^d} e(k) n_N(\boldsymbol{k}), \tag{4.12}$$

where the dispersion of non-relativistic particles

$$e(k) = \frac{\hbar^2}{2m}k^2, \tag{4.13}$$

and $n_N(\boldsymbol{k})$ is the momentum distribution of these particles at the given system size N. It is crucial to distinguish the finite-size $n_N(\boldsymbol{k})$ from its thermodynamic limit $n_\infty(\boldsymbol{k})$, because it is a nonlocal quantity that

converges slowly with system size [59]. Similar to eq. (4.3), the finite-size correction to the kinetic energy

$$\Delta T_N = \left[\frac{1}{\rho}\int \frac{d^d\boldsymbol{k}}{(2\pi)^d} e(k) n_\infty(\boldsymbol{k})\right] - \left[\frac{1}{N}\sum_{\boldsymbol{k}} e(k) n_N(\boldsymbol{k})\right]. \tag{4.14}$$

The key difficulty in using eq. (4.14) is finding a reasonable approximation to $n_\infty(\boldsymbol{k})$. Some progress can be made by analyzing the Monte Carlo estimator for the Fourier transform of the momentum distribution, i.e. the off-diagonal one-particle density matrix [69]

$$n(\boldsymbol{r}) = \left\langle \frac{\Psi(\boldsymbol{R} : \boldsymbol{r}_i \to \boldsymbol{r})}{\Psi(\boldsymbol{R})} \right\rangle_{|\Psi|^2}, \tag{4.15}$$

where $\boldsymbol{R}$ denotes the positions of all N particles, and the notation "$: \boldsymbol{r}_i \to \boldsymbol{r}$" means that particle i is moved from $\boldsymbol{r}_i$ to $\boldsymbol{r}$. As noted by W.R. Magro and D.M. Ceperley [70], direct application of eq. (4.15) with periodic boundary condition can result in superfluous contributions, because all periodic images of particle i are moved. The images will contribute to the ratio in eq. (4.15) if Ψ has long-range components, e.g., eq. (4.5). Chiesa et al. [65] and Holzmann et al. [59] later used this observation to design a finite-size correction to the momentum distribution and the kinetic energy. To leading-order [59]

$$n_\infty(\boldsymbol{k}) - n_N(\boldsymbol{k}) \approx \int_{\frac{(2\pi)^d}{\Omega}} \frac{d^d\boldsymbol{q}}{(2\pi)^d} \left[u_{\boldsymbol{q}}(1 - S(\boldsymbol{q})) - \rho u(\boldsymbol{q})^2 S(\boldsymbol{q})\right] \left(n_N(\boldsymbol{k}+\boldsymbol{q}) - n_N(\boldsymbol{k})\right), \tag{4.16}$$

where $u_{\boldsymbol{q}}$ is the Jastrow pair function in the wave function eq. (4.5). As shown in Fig. 8 of Ref. [71], the leading-order correction to $n(\boldsymbol{k})$ works well for lithium. Further, Table III in the Supplemental materials of Ref. [71] shows that the corrected $n_N(\boldsymbol{k})$ can be used to accurately correct the finite-size error in the kinetic energy using eq. (4.14). To achieve this good result for a metal with a sharp Fermi surface such as lithium, it is crucial to densely sample momentum space while preserving the Fermi surface using grand-canonical twist averaging.

4.2.2 From wave function

Instead of using the relation between kinetic energy and the momentum distribution eq. (4.12), one can directly analyze the QMC estimator for kinetic energy to find its finite-size correction. The VMC estimator for the kinetic energy of a Slater-Jastrow wave function $\Psi = De^{-U}$ is (from eq. (14) of Ref. [60])

$$T_N^{VMC} = \frac{1}{N}\left\langle -\sum_{i=1}^{N} \frac{\hbar^2}{2m}\left[\frac{\nabla_i^2 D}{D} - (\boldsymbol{\nabla}_i U)^2\right]\right\rangle \equiv T_N^D + T_N^U. \tag{4.17}$$

The dominant finite-size correction in the determinant term is due to one-particle "shell filling" effects, whereas the dominant correction in the Jastrow term is due to long-range two-particle correlation. I will now discuss these two effects in turn.

4.2.2.1 Single-particle "shell filling" effect

If the orbitals in the determinant are from some effective one-particle theory such as HF or KS-DFT, then they are solutions of some effective one-particle potential v_{eff}

$$\left[-\frac{\hbar^2\nabla^2}{2m} + v_{\text{eff}}\right]\phi_n(\boldsymbol{r}) = \epsilon_n\phi_n(\boldsymbol{r}). \tag{4.18}$$

Thus, one can work out the determinant contribution to the kinetic energy

$$T_N^D \equiv -\frac{\hbar^2}{2m}\sum_{i=1}^{N}\frac{\nabla_i^2 D}{D} = \left[\sum_{n=1}^{N}\epsilon_n - \sum_{i=1}^{N} v_{\text{eff}}(\boldsymbol{r}_i)\right], \tag{4.19}$$

by eq. (19) in Ref. [60]. As the number of electrons is increased, the kinetic contribution eq. (4.19) increases by the energies of the new orbitals being occupied. Consider the ideal Fermi gas in a 2D square box. As the number of same-spin particles increase from $N = 2$ to 5, the first shell of states in reciprocal space become filled. They all have the same single-particle energy, so the total kinetic energy increases linearly with N. However, when one adds a 6^{th} particle, it increases the total energy by twice the amount as one in the first shell. As shown in Fig. 4.2, this shell filling effect causes oscillation in the kinetic energy as a function of the number of particles, making size extrapolation difficult. It can be drastically reduced by adopting canonical twist averaged boundary conditions (TABC), where the number of particles is the same across all twists. Further, grand-canonical twist averaged boundary condition (GC-TABC), where the number of particles change according to the exact Fermi surface, can exactly remove this single-particle finite-size effect. Finally, there is another "pocket" method which reduces the number of twists needed. Within a pocket in reciprocal space, the orbitals in the determinant smoothly acquire a phase as the twist is varied. Once these pockets are mapped out, one can perform one calculation per pocket and weigh it by the volume of the pocket to exactly remove the one-particle finite-size error [60].

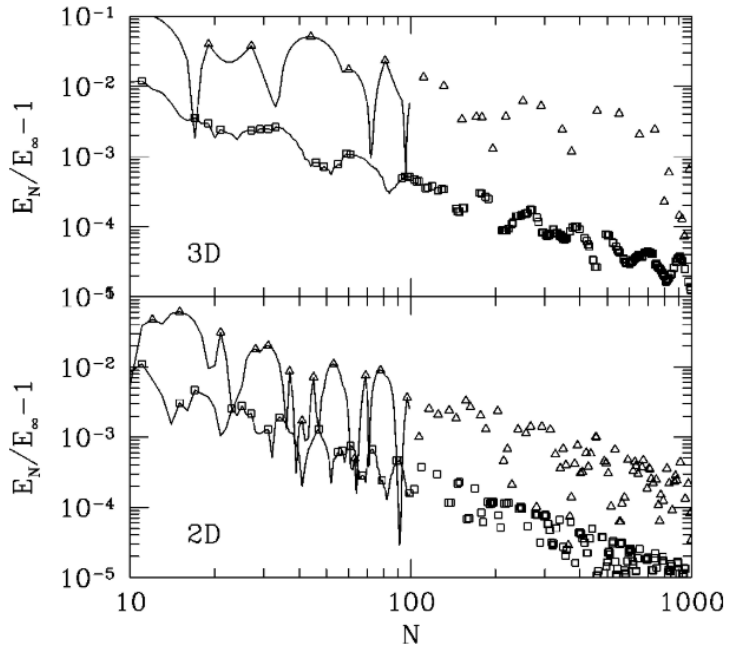

Figure 4.2: Relative error of total energy vs. number of particles with PBC (up triangles) and TABC (squares) in 2D and 3D [72]

4.2.2.2 Two-body size effect

Using the RPA Jastrow pair potential from eq. (4.5), its contribution to eq. (4.17) becomes

$$T_N^U \equiv \frac{1}{N}\left\langle \sum_{i=1}^{N} \frac{\hbar^2}{2m}(\boldsymbol{\nabla}_i U)^2 \right\rangle \approx \frac{1}{\Omega}\sum_{\boldsymbol{k}\neq\boldsymbol{0}} \frac{\hbar^2}{2m}\rho u_{\boldsymbol{k}} u_{-\boldsymbol{k}} S(\boldsymbol{k}), \tag{4.20}$$

by eq. (33) in Ref. [60]. Recall the general relation between $S(\boldsymbol{k})$ and $u(\boldsymbol{k})$ eq. (3.22)

$$2\rho u_{\boldsymbol{k}} \approx S^{-1}(\boldsymbol{k}) - S_0^{-1}(\boldsymbol{k}). \tag{4.21}$$

Since $S^{-1}(\boldsymbol{k})$ diverges faster than $S_0^{-1}(\boldsymbol{k})$ as $k \to 0$, eventually $2\rho u_{\boldsymbol{k}} \approx S^{-1}(\boldsymbol{k})$. Thus, to leading-order eq. (4.20) becomes

$$T_N^U \approx \frac{1}{2\Omega}\sum_{\boldsymbol{k}\neq\boldsymbol{0}} e(k) u_{\boldsymbol{k}}, \tag{4.22}$$

which should be compared with eq. (4.2) for potential energy. Thus, the procedure to correct the two-body finite-size error in the kinetic energy is analogous to the potential correction scheme eq. (4.3)

$$\Delta T_N \equiv T_\infty - T_N = \left[\int \frac{d^d \boldsymbol{k}}{(2\pi)^d} - \frac{1}{\Omega} \sum_{\boldsymbol{k}} \right] \frac{e(k)}{2} u(\boldsymbol{k}), \tag{4.23}$$

where $u(\boldsymbol{k})$ is an interpolation of the converged Jastrow pair potential, which can be approximated using the converged static structure factor in the long wavelength limit.

4.2.2.3 Finite-temperature correction

Based on notes from D. M. Ceperley

At finite temperature and under the RPA, the long-range part of the action can be optimized to minimize the variance of the local energy, resulting in

$$2\rho u_k = Q(\boldsymbol{k}, \beta)^{-1} \tanh\left(\frac{\beta}{2} \frac{e(k)}{Q(\boldsymbol{k}, \beta)} \right) - S_0(\boldsymbol{k}, \beta)^{-1}, \tag{4.24}$$

where β is inverse temperature, $e(k) = \lambda k^2$ is the dispersion of the particle, $\rho = N/\Omega$ is density, and $S_0(\boldsymbol{k}, \beta)$ is the non-interacting structure factors.

$$Q(\boldsymbol{k}, \beta) \equiv \left(S_0(\boldsymbol{k}, \beta)^{-2} + \frac{2\rho v_{\boldsymbol{k}}}{e(k)} \right)^{-1/2}. \tag{4.25}$$

$Q(\boldsymbol{k}, \beta)$ reduces to Gaskell RPA $S(\boldsymbol{k})$ as $\beta \to \infty$. Since $\lim_{x \to \infty} \tanh(x) = 1$, eq. (4.24) becomes eq. (3.22) in this limit. Assuming the relation between $S(\boldsymbol{k})$ and $u_{\boldsymbol{k}}$ eq. (3.22) holds, the finite-temperature RPA structure factor is

$$S(\boldsymbol{k}, \beta) = Q(\boldsymbol{k}, \beta) / \tanh\left(\frac{\beta}{2} \frac{e(k)}{Q(\boldsymbol{k}, \beta)} \right). \tag{4.26}$$

Equations (4.24) and (4.26) can be used to derived leading-order finite-size corrections to the kinetic and potential energies using eq. (4.23) and (4.3), respectively.

Chapter 5

Benchmark of dynamic-ion DMC on small molecules

This chapter is based on the following article(s):

I. Yubo Yang, Ilkka Kylänpää, Norm Tubman, Jaron Krogel, Sharon Hammes-Schiffer, and David Ceperley, "How large are nonadiabatic effects in atomic and diatomic systems?" J. Chem. Phys. **143**, 124308 (2015).

II. Norm Tubman, Yubo Yang, Sharon Hammes-Schiffer, and David Ceperley, "Interpolated wave functions for nonadiabatic simulations with the fixed-node quantum Monte Carlo method," ACS Symp. Ser. **1234**, pp. 47-61 (2016).

5.1 Introduction

There have been several recent discoveries [73–77] suggesting that quantum wave functions, which include both electronic and ionic degrees of freedom, have many interesting properties that have yet to be explored. This includes the development of equations that exactly factorize a wave function into electronic and ionic components, [74, 78] the disappearance of conical intersections in wave functions of model systems, [75] and the use of quantum entanglement to study electronic and ionic density matrices. [76] Extending such studies to realistic systems is of broad interest and will considerably expand our understanding of electron-ion systems. However, treatment of *ab initio* electron-ion systems is challenging, and applications have thus been limited. The most accurate simulations of electron-ion wave functions are generally done with very specialized wave functions, which are limited to rather small systems. [79] Methods are also being developed to treat larger systems with different regimes of validity. [80–93]

As a framework to address these problems in general realistic systems, we recently demonstrated that quantum Monte Carlo (QMC) can be combined with quantum chemistry techniques to generate electron-ion wave functions. [73] We treated realistic molecular systems and demonstrated that our method can be scaled to larger systems than previously considered while maintaining a highly accurate wave function. In the following, we extend our previous work by considering the simulation of a larger set of atoms and

molecules. We calculate ionization energies and atomization energies that can be directly compared with previous results for benchmarking purposes.

5.2 Method

5.2.1 Fixed-Node Diffusion Monte Carlo (FN-DMC)

Diffusion Monte Carlo [94–99] is a projector method that evolves a trial wave function in imaginary time and projects out the ground-state wave function. For practical simulations of fermions, the fixed-node approximation is introduced, which depends only on the set of electronic positions where a trial wave function is equal to zero. This approximation is different than approximations typically used in quantum chemistry calculations. In this work, we demonstrate that we can generate high-quality nodal surfaces for a range of systems that include full electron-ion wave functions.

If the trial wave function has the same nodal surface as the exact ground-state wave function, FN-DMC will obtain the exact ground-state energy. Approximate nodal surfaces can be generated through optimization of the full wave function. Such approximate nodal surfaces have been tested and validated on a wide range of systems, and consistently provide an excellent approximation of the exact ground-state energy, comparable to the state of the art in *ab initio* simulations. [100] In addition, the energies generated with FN-DMC are variational with respect to the ground-state energy.

In all but a handful of previous QMC simulations, [101–107] calculations are performed with nuclei "clamped" to their equilibrium positions. However, such an assumption is not fundamentally required by FN-DMC.

5.2.2 Electronic Wave Function and Optimization

There are several different approaches for generating electronic wave functions for a FN-DMC calculation. [108–111] Recent advances [110, 112, 113] have made it possible to simultaneously optimize thousands of wave function parameters using variational Monte Carlo with clamped nuclei. We use an initial guess for the wave function that is generated from complete active space self-consistent-field (CASSCF) [114, 115] calculations using the quantum chemistry package GAMESS-US. [116] The optimized orbitals are then used in a configuration interaction singles and doubles (CISD) calculation to generate a series of configuration state functions (CSFs). [117] For the small systems Li^+, Be^+, LiH and BeH, a CASSCF calculation with a large active space is used in place of CISD. The multi-CSF expansion of the wave function can be expressed

in the following form,

$$\Psi_{\mathrm{CISD}}(\vec{r};\vec{R}_o) = \sum_{i=1}^{N_{\mathrm{CSF}}} \alpha_i \phi_i(\vec{r};\vec{R}_o), \tag{5.1}$$

where $\vec{r}$ refers to the spatial coordinates of all the electrons and $\vec{R}_o$ refers to the equilibrium positions of all the ions. $\phi_i(\vec{r})$ and $\vec{\alpha} = \{\alpha_1, \alpha_2, \dots\}$ are the CSFs and CI coefficients generated from CISD. The cc-pV5Z basis [118] is used for the atomic systems and the Roos Augmented Triple Zeta ANO basis [119] is used for the molecular systems except for the smallest system LiH, where the cc-pV5Z basis is used.

After the multi-CSF expansion is generated, we impose the electron-nucleus cusp condition on each molecular orbital [120] and add a Jastrow factor to the wave function to include electron correlation. [121] Our Jastrow factor contains electron-electron, electron-nucleus and electron-electron-nucleus terms. The full electronic wave function used in FN-DMC is,

$$\psi_e(\vec{r};\vec{R}) = e^{J(\vec{r},\vec{R},\vec{\beta})}\Psi_{\mathrm{CISD}}(\vec{r};\vec{R}). \tag{5.2}$$

We optimize the CSF and Jastrow coefficients, $\vec{\alpha}$ and $\vec{\beta}$, respectively, simultaneously with QMCPACK. [122, 123] Optimization is performed with the ions clamped to their equilibrium positions $\vec{R}_o$. The equilibrium geometries for BeH and BH are chosen to be the ECG-optimized distances for comparison with the ECG (explicitly correlated Gaussian) method, and the geometries for the rest of the hydrides are taken from experimental data[124]. We use 3.015 a.u. as the equilibrium inter-nuclei distance for LiH, as this geometry is found to provide a lower clamped-nuclei ground-state energy than the ECG optimized distance of 3.061 a.u.. We include all CSFs with coefficients larger than a specific cutoff ϵ to lend reasonable flexibility to the wave function during optimization. We include as many CSFs as possible to maximize the flexibility of the wave function. However, the inclusion of too many CSFs with small expansion coefficients can introduce noise as they require a large number of samples in the optimization step to be optimized. We have chosen ϵ to restrict the number of CSFs in the wave function to be $\sim$1000 in all systems studied. Optimization is performed with the linear method [113] with roughly 10^6 statistically independent samples.

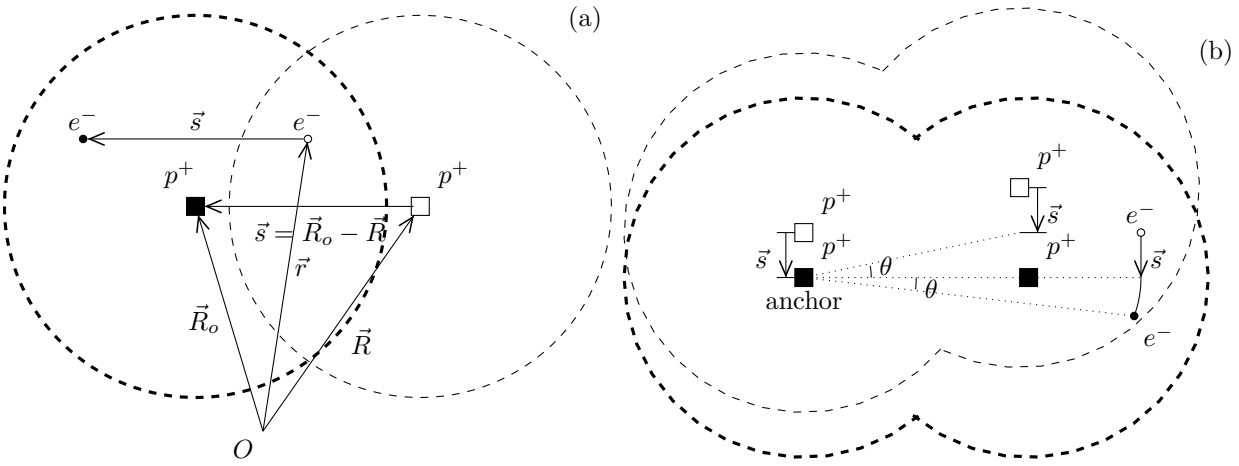

Figure 5.1: Dragged-node approach for simulation of atomic and molecular systems in QMC. **(a)** For atomic systems we can consider the entire wave function shifting with the ion. This process can be visualized by following a contour of the wave function. The thick dashed circle represents a contour of the electronic wave function when the proton is at its reference position $\vec{R}_o$, and the thin dashed circle represents the same contour when the proton has moved to a new position $\vec{R}$. To evaluate the ion-dependent electronic wave function $\bar{\psi}_e(\vec{r}, \vec{R})$, we simply map the electron to its proper place in the reference wave function $\psi_e(\vec{r}; \vec{R}_o)$. That is, $\bar{\psi}_e(\vec{r}, \vec{R}) = \bar{\psi}_e(\vec{r} + \vec{s}, \vec{R}_o) = \psi_e(\vec{r} + \vec{s}; \vec{R}_o)$ where $\vec{s}$ is the shift required to put the proton back to its reference position. **(b)** For H_2^+, we pick one of the protons as an "anchor" and approximate the new wave function by dragging the reference wave function with the "anchor" proton. We also rotate the wave function to align its axis of symmetry with the orientation of the two protons.

5.2.3 Electron-Ion Wave Function

Once a satisfactory electronic wave function has been obtained, we construct the electron-ion wave function using the ansatz,

$$\Psi_{eI}(\vec{r}, \vec{R}) = \psi_I(\vec{R})\bar{\psi}_e(\vec{r}, \vec{R}), \tag{5.3}$$

where $\vec{R}$ denotes the spatial coordinates of all ions and $\bar{\psi}_e(\vec{r}, \vec{R})$ is an ion-dependent electronic wave function adapted from the clamped-nuclei wave function $\psi_e(\vec{r}; \vec{R}_o)$ through basis set dependence. Due to the localization of Gaussian basis sets around nuclei, as used in quantum chemistry calculations, the nodes of $\bar{\psi}_e$ change based on the ionic positions, which we have previously called the dragged-node approximation. [73] Although there are approaches for going beyond the dragged-node approximation, it was demonstrated to be highly accurate over a range of molecules in previous work. [73] For the systems considered here, we can impose various symmetries of the Hamiltonian onto the wave function that arise from the relative motion of the ions. In Fig. 5.1 we demonstrate this approach for the simple cases of a hydrogen atom and an H_2^+ molecular ion. This approach can be generalized for use in larger systems or even applied to parts of a bigger system, e.g., treating light ions as quantum particles and heavy ions as "clamped".

The term ψ_I consists of simple products of Gaussian wave functions over each pair of nuclei,

$$\psi_I(\vec{R}) \propto \prod_{i,j>i} e^{-a_{ij}(|\vec{R}_i - \vec{R}_j| - b_{ij})^2}, \tag{5.4}$$

where a_{ij} is a coefficient that is optimized and b_{ij} are taken to be the equilibrium distances between the nuclei. Since ψ_I is nodeless, the choice of the variational parameters a_{ij} and b_{ij} does not affect the converged FN-DMC energy. FN-DMC is then performed with the fully optimized electron-ion wave function. We perform timestep extrapolation for all of the tested systems. At least four timesteps from 0.005 Ha^{-1} to 0.0005 Ha^{-1} are used for all systems studied in the clamped-nuclei FN-DMC calculation, and at least three timesteps from 0.005 Ha^{-1} to 0.0001 Ha^{-1} are used in the nonadiabatic FN-DMC calculation.

Using definitions from Ref. [125], the adiabatic approximation will refer to the complete neglect of the nonadiabatic coupling matrix when the Schrödinger equation is expressed in the basis of eigenstates of the electronic Hamiltonian. In this context, the nonadiabatic contribution to an eigenvalue of the electronic Hamiltonian can be partitioned into two parts: the diagonal Born-Oppenheimer correction (DBOC), which involves only the single electronic state of interest, and the remaining corrections arising from terms that involve excited eigenstates of the electronic Hamiltonian. The DBOC discussed in this work is the expectation value of the nuclear kinetic energy operator in the ground adiabatic electronic state. We define the clamped-nuclei ground-state energy E_c as the lowest eigenvalue of the electronic Hamiltonian and the nonadiabatic ground-state energy E_n as the lowest eigenvalue of the full molecular Hamiltonian that includes the nuclear kinetic energy operator. The zero-point energy (ZPE) for a diatomic molecule is the energy of the ground vibrational state of the one-dimensional vibrational mode. Note that the ZPE of the nuclei is part of the difference $E_n - E_c$. The ZPE is not considered to be nonadiabatic, but its contribution is included in the full molecular Hamiltonian.

5.3 Results and Discussion

5.3.1 Atoms and Ions

To assess the quality of our results for atoms and ions [1], we compare to previous results from highly accurate simulations, as presented in Table 5.1. For the clamped-ion results, QMC [109–111, 139, 140] and quantum chemistry benchmarks are available for comparison. To illustrate the high-quality QMC techniques

[1] All calculations are performed for the most abundant isotope. In units of electron mass, the isotope masses for Li, Be, B, C, N, O, F are taken to be 12782.4327, 16419.2608, 20214.7648 6, 21862.7553, 25512.1484, 29141.0754, 34613.1200, respectively. The Li mass used for the LiH molecule is 12649.6690, which is slightly different from that used for the atomic Li simulations, but we do not expect this to affect our results within our statistical errors.

used in this work, we compare our clamped-ion atomic results with a recent QMC benchmark study. [111] The ground-state FN-DMC energies consistently agree across all systems studied (except for O^+) within 0.1 mHa. This shows that similar nodes can be obtained with different forms of the wave function. In particular, our large ($\sim$ 1000 CSF) multi-determinant expansions can be compared with the approach used by Seth *et al.*, [111] which relies on moderately-sized multi-determinant expansions ($\sim$ 100 CSF) with a backflow transformation. For certain atoms, we can compare to more accurate simulation techniques. For C^+ as well as the neutral and ionized Li, Be and B, well-converged ECG calculations are available, where basis set error is converged to less than 0.1 mHa. This convergence is corroborated by results from the Hylleraas method for Li [126] and Be^+. [134] In Table 5.1, we have used the lowest variational results as our references for these systems, as the convergence is such that the accuracy is higher than other current theoretical or experimental estimates.

All of our clamped-ion results agree within 0.2 mHa of the ECG references, as shown in Figure 5.2. The error bars for the reference ECG results are absorbed into the DMC error bars for clarity, because the ECG error bars are orders of magnitude smaller compared to the DMC error bars. While ECG results exist for C and N, they are not well converged and are not suitable references. [132, 141] The benchmark results in Ref. [129] are a standard for atomic energies, and we report them as our references in Table 5.1 for the larger atoms. However, these benchmark results are not consistently accurate to 0.1 mHa. For instance, if we use the ECG results for C^+ with the most accurate ionization reference energy, then we find a reference energy for the C atom of -37.84489 Ha, which is 0.1 mHa higher than that reported in Ref. [129]. The systems with the most error are O and F, for which other QMC studies seem to experience similar difficulties. [110, 111, 142, 143] We note that for some of these systems it may be possible to absorb the sign problem and increase the accuracy further in future studies. [144, 145]

It is more difficult to find accurate references for the nonadiabatic results. We provide the first nonadiabatic QMC benchmarks for the first-row atoms. There are six ECG calculations of nonadiabatic ground-state energies that are reportedly converged beyond 0.1 mHa, which we use as references. Our reported nonadiabatic ground-state energies for Li, Be, Be^+, B, B^+ and C^+ are in agreement with the ECG results to within 0.2 mHa, as shown in Figure 5.2. For these systems, the ECG results are converged to essentially the exact ground-state energies in both the clamped-ion and nonadiabatic cases. The difference between our DMC ground-state and ECG reference is the fixed-node error present in our wave functions. We would expect the clamped ion results to be more accurate than the nonadiabatic results, since the nonadiabatic wave functions are inherently more difficult to construct. However, for the systems in Figure 5.2, this difference in quality is less than 0.1 mHa.

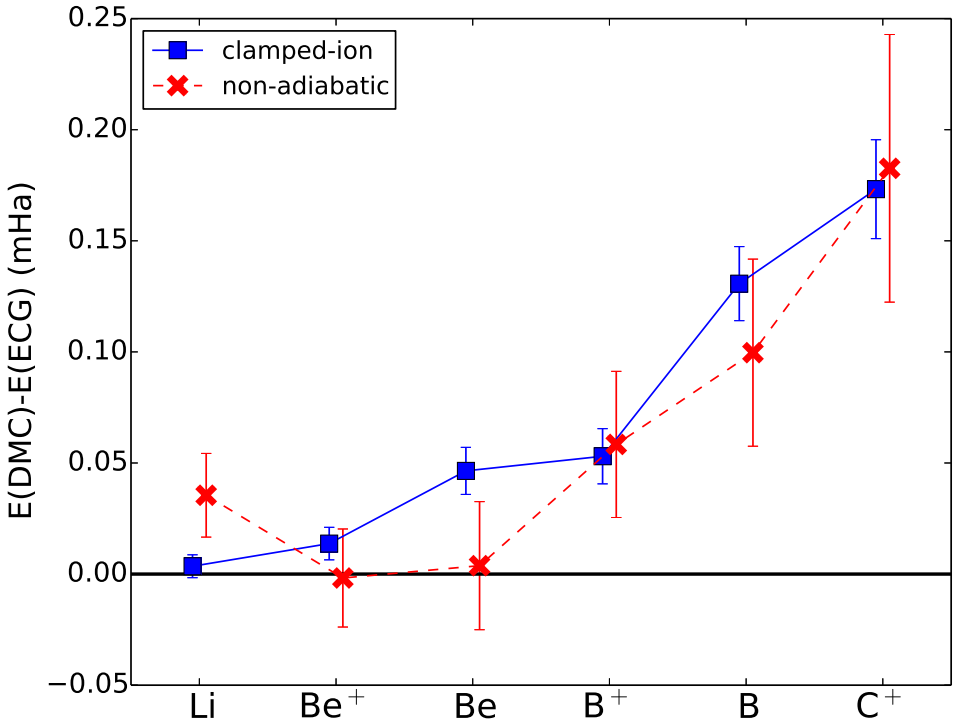

Figure 5.2: FN-DMC ground state energies for Be^+, Be, B^+, B, C^+ relative to ECG references [127, 128, 131, 134–136] for either clamped-ion or nonadiabatic calculations. These relative energies provide an estimate for the fixed-node error in the electronic and electron-ion wave functions, respectively.

No reference calculations exist for the heavier atoms N, O, and F. However, it is possible to apply finite-mass correction [129, 146] (i.e., divide by $1 + m_e/M$, where m_e is the mass of an electron and M is the mass of the nucleus) to the best clamped-ion references to estimate the nonadiabatic references. The energies for N, O, and F obtained in this way are -54.5871, -75.0647 and -99.7310 Ha, respectively. For the ionized states, we obtain -54.0525, -74.5643 and -99.0900 Ha.

The ionization potentials are reported in Table 5.1 and shown in Figure 5.3. For determining a set of nonadiabatic reference data, we subtract the spin-orbit and relativistic corrections (estimated by Klopper et. al. [137]) from the NIST experimental data. [138] Ref. [137] is considered to have the most accurate ionization energies due to its usage of state-of-the-art quantum chemistry techniques shown to provide close agreement with experiment. For the atoms considered in this work, ionization energies have previously been predicted to be independent of all nonadiabatic effects beyond the DBOC to within an accuracy of 0.1 mHa. [137] This prediction is based on calculations that are reported to be exact and agree to high accuracy with experiment. As shown in Figure 5.3, the ionization potentials calculated with and without the Born-Oppenheimer approximation are all within 1 mHa of the reference energies. Further, the clamped-ion and nonadiabatic predictions for the ionization potentials are statistically indistinguishable for all systems

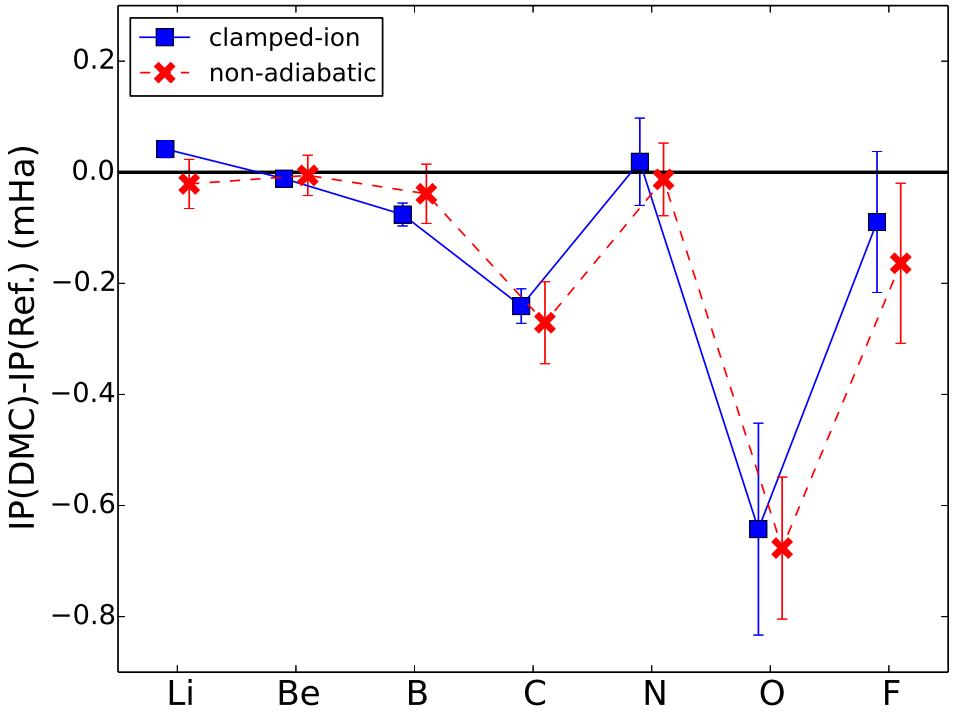

Figure 5.3: Calculated ionization energies relative to reference data. The same reference is used for both clamped-ion and nonadiabatic results. The calculated energies are all within 1 mHa of the reference.

studied, consistent with the previous study. [137]

In Table 5.2 and Figure 5.4, we demonstrate the amount of nonadiabatic contribution to the ground-state energies in atoms and ions calculated as the difference between the nonadiabatic and clamped-ion ground-state energies. The amount of nonadiabatic contribution is always positive for these systems and mostly increases with atomic number. Using previous benchmark values for the DBOC, we can break down the nonadiabatic contribution of our system into a DBOC contribution and everything beyond the DBOC.[2][3] [147] The DBOC is relatively insensitive to the level of theory. Figure 5.4 indicates that in the atomic systems, the DBOC is the dominant contribution to the nonadiabatic energy, with the remaining amount being close to zero within error bars. The nonadiabatic energy is relatively constant between the neutral and cationic species. This observation suggests that the amount of nonadiabatic contribution is insensitive to the addition or removal of a valence electron. Physically, the valence electrons are farther from the nucleus than the core electrons, thus are likely to be affected to a lesser degree by the delocalization of the nucleus.

The nonadiabatic contributions in the cations can also be compared with those in their corresponding

[2]The DBOC values for the atoms and ions provided by Prof. Wim Klopper are calculated at the CCSD/d-aug-cc-pwCVQZ level using CFOUR.

[3]CFOUR, a quantum chemical program package written by J.F. Stanton, J. Gauss, M.E. Harding, P.G. Szalay and others.

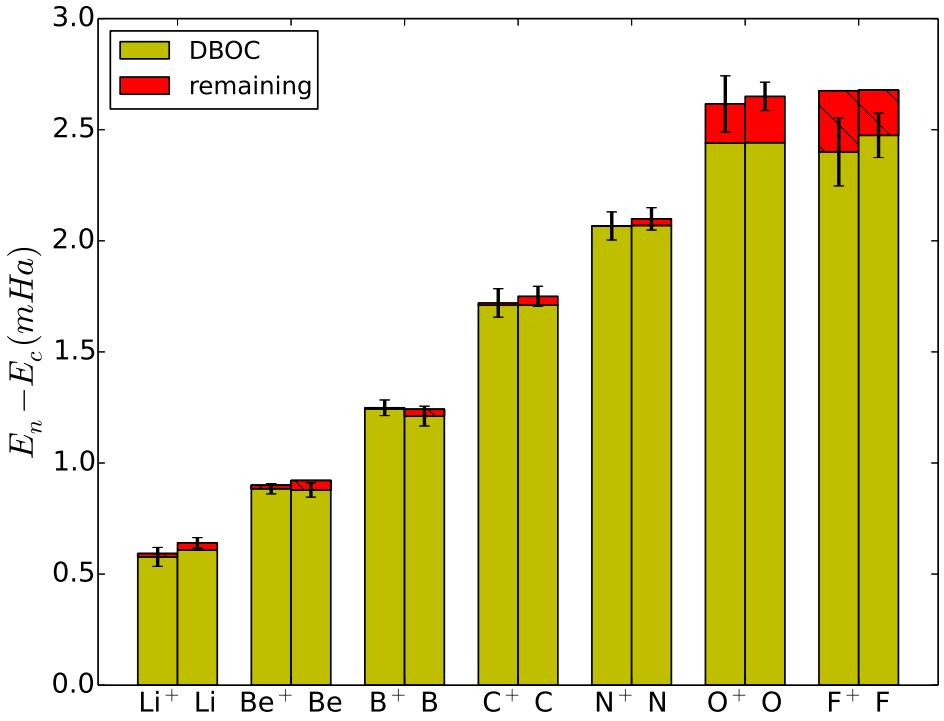

Figure 5.4: The nonadiabatic contribution to ground-state energies of atoms and ions calculated with FN-DMC. The nonadiabatic contribution is partitioned into the DBOC and the remaining correction. A hatched bar indicates the contribution is negative. The numerical DBOC data is provided in Table 5.2.

hydrogen-like atoms for a more in-depth analysis. The nonadiabatic contribution in a hydrogen-like atom can be obtained analytically. The result in Hartree atomic units is

$$E_n - E_c = \frac{Z^2}{2}(1-\mu) \tag{5.5}$$

where $\mu = \frac{M}{M+1}$ is the reduced mass of the hydrogen-like atom and M and Z are the mass and atomic number of the nucleus, respectively. The increase in the nonadiabatic contribution with increasing Z for hydrogen-like atoms reflects the stronger Coulombic attraction between the electron and the nucleus, which enhances the effects of the delocalization of the nucleus. An interesting case to consider is the transition from Li^{2+} to Li. As shown in Figure 5.4 and Figure 5.5, the addition of a core electron to Li^{2+} decreases the nonadiabatic contribution, while the addition of a valence electron has no further effect within our error bars. We also calculate the nonadiabatic contribution in Be^{2+} to be 0.78(5) mHa, which is 0.29(5) mHa lower than the nonadiabatic contribution in Be^{3+} and is closer to that in Be^+ of 0.88(2) mHa. Because the core electrons interact more strongly with the nucleus than do the valence electrons, the core electrons are affected more by the delocalization of the nucleus. Moreover, the addition of a second core electron

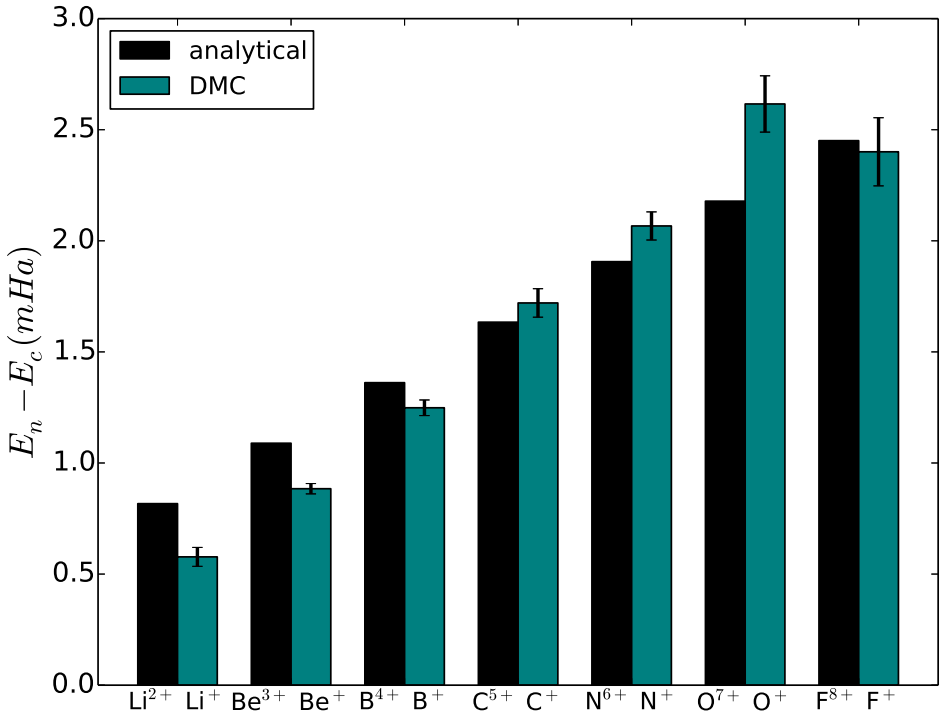

Figure 5.5: The nonadiabatic contribution to ground-state energies of ions and their corresponding hydrogen-like atoms calculated with FN-DMC and analytically as shown in Eq. 5.5.

decreases the nonadiabatic contribution for Li^{2+} and Be^{3+}. We note that the nonadiabatic correction to the atomic ground-state energies of Eq. (5.5), which only holds for single electron systems, is roughly linear in Z, while the relativistic recoil correction [148] scales as Z^4. Therefore, the nonadiabatic effect is not seen experimentally, as it is less significant than this relativistic effect.

5.3.2 Hydrides

In Table 5.3, we present our results on a series of molecular systems (hydrides). Finding accurate reference data for these systems to 0.1 mHa is not straightforward. We will use highly converged ECG data when available. Two ECG calculations have been performed in the clamped-nuclei limit for LiH [146, 152] and we agree within 0.03 mHa with the more recent reference. For the rest of the systems, we combined the best clamped-ion atomic references in Table 5.1 and thermochemistry [153] estimates of atomization energy D_e in Table 5.3 to produce the reference ground-state energies. For BeH and BH, we are within 1 mHa of the reference values, and our energies are lower than the best available quantum chemistry results of -15.247846 Ha [154] and -25.287650 Ha [155] for BeH and BH, respectively.

Nonadiabatic ECG calculations only exist for the three smallest hydrides. Our results for LiH and BeH

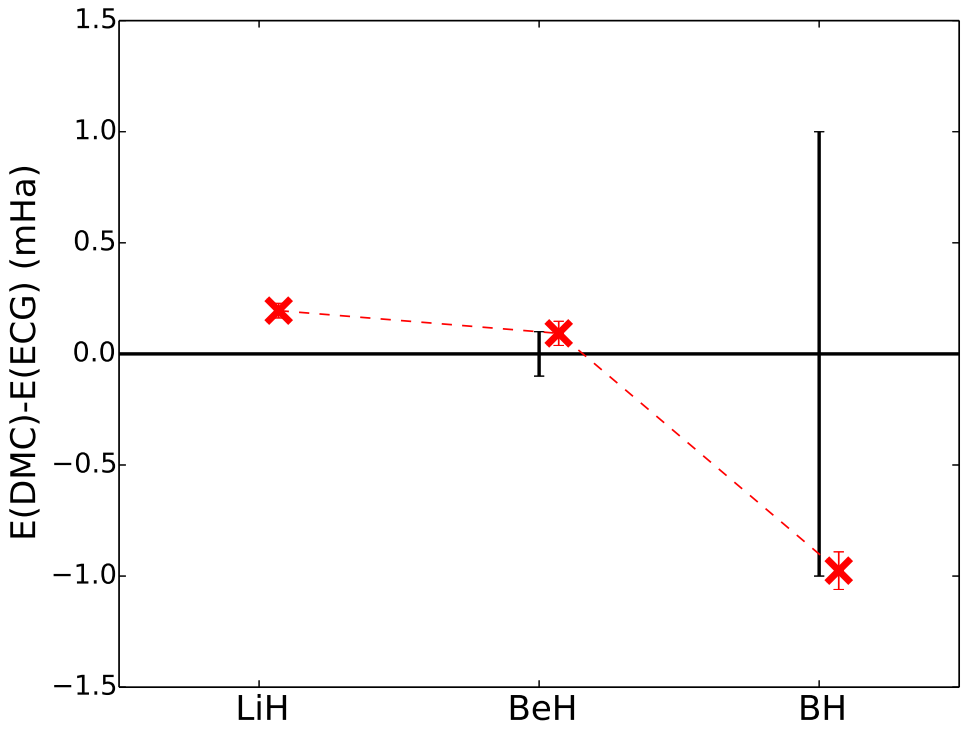

Figure 5.6: The nonadiabatic FN-DMC ground-state energies of LiH, BeH and BH relative to ECG references. The error bars for the nonadiabatic ECG references are shown as thick dark lines, and the error bars for the FN-DMC calculations are comparable to the size of the symbols.

agree with the ECG references to within 0.2 mHa, as shown in Figure 5.6. The ECG reference for LiH is converged to the true ground-state energy beyond 0.1 mHa; thus, it is likely that our wave function has a fixed-node error of 0.2 mHa. For BeH, our result is within 0.1 mHa of the ECG reference and agrees within error bars. With BH being one of the largest ECG simulations performed, the DMC result is actually lower in energy, in this case by 1 mHa. The ECG error bar on BH is large, and it is not evident how close our result is to the true ground state, although extrapolating the ECG result with basis set size suggests we are within 1 mHa. [131] For these nonadiabatic systems, we have the lowest variational result for BH, and the only simulated results of for CH, OH, and HF, to the best of our knowledge.

The atomization energies of the diatomic systems are reported in Table 5.3. High-quality thermochemistry benchmarks are used for comparison. [153] We take the reference energies from the last column of Table VI of Ref. [153] and subtract the corrections in the ΔE_{SR} (scalar relativistic) and SO (spin-orbit coupling) columns for the comparison with our non-relativistic energies. For the comparison with our clamped-nuclei results, we further subtract the DBOC and ZPE (zero-point energy) corrections. The atomization energies estimated in the clamped-nuclei limit agree within 1 mHa of the references for all but the largest molecule, HF. Within quantum Monte Carlo, it is generally more difficult to obtain an accurate nodal surface for a

molecule than for an atom. As a result, our estimates for the clamped-nuclei atomization energies are lower than the references in all cases. A similar trend can be observed when comparing our nonadiabatic results with the references. For each molecule, the deviation from the reference is similar in the clamped-nuclei and nonadiabatic cases except for CH.

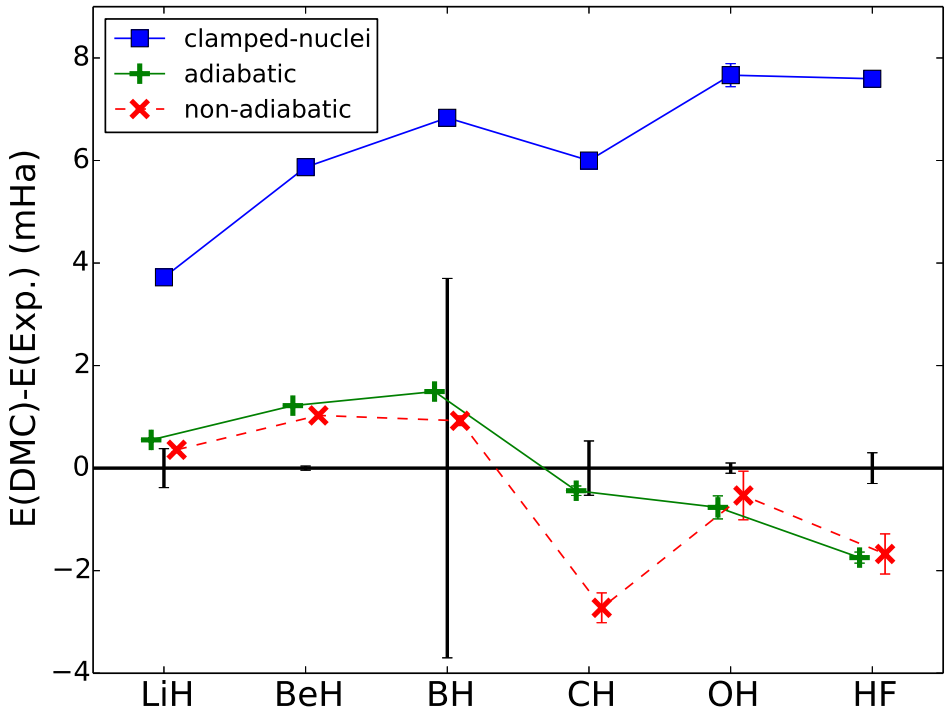

Figure 5.7: Atomization energies of first row hydrides obtained with FN-DMC relative to experimental data. The adiabatic results are estimated by adding zero-point energies from Ref. [153] to the clamped-nuclei results.

In Figure 5.7, we compare both our clamped-nuclei and our nonadiabatic results to experimental data. We also provide adiabatic estimates by adding the zero-point energies calculated with coupled-cluster techniques in Ref. [153] to our clamped-nuclei results. To calculate experimental atomization energies starting from the clamped-nuclei results, energetic corrections due to zero-point motion of the nuclei, nonadiabatic effects, spin-orbit coupling and relativistic effects should be included. For these highly adiabatic systems, the inclusion of zero-point motion alone is sufficient to bring our clamped-nuclei results to within 2 mHa of the experimental results. Except for the case of CH, the nonadiabatic results agree closely with their adiabatic counterparts and are closer to the experimental values, although for BH the experimental error bar is too large to provide a high-accuracy comparison. For CH, the experimental result suggests that our electron-ion wave function for this molecule has an unusually large fixed-node error.

To estimate the nonadiabatic contribution to the ground-state energies for these hydrides, we calculate

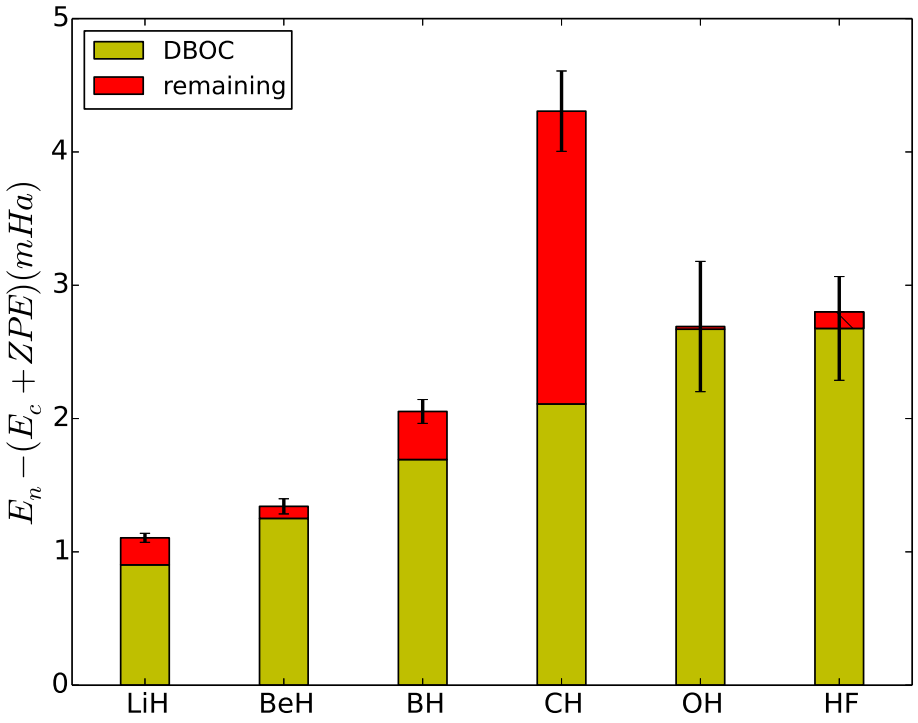

Figure 5.8: The nonadiabatic contribution to the ground-state energies in hydrides calculated with FN-DMC. The adiabatic reference energies are calculated by adding zero-point energy contributions from Ref. [153] to our clamped-nuclei results. The nonadiabatic contribution is partitioned into the DBOC and the remaining correction. A hatched bar indicates the contribution is negative.

the difference between our nonadiabatic and adiabatic results, as shown in Figure 5.8. Similar to the atomic case, we break down the nonadiabatic energy of our system into a DBOC contribution and everything beyond the DBOC.[4] [147] The ZPE and DBOC contributions to this difference are listed in Table 5.4. We also calculate the nonadiabatic correction to the dissociation energies of the hydrides. For BeH, OH, and HF, the nonadiabatic contribution is almost entirely accounted for by the DBOC with the remaining correction being zero within error bars. For LiH, BH, and CH, the remaining amount of nonadiabatic contribution seems to be nonzero, and appears quite significant in CH. However, if the electron-ion wave function is significantly lower in quality than the electronic wave function for a given system, then the amount of nonadiabatic contribution will be overestimated. We also use the zero-point energies from Feller et. al. [153] as corrections, which may introduce some additional uncertainty. Regardless, our current predictions suggest that nonadiabatic effects in BH and CH are larger than in the other systems we considered.

For the LiH molecule, we also calculated the electron affinity for comparison to ECG results. We calculated the ground-state energy of LiH^- to be $-8.08222(2)$ Ha for the case of clamped-nuclei. With nona-

[4]The DBOC references provided by Prof. David Feller are calculated at the CCSD(T)/aug-cc-pVTZ level using CFOUR

diabatic effects included, our result is −8.07811(3) Ha. Our nonadiabatic result is in good agreement with a previous ECG study, [156] which reported a value of −8.07856887 Ha. We report an electron affinity of 0.01187(4) Ha, which can be compared to the ECG prediction of 0.012132(2) Ha and agrees with the experimental value of 0.0126(4) Ha.[5]

5.3.3 Dragged Node Approximation

In our current approach, the fixed-node approximation generally causes an overestimate the nonadiabatic effects. This is a result of the increased complexity of optimizing wave functions for the full electron-ion system. When the clamped-ion energies are more accurate than the electron-ion energies, we overestimate the nonadiabatic energy. It should be noted that in some cases the energies for the full electron-ion simulations can be more accurate than for the corresponding clamped-ion simulations, as suggested by the comparisons of Be, Be+, B, B+, and C+ in Fig. 5.3. However, this is less likely for molecular systems in which the ions can move relative to each other. All our simulations up to this point have used a particular type of approximation to the nodal structure called the dragged-node approximation. This approximation can be used for wave functions in the form of Eq. 5.1 in which we start by generating a wave function defined at the equilibrium geometry. When the ions change position the wave function changes based on the basis set dependence of the ion coordinates. The change in the wave function causes a corresponding change in the nodes. The dragged-node approximation is completely variational when used in FN-DMC. For systems that do not show strong nonadiabatic behavior the dragged-node approximation should yield excellent results. It was surprising that the energy contribution from nonadiabatic effects of the CH molecule was larger than other hydrides, indicating that we might need to use better wave function forms to accurately simulate CH.

5.3.4 Improving Wave Functions

We can improve the electron-ion wave function by updating the electronic part using quantum chemistry rather than relying on the dragged-node approximation

$$\Psi_{CISD}(\boldsymbol{r}, \boldsymbol{R}) = \sum_i c_i(\boldsymbol{R})\phi_i(\boldsymbol{r}, \boldsymbol{R}_o), \tag{5.6}$$

where the determinant expansion coefficients $c_i(\boldsymbol{R})$ now depend on the positions of the ions as opposed to being fixed to their equilibrium values as in Eq. 5.1.

The wave function in Eq. 5.6 is more general than Eq. 5.1 but is more difficult to generate. In practice,

[5] We note that LiH ground state energies which we compare against are mislabeled in Ref. [156], with LiH^- and LiD being switched.

it is not feasible to regenerate both the orbitals and expansion coefficients for each new configuration of the ions. However, for diatomic molecules we can precompute and optimize wave functions at different distances and then use the precomputed wave functions to interpolate wave function amplitudes at other ion positions. There are several different ways this can be done. The first approach we considered is to use a grid of bond lengths and calculate a fully optimized electronic wave function at each grid point. Then one would calculate the electronic wave function at each grid point and use an interpolation scheme to determine the electron-ion wave function. Although technically feasible, we found it difficult to maintain a smooth wave function within this approach. A second approach, for which we present results here, parameterizes the determinant coefficients as a function of the ion positions. For a diatomic system, this corresponds to generating a 1D function for each determinant coefficient. This is an improvement over the dragged-node approximation, because the coefficients of the determinants are allowed to change with ion distance and can capture complicated ion dependence of the node.

We tested the improved wave function Eq. 5.6 for the CH molecule by implementing the following additional steps. At the equilibrium C-H separation R_o=2.1165 a.u., we optimize the electronic wave function, which includes all determinant coefficients and a Jastrow. At two C-H separations near equilibrium R_{left}=2.0 a.u., R_{right}=2.25 a.u., we reoptimize only the determinant coefficients of the electronic wave function, keeping all other parameters fixed. For each determinant coefficient, we approximate its dependence on the distance between the ion separations R using a linear interpolation

$$c_i^*(R) = c_i(R_{\text{left}}) + \frac{c_i(R_{\text{right}}) - c_i(R_{\text{left}})}{R_{\text{right}} - R_{\text{left}}} \times (R - R_{\text{left}}). \tag{5.7}$$

5.3.5 Results and Discussion

We present here a diagnostic test to determine when this type of improvement might be important. The potential energy surface as a function of the C-H distance is plotted for several different nodal surfaces in Figure 5.9. In particular, we calculate clamped-ion energies that correspond to the dragged-node approximation as well as energies from a linear interpolated wave function as given by Eq. 5.7. The reference result is obtained by re-optimizing the Jastrow factor and the determinant coefficients at every C-H separation. The region for the most probable ion distances is indicated by the vertical dashed lines. Over the region of important ion separations, the potential energy surface from the interpolated wave function is improved over the dragged-node potential energy surface when compared to the fully optimized potential energy surface. Further away from the region of interest, both the dragged-node and the interpolated wave functions deviate significantly from reference data. However, this region is seldom sampled during our FN-DMC simulations

and is not expected to introduce a large bias into our results.

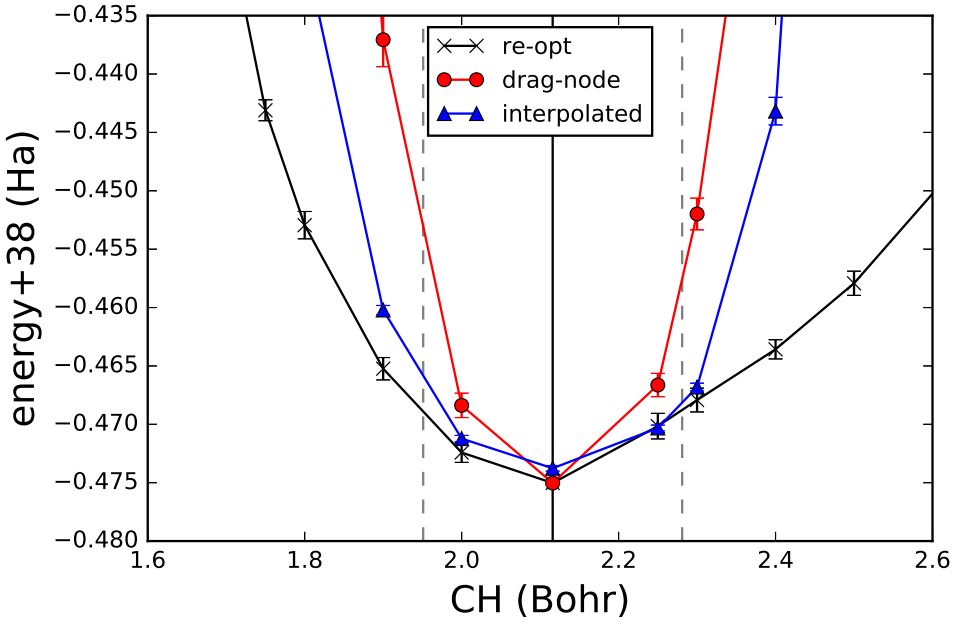

Figure 5.9: Clamped-ion VMC total energy as a function of C-H separation using a hierarchy of wave functions. The dashed lines mark the FWHM of the distribution of C-H separation. Within the region marked by the dashed lines it can be seen that the interpolated wave function results are a closer match to the reference 're-opt' energies than the dragged-node energies.

To determine the nonadiabatic contribution for each system, we partition the energy into different components, which includes the clamped-ion energies, the zero point energy (ZPE) and the diagonal Born-Oppenheimer correction (DBOC). Everything that remained we consider to be the nonadiabatic energy. Using standard quantum chemistry tools all of the above terms can be calculated or approximated to high accuracy with the exception of the nonadiabatic energy. As a result the nonadiabatic energy is a quantity that has not been theoretically calculated for many systems. We see from Fig. 5.8 that the nonadiabatic energy was less than 0.1 mHa for most of the systems considered. There are two exceptions, where the nonadiabatic energy was larger, for the cases of BH and CH molecules. Our new results for CH with the improved wave functions can be seen in Table 5.5. Due to the variational property of FN-DMC, it is evident that these energies are improved over the previous best results for the CH molecule, which is not unexpected given the differences between the interpolated wave function and the dragged-node wave function as seen in Figure 5.9. Our previous results showed a nonadiabatic energy of 1.9 mHa, whereas our new results show a nonadiabatic energy of 0.9 mHa, which can be seen for the largest determinant expansion in Table 5.5. This is consistent with our previous results, mainly that the CH molecule is somewhat nonadiabatic, even though our new estimate of the nonadiabatic energy is smaller. For a system with a moderate amount of

nonadiabatic energy, more effort is needed in generating accurate wave functions. Improving the wave functions beyond the dragged-node approximation will lower the estimate of the nonadiabatic energy, but it is likely to remain somewhat large if the improvements of the wave function correspond to degrees of freedom beyond the Born-Oppenehimer approximation. This is what we see for CH, as the nonadiabatic energy is still relatively large in comparison to other systems. We note that this is still not a definitive estimate of the nonadiabatic energy, but it is likely the best estimate ever calculated for this system.

We also noticed interesting behavior that results from improving the quality of the electron nodes. We performed clamped-ion (static) and fully nonadiabatic (dynamic) calculations using different truncations levels for the determinant expansion. The FN-DMC energy and variance for the various calculations are shown in Table 5.5. As we include more determinants in our wave function, both the energy and variance of the static calculation decrease. However, the same does not happen for the variance of the dragged-node approximation, in which we see the surprising result that the variance increases. This suggests that the clamped-ion wave functions are being improved to a larger extent than the dragged-node wave functions with increasing determinant number. It is also interesting to note that for the wave functions with the smallest determinant expansion ($N_{det} = 35$), the variance is almost the same between the clamped-ion and dragged-node wave functions. The energy and variance with determinant coefficient interpolation is generally improved from our previous wave function with the dragged-node approximation. A comparison between the dynamic runs with and without interpolation also shows that coefficient interpolation becomes more important for larger determinant expansions. In particular, the variance improves with increasing determinant number, showing similar behavior to that of the static wave function.

In Figure 5.10, we show the various contributions to the difference between the static and dynamic ground-state energies. Due to the difference in energy scales for the quantities of interest, we only plot the diagonal Born-Oppenheimer energy and the nonadiabatic energy. To calculate the nonadiabatic energy we take the estimated zero-point energy for CH to be 6.438 mHa [153]. The diagonal Born-Oppenheimer correction is estimated to be 2.11 mHa. Our best result is given by the 4739 determinant interpolated wave function in Figure 5.11. There is an apparent increase in the nonadiabatic energy of the CH molecule that results from using the dragged-node approximation. The improvement seen by using the interpolated wave function instead of the dragged-node approximation is 1 mHa for the CH molecule; a relatively large change in the energy. That the dragged-node approximation produced such a large error for the CH molecule suggests at the very least that the nodal structure of its wave function has more complex dependence on the ion configuration than the rest of the molecules under consideration.

Figure 5.10 also reveals that the nonadiabatic energy is only observed with the large determinant ex-

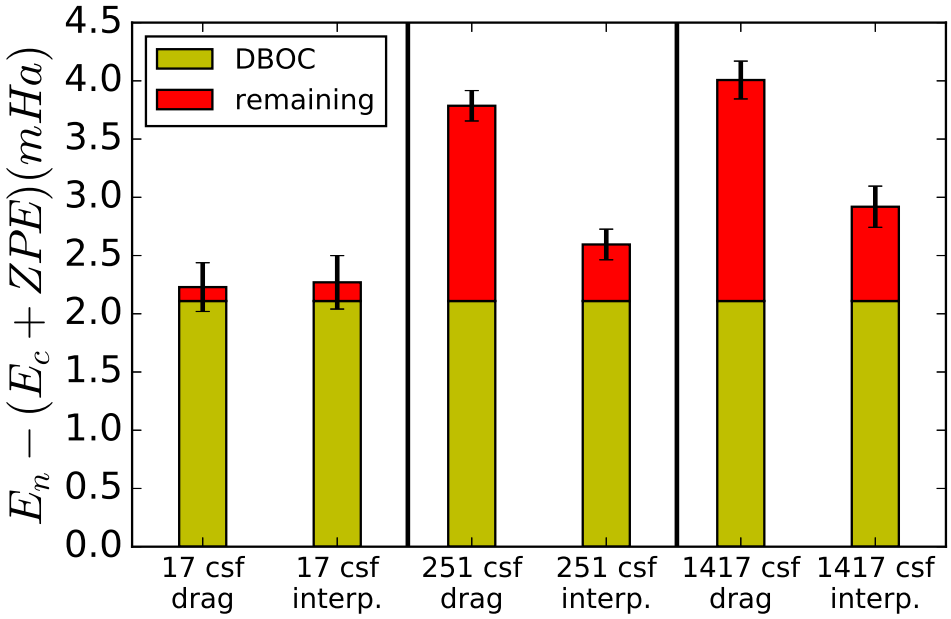

Figure 5.10: Nonadiabatic energy of CH with and without determinant coefficient interpolation. The wave function "interp" denotes that the determinant coefficients depend on C-H separation through linear interpolation. For the largest two determinant expansions a more significant contribution from nonadiabatic effects is observed than the smallest determinant expansion.

pansions. There are several possible explanations for this. It is possible we are optimizing the static wave function significantly better than the electron-ion wave function. There is some indication of this from the variance of the dragged-node approximation, but this is less evident for the interpolated wave function. Another possible explanation is that only when the wave function is highly optimized do significant changes arise in the wave function amplitudes with regard to ion positions. A related effect is that large fluctuations of the ion distance can be suppressed if the wave function and the related nodal surface is not well optimized at large ion distances. Such effects can be mitigated with the interpolated wave function approach, and are likely to be suppressed with increasing the number of determinants for the electronic part of the wave function, even for the dragged-node wave function. In Fig. 5.11, we compare our improved results for CH with the nonadiabatic contributions from previous work. It is evident that the CH nonadiabatic energy is still larger than all the other molecular systems.

5.4 Conclusion

We calculated the ground-state energies of first-row atoms and their corresponding ions and hydrides with and without the Born-Oppenheimer approximation. In addition, we examined the amount of nonadiabatic

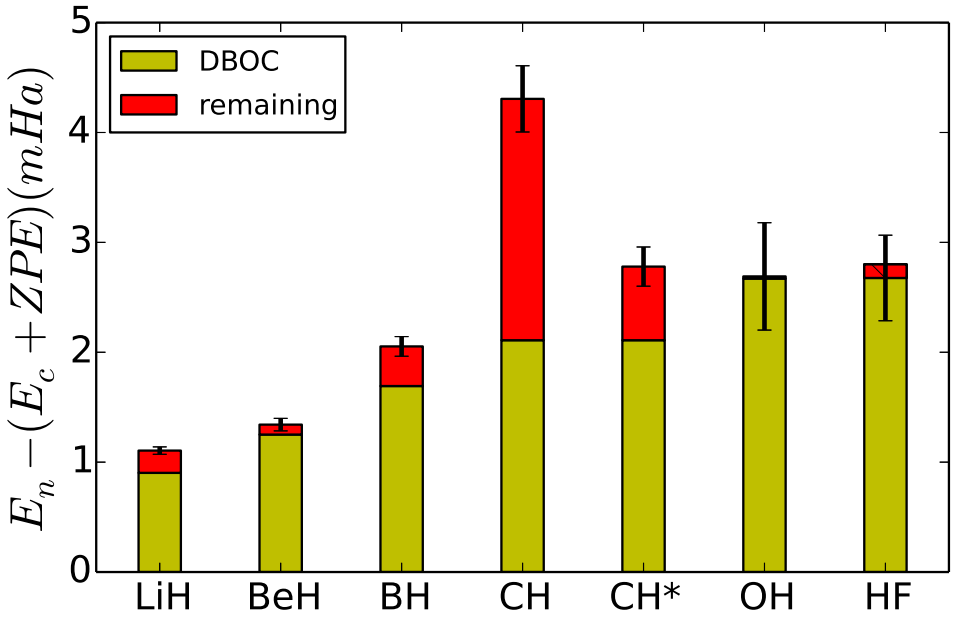

Figure 5.11: Nonadiabatic energy of diatomic molecules. The best (4739 determinant) result for CH with determinant coefficient interpolation is shown with *. Note that for all the molcules except for BH and CH the nonadiabatic energies are roughly 0.1 mHa or smaller.

contribution to the ground-state energies of all systems studied and determined the amount to be up to a few mHa. In the case of CH, the nonadiabatic effects beyond the DBOC appeared to be unusually large, although we found that a large part of this discrepancy was due to the fixed-node error. To this end, we improved the electron-ion wave functions for diatomic systems by interpolating determinant coefficients as a function of ion separation. Even with the improved wave function, there is still a slightly larger contribution from nonadiabatic effects in CH.

We found the ionization energies of the atoms to be independent of the Born-Oppenheimer approximation, consistent with a previous high-level quantum chemistry study. [137] In contrast, the atomization energies of the hydrides showed effects of nonadiabaticity, although they were generally much less than 1 mHa. This work obtained the first nonadiabatic QMC benchmark data for non-relativistic ground-state energies and obtained the lowest variational result for BH and the only results for CH, OH and HF, to the best of our knowledge.

Table 5.1: Ground-state energies for atoms and ions and the ionization energies for the atoms: fixed-node DMC results of this work (FN-DMC) for atoms and ions with and without the Born-Oppenheimer approximation. The rows marked with bold **FN-DMC** are our nonadiabatic results. The ionization potentials (IPs) are reported in the last section of the table. Energies are given in units of Hartree. For the highly accurate Hylleraas and ECG results, up to 8 digits are reported in the table.

Atom	Li(^{2}S)	Be(^{1}S)	B(^{2}P)	C(^{3}P)	N(^{4}S)	O(^{3}P)	F(^{2}P)
			clamped-ion				
FN-DMC	-7.478057(5)	-14.66731(1)	-24.65374(2)	-37.84448(2)	-54.58851(6)	-75.0658(2)	-99.73177(6)
Seth DMC [111]	-7.478067(5)	-14.667306(7)	-24.65379(3)	-37.84446(6)	-54.58867(8)	-75.0654(1)	-99.7318(1)
E_{ref}[a]	-7.4780603	-14.667356	-24.653866	-37.8450	-54.5892	-75.0673	-99.7339
			nonadiabatic				
FN-DMC	-7.47742(2)	-14.66643(3)	-24.65252(4)	-37.84273(4)	-54.58641(5)	-75.06313(6)	-99.7293(1)
ECG [b]	-7.4774519	-14.666435	-24.652624	-37.841621	N/A	N/A	N/A
Ion	Li$^+$(^{1}S)	Be$^+$(^{2}S)	B$^+$(^{1}S)	C$^+$(^{2}P)	N$^+$(^{4}S)	O$^+$(^{3}P)	F$^+$(^{2}P)
			clamped-ion				
FN-DMC	-7.27989(2)	-14.324749(7)	-24.34883(1)	-37.43071(2)	-54.05371(5)	-74.56597(6)	-99.0909(1)
Seth DMC [111]	-7.279914(3)	-14.324761(3)	-24.34887(2)	-37.43073(4)	-54.05383(7)	-74.56662(7)	-99.0911(2)
E_{ref}[c]	-7.2799134	-14.324763	-24.348884	-37.430880	-54.0546	-74.5668	-99.0928
			nonadiabatic				
FN-DMC	-7.27931(4)	-14.32387(2)	-24.34758(3)	-37.42899(6)	-54.05165(4)	-74.5634(1)	-99.0885(1)
ECG [d]	N/A	-14.323863	-24.347641	-37.429169	N/A	N/A	N/A
			clamped-ion				
IP (FN-DMC)	0.198 17(2)	0.342 56(1)	0.304 90(2)	0.413 77(3)	0.534 79(8)	0.4998(2)	0.6409(1)
			nonadiabatic				
IP (**FN-DMC**)	0.198 11(4)	0.342 57(4)	0.304 94(5)	0.413 74(7)	0.534 76(7)	0.4998(1)	0.6408(1)
IP (Ref.)[e]	0.198 130	0.342 572	0.304 980	0.414 014	0.534 775	0.500 452	0.640 946

[a] For the atomic references, we use the Hylleraas result for Li, [126] and ECG results for Be [127] and B. [128] Ref. [129] is used for C,N,O and F where the ground-state energies are taken from Table XI.

[b] We use nonadiabatic ECG results as the reference for Li, [130] Be [131] and B [128], which are converged to the true ground-state to well within 0.1 mHa. The result for C, [132] however, may have error on the order of 1 mHa.

[c] For the ionic references, we use the ICI result for Li$^+$, [133] Hylleraas result for Be$^+$ [134] and ECG results for B$^+$ [135] and C$^+$. [79, 136] Ref. [129] is used for N$^+$,O$^+$,F$^+$.

[d] ECG references only exist for Be$^+$, [131] B$^+$ [135] and C$^+$. [136]

[e] Spin-orbit coupling and relativistic corrections [137] are removed from experimental data [138] for comparison.

Table 5.2: Nonadiabatic corrections for the ground-state energies of atoms and ions. E_n and E_c are the FN-DMC calculations of the nonadiabatic and clamped ground-state energies, respectively. The DBOC contribution is provided by Wim Klopper (personal communication). All energies are reported in units of mHa.

System	$E_n - E_c$	DBOC	System	$E_n - E_c$	DBOC
Li^+	0.58(4)	0.591970	Li	0.64(2)	0.608411
Be^+	0.88(2)	0.899706	Be	0.88(3)	0.920848
B^+	1.25(4)	1.242988	B	1.21(5)	1.241669
C^+	1.72(6)	1.710382	C	1.75(5)	1.710900
N^+	2.07(6)	2.066914	N	2.10(8)	2.069149
O^+	2.6(1)	2.440320	O	2.6(2)	2.441821
F^+	2.4(2)	2.675128	F	2.5(1)	2.678181

Table 5.3: Ground-state energies and atomization energies: fixed-node DMC results of this work for all first row hydrides with and without the Born-Oppenheimer approximation. The rows marked with bold **FN-DMC** are our nonadiabatic results. All atomization energies are estimated for 0K. D_o includes zero-point energy contribution, while D_e does not. Both total energies and dissociation energies are given in units of Hartree.

Molecule	LiH($^1\Sigma^+$)	BeH($^2\Sigma^+$)	BH($^1\Sigma^+$)	CH($^2\Pi$)	OH($^2\Pi$)	HF($^1\Sigma^+$)
			clamped-nuclei			
FN-DMC	-8.070518(7)	-15.24793(2)	-25.28867(3)	-38.4780(1)	-75.7356(1)	-100.4552(1)
E_{ref} [a]	-8.0705473	-15.2483(4)	-25.2893(2)	-38.4792(2)	-75.7382(2)	-100.4600(3)
			nonadiabatic			
FN-DMC	-8.06624(3)	-15.24194(5)	-25.28128(9)	-38.4672(3)	-75.7245(5)	-100.4431(4)
ECG [131, 149, 150]	-8.0664371(15)	-15.24203(10)	-25.2803(10)	N/A	N/A	N/A
			clamped-nuclei			
D_e (FN-DMC)	0.092 46(1)	0.080 62(2)	0.134 93(3)	0.1335(1)	0.1699(2)	0.2234(1)
D_e Feller [b]	0.092 62(5)	0.0809(4)	0.1354(2)	0.1342(2)	0.1709(2)	0.2258(3)
			nonadiabatic			
D_o (**FN-DMC**)	0.089 10(4)	0.075 78(6)	0.1290(1)	0.1248(3)	0.1617(5)	0.2141(4)
D_o Feller [c]	0.089 40(5)	0.0761(4)	0.1299(2)	0.1276(2)	0.1622(2)	0.2166(3)
D_o Exp. [124, 151]	0.088 74(38)	0.074 75(4)	0.1281(37)	0.1275(5)	0.1622(1)	0.2158(3)

[a] For LiH, ECG provides the best reference energy. [152] For the rest of the systems, we combined the best clamped-ion atomic references in Table 5.1 and thermochemistry estimates of D_e in this table to produce the reference ground-state energies.

[b] Estimates for D_e are calculated by subtracting the scalar relativistic, spin-orbit coupling and zero-point energy corrections from the reference D_o in Table VI of Ref. [153].

[c] Here only the scalar relativistic and spin-orbit coupling corrections are subtracted.

[d] The atomization energy for BeH in Ref. [124] disagrees with previous high-level theoretical benchmarks, [131, 153] thus we use Ref. [151] instead. For several of the systems, multiple experimental values are available in the literature. We report experimental values that were aggregated in one single reference, [124] except for BeH. [151]

Table 5.4: Nonadiabatic corrections for the ground-state energies of diatomic molecules. E_n and E_c are the FN-DMC calculations of the nonadiabatic and clamped ground-state energies, respectively. The ZPE and DBOC contributions are provided by David Feller (personal communications).The nonadiabatic correction for the dissociation energy estimated with FM-DMC are included in the ΔD_o column. All energies are reported in units of mHa.

System	$E_n - E_c$	ZPE	DBOC	ΔD_o
LiH	4.28(3)	3.17	0.902410	-0.19(4)
BeH	5.99(6)	4.65	1.251000	-0.19(6)
BH	7.39(9)	5.34	1.692559	-0.6(1)
CH	10.8(3)	6.44	2.109487	-2.3(3)
OH	11.1(5)	8.43	2.670397	0.2(5)
HF	12.0(4)	9.34	2.799624	0.1(4)

Table 5.5: DMC energy and variance with static ions, dynamic ions with dragged-node ("drag") and dynamic ions with determinant coefficient interpolation ("interp.").

N_{det}	Energy (Ha)	Variance (Ha^2)	method
35	-38.4709(1)	0.3130(5)	static
35	-38.4622(2)	0.3169(3)	drag
35	-38.4621(2)	0.3173(3)	interp.
723	-38.4770(1)	0.2489(3)	static
723	-38.4667(1)	0.334(2)	drag
723	-38.4679(1)	0.2713(7)	interp.
4739	-38.4781(1)	0.2300(4)	static
4739	-38.4676(1)	0.334(5)	drag
4739	-38.4687(2)	0.267(7)	interp.

Chapter 6

Dynamic-ion DMC Study of Solid Hydrogen at Megabar Pressures

6.1 Introduction

The properties and phase transitions of hydrogen under megabar pressures are important in diverse fields of study. For astronomy, models of the interior of gas giants such as Jupiter and Saturn depend critically on the nature of the molecular liquid to atomic liquid transition (LLT), namely whether it is first-order or continuous [12, 157]. For condensed matter, metallic hydrogen holds promise for a room temperature conventional (BCS) superconductor [158, 159]. For computational physics, hydrogen remains an important benchmark for both electronic structure [160] and ion dynamics methods. With no need for a pseudopotential, simulations of hydrogen avoid a significant source of bias. However, the low mass of the nuclei necessitates quantum treatment of the lattice degree of freedom, often beyond the harmonic approximation.

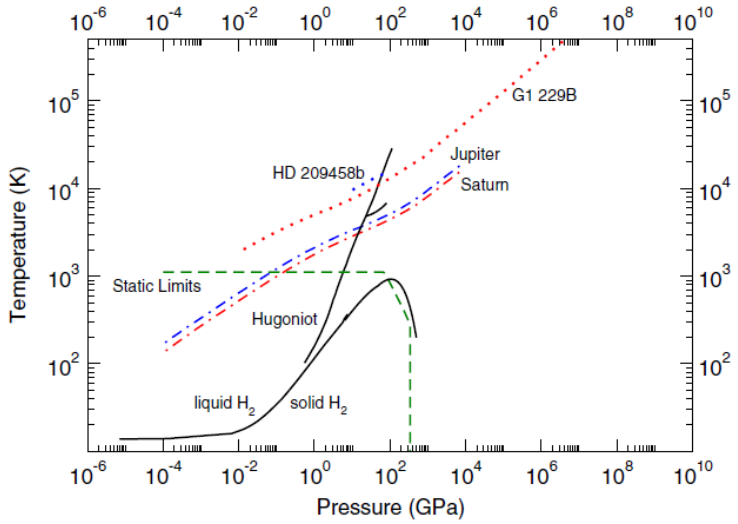

Figure 6.1: Partial phase diagram of hydrogen on log-log scale [161].

Established experimental results on high-pressure hydrogen are limited. At room temperature and below, diamond anvil cell (DAC) is the dominant apparatus to achieve such high pressures. Small size of the cell and fragility of the sample limit experimental probes to low-power optics such as infrared and Raman

spectroscopy[162]. Hydrogen is a weak scatterer of X-Rays [163], thus excluding this excellent tool for structural determination in most experiments. Only recently has X-ray analysis been performed up to 254 GPa [164, 165]. At high temperatures, shock wave compression is the main method to achieve megabar pressures. Due to the transient nature of theses experiments, acquiring and analyzing shock-wave data is challenging. Most notably, one cannot directly measure temperature, which may cause misinterpretation of raw data [5, 166, 167]. Given the experimental difficulties, predictive simulations are highly desirable as they can inform and verify experiments [4].

Simulation of high-pressure hydrogen is also challenging. Without experimental structural information from X-ray, many theoretical calculations have been performed on structures found in density functional theory (DFT) random structure searches [168]. Constrained by computational cost, these searches are limited to classical protons, causing the methods to miss, for example, saddle-point structures that can be stabilized by nuclear quantum effect [169]. Predictive simulations of hydrogen require accurate methods both in the description of the electronic ground-state Born-Oppenheimer (BO) potential energy surface (PES) and in the inclusion of nuclear quantum effect beyond the quasi-harmonic approximation. The popular Perdew-Burke-Ernzerhof (PBE) density functional in DFT erroneously predicts some molecular structures to be metallic [3]. However, its use in conjunction with Classical molecular dynamics (MD) results in reasonable transition pressure for the LLT at certain temperatures due to error cancellation [170]. This and other fortuitous cancellations of error has led many to believe that the PBE functional provides a good description of solid hydrogen and caused much confusion in the community. PBE predicts a conductive molecular structure above 200 GPa, a molecular-to-atomic transition around 300 GPa [2], and low-temperature superconducting liquid. All these predictions contradict experimental evidence. Systematic benchmark of the PES from various DFT functionals against QMC found the vdW-DF1 functional to be the most accurate for molecular hydrogen at megabar pressures [67]. However, this functional has yet to gain widespread adoption due to its higher computational cost and lower popularity compared to PBE.

In this chapter, I will focus on the solid phases of hydrogen. Sec. 6.1.1 summarizes experimental observations, Sec. 6.1.2 summarizes relevant computational studies, Sec. 6.2 details the approach taken in this study, and Sec. 6.3 presents the computational results.

6.1.1 Experiments

As element number one with the simplest atomic structure, hydrogen has surprisingly complex phases at megabar pressures. Further complicating matters, the phase diagram depends on the isotopes, e.g., hydrogen H, deuterium D, and spin isomers of molecular hydrogen. The proton spins anti-align to form a singlet in

para-hydrogen (p-H_2), whereas they align to form a triplet in ortho-hydrogen (o-H_2). To clarify the narrative, I will first introduce the well-established phases in pure samples, then discuss changes due to isotopic and ortho-para conversion.

For pure p-H_2 at low temperature (5∼10 K), three solid phases are well-established. The low-pressure phase (LP) below 100 GPa is a molecular crystal having spherically symmetric H_2 molecules on hcp lattice sites. Above 110 GPa, hydrogen enters a broken-symmetry phase (BSP), where anisotropic intermolecular interactions favor the $J = 2$ $v = 1$ vibrational state of the H_2 molecules rather than the spherically symmetric $J = 0$ $v = 1$ state [171]. Above 160 GPa, after crossing a first-order transition, one finds an orientationally-ordered phase known as the A phase (H-A) [172].

As shown in Fig. 6.2, the transition from LP to BSP phase is sensitive to isotope and nuclear spin. o-D_2, HD, and p-H_2 enters the BSP at 28 GPa [173], 70 GPa [174], and 110 GPA [171], respectively. In contrast, the transition to the A phase is fairly robust across isotope and spin isomer variants. HD, o-D_2, and p-H_2 all enter the A phase between 150 and 160 GPa [172, 174–176]. The phase lines for o-D_2 and HD are shown in Fig. 6.2. The p-H_2 LP-BSP phase line near 100 GPa is not shown. The size and shape of the BSP is the only difference between the phase diagrams of p-H_2, o-D_2, and HD. These orientation transitions are not relevant to o-H_2 and p-D_2, which have a hcp to fcc transition at ambient pressure.

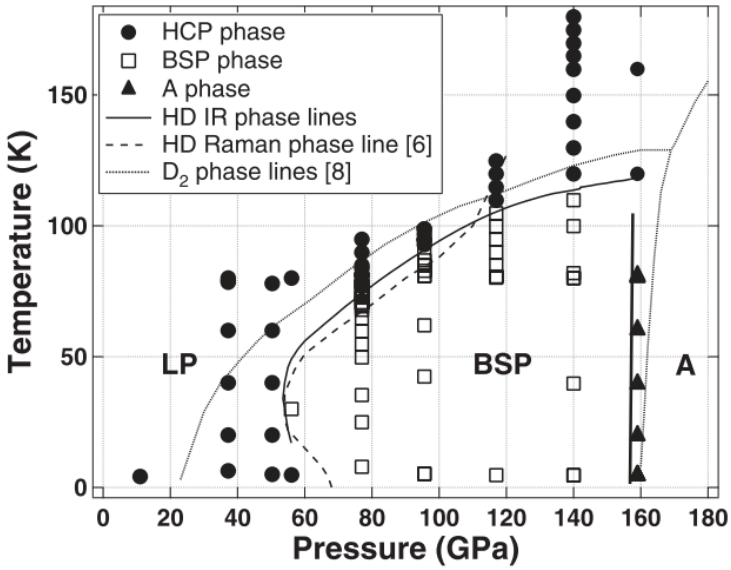

Figure 6.2: Phase diagram of o-D_2 and HD below 200 K and 200 GPa [174].

Transitions to these orientationally ordered phases are detected by changes in Raman and IR spectra. As shown in Fig. 6.3, during the LP to BSP transition, one can observe clear broadening and weakening of the low-frequency roton bands around 350 cm^{-1} and an associated small (15 cm^{-1}) discontinuity in the position

of the vibron peak, which is about 4150 cm^{-1} near the transition pressure 110 GPa [171]. Upon further increase of pressure past 160 GPa, a much larger discontinuity of the Raman vibron (100 cm^{-1}) signals the onset of the A phase [172, 175]. A direct transition from H-A back to the LP phase can be achieved by raising temperature. Across this transition, the intensities of the libron bands decrease discontinuously [171].

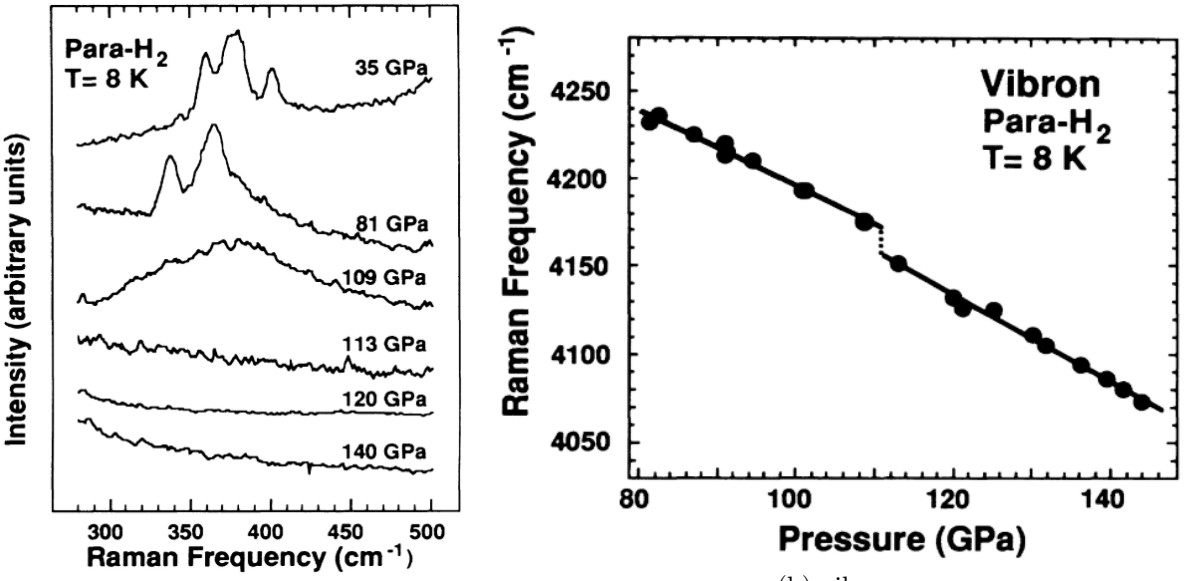

(a) rotons (b) vibron

Figure 6.3: Roton and vibron changes in p-H_2 across the BSP transition [171].

The optical signatures for the LP to BSP transition in o-D_2 are qualitatively similar to those in p-H_2. The vibron decreases discontinuously by 3 cm^{-1} rather than 15 cm^{-1}, while the roton bands broaden and weaken near the transition pressure of 28 GPa rather than 110 GPa [173]. Further confirmation of these two phase transitions were later obtained from IR absorption spectra [176]. Three absorption peaks appear around 3150 cm^{-1} upon entering the BSP phase and are replaced by a single broad peak at the same frequency range when the A phase is reached. The same signatures were used to identify the BSP and A phases of HD at 70 and 160 GPa, respectively [174]. In the A phase, the rather broad and pressure-independent roton band weakens, disappears, and is replaced by a few sharp and strongly pressure-dependent peaks in the frequency range 100∼700 cm^{-1} [177]. These new modes are considered to be lattice libration modes due to their pressure dependence.

Phases with mixed ortho-para concentrations of H_2 are labeled I, II, and III [16, 178], which correspond to the LP, BSP, and H-A phases of pure p-H_2, respectively. As shown in Fig. 6.4, at 300 K and above 220 GPa, we enter yet another solid phase IV, characterized by a splitting of the vibron peak [179]. Both theory and experiment suggest that phase IV consists of alternating layers having rather different in-plane

structures, possibly with two types of molecules. Below 100 K and above 350 GPa, molecular hydrogen becomes semi-metallic, possibly due to the closure of an indirect band gap [180]. Then, above 425 GPa, all IR radiation is absorbed indicating a closure of the direct band gap [17]. Finally, at sufficiently high pressures, the hydrogen molecules will dissociate to form an atomic solid, reportedly at 495 GPa [181], although consensus has yet to be reached.

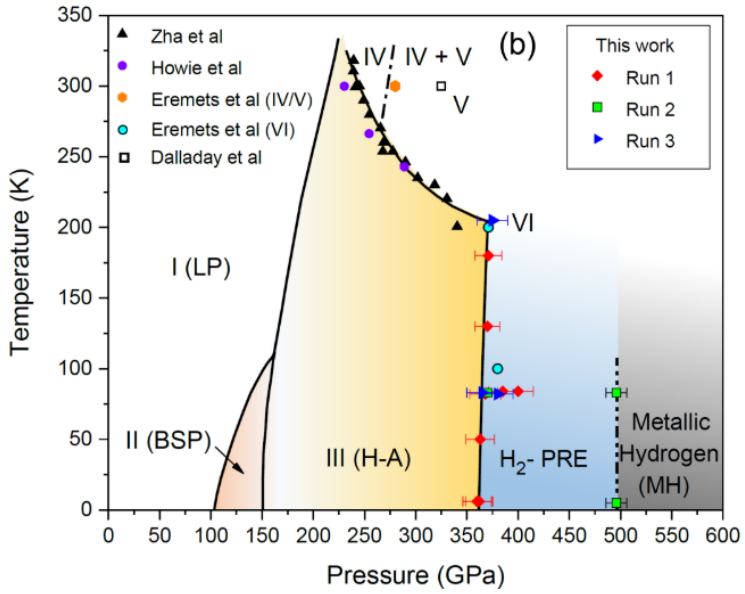

Figure 6.4: Tentative phase diagram of solid hydrogen below 400 K [178].

While the phase boundaries of solid hydrogen are reasonably well-established below 400 K and 400 GPa by diamond-anvil cell (DAC) experiments, characterizations of the solid structures are limited. Due to the small scattering cross section and small sample size in DAC experiments, only a handful of X-ray [164, 165, 182–186] and only one neutron [186] scattering experiments have been published over the past 40 years. Most of our understanding of solid hydrogen is built upon IR and Raman spectra, which provide partial information on the microscopic details of the solid structures. This lack of definitive structural information poses significant difficulty for both theoretical and experimental understanding of solid hydrogen. Experimentally, this has lead to the misidentification of a triple point as a critical point [171, 176], subtlety in the detection of a new phase [187, 188], among many debates over interpretation of optical data.

6.1.2 Calculations

Early computational studies of solid hydrogen rely on assumed crystal structures from known high-pressure phases of other materials or simple symmetry and energetic arguments. Even before the observation of the oriented A phase of solid hydrogen [175], S. Raynor [189] used Hartree-Fock and perturbation theory to show

that the molecular hexagonal closed packed structure with H_2 molecules aligned along the c-axis (mhcp-c) is more energetically favorable than previous considered cubic structures. While a promising candidate for phase III [190], the mhcp-c structure has an early band overlap, rendering it metallic below 150 GPa, resists compression along the c-axis, and has no IR-active vibron [191, 192], all in contradiction with experimental evidence. Thus, E. Kaxiras *et al.* [191] explored different orientations of H_2 molecules in the 2-atom hcp unit cell and found a more energetically favorable insulating structure with molecules oriented $\sim 60^\circ$ from the c-axis. This static-lattice LDA study was later validated by a dynamic-lattice QMC calculation [7], and the structure named mhcp-o. In addition to the hcp structures, H. Nagara and T. Nakamura [193] proposed various rutile structures by minimizing the static-lattice electric quadrupole-quadrupole (EQQ) interactions, while B. Edwards, N. W. Ashcroft, and T. Lenosky [194] proposed an orthorhombic layered structure of Cmca symmetry, which turned out to be metallic at pressures relevant to phase III [195]. This Cmca crystal structure also appeared spontaneously in path integral simulation [196]. These theoretical calculations drove much debate about the fate of phase III at pressures over 300 GPa. Does it become a metallic molecular solid or does it dissociate into an atomic solid without the band gap closing?

In 2007, the advent of random structure searching algorithms produced new candidate crystal structures that have lower enthalpy than previous proposals [168]. The insulating layered structure having C2/c symmetry became the main candidates for phase III. Three diffusion Monte Carlo studies followed to characterize the candidate structures: Azadi *et al.* [1], McMinis *et al.* [2], and Drummond *et al.* [3]. Azadi *et al.* used PBE-optimized geometries and included anharmonic phonon zero-point energy, leading to a molecular dissociation at 374 GPa, from Cmca-12 to $I4_1/amd$. In contrast, McMinis *et al.* used vdW-DF-optimized geometries and harmonic phonon zero-point energy to predict a dissociation pressure of 447(3) GPa. In hind sight, the prediction by McMinis *et al.* is in better agreement with subsequent experiments.

On the low pressure side, a new hexagonal candidate structure for phase III was proposed by Monserrat *et al.* [169] in 2016, then calculated to be more stable than C2/c below 210 GPa [197]. Band gap of the C2/c structure shows closure around 460 GPa, when extrapolated using IR measurements up to 420 GPa [17]. This gap closure pressure agrees with the most recent DMC calculation [18], which is at variance with the previous prediction by Azadi *et al.* [197], presumably due to different treatments of finite-size effects. Finally, a recent coupled cluster calculation of the molecular candidate structures show good agreement with DMC results [198] at the static lattice level, although lattice zero-point energy has yet to be included.

In this chapter, we examine the most promising candidate structures of solid hydrogen using dynamic-lattice DMC. This method treats the electrons and ions on the same footing while harnessing the accuracy of DMC. Lattice vibrations are included beyond the harmonic approximation. Further, nonadiabatic effects

can be captured. The goal is to provide the most accurate properties of the solid hydrogen phases.

6.2 Methods

6.2.1 Candidate Structure Optimization

We consider three candidates C2/c-24 [168], Cmca-4 [195], Cmca-12 [168] for the molecular phase and one candidate $I4_1/amd$ [158] for the atomic phase at $T = 0K$ over the pressure range 350 GPa to 700 GPa. The static-lattice structures in the molecular phase are optimized using the vdW-DF functional at constant pressure. As shown in Table 6.1, all three molecular structures optimize to similar density at each pressure. In contrast, the atomic structure is optimized using DMC at constant volume. While both constant-volume

Table 6.1: vdW-DF pressure-density (expressed in r_s) relation of relaxed molecular candidate structures.

vdW-DF P(GPa)	360	400	440	480	520	560	650	700	780
Cmca-4	1.303	1.283	1.265	1.250	1.235	1.222	1.196	1.183	1.164
Cmca-12	1.306	1.286	1.268	1.252	1.237	1.224			
C2/c-24	1.307	1.287	1.269	1.253	1.239	1.225	1.198	1.185	

and constant-pressure optimizations are valid ways to find the minimum energy structure, the final density and pressure differ in general. The DMC optimizations for the atomic structure have been carried out at evenly spaced r_s values: 1.31, 1.29, 1.27, ..., 1.17. At a given pressure, the density difference between the atomic and molecular structure is appreciably larger than that among molecular-phase candidate structures. Thus, when calculating energy and enthalpy differences, interpolation is needed further from data for the atomic structure than for the molecular structures.

All three molecular structures are monoclinic having $a = b \neq c$, $\alpha = \beta = 90° + \eta$, and $\gamma = 120° + \delta$. The slight distortions differ for each structure: $\eta = 0$, $\delta \approx -0.5°$ for Cmca-4, $\eta = 0$, $\delta \approx +3.5°$ for Cmca-12, and $\eta \approx 0.1°$, $\delta \approx -0.1°$ for C2/c-24. The evolution of the lattice parameters as a function of pressure are shown in Fig. 6.5(a). Both a and c decrease with increasing pressure. However, the c/a ratio remains roughly constant at 1.062 ± 0.003 and 1.771 ± 0.003 for Cmca-12 and C2c-24, respectively. In contrast, the c/a ratio of the Cmca-4 structure decreases from 1.562 at 350 GPa to 1.530 at 560 GPa linearly with pressure. Besides having a slightly different unit cell, the Cmca-4 structure has only one type of H_2 molecule, whereas Cmca-12 and C2/c each have two. The bond length of the H_2 molecules in the optimized geometry is shown as a function of pressure in Fig. 6.5(b).

The vdW-DF optimized H_2 bond lengths of all three molecular structures are shown in Fig. 6.5(b). The bond length in Cmca-4 is comparable to its isolated value of 1.4 Bohr, whereas in C2/c-24 it is 3 to 4%

compressed. One type of the H_2 molecules in Cmca-12 has pressure-sensitive bond length, increasing from ~ 1.38 Bohr at 360 GPa to ~ 1.4 Bohr at 560 GPa, while the other type has 3% compressed bond length irrespective of pressure.

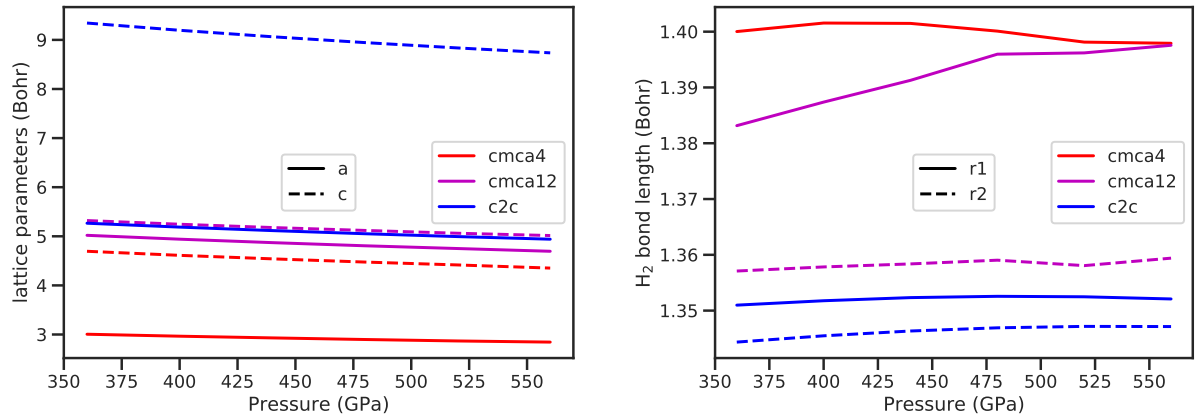

(a) a and c lattice parameters

(b) H_2 bond length

Figure 6.5: vdW-DF optimized molecular candidate structures at target pressures. (a) lattice parameters (b) molecular bond length. C2/c and Cmca-12 each have two types of H_2 molecules, whereas Cmca-4 has only one.

The atomic candidate structure $I4_1/amd$ has only one free parameter, the c/a ratio, at each density. Therefore, we can afford to optimize its geometry using DMC within the clamped-ion approximation. As shown in Fig. 6.6, the DMC-optimized c/a ratio is 4 to 8% below the PBE-optimized ones. It increases continuously as density increases, whereas the PBE-optimized c/a ratio exhibits discontinuities around $r_s = 1.21$ and 1.14. We fit c/a as a linear function of r_s to smooth out noise from the optimization process.

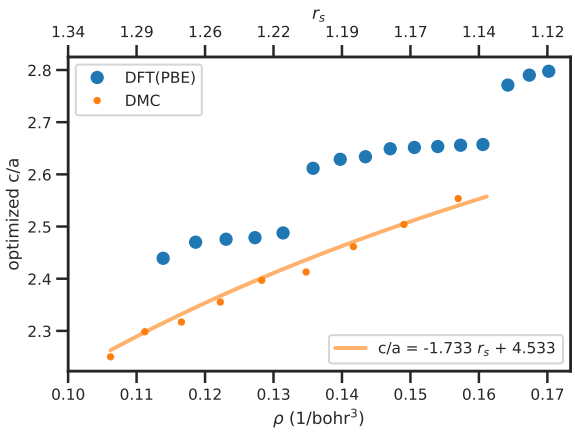

Figure 6.6: DMC optimized atomic structure c/a ratio as a function of density. The blue points are DFT(PBE) optimized c/a ratios.

While the vdW-DF optimized structures in Ref. [2] are not published, we can infer from the enthalpy-pressure relations that the same structures as in Ref. [2] have been reproduced in this study. Figure 6.7 shows the enthalpy of each candidate structure relative to C2/c-24 at the vdW-DF static-lattice minimum. The results agree well with those from McMinis *et al.* [2] where available. In comparison to predictions by Drummond *et al.* [3], our C2/c structure is slightly more stable and Cmca-4 slightly less stable. They used BLYP rather than vdW-DF functional, so differences are expected. In fact, it is encouraging to see two different functionals give similar results (within a few meV/p).

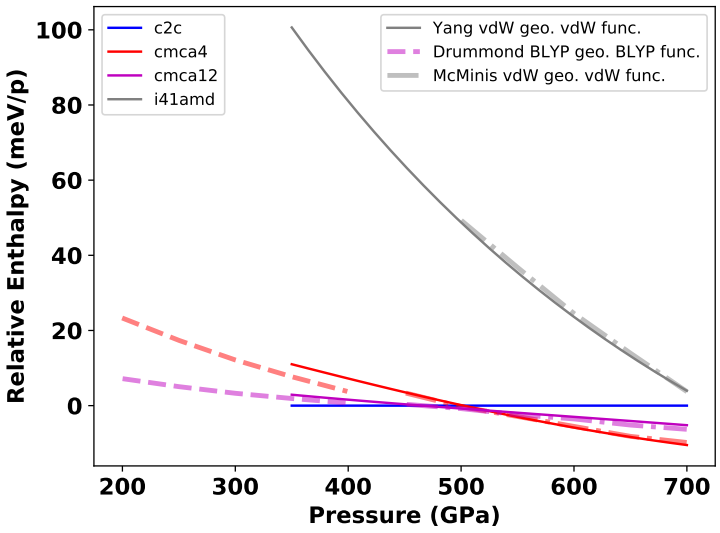

Figure 6.7: DFT(vdW-DF) static-lattice enthalpy of optimized structures relative to C2/c-24. Thin solid lines are enthalpies of the Cmca-4, Cmca-12 and $I4_1/amd$ using our optimized structures. Dashed lines are DFT(BLYP) enthalpies of Cmca-4 and Cmca-12 from Drummond *et al.* [3]. Dash-dot lines are DFT(vdW-DF) enthalpies from McMinis *et al.* [2].

6.2.2 Supercell Construction

To reliably obtain QMC energies in the thermodynamic limit, we need to tile the optimized primitive cells to sufficiently large supercells so that pair correlation functions are converged. The remaining finite-size error can be removed using methods discussed in Chap. 4. The supercells also need to be small enough for dynamic-ion QMC to be practical. In the end, we use 72-atom simulation cells for all QMC calculations.

Each simulation cell is tiled from the optimized unit cell using a non-diagonal *supercell matrix* [199], which is optimized to maximize the distance between minimum images under periodic boundary conditions. A supercell matrix in 3D is a 3×3 matrix of integers that map primitive lattice vectors $\boldsymbol{a}, \boldsymbol{b}, \boldsymbol{c}$ to supercell

lattice vectors $\boldsymbol{a}_s, \boldsymbol{b}_s, \boldsymbol{c}_s$

$$\begin{pmatrix} \boldsymbol{a}_s \\ \boldsymbol{b}_s \\ \boldsymbol{c}_s \end{pmatrix} = \begin{pmatrix} S_{11} & S_{12} & S_{13} \\ S_{21} & S_{22} & S_{23} \\ S_{31} & S_{32} & S_{33} \end{pmatrix} \begin{pmatrix} \boldsymbol{a} \\ \boldsymbol{b} \\ \boldsymbol{c} \end{pmatrix}. \tag{6.1}$$

Once a supercell is chosen, the crystal structure can be created using the following cropping method: first, tile the atoms from the primitive cell a large number of times along each lattice vector, then crop out only the atoms that fall inside the supercell. The total number of atoms in the supercell should be $\det(S)$ times that in the primitive cell.

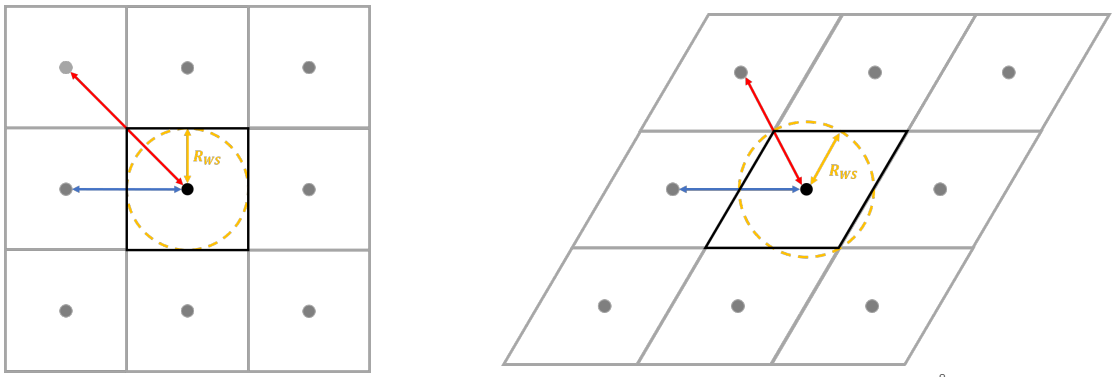

(a) square $a = 2$ Å (b) rhombus $a = 2.149$ Å

Figure 6.8: Cubic vs. rhombus supercells. The black cell is the supercell. The gray cells are periodic images. The blue line points between nearest-neighbor images, while the red line between second-nearest neighbors. The yellow circle is the inscribed circle in the Wigner-Seitz cell (not shown) of the supercell.

Non-diagonal supercell matrices can be used to maximize the minimum image radius, radius of the real-space Wigner-Seitz cell R_{WS}. As shown in Fig. 6.8, a rhombus supercell provides a larger R_{WS} than a square having the same area. This is because the periodic images form a closed-packed lattice given a rhombus supercell. If the primitive cell is square, then all diagonal supercell matrices result in square supercells. In contract, one can construct a rhombus-like supercell using a non-diagonal matrix. A more useful application of non-diagonal supercell matrix is for accessing a particular momentum to address a certain excitation [199], but that is beyond the scope of this study.

The chosen supercell matrices and their resulting image radii are shown in Table 6.2 and Fig. 6.9, respectively. The inscribing radius of each supercell R_{sc} are also shown in Fig. 6.9 to give a sense of how far each supercell is from being orthorhombic. An orthorhombic cell has $R_{WS} = R_{sc}$.

Table 6.2: Optimized 72-atom non-diagonal supercell matrices.

Cmca-4	Cmca-12	C2/c-24	$I4_1/amd$
$\begin{pmatrix} -1 & 2 & 1 \\ 2 & -1 & 1 \\ 3 & 3 & 0 \end{pmatrix}$	$\begin{pmatrix} 2 & 1 & -1 \\ 2 & 1 & 1 \\ -1 & 1 & 0 \end{pmatrix}$	$\begin{pmatrix} 2 & 1 & 0 \\ 1 & 2 & 0 \\ 0 & 0 & 1 \end{pmatrix}$	$\begin{pmatrix} 2 & -2 & 1 \\ 2 & 3 & 0 \\ -2 & 1 & 1 \end{pmatrix}$

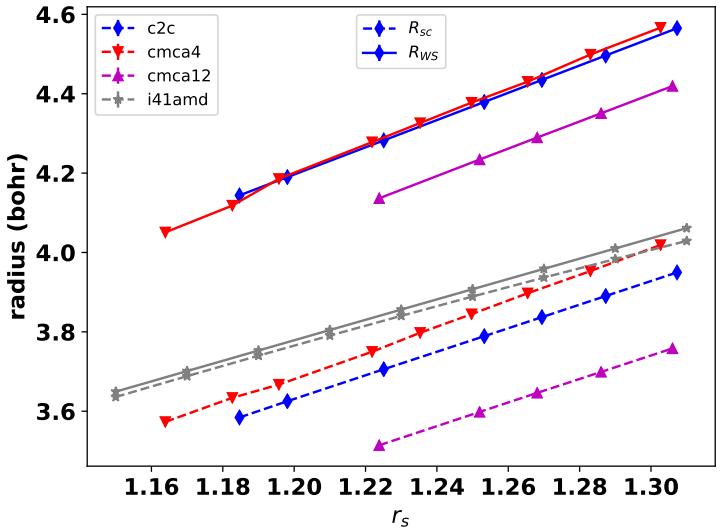

Figure 6.9: Supercell radius as a function of density. r_s is the Wigner-Seitz radius, which is determined by the average electron density $\frac{4\pi}{3} r_s = \rho$, where $\rho = N_e/\Omega$, with Ω the supercell volume. R_{WS} is the radius of the real-space Wigner-Seitz cell of the supercell. $2R_{WS}$ is the minimum distance between periodic images.

6.2.3 Wavefunction Optimization

6.2.3.1 Electronic Components

For the electronic wave function, we use the standard Slater-Backflow-Jastrow (SBJ) form

$$\Psi(\boldsymbol{R}; \boldsymbol{R}_I) = \det\left(\{\phi_i(\boldsymbol{r}_j + \Delta\boldsymbol{r}_j; \boldsymbol{R}_I)\}\right) e^{-U(\boldsymbol{R}, \boldsymbol{R}_I)}, \tag{6.2}$$

$$U = \frac{1}{2} \sum_{\alpha,\beta} \sum_{i=1}^{N_\alpha} \sum_{j=1}^{N_\beta, (j,\beta)\neq(i,\alpha)} u_{\alpha\beta}(\boldsymbol{r}_i, \boldsymbol{r}_j), \tag{6.3}$$

where α, β denote unique particle species, including up-electron, down-electron, and proton, although the proton-proton contribution is always set to zero in static-lattice calculations. $\boldsymbol{r}_j + \Delta\boldsymbol{r}_j$ is the quasi-particle coordinate of particle j as determined by the back flow function η as follows

$$\Delta\boldsymbol{r}_j = \frac{1}{2} \sum_{\alpha,\beta} \sum_{i=1}^{N_\alpha} \sum_{j=1}^{N_\beta, (j,\beta)\neq(i,\alpha)} \eta_{\alpha\beta}(\boldsymbol{r}_i^\alpha, \boldsymbol{r}_j^\beta)(\boldsymbol{r}_i - \boldsymbol{r}_j). \tag{6.4}$$

Isotropic Jastrow $u(r)$ and back flow $\eta(r)$ functions are optimized in VMC to lower the variational energy. The single-particle orbitals in the determinant are taken as the Kohn-Sham orbitals with the lowest eigenvalues. These orbitals are generated using the vdW-DF functional for the molecular candidates and PBE for the atomic structure. We remove the approximate cusp of each orbital by dividing out the RPA e-p Jastrow following Refs. [7, 200, 201]. This allows the exact e-p Jastrow to be re-introduced in the e-p Jastrow and is always maintained as the protons move. Before back flow transformation, the static structure factor of the Slater determinant is quite similar to that of the unpolarized homogeneous electron gas, as shown in Fig. 6.10(a). However, as shown in Fig. 6.10(a), the momentum distribution of the metallic atomic structure is different from the rest, because the molecular structures are insulating.

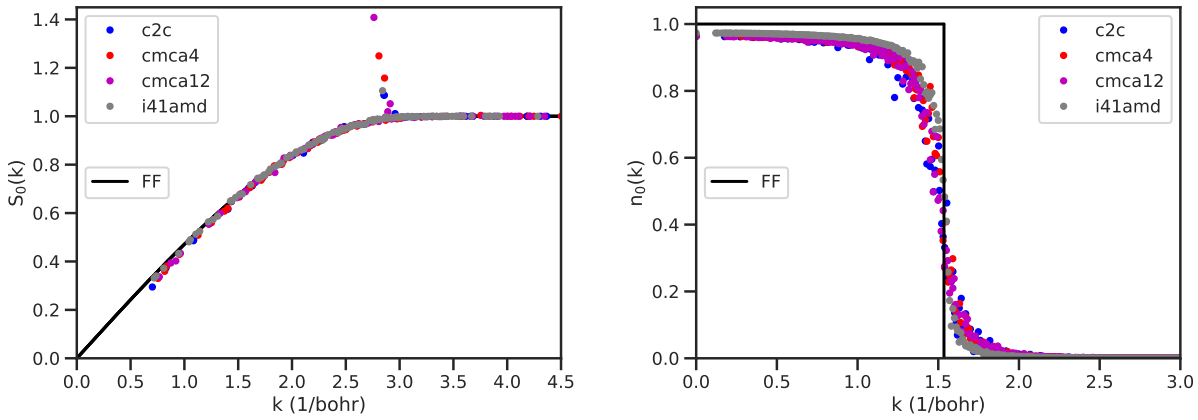

(a) structure factor

(b) momentum distribution

Figure 6.10: Static structure factor $S_0(k)$ and momentum distribution $n_0(k)$ calculated using the Kohn-Sham determinant wave function at $r_s = 1.25$. The black lines show the same functions for the free Fermi (FF) gas as reference.

The Jastrow and back flow functions are variationally optimized using the electronic hamiltonian at vdW-DF optimized clamped-ion geometries. The optimized functions at 480 GPa ($r_s \approx 1.25$) are shown in Fig. 6.11. These functions remain quantitatively similar across all densities explored. The electronic components of the Jastrow and back flow functions are nearly identical for all three molecular candidates. The largest contribution is the u-d term, which introduces correlation between opposite-spin electrons to keep them apart. However, the electron-ion components show some variation among candidate structures, with Cmca-4 being the standout among molecular candidates. Its optimized e-p Jastrow and back flow have much in common with those of the atomic phase. This is likely an artifact of either the clamped-ion approximation or under-converged optimization. Once these functions are reoptimized with dynamic ions, all Jastrow and back flow components involving the electrons become essentially identical across all candidate structures, as shown in Fig. 6.12.

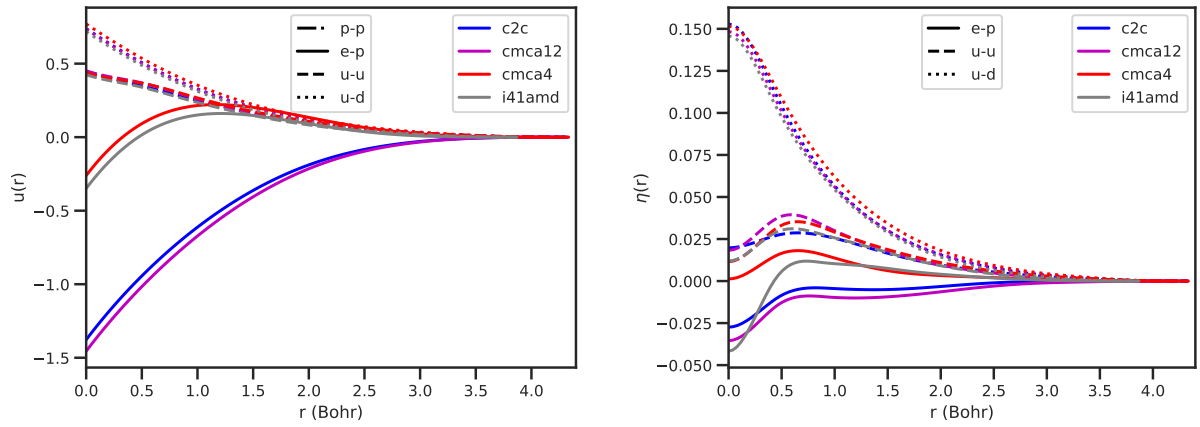

(a) Jastrow pair functions

(b) Back flow pair functions

Figure 6.11: Jastrow and back flow pair functions optimized at static-lattice minimum at 480 GPa. Color denotes the crystal structure. The solid line is the pair function for electron-proton, the dashed line for same-spin electrons, and the dotted lines for opposite-spin electrons.

6.2.3.2 Ionic Components

For an electron-ion simulation, the SBJ wavefunction has an additional Hartree product for distinguishable ions as well as an ion-ion Jastrow

$$\Psi_{ei}(\boldsymbol{R}, \boldsymbol{R}_I) = \det\left(\{\phi_i(\boldsymbol{r}_j + \Delta\boldsymbol{r}_j; \boldsymbol{R}_I^0)\}\right) e^{-U(\boldsymbol{R},\boldsymbol{R}_I)} \prod_{I=1}^{N_p} \chi(\boldsymbol{r}_I, \boldsymbol{r}_I^0), \tag{6.5}$$

where the proton orbital is an isotropic gaussian centered around its optimized geometry

$$\chi(\boldsymbol{r}_i, \boldsymbol{r}_I^0) = \left(\frac{2C_p}{\pi}\right)^{3/4} \exp\left(-C_p|\boldsymbol{r}_I - \boldsymbol{r}_I^0|\right). \tag{6.6}$$

The expressions for the Jastrow and back flow terms remain unchanged, i.e. eq. (6.3) and (6.4), although the proton coordinates are now dynamic variables rather than parameters. We take the electronic orbitals ϕ_i from the clamped-ion DFT calculation, performed at the vdW-DF optimized geometry, for practical purposes. This is a severe approximation as the ideal orbitals for a system with small nonadiabatic effects should come from a Born-Oppenheimer calculation, i.e. rerun DFT at every ion position update. Fortunately, the back flow transformation effectively changes the electronic orbitals as the ions move, because the quasi-particle position of an electron is influenced by the protons around it.

We re-optimize the Jastrow and back flow functions in dynamic-lattice VMC, using the optimized functions from static-lattice calculations as starting points. The electron-ion Jastrow of the Cmca-4 Jastrow and back flow functions fall into good agreement with those from other candidate structures. As shown in

Fig. 6.12, after re-optimization, the only noticeable difference among the three structures lie in the proton-proton Jastrow.

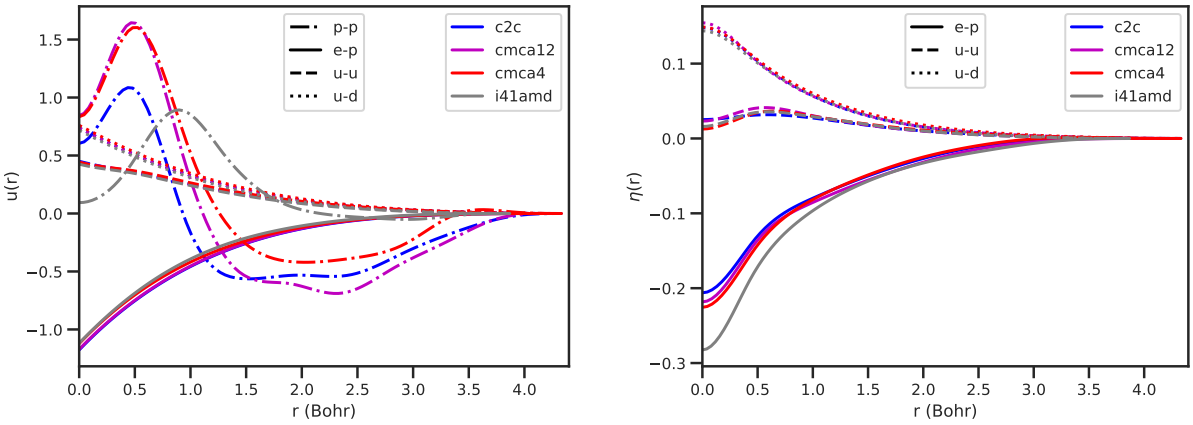

(a) Jastrow pair functions

(b) Back flow pair functions

Figure 6.12: Jastrow and back flow pair functions optimized using dynamic-lattice VMC. The dash-dotted line is the pair function for proton-proton correlation. All other notations are identical to those in Fig. 6.11.

The width of the gaussians in the proton orbital C_p are optimized using *maximum overlap* [7, 201, 202]. In this method, we measure the mean-squared deviation (MSD) of each proton from its ideal site, as determined by vdW-DF, and adjust the gaussian exponent in the proton wave function C_p until the VMC and DMC estimates of the MSD agree. This method works by maximizing the overlap between the trial and ground-state wave function along the dimension controlled by C_p. Since proton MSD is a rather direct measure of the shape of the wave function and DMC pushes the VMC MSD towards its ground-state value, the optimal C_p is obtained when DMC and VMC MSDs agree. Consider an isolated proton having a normalized gaussian wave function

$$\chi(x,y,z) = \left(\frac{2C_p}{\pi}\right)^{3/4} \exp\left(-C_p(x^2+y^2+z^2)\right). \tag{6.7}$$

The mean squared deviation of this wave function is

$$\langle x^2\rangle = \langle y^2\rangle = \langle z^2\rangle = \frac{1}{4C_p}. \tag{6.8}$$

We expect some deviation from eq. (6.8) due to electron-proton and proton-proton correlations. When C_p is large, the confining effect of the gaussian wave function dominates over correlation due to Jastrow and back-flow components, making each proton approximately independent of all other particles. However, as C_p decreases, the effects of correlation become more important. As shown in Fig. 6.13(a), at large values of

C_p (localized protons) VMC MSDs are accurately approximated by eq. (6.8), whereas the DMC MSDs and VMC ones at small C_p differ from this independent-particle approximation. Note that the DMC runs here are short and likely under-converged. Fortunately, they are sufficient for determining the point of maximum overlap between the VMC and DMC wave functions. As such, the computational cost of maximum overlap optimization is more similar to VMC optimization than to a converged DMC run. We further note that optimal C_p is the same along x, y, and z directions, so an isotropic Gaussian wave function is flexible enough to optimally sample the proton wave function. Finally, the exact value of C_p will not bias the DMC result so long as the projection time is sufficiently converged. This is because the protons are treated as distinguishable particles for which DMC is exact at infinite projection time.

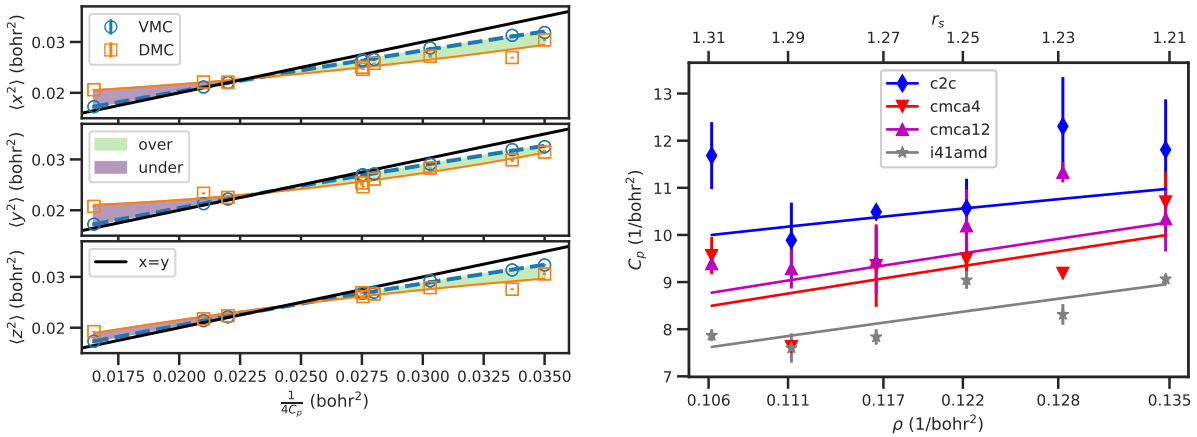

(a) Lattice deviations vs. prediction from isolated gaussian wave function with exponent C_p

(b) optimized exponents as a function of density

Figure 6.13: Maximum overlap optimization of the proton wave function. (a) Optimization of the C2/c-24 proton wave function at $r_s = 1.269$. (b) Optimized proton wave function exponent C_p of all candidate structures. The markers show the C_p value at the intercept of VMC and DMC. The lines are linear fits, but shifted down slightly to error on the side of oversampling. These fits are used to determine the C_p value in the dynamic-lattice calculations.

In practice, the choice of C_p is important. Since the proton-electron mass ratio is more than 1836, the RMSD of a proton during the diffusion process is roughly 1/43 that of an electron in the same amount of imaginary time. Thus, it takes more simulation time to fix errors in the proton wave function than those in the electron wave function. Fortunately, the proton wave function is highly localized and alleviates the problem to some extend. As shown in Fig. 6.13(a), the standard deviation of the proton orbital of C2/c-24 is < 0.5 bohr at $r_s = 1.27$. Nevertheless, it pays to choose an optimal value for C_p. If C_p is too large, then the proton wave function will be too localized. This results in undersampling of the ground-state wave function and is a dangerous scenario. During the DMC run, the kinetic energy of the protons will likely have mostly small fluctuation in this case. However, occasional spikes, which are important for an

unbiased mean, will occur infrequently. If one misses or discards these spikes, then the results will be biased. In contrast, oversampling will increase the variance of the wave function without biasing the mean. The resultant calculation will require more time to reach a certain accuracy target, so a balance needs to be sought. As shown by the lines in Fig. 6.13(b), we choose isotropic gaussian exponent that are close to optimal but error slightly on the side of oversampling (smaller C_p than optimal).

6.3 Results and Discussion

6.3.1 Static-Lattice Energy, Pressure, and Local Energy Variance

The dominant variation of the total energy as pressure increases is due to the isotropic compression of the electron liquid and the crystal lattice. This variation is on the order of 1 eV/p, which is roughly 50 times the energy difference among the candidate structures. To better observe these small differences, we plot energy and pressure relative to a reference equation of state (EOS). As a definition of zero energy at each density, this reference EOS need not be overly precise. Nevertheless, we use a fit to high-quality DMC data for the C2/c-24 molecular crystal structure obtained by Drummond *et al.* [3], because they are freely accessible online [203] and are well approximated by a quadratic polynomial in density. The data file `E_SJDMC_dt0_KZKcorr_v_V.dat` in directory `DMC/N096/C2c-24/` contains the size-corrected DMC energy-density relation needed to fit an EOS. As shown in Fig. 6.14, we fit the high-density region of the reference data to obtain:

$$E_0(\rho) = 1.605872\rho^2 + 0.699501\rho - 0.610902, \tag{6.9}$$

where $\rho = N/\Omega$ is the electron density in bohr^{-3}, and E_0 is in hartree. We choose to fit the size-corrected 96-proton data obtained using a Slater-Jastrow wave function, because the results are easier to reproduce than its large-cell and back-flow counterparts. The LDA-based finite-size correction scheme designed by H. Kwee, S. Zhang, and H. Krakauer (KZK) [204] is not general in principle. However, it was shown to work well for solid hydrogen comparing 768-proton and 96-proton results [3]. Equation (6.9) reproduces the QMC data to well within 1 meV/p while interpolating between 212 and 413 GPa, but deviates by 1.5 meV/p when extrapolated by 50 GPa to 163 GPa. Thus, we can expect the reference EOS to be accurate over the pressure range 150 ($r_s = 1.48$) to 460 GPa ($r_s = 1.26$), but fail when extrapolated much beyond these limits.

The static-lattice DMC energy is plotted relative to reference in Fig. 6.15(a). At the same density, we obtain lower total energy than Drummond *et al.* [3] partly due to our use of vdW-DF, rather than PBE, to

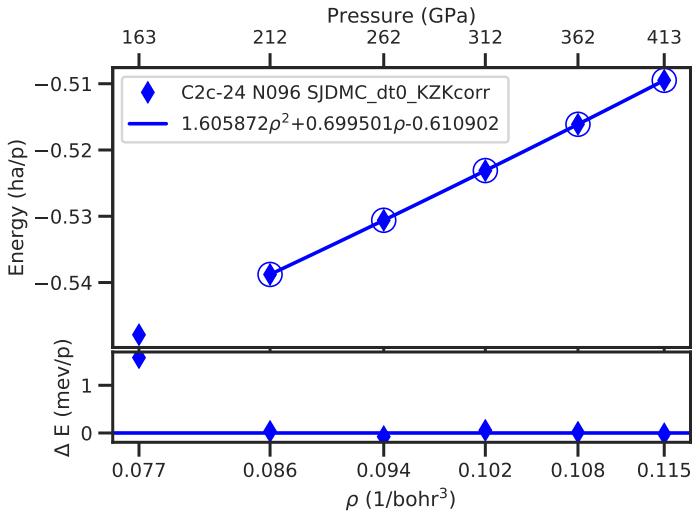

Figure 6.14: Fitting of reference equation of state. The solid symbols are DMC data from Ref. [3], while the line is a quadratic fit to the circled points. The bottom panels shows the error in the fit.

optimize the crystal structure; and partly due to in the inclusion of back flow transformations. At the same geometry, DMC energy is unchanged to within 3 meV/p whether PBE or vdW-DF is used to generate the orbitals in the determinant wave function. Our C2/c curve is relatively flat at densities lower than $r_s = 1.25$ and starts to bend downwards as density increases. Thus, our C2/c pressure-density relations will be roughly identical to that of the reference EOS in the low-density region. This is encouraging, because it implies that the fixed-node error on the pressure is small. Even with improved geometry and wave function, we get back very similar pressure as PBE geometry and Slater-Jastrow wave function at the same density.

QMC enthalpy can be calculated from virial pressure and plotted relative to the reference EOS as shown in Fig. 6.15(b). We observe a transition from C2/c-24 to Cmca-4 around 640 GPa and no transition to the atomic structure up to 800 GPa. This disagrees with the previous QMC study [2], showing a 450 GPa transition from C2/c-24 to Cmca-4, which then transitions to the atomic structure around 700 GPa. The reason for this disagreement is unknown.

The QMC *virial pressure*, calculated from kinetic energy T, potential energy V, and volume Ω

$$P = \frac{2T - V}{3\Omega} \tag{6.10}$$

is shown as a function of density in Fig. 6.23(a). We first note that the QMC pressure is consistently lower than vdW-DF pressure at the same density. Plotting the same data on a relative scale in Fig. 6.23(c), we see that the QMC virial pressure is 4.2% and 3.2% lower than vdW-DF pressure at 340 GPa ($r_s \approx 1.21$) and

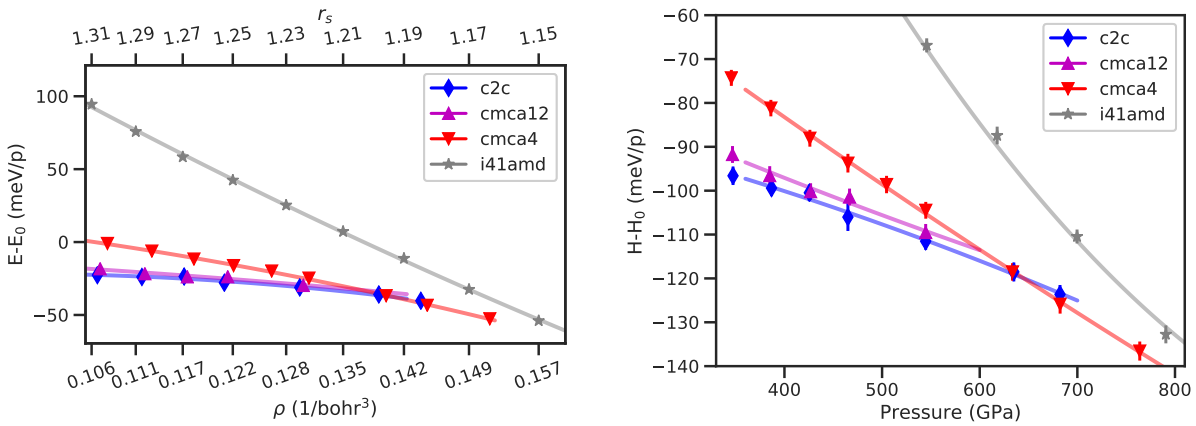

(a) energy-density relation

(b) enthalpy-pressure relation

Figure 6.15: Static-lattice DMC energy and enthalpy relative to Drummond *et al.* [3] reference eq. (6.9). Relative energies are shown in meV per proton (meV/p). Each solid line is obtained using a fitted energy-density EOS, which is obtained by fitting the finite-size corrected (FSC) total energy as a quadratic function of ρ. The markers are finite-size corrected simulation data without performing a fit. P_0 is the pressure calculated from the reference EOS $P_0 = -dE_0/d\Omega$.

460 GPa ($r_s \approx 1.25$), respectively. This agrees well with the findings of R. C. Clay III *et al.*, i.e. Fig. 4 in Ref. [67]. In this plot, we also see that the mixed estimator error is 1 to 5 GPa, so the linearly-extrapolated static-lattice DMC pressure should be accurate to 1 GPa.

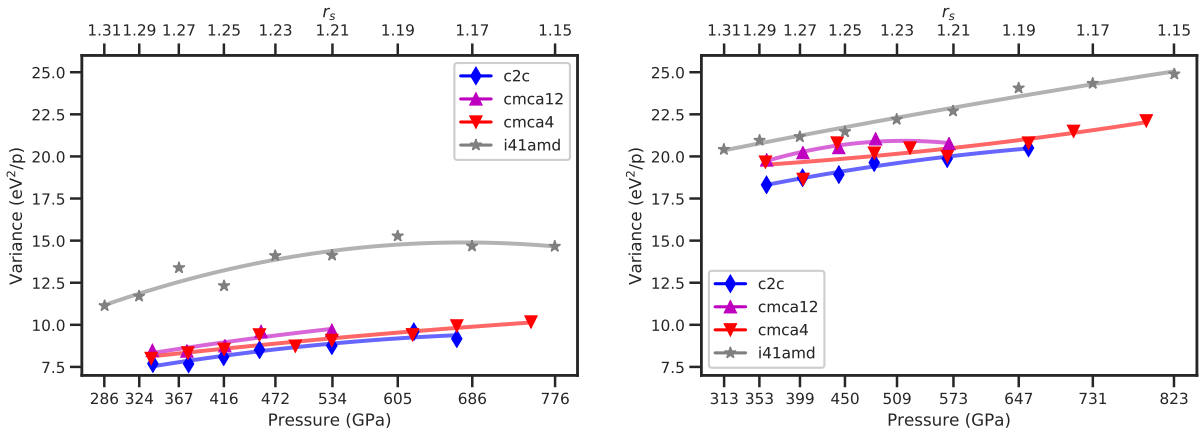

(a) static lattice

(a) dynamic lattice

Figure 6.16: QMC variance vs. pressure. The lines are guides to the eye.

Finally, the variance of the optimized static-lattice wave functions are shown in Fig. 6.16(a) as a function of pressure. The variance of the molecular structures are $7.5 \sim 8.5$ eV^2/p below 400 GPa and increases to $8.5 \sim 9.5$ eV^2/p at 550 GPa. The increase in variance may be due to the closing band gaps of the molecular structures around 400 GPa. If true, then it may be better to generate orbitals above 400 GPa using the PBE

functional, because it prefers metallic rather than insulating states when compared to vdW-DF. The variance of the atomic structure is about 50% higher than that in the molecular phase, ranging from 11 eV^2/p at $r_s = 1.31$ to 15 eV^2/p at high densities. For comparison, the variance of the best analytical wave function for bcc hydrogen is 13.2(1) eV^2/p at $r_s = 1.31$ (Table III in Ref. [10]) and 7.40(3) eV^2/p at $r_s = 1.40$ (Table 2 in Ref. [31]). Small mixed-estimator error and low energy variance are hallmarks of a well-optimized wave function. We demonstrate both in Fig. 6.23 and Fig. 6.16 for the static-lattice electronic wave function. The same cannot be said about the electron-ion wave function. As shown in Fig. 6.16, the local energy variance of all structures in the dynamic-lattice calculations are twice as high as their static-lattice counterparts. The atomic-phase variance is still roughly 3 eV^2/p above the molecular structures. This large increase in variance is due, in large part, to the use of static-lattice orbitals eq. (6.5) at all proton configurations. They can be lowered by re-optimizing the electronic wave function upon every proton-position update, albeit at a significantly increased computational cost.

6.3.2 Effect of Dynamic Ions on Energy and Pressure

When clamped protons are allowed to move, the energy of the electron-ion system changes in two ways. First, proton kinetic energy contributes a sizable positive term to the total kinetic energy of the system. As shown in Fig. 6.17(d), the kinetic energy of the protons increases from $\sim$ 230 meV/p at 360 GPa ($r_s \approx 1.31$) to $\sim$ 265 meV/p at 600 GPa ($r_s \approx 1.20$), increasing by roughly 7.3 meV/p every 50 GPa. Second, the electronic wave function changes as the protons move. Thus, the electronic potential and kinetic energies change as well. As shown in Fig. 6.17(b) and (c), the increase of the total potential energy is roughly twice that of the electron kinetic energy, which is around 80 ± 20 meV/p for all candidate structures. Unlike the increase of proton kinetic energy, the electron kinetic and total potential increases are insensitive to the electron density. The increase of electron kinetic energy for C2/c-24 and $\mathrm{i4_1/amd}$ is $\sim$ 20 meV/p higher than that of the Cmca structures, while the increase in their potential energies is $\sim$ 40 meV/p lower. The sum of all three contributions make up the total energy change from static- to dynamic-lattice, i.e. the zero-point energy (ZPE). As shown in Fig. 6.17(a), the ZPE increases from $\sim$ 470 meV/p at 360 GPa to $\sim$ 510 meV/p at 600 GPa, i.e. 8.3 meV/p every 50 GPa. Most of the density dependence of the ZPE comes from the proton kinetic energy.

An immediate consequence of the higher kinetic and potentials energies in the dynamic-lattice simulation is higher virial pressure, about 20 GPa higher than its static-lattice counterpart. Interestingly, this brings the dynamic-lattice QMC pressures into better agreement with static-lattice vdW-DF pressures, as we saw in Fig. 6.23 that the static-lattice QMC pressures are systematically lower by $\sim$ 15 GPa.

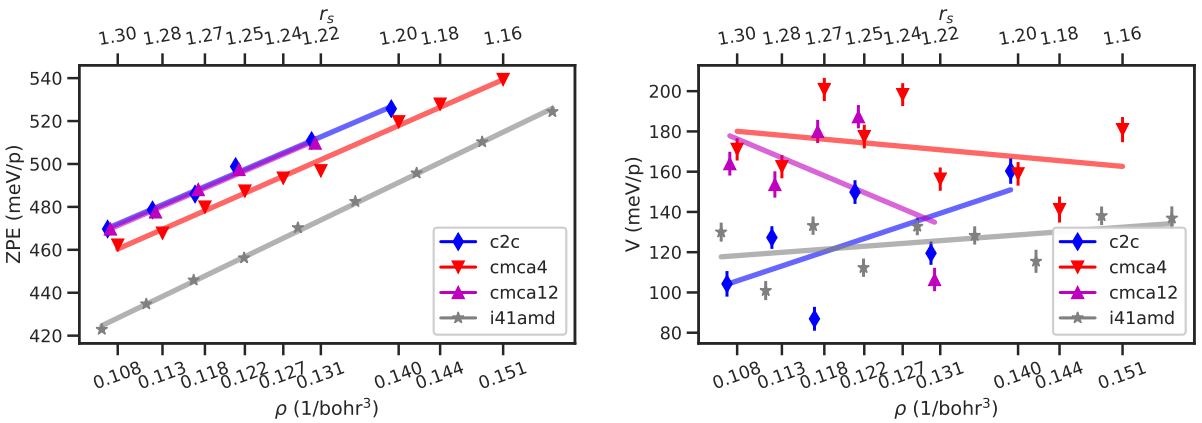

(a) total energy change (zero-point energy)

(b) potential energy change

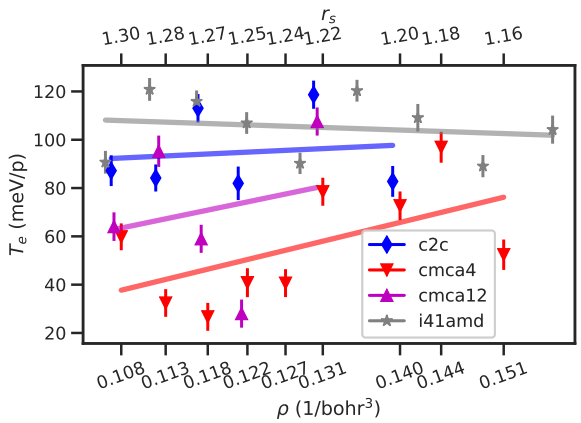

(c) electronic kinetic energy change

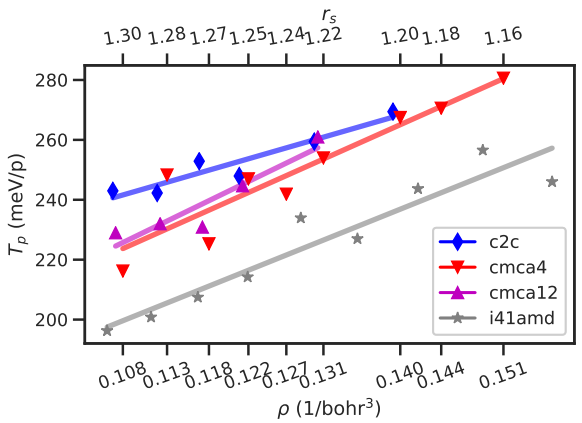

(d) proton kinetic energy

Figure 6.17: Energy changes from static-lattice to dynamic-lattice simulations as functions of electron density $\rho = N/\Omega$. (a) zero-point energies of the candidate structures. (b) total potential energy change due to dynamic protons. (c) electronic kinetic energy change due to dynamic protons. (d) proton kinetic energy. Color and marker label candidate structures. The solid lines are guides to the eyes.

The energy-density and enthalpy-pressure relations from the dynamic-lattice simulations are shown relative to the same reference EOS eq. 6.9 in Fig.6.18. Figure 6.18(a) shows the total energy as a function of density. First, due to ZPE, the window of energy is shifted up by roughly 500 meV/p from its static-lattice counterpart Fig. 6.15(a). Second, the relative energy among molecular structures remain similar. The C2/c-24 and Cmca-12 structures remain almost degenerate at all densities, whereas the Cmca-4 transitions from being 20 meV/p higher in energy at $r_s = 1.31$ to being the lowest-energy structure at sufficiently high density. The transition density for Cmca-4 does decrease significantly, from $r_s = 1.19$ in the static-lattice case to $r_s = 1.25$ when ZPE is included. In contrast, the overall trend of the molecular-phase total energy is noticeably changed by the inclusion of ZPE. Instead of staying flat relative to the reference EOS, the dynamic-lattice energies of the molecular structures all trend upwards. Similar effects can be observed in

the atomic-phase energy-density relation, although the overall upward shift due to ZPE is about 40 meV/p less. In summary, ZPE stabilizes the atomic phase by roughly 40 meV/p and the Cmca-4 phase by 10 meV/p relative the C2/c-24 and Cmca-12 without changing the relative angles at which their EOSs cross.

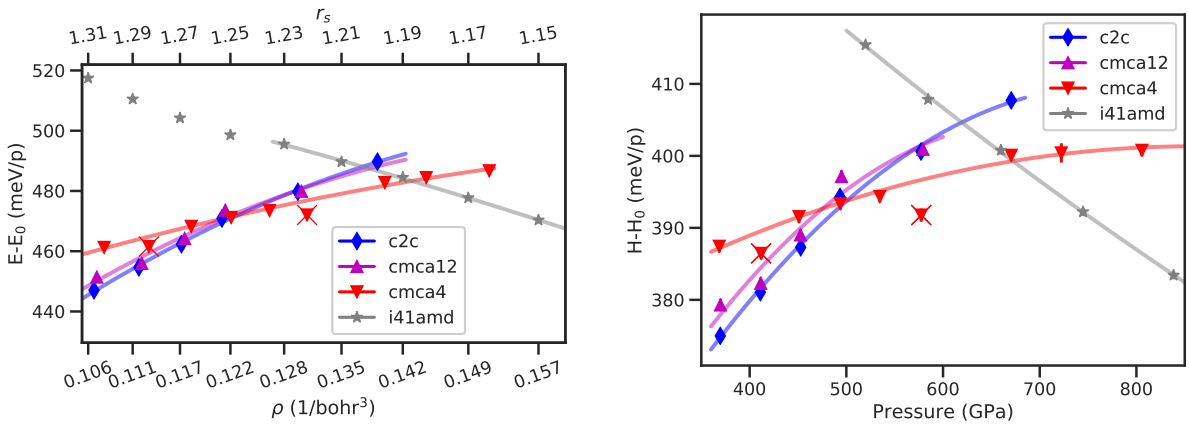

(a) energy-density relation

(a) enthalpy-pressure relation

Figure 6.18: Dynamic-lattice energy and enthalpy relative to reference. Lines are quadratic fits. The crossed out points are excluded from the fit.

The enthalpy-pressure relation in Fig. 6.18(b) tells the same story and we can read off the transition pressures among the candidate structures. We see a transition from C2/c-24 to Cmca-4 slightly below 500 GPa, then a molecular-to-atomic transition around 660 GPa from Cmca-4 to I4$_1$/amd. The calculated transition pressure to the atomic phase is 160 GPa higher than the previous QMC calculation [2] and a reported experimental observation [181]. However, the previous calculation used the harmonic approximation to calculate proton ZPE, while the experiment made little characterization of the final sample and has yet to be reproduced. As such, a 660 GPa transition pressure is not outside the realm of possibilities. Admittedly, the current approach has its own drawbacks. The most concerning approximation is the use of static-lattice orbitals in the electron-ion wave function eq. (6.5). This "frozen orbital" approach incurs around 80 meV/p more fixed-node error than a Born-Oppenheimer wave function fully-optimized at each new geometry, although this error cancels to a large extent between molecular and atomic phases.

6.3.3 Effect of Dynamic Ions on Electronic Correlation Functions

The electron-electron pair correlation function in real space, $g(r)$, are shown in Fig. 6.19. The correlation functions of the 3D unpolarized homogeneous electron gas are also shown as reference. The bottom panel of each plot shows the difference between the hydrogen $g(r)$s from those of the electron gas. This difference highlights the modification of the electron liquid due to the ionic lattice. The dynamic-lattice electronic

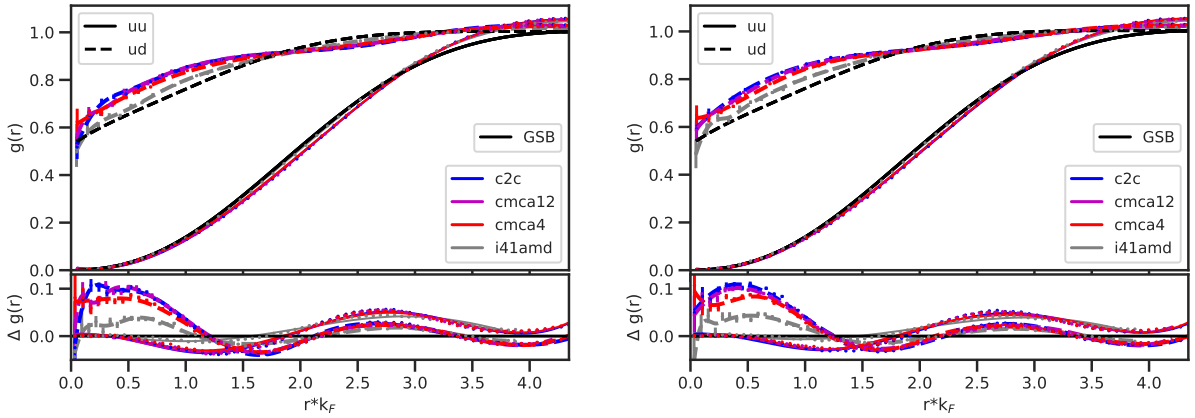

(a) static lattice (b) dynamic lattice

Figure 6.19: DMC electronic pair correlation functions at $r_s = 1.25$. Color denotes candidate structure, while the black lines are $g(r)$ of the unpolarized homogeneous electron gas at the same density as parametrized by P. Gori-Giorgi, F. Sacchetti and G. B. Bachelet (GSB) [61].

$g(r)$s are identical to those from the static-lattice calculations on the scale of the difference panel (0.1). For the molecular structures, both the same-spin (u-u) and opposite-spin (u-d) $g(r)$s are the same over the entire range from zero ($r = 0$) to the supercell image distance ($r = R_{WS}$). The most notable deviation from the electron gas is an enhanced correlation between opposite-spin electrons at small separation. This is likely due to the presence of covalent bonds, formed by a pair of opposite-spin electrons at the center of each H_2 molecules. A more subtle difference is the presence of small periodic modulations of the electronic $g(r)$ that appear to persist at long distances. The atomic structure shows no enhancement of opposite-spin correlation function at $r = 0$, whereas it shows the same periodic modulations as the molecular structures at long range.

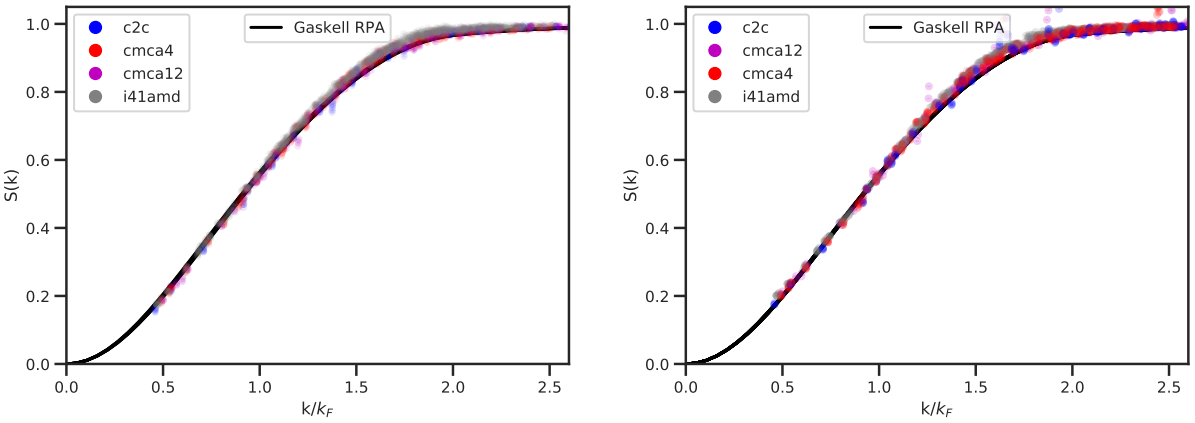

(a) static (b) dynamic

Figure 6.20: Electron-electron static structure factor $S(k)$.

Pair correlation function in reciprocal space, the electron-electron static structure factor $S(k)$, is shown in Fig. 6.20. At all densities and for all structures, both static-lattice and dynamic-lattice results are in excellent agreement with RPA $S(k)$ for the electron gas. However, small increase in correlation can be seen at intermediate range $k/k_F \approx 1.5$. Further, subtle differences at long-range ($k \to 0$) can make the electronic properties of the candidate structures qualitatively different from those of the electron gas and from each other.

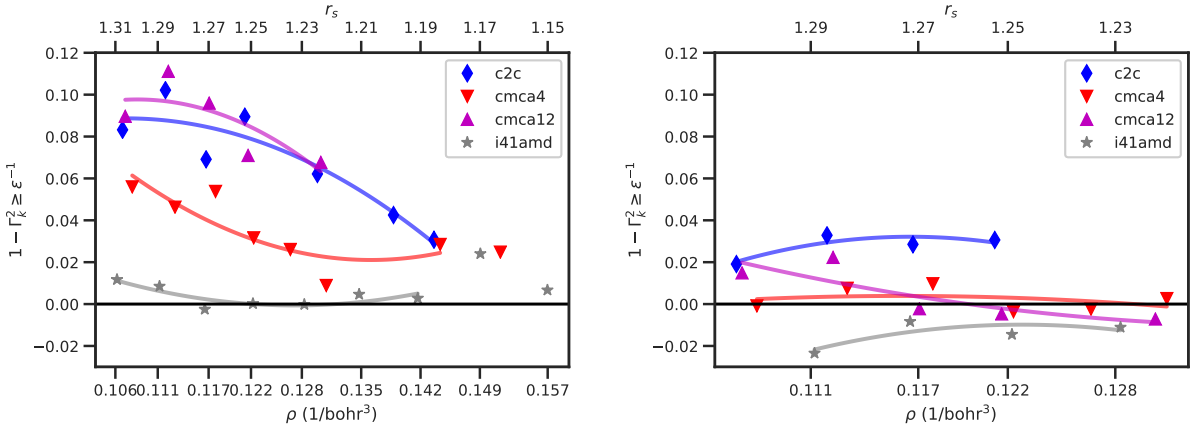

(a) static lattice

(b) dynamic lattice

Figure 6.21: Upper bound on inverse dielectric constant.

The inverse dielectric function is bounded from above by $\epsilon^{-1}(\boldsymbol{k}) \leq 1 - \Gamma_{\boldsymbol{k}}^2$, where

$$\Gamma_{\boldsymbol{k}} = \frac{2mS(\boldsymbol{k})}{\hbar^2 \boldsymbol{k}^2}. \tag{6.11}$$

The inequality becomes an equality if there is only a single excitation, such as plasmon, at long wavelength. The limit $\lim_{k\to 0} 1 - \Gamma_k^2$ can be a good approximation to the inverse dielectric constant of an isotropic system. Importantly, if this limit reaches zero, then the material is metallic. In Fig. 6.21, the isotropic limit is shown as a function of density. There are sizable systematic errors in these results due to a lack of data at small k and the choice of fitting range. These systematic errors are not precisely estimated, but its size should be comparable to the oscillation of the data points. The inaccessible region around $\boldsymbol{k} = \boldsymbol{0}$ increases with density, so the high-density results are less reliable than the low-density ones. In the static-lattice results Fig. 6.21(a), the atomic structure is metallic at all densities as expected. The Cmca-4 and C2/c-24 structures become metallic at roughly $r_s = 1.22$ and $r_s = 1.17$, respectively. These densities correspond to 550 GPa and 800 GPa, which are higher than experiment [17] and calculation [18]. It is possible that the molecular structures first start to conduct in-plane while being insulating across the planes. In this case, the isotropic

dielectric bound derived from spherically averaged $S(k)$ will overestimate the metalization pressure. The dynamic-lattice results Fig. 6.21(b) show all structures as metallic at densities higher than $r_s = 1.26$ (460 GPa) except for C2/c-24, which remains borderline insulating.

6.3.4 Proton-proton g(r) and S(k)

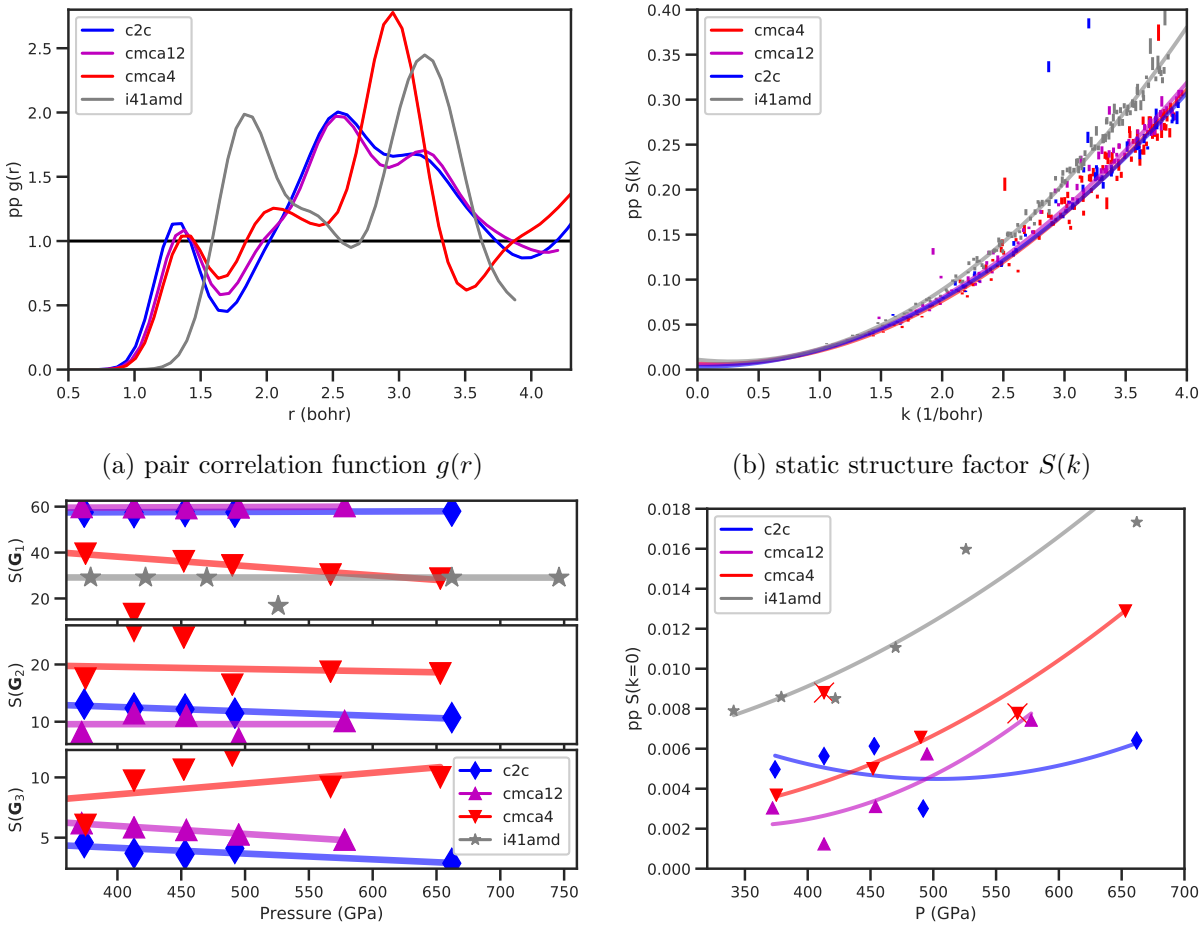

(a) pair correlation function $g(r)$

(b) static structure factor $S(k)$

(c) Bragg peaks of p-p $S(k)$

(d) long wavelength limit

Figure 6.22: Proton-proton pair correlation functions around $r_s = 1.25$ (480 GPa). The solid lines in (b) are quadratic fits to the smooth part of $S(k)$. (c) Bragg peaks of the p-p $S(k)$ (d) long wavelength limit $S(0)$. $|\boldsymbol{G}_1| \approx 1.81$ bohr^{-1}, $|\boldsymbol{G}_2| \approx 1.87$ bohr^{-1} for all three molecular structures. $|\boldsymbol{G}_3| \approx 2.5$ for C2/c-24 and Cmca-4 and 1.93 for Cmca-12. The atomic structure's Bragg peak can be found between 1.83 and 1.88 bohr^{-1}. The same outliers as Fig. 6.18 are excluded from the quadratic fits in (d).

The proton-proton pair correlation function of all candidate structures at $r_s \approx 1.25$ are shown in Fig. 6.22(a). Every molecular structure has a peak at the molecular bond length, in agreement with the DFT bond lengths shown in Fig. 6.5(b). C2/c-24 bond length is around 1.35 bohr, Cmca-4 around 1.40 bohr, and the Cmca-12 structure is in between. The C2/c-24 and Cmca-12 structures have remarkably similar p-p

g(r). Since they are almost degenerate over the entire density range explored, we can infer that the slight monoclinic distortions of their unit cells and the small differences in their molecular bond lengths do not contribute significantly to the total energy. The less distorted C2/c-24 structure is more stable. The Cmca-4 structure is significantly different from C2/c-24. Cmca-4 has second- and third-nearest neighbor peaks at 2 and 3 bohr, respectively, rather than C2/c-24's 2.5 and 3.2. The size and shape of these peaks are more similar to those in the atomic structure than to the other molecular candidates.

The long-range fluctuation and order of the protons can be observed in the proton-proton static structure factor. Its fluctuating part is shown in Fig. 6.22(b). All three molecular candidates have very similar levels of long-range fluctuations, whereas the atomic structure has noticeably more.

The molecular structures have more crystalline signatures than the atomic phase. As shown in Fig. 6.22(c), after spherical average, each molecular structure has at least three Bragg peaks for $k < 4$ bohr^{-1}, while the atomic structure has only one. The C2/c-24 and Cmca-12 Bragg peaks have very similar intensities and remain relatively unchanged by pressure. However, the Cmca-4 structure's most intense Bragg peak is comparable with that in the atomic structure and decreases in intensity as pressure increases. Finally, the long wavelength limit of the static structure factor can be related to the isothermal compressibility $\kappa \equiv n(\frac{\partial P}{\partial n})|_T$

$$nk_BT\kappa = S(\mathbf{0}), \tag{6.12}$$

where n is the density. We can extract the long wavelength limit of the p-p $S(k)$ by fitting its fluctuating part to a quadratic polynomial as shown in Fig. 6.22(a). The value of the fit extrapolated to $k = 0$ is shown as a function of pressure for all candidates in Fig. 6.22(d). The compressibility of C2/c-24 is approximately independent of pressure, whereas that of the Cmca structures and the atomic structure increase with pressure at a similar rate. The atomic structure is twice as compressible as the molecular structures at all pressures.

6.4 Conclusion

The ordering of the candidate structures from this dynamic-lattice study show similar features as the previous QMC study using vdW-DF geometries and harmonic ZPE [2]. The Cmca-12 structure is nearly degenerate with C2/c-24 but slightly less stable at low pressures. There is a transition from C2/c-24 to Cmca-4 around 500 GPa. Then, a Cmca structure transitions to the $I4_1/amd$ atomic structure at a higher pressure. However, we predict no stability range for the Cmca-12 structure, whereas in Ref. [2], C2/c-24 transitions to it at 424(3) GPa. The most significant disagreement lies in the atomic phase. We see the atomic phase becomes more stable relative to C2/c-24 around 610 GPa, whereas Ref. [2] shows this crossing around 450 GPa.

Our final prediction for the molecular-to-atomic transition pressure is 660 GPa, which is significantly higher than the previous experimental result [181]. However, as already mentioned in Sec. 6.3.2, this prediction is not impossible. The dynamic-lattice DMC method is a conceptually simple way to directly simulate an electron-ion system and offers more ionic observables as well as direct comparisons with the static-lattice system than a single clamped-ion calculation. A Born-Oppenheimer study using the DMC energy surface is needed to bridge the previous static-lattice and harmonic ZPE study with the current dynamic-lattice nonadiabatic calculation. A detailed comparison among the three variants will hopefully resolve some of the disagreements we currently have.

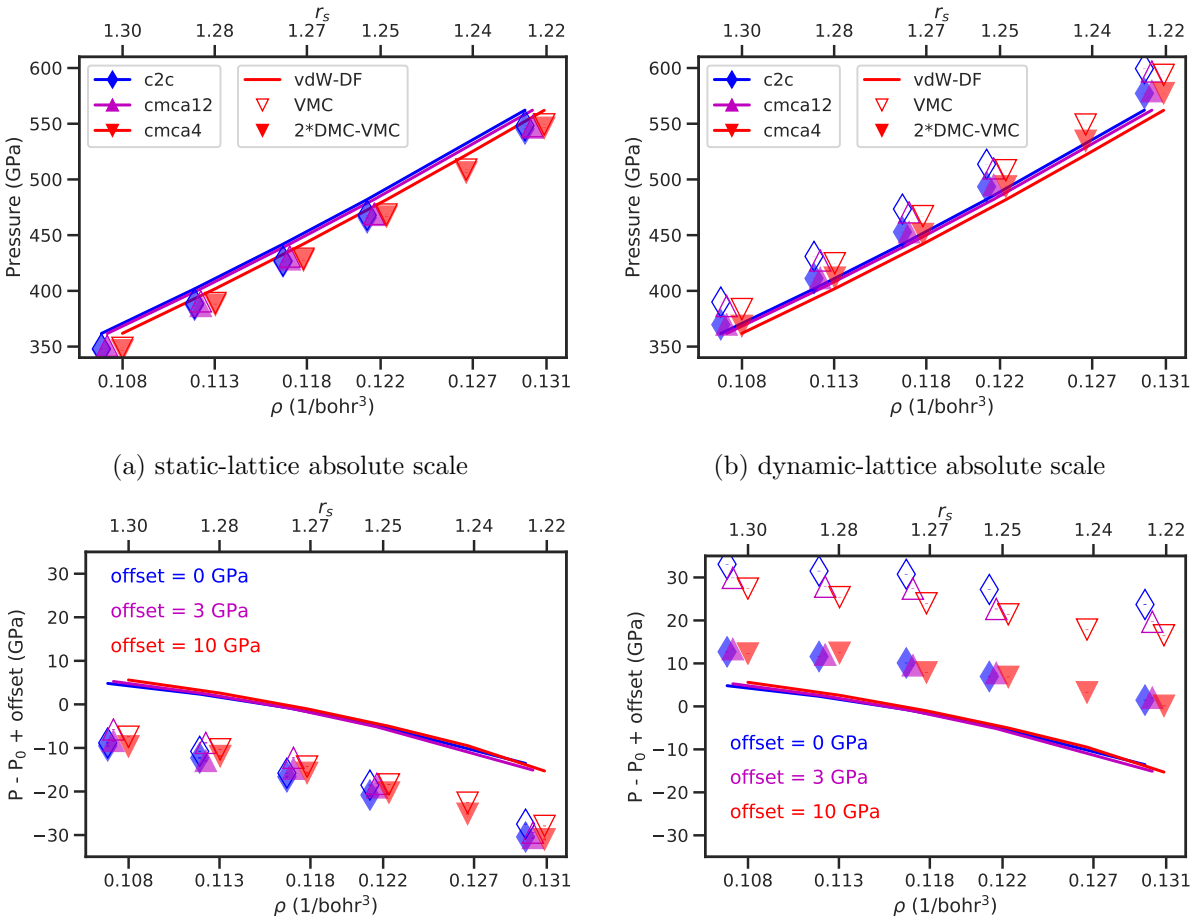

(a) static-lattice absolute scale

(b) dynamic-lattice absolute scale

(c) static-lattice relative to P_0

(d) dynamic-lattice relative to P_0

Figure 6.23: Pressure-density relation. The solid lines are clamped-ion vdW-DF pressures, whereas the symbols are QMC pressures. (a) (c) show static-lattice results, while (b) (d) show dynamic lattice results. Color denotes different candidate structures. The open and filled symbols represent VMC and linearly extrapolated DMC estimator results. They overlap on the absolute scale in (a) but can be seen to differ by 1 to 5 GPa on a relative scale in (b). The reference pressure-density relation $P_0 = -dE_0/dv$ is calculated from the reference EOS $E_0(1/v)$. The same clamped-ion reference is used for both static-lattice and dynamic-lattice results.

Chapter 7

Effect of ions on the electronic momentum distribution

This chapter is based on the following article(s):

I. Nozomu Hiraoka, Yubo Yang, Toru Hagiya, Akinobu Niozu, Kazuhiro Matsuda, Simo Huotari, Markus Holzmann, and David M. Ceperley, "Direct observation of the momentum distribution and renormalization factor in lithium," Phys. Rev. B **101**, 165124 (2020).

II. Yubo Yang, Nozomu Hiraoka, Kazuhiro Matsuda, Markus Holzmann, and David M. Ceperley, "Quantum Monte Carlo Compton profiles of solid and liquid lithium," Phys. Rev. B **101**, 165125 (2020).

7.1 Introduction

The Compton profile is a bulk-sensitive probe of the electronic structure of a material accessible to both theory and experiment. Using the "impulse approximation" [205], the double differential cross section of inelastic light scattering is directly proportional to the Compton profile, the Radon transform of the electronic momentum distribution along the scattering vector.

$$J(p_z) = \iint dk_x dk_y \; n(k_x, k_y, k_z = p_z), \tag{7.1}$$

where $n(\boldsymbol{k})$ is the electronic momentum distribution. Since the pioneering work of Eisenberger et al. [205, 206], Compton scattering experiments have been performed on simple metals such as Li [207–211], Be [212, 213], Na [214] as well as more complicated materials. Accompanying the scattering experiments are numerous theoretical calculations using different electronic structure theories including density functional theory (DFT) [207, 208, 211, 215–220], QMC [214, 221], and GW [222–225]. The Compton profiles in ref. [207, 208] were compared to DFT results using the local density approximation (LDA) with the Lam-Platzman correlation correction [226]. While the Lam-Platzman correction has been shown to be accurate by QMC [217, 221, 227], the theoretical Compton profile is still larger at low momenta and smaller at high momenta compared with experiment. In other words, the predicted Compton profile is typically narrower than observed.

Both theoretical approximations and experimental procedures may be responsible for a significant fraction

of the aforementioned discrepancy. In the experiment, finite momentum resolution and final-state effects [228, 229] broaden the measured Compton profile. In the theoretical calculations, the lack of electronic correlation and the use of pseudopotentials both narrow the computed Compton profile. Furthermore, many subtle complications may also be responsible for part of the discrepancy. Examples include: multiple scattering corrections, background subtraction, thermal expansion, electron-phonon coupling, and relativistic effects.

In this work, we present much improved QMC calculations on the solid and liquid states of lithium. Firstly, we use grand-canonical twist-averaging [60, 72] to access the momentum distribution at arbitrary momentum while preserving a sharp Fermi surface. We obtain a momentum resolution of 0.040 a.u., which is higher than the 0.068 a.u. achieved previously [221] (It is straight-forward to further increase momentum resolution given more computational resources). Secondly, we perform diffusion Monte Carlo (DMC) to remove effects of the trial wavefunction. Thirdly, we use all-electron QMC to explore the pseudopotential bias in the Compton profile. We find that the pseudopotential bias is responsible for the majority of discrepancy between pseudopotential QMC and experimental Compton profiles away from the Fermi surface. Fourth and finally, we apply finite-size corrections [59, 230] to obtain the momentum distribution in the thermodynamic limit. Using these improved procedures, we calculate the disorder-averaged Compton profiles for polycrystal and liquid lithium and obtain good agreement with recent high-resolution synchrotron experiment [231].

This chapter is organized as follows. In section 7.2, we describe the simulation methods used to obtain the QMC momentum distributions. In section 7.3, we show the QMC momentum distributions and the resulting Compton profiles in comparison with experiment. In section 7.4, we discuss the influence of various physical effects on the momentum distribution in an attempt to explain the remaining discrepancy between QMC and experiment.

7.2 Method

Full-core and pseudopotential QMC calculations have been performed on both the perfect crystal and disordered lithium configurations. We use Slater-Jastrow trial wavefunction

$$\Psi_T = D^{\uparrow} D^{\downarrow} \exp\left[-\sum_{i<j}^{N} u(\boldsymbol{r}_i - \boldsymbol{r}_j) - \sum_{i=1}^{N} \chi(\boldsymbol{r}_i) \right], \tag{7.2}$$

where $u(\boldsymbol{r})$ is the electron-electron Jastrow pair function, $\chi(\boldsymbol{r})$ is the electron-ion Jastrow pair function and $\boldsymbol{r}_i$ is the position of the ith electron. The Slater determinant $D^{\uparrow/\downarrow}$ is composed of single-particle orbitals obtained using Kohn-Sham (KS) DFT with the LDA functional. In the full-core calculation, we remove the

approximate electron-ion cusp from the orbitals and re-introduce the exact cusp condition in the Jastrow function [6]. The electron-ion Jastrow pair function is split into a sum of core and valence pieces. A flexible B-spline with 16 adjustable knots is used for the core piece ($r < 2$ bohr). An electron-electron-ion three-body Jastrow consisting of cubic terms in separations with a cutoff of 4 bohrs further improves the all-electron wave function [232]. In the pseudopotential calculation, we treat the lithium atoms as pseudo ions of charge +1. The core, screened by 1s electrons, is replaced by the Burkatzki-Filippi-Dolg (BFD) pseudopotential [233]. The electron-electron Jastrow pair function is expressed as a sum of real-space and reciprocal-space parts to accurately describe long-range plasmon fluctuations.

In variational Monte Carlo (VMC), we sample $|\psi_T|^2$ using Metropolis Monte Carlo and directly calculate properties from the many-body wavefunction. The momentum distribution is calculated using the direct estimator in reciprocal space [234]. In DMC, an ensemble of electron configurations evolve according to the Green's function of the non-relativistic Schrödinger equation in imaginary time. Using the trial wavefunction ψ_T as guiding function and phase reference, the long-time solution samples the mixed distribution $\psi_T^* \psi_{FP}$, in the limit of small time step. ψ_{FP} is the fixed-phase ground-state wavefunction. If the phase of ψ_T were exact, then ψ_{FP} would be the exact ground-state wavefunction. [235] The difference between the expectation value of an observable in the fixed-phase and the mixed distributions is the mixed-estimator bias. We gauge simulation quality by monitoring kinetic, potential, and total energies as well as pair correlation functions and the momentum distribution. We observe fast equilibration, small variance and small mixed-estimator bias in all monitored quantities. The DMC momentum distribution is linearly extrapolated to remove the mixed-estimator bias. For more details on the computational methods and data processing, see the Supplemental Materials [1].

We use grand-conical twist average boundary condition to improve the momentum distribution [59, 236]. A previous QMC calculation [221] used real wavefunctions and canonical twist average boundary condition (CTABC); each boundary condition (twist) had the same number of electrons. Use of real trial functions restricted the accessible momenta to those commensurate with the simulation cell. CTABC can occupy states outside of the Fermi surface at certain twists, which artificially smears the Fermi surface. In contrast, the grand-canonical twist average technique enforces constant chemical potential at all twists. We adjust the number of electrons at each twist such that no state outside the Fermi surface is occupied. This allows us to sample the momentum distribution at momenta arbitrarily close to the Fermi surface while maintaining a sharp Fermi surface. In practice, we impose the occupation of the orbitals in the Slater determinant according to the LDA Fermi energy. In principle, one might modify the Fermi surface by estimating the chemical potential directly within QMC [237]. However, this is much more com- putationally demanding and

is beyond the scope of the current study and not thought to be necessary for lithium based on comparison with de Haas–van Alphen estimations of the anisotropy of the Fermi surface. As discussed in Sec. IV,we have determined that the DFT Fermi surface is quite accurate.

In the perfect crystal, the full-core simulation contains 54 lithium atoms, while the pseudopotential simulations contain 54 or 432 atoms. We use MD with the modified embedded-atom potential (MEAM) [238] to generate the disordered configurations. The MD temperatures were elevated to model quantum fluctuations of the nuclei [239]. We sample the canonical distribution with 432 lithium atoms at 330K and 500K for experiments at 298K and 493K, respectively.

All calculations have been performed at the same density $r_s = 3.25$, consistent with the previous QMC study [221]. After obtaining QMC results at $r_s = 3.25$, we rescale the density of QMC Compton profiles to match the experimental densities: $r_s = 3.31$ for the liquid and $r_s = 3.265$ for the solid.

In both QMC and experiment, we assume the momentum distribution of the core electrons to remain unmodified from that in the isolated atom. The atomic core orbital is calculated using Hartree-Fock (HF) and removed from all-electron results to produce valence electron contributions.

We convolved our QMC Compton profile with a broadening function to model instrument resolution and final-state interaction. For this we used the *extended Lorentzian*

$$b(x) = \frac{1}{\tilde{\Omega}} \frac{1}{a_0 + a_1(\frac{2x}{\Gamma})^2 + a_2(\frac{2x}{\Gamma})^4} \tag{7.3}$$

with $\Gamma = 0.024$ a.u., $a_0 = 1$, $a_1 = 0.85$ and $a_2 = 0.15$ chosen to fit the convolution of the elastic line in the X-ray experiment and the spectral density function of the electrons and $\tilde{\Omega}$ such that $\int dx\ b(x) = 1$.

We used LAMMPS [240] for the MD simulations, QE [241, 242] for DFT, PySCF [243] for HF, and QMCPACK [244] for QMC. The disordered calculations have been automated using the nexus suite of tools [245].

7.3 Results

Figure 7.1 shows the valence Compton profiles of solid and liquid lithium from experiment and processed QMC data. The raw QMC data have been processed to account for finite-size effects, thermal disorder, pseudopotential bias, density change, final-state effects, and instrument resolution. The QMC Compton profiles agree with experiment immediately inside the Fermi surface (0.2 a.u.<p<0.4 a.u.) and at large momenta (p>0.9 a.u.). However, the QMC Compton profiles show less high-momentum component immediately outside the Fermi surface and too much low-momentum component. Both the theoretical and experimental

valence Compton profiles satisfy the normalization sum rule ($\int_{-\infty}^{\infty} J(p)dp = 1$) to better than 0.3%. The difference between QMC and experiment Compton profiles can be interpreted as a shift of momentum density from zero to slightly above the Fermi momentum.

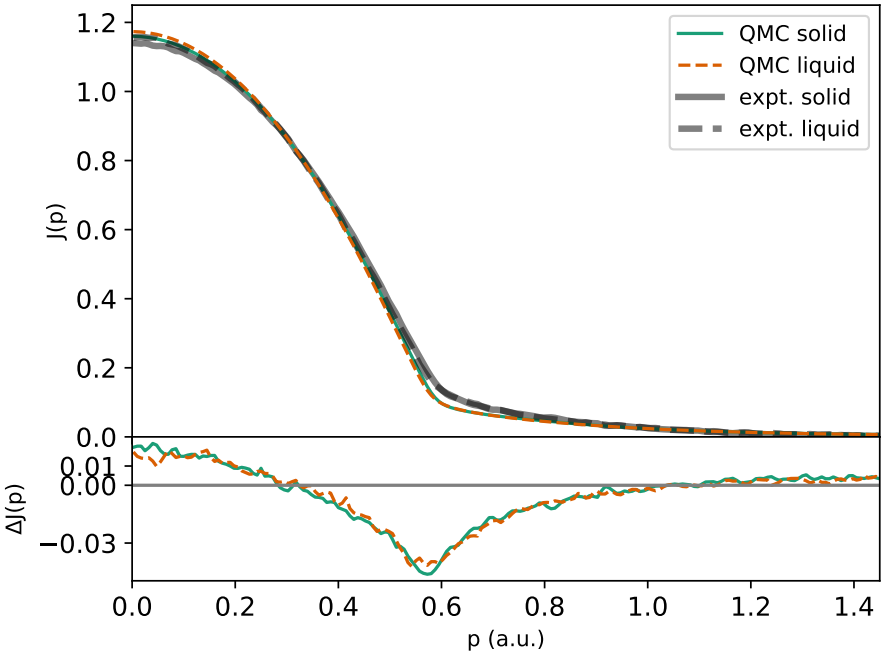

Figure 7.1: Valence electronic Compton profiles of solid (solid line) and liquid (dashed line) lithium from QMC (thin) and experiment (thick). The top panel shows the Compton profiles on an absolute scale. The bottom panel shows $\Delta J(p) = J_{QMC} - J_{expt}$.

Figure 7.2 shows the change of the Compton profile when the liquid freezes into a solid. The systematic difference between QMC calculations and experiment is almost identical in the solid and liquid. Thus, cancellation of error allows us to capture the difference between the solid and liquid Compton profiles almost perfectly. The main change is a density-induced outward shift of the Fermi surface. This shift manifests in Fig. 7.2 as a peak at the solid Fermi momentum $p_F \approx 0.578$ a.u. and a parabolic dip centered around $p = 0$. Another important difference is the emergence of secondary Fermi surfaces, due to Umklapp scattering in the solid. We expect secondary Fermi surfaces to center around the reciprocal lattice of the lithium crystal. Crystalline lithium is BCC with a lattice constant of ~ 6.63 bohr, so its reciprocal lattice is FCC with a lattice constant of ~ 1.895 a.u.. The nearest neighbor to Γ is $p_1 = 1.34$ a.u. along [110]. Therefore, the closest secondary Fermi surface is located at $p_1 - p_F = 0.762$ a.u., which is exactly where we observe a small peak in Fig. 7.2.

As mentioned at the beginning of this section, we process the raw QMC data in several steps to make

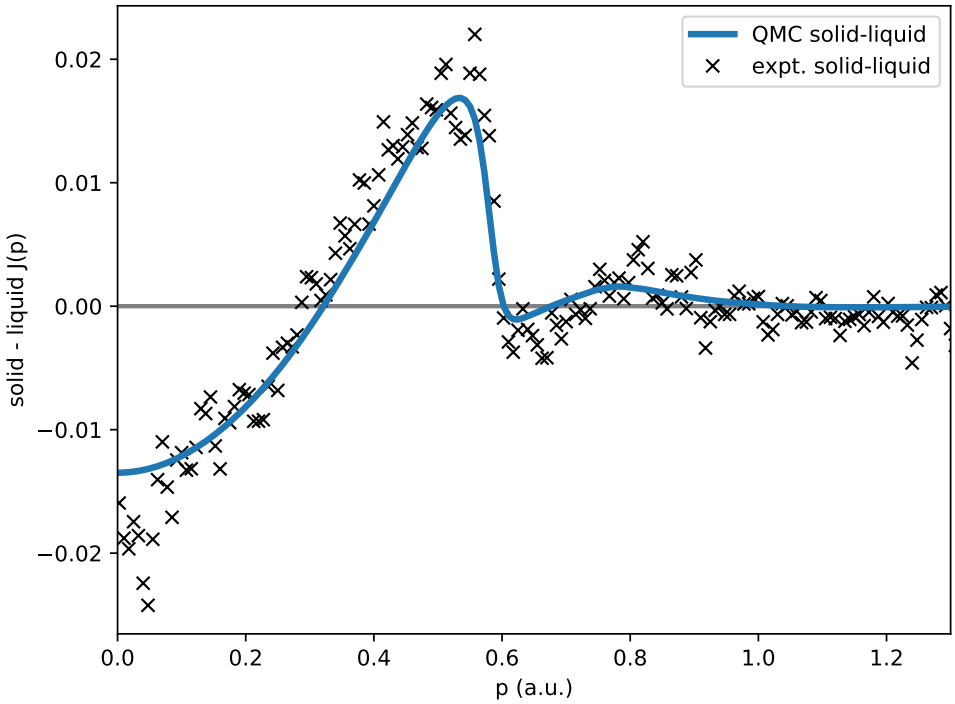

Figure 7.2: Difference between solid and liquid valence electronic Compton profiles.

them comparable to experiment. In the following, we present perfect lithium crystal QMC calculations, which we use to validate the processing steps.

In Fig. 7.3, 1D slices of the QMC valence momentum distributions are shown. The momentum distribution is free-electron-like along the [100] and [111] directions. Along the [110] direction, however, there is a pronounced secondary Fermi surface. The valence profile from the full-core calculation is flatter inside the Fermi surface and has enhanced secondary features when compared to the pseudopotential calculation.

To obtain the valence momentum distribution from the full-core QMC calculation, we remove the momentum distribution of the 1s core electrons. The 1s orbital of the neutral lithium atom is calculated using Hartree-Fock (HF) with a cc-pV5Z basis. The most pronounced effect of the pseudopotential is to increase the electronic momentum density inside the Fermi surface, raising $n(0)$ by more than 5%. In contrast, the effect of increasing system size peaks at the Fermi momentum. The main effect of finite system size is to increase the magnitude of the discontinuity at the Fermi momentum. The effects of pseudopotential and finite system size can be better shown in the momentum distribution differences.

In Fig. 7.4, we show two sets of momentum distribution differences in direct correspondence with Fig. 7.3. The first is the difference between full-core and pseudopotential momentum distributions. This difference can be considered a pseudopotential correction (PPC). The PPC is largest inside the Fermi surface. It has a

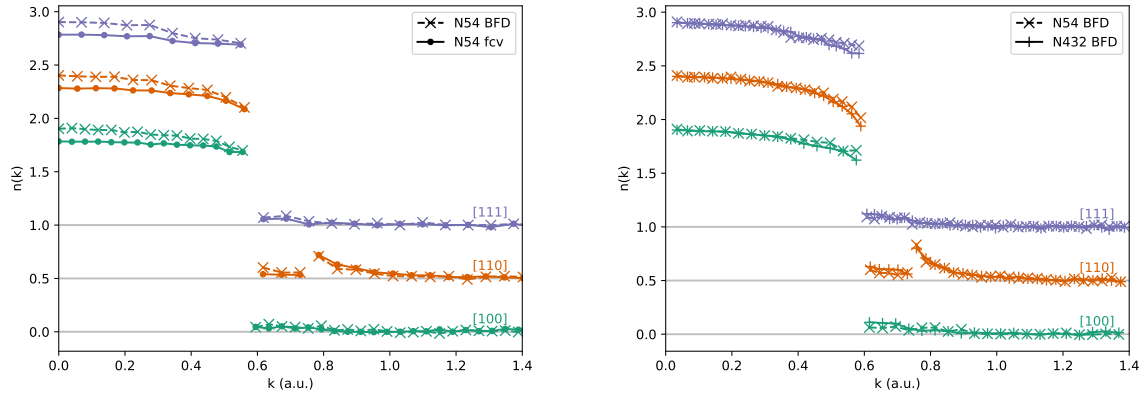

(a) full-core valence *vs* pseudopotential

(b) 432 atoms *vs* 54 atoms

Figure 7.3: Momentum distribution of valence electrons in lithium BCC crystal. The top panel compares pseudopotential (crosses) to full-core (dots) result. The bottom panel compares 54-atom (crosses) to 432-atom (pluses) pseudopotential results.

parabolic shape and is mostly negative along the [100] and [111] directions. However, it shows positive peaks near the secondary Fermi surface along the [110] direction. The PPC is spherically-averaged and applied to the momentum distributions of the disordered structures.

Now consider how the finite size of our supercell affects the results: the finite-size correction (FSC). Figure 7.4(b) shows the difference between the 432-atom and 54-atom pseudopotential calculations. The difference peaks at the Fermi surface and goes to zero at high momenta. The FSC results shown here are used to validate the approach outlined in ref. [59] and ref. [230].

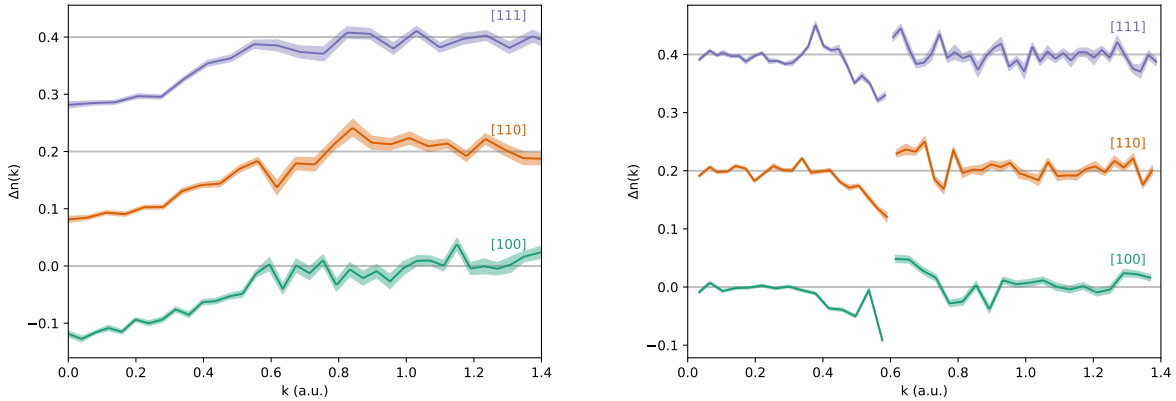

(a) full-core valence - pseudopotential

(b) 432 atoms - 54 atoms

Figure 7.4: Momentum distribution differences. The top panel is the difference between full-core and pseudopotential results. The bottom panel is the difference between the 432-atom and 54-atom pseudopotential results. The shaded region show one standard deviation of statistical uncertainty. These results are used to inform pseudopotential and finite-size corrections.

In Fig. 7.5, we show our best QMC Compton profile in the crystal as the red line. It is the spherically-averaged Compton profile from the 432-atom pseudopotential calculation with PPC and FSC applied. Further, we rescaled the QMC data to change density from $r_s = 3.25$ to $r_s = 3.265$ and convolved the QMC Compton profile with Eq. (7.3) to approximately account for experimental resolution and final-state effects. The full-core QMC profiles agrees well with the most recent experiment away from the Fermi surface.

The Compton profile reported by Filippi and Ceperley [221] is closer to our full-core than to our pseudopotential result. This is because they accounted for proper core-valence orthogonalization using full-core LDA. Pseudopotential QMC was used to estimate the correlation correction, rather than directly provide the Compton profile.

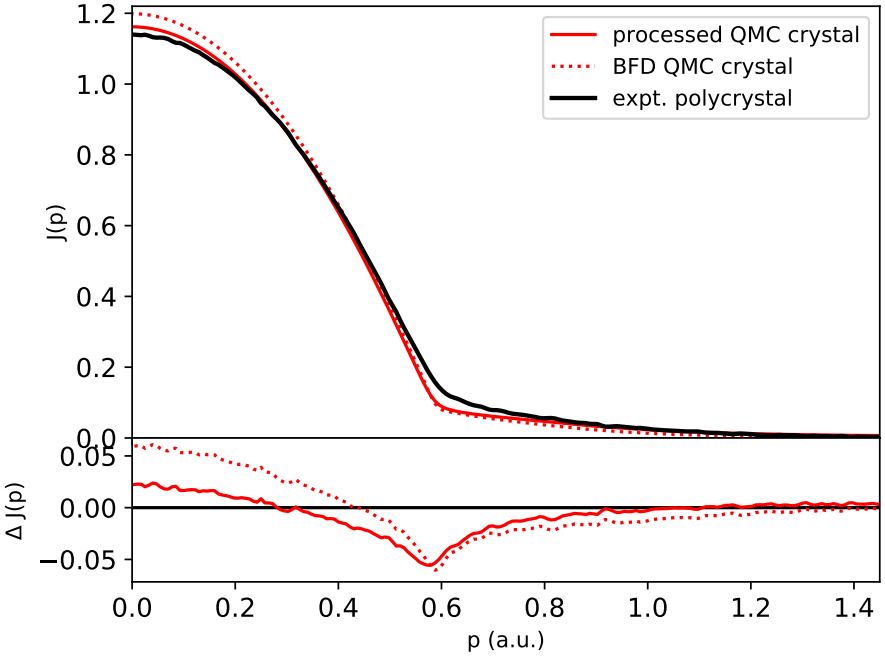

Figure 7.5: Spherical average of the valence Compton profile of lithium BCC crystal at $r_s = 3.25$. The red solid line is the best QMC result with all processing steps applied. The red dotted curve is our pseudopotential QMC result. The black curve is experiment on polycrystal lithium.

Taking our best QMC Compton profiles (thin lines in Fig. 7.1) as reference, we show the remaining difference between the QMC and the experiment Compton profiles as the black curves in Fig. 7.6. We also show the effect of each processing step in the calculation of $J(p)$. Finite-size and convolution corrections both peak at the Fermi momentum and are small at the scale of the remaining discrepancy. The density correction is small in the solid but substantial in the liquid, because QMC calculations have been performed close to the solid density. In both cases, the density correction contracts the Fermi sphere and has little effect above

the Fermi momentum. In contrast, the pseudopotential correction nearly vanishes at the Fermi momentum, smoothly transfers low-momentum components to high momenta, and remains non-zero well above the Fermi momentum. The $n(k)$ tail correction is needed to recover the normalization sum rule, because the QMC $n(k)$ is truncated at a finite momentum k_c. The exact shape of $n(k)$ tail may not be accurate above k_c, because the assumed functional form is simple (see Supplemental Materials [1]). Fortunately, the effect of $n(k)$ tail within k_c is simply to shift the entire Compton profile up by a constant as dictated by the normalization sum rule. The tail and pseudopotential corrections are the only ones that can change the high-momentum tail of the Compton profile.

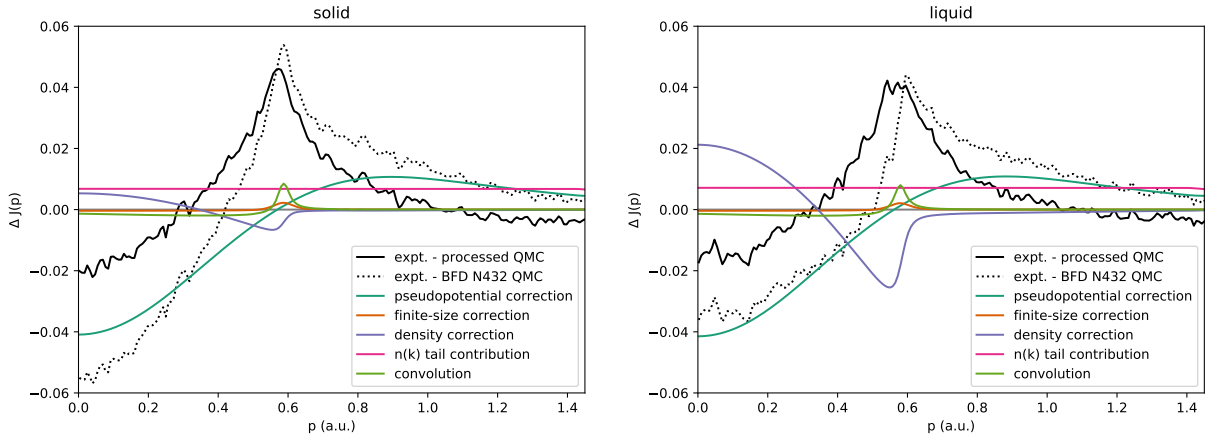

Figure 7.6: Valence Compton profile corrections. The solid black curve is experiment relative to "best" theory. The dotted black curve is experiment relative to pseudopotential QMC result with no correction. Each colored curve shows the effect of neglecting a processing step from the theoretical Compton profile. When added to the processed result (solid black curve), the sum of all colored curves approximately recovers the unprocessed result (dotted black curve).

7.4 Discussion

In the following, we discuss possible explanations for the remaining discrepancy in Fig. 7.1, which is shown separately for the solid and liquid in Fig. 7.6.

Electron-Ion interaction The crystal lattice introduces inhomogeneity to an otherwise homogeneous valence electron density. Umklapp processes send electronic momentum density to secondary Fermi surfaces, thereby enhancing the high-momentum components of the momentum distribution and reducing the momentum distribution inside the Fermi surface. Further, its discontinuity at the Fermi surface is reduced [206]. In the absence of other interactions, the ground-state electronic density will be exact if the electron-ion

[1] See Supplemental Material at http://link.aps.org/supplemental/10.1103/PhysRevB.101.165125, which includes Refs. [57, 246–248], for more details on the computational methods and data processing.

interaction is perfectly captured. DFT is designed to obtain the correct ground-state electronic density, so we expect it to treat electron-ion interaction well. However, pseudopotential is not designed to faithfully reproduce the charge inhomogeneity of the valence orbital in the core region. Therefore, pseudopotential introduces a bias in the valence momentum distribution.

The qualitative effect of the pseudopotential is clear from its construction. When designing a pseudopotential, one smooths the valence orbital inside the core region. This will decrease the electronic momentum density at high momenta, and increase it at low momenta. Indeed, one can reproduce the pseudopotential correction semi-quantitatively by considering the smoothing of the pseudized valence orbital in the lithium atom (Fig. 7.7). We see that augmented planewave (APW) calculations [216, 217, 249, 250] tend to reproduce the experimental Compton profiles better at low momenta than pseudopotential calculations.

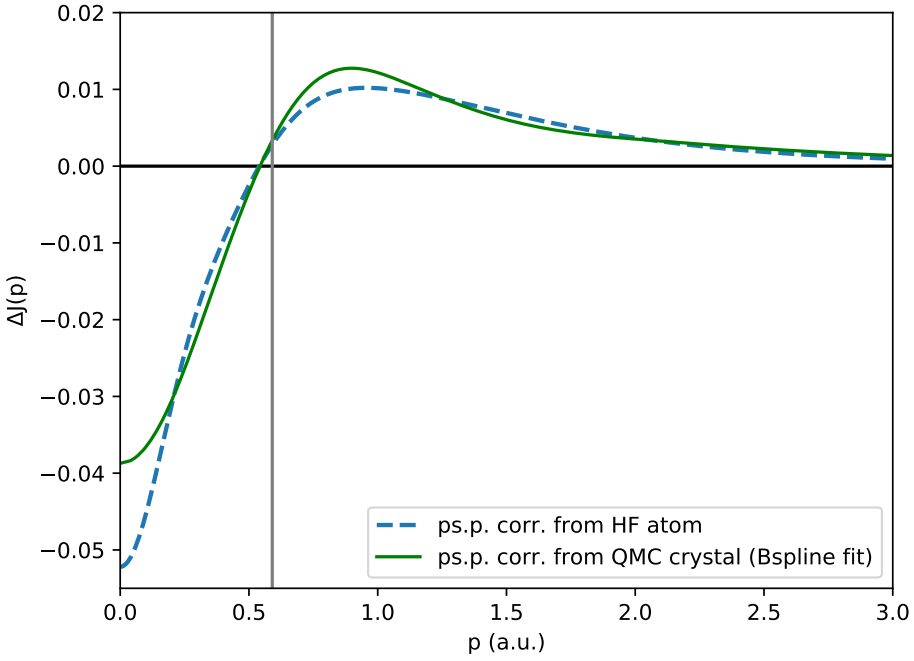

Figure 7.7: Pseudopotential correction derived from QMC and HF. The green curve is the same QMC pseudopotential correction as shown in Fig. 7.6. The dashed blue curve is the pseudopotential correction derived from the all-electron v.s. pseudized lithium atom using HF. The gray vertical line marks the Fermi momentum.

Our pseudopotential correction (PPC) is not perfect. It was derived in the perfect crystal, then applied to the disordered configurations. Ideally, one would directly perform all-electron QMC on the disordered configurations. However, this is computationally expensive. We do not consider all-electron calculation to be necessary in the solid phase, because the effect of disorder is small. The current PPC does over correct the

liquid Compton profile at high momenta, because the corrections meant for the secondary Fermi surfaces are extraneous. Nevertheless, we think the pseudopotential bias is mostly captured, i.e. at the scale of Fig. 7.7. The corrected Compton profile in Fig. 7.5 is in better agreement with experiment than its pseudopotential counterpart, especially at $p = 0$. We do not think the pseudopotential bias is responsible for the remaining discrepancy, because the PPC is concentrated around $p = 0$. If it were underestimated, then the remaining correction would lower $J(0)$ much more than it would raise $J(p_F)$, worsening the agreement with experiment.

Disorder Disorder mostly reduces the effect of the crystal lattice, because deviations from the perfect lattice weaken Umklapp processes. A confirmation was obtained when Sternemann et al. reproduced the temperature effect on the Compton profile of lithium by smearing out the pseudopotential with a Debye-Waller factor [210].

Thermal disorder is also unlikely to be responsible for the remaining discrepancy because disorder-correction is small at the scale of the remaining correction. This can be seen by comparing the discrepancy in the perfect crystal (Fig. 7.5) to the discrepancy in the disordered solid (Fig. 7.1). The two remaining discrepancies are similar in both shape and magnitude.

Electron-Electron Correlation The effect of electron-electron (ee) correlation on the momentum distribution is similar to electron-ion interaction in that it increases high-momentum components, decreases low-momentum components and reduces the discontinuity at the Fermi surface. The Slater-Jastrow wavefunction is a first-order modification of the free-electron Slater determinant by the Coulomb interaction [10] but it does not capture all correlation effects. However, we expect the Slater-Jastrow wavefunction to be accurate for simple metals. Further, it can be systematically improved, for example by using backflow transformations [58]. Calculations on the homogeneous electron gas indicate a small decrease of the discontinuity at the Fermi surface [230] reducing the discrepancy with experiment. Quantitative studies of backflow effects on the lithium Compton profiles should be addressed in the future.

Fermi surface The Fermi surface of BCC lithium is anisotropic with pronounced secondary features. The DFT Fermi surface is used in the QMC simulation to determine which momentum states to occupy. For solid lithium, the Fermi surface is nearly spherical. Our DFT Fermi surface of the BCC crystal has a maximum anisotropy of $\delta = 5.0\%$, where

$$\delta \equiv \frac{k_F^{[110]} - k_F^{[100]}}{k_F^{HEG}}. \tag{7.4}$$

This is in good agreement with the de Haas-van Alphen experiment performed by M. B. Hunt et al. [251], which reported a maximum anisotropy of $\delta = 4.8 \pm 0.3\%$. Our DFT result differs from previous calculations

by A. H. MacDonald $\delta = 3.3\%$ [252] and H. Bross $\delta = 5.9\%$ [217], likely due to differences in the density functional and pseudopotential. While the DFT Fermi surface may not be accurate in the crystal, a liquid is isotropic and will have a spherical Fermi surface. Given that our solid - liquid Compton profile difference agrees well with experiment (Fig. 7.2), we do not consider Fermi surface shape to be responsible for the remaining discrepancy.

Electron-phonon interaction We capture disorder effects due to phonons by averaging over thermal atomic configurations. However, other phonon effects are absent from our QMC simulations because the lithium ions are clamped. Phonons scatter quasi-particles and decrease their life times. Thus, we expect the inclusion of electron-phonon interaction to decrease the magnitude of the discontinuity in the momentum distribution. Calculations of the coupled electron-phonon system within the Einstein or Debye model [253] show that the resulting broadening at zero temperature is essentially given by the Debye frequency. The Debye temperature of lithium (<400K) is much lower than the Fermi temperature of the electrons, so we expect the remaining electron-phonon coupling (not included in our QMC calculations) to be limited very close to the Fermi surface in momentum space, rendering the effect invisible at the scale of Fig. 7.2.

Finite size effects Finite-size effects (FSE) are more challenging to deal with in a many-body simulation than in an effective one-particle theory such as DFT which is formulated for an infinite lattice. In DFT, a calculation performed in a larger simulation cell simply makes the momentum-space grid denser. In contrast, finite system size increases the magnitude of the discontinuity at the Fermi surface in QMC. This effect was found to decrease slowly with system size in the homogeneous electron gas [59]. This FSE was analyzed and understood in the homogeneous electron gas [59, 230]. We adopted the same approach here and found good results. In particular, we corrected the FSE using the leading-order expression

$$\delta n^{(1)}_{\boldsymbol{k}} = \int_{-\pi/L}^{\pi/L} \frac{d^3\boldsymbol{q}}{(2\pi)^3} \left[u_q(1-S_q) - n u_q^2 S_q\right] (n_{\boldsymbol{k}+\boldsymbol{q}} - n_{\boldsymbol{k}}), \tag{7.5}$$

where u_q and S_q are the Jastrow pair function and the structure factor in reciprocal space, which are assumed to take RPA forms at small q and n is the valence electron density. The corrected $n(k)$ from the 54-atom and 432-atom simulations agree well with each other as shown in Fig. 7.8. Therefore, we think finite-size error has been satisfactorily accounted for, and is not responsible for the remaining discrepancy.

Density change The electronic density is a crucial parameter since it determines the Fermi surface. It can change due to thermal expansion and phase transition from solid to liquid. We accounted for density change between our calculations and experiment by rescaling our computed momentum distributions to the experimental densities by scaling the value of k to match the Fermi momentum ($k_F = (9\pi/4)^{1/3}/r_s$) and

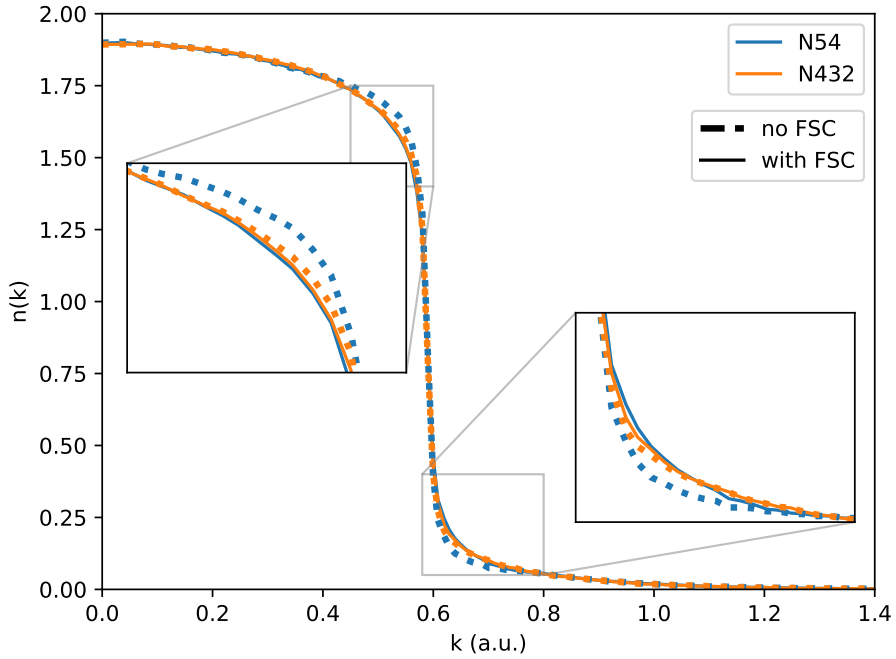

Figure 7.8: Finite-size correction in the liquid phase. Dotted lines are pseudopotential QMC $n(k)$ with no correction. Color encodes the number of lithium atoms in the simulation cell. The solid lines correspond to the dotted lines in color and have been corrected using the leading-order expression Eq. (7.5).

then correcting the overall normalization. This brought the Compton profile into excellent agreement with experiment as shown in Fig. 7.2. Of course it would be possible to perform additional QMC simulations at the experimental density.

Final state effects Finally, the "impulse approximation" is known to be inaccurate for core electrons and cause asymmetry in the measured Compton profile [205, 228, 254]. To go beyond the "impulse approximation", one must consider interaction of the scattered electron with the rest of the system in the final state. Final-state effects are often attributed to three physical interactions. The first is the interaction between the excited quasi-particle with its surrounding medium (self-energy). The second is the interaction between the excited quasi-particle and the hole it lefts behind (vertex correction). The third is the interaction between the hole and a plasmon (plasmaron). C. Sternemann et al. showed that the self-energy combined with the vertex correction can satisfactorily explain the asymmetry of the Compton profile [228]. The effect of final-state interaction on the Compton profile can be approximated by convolving the spectral density function (SDF) of the excited electron with the ground-state Compton profile [229]. This convolution smears out the derivative-discontinuity of the Compton profile at the Fermi momentum. Thus the convolution correction also peaks at the Fermi momentum.

We account for final-state effects by convolving the QMC Compton profiles with the broadening function Eq. (7.3), which is an accurate representation of the convolution of the experimental resolution function and the SDF obtained by Soininen et al. [229]. However, the SDF in ref. [229] did not include plasmaron or electron-hole effects. Further, we find near perfect agreement with experiment if the QMC profiles were broadened using a Lorentzian having FWHM $\Gamma = 0.026$. In other words, if the neglected final-state effects were to introduce long tails into the SDF, then the QMC profiles would agree much better with experiment. Therefore, final-state effect is a plausible explanation for much of the remaining discrepancy.

7.5 Conclusion and Outlook

Leveraging new algorithms and hardware, we improved the QMC Compton profile of lithium and provided the first QMC results in the disordered solid and the liquid states. Our QMC Compton profiles agree very well with the most recent synchrotron experiment [231]. We resolved the discrepancy between pseudopotential QMC and experiment at zero and high momenta using an all-electron QMC calculation. We discussed potential explanations for the remaining discrepancy, which is concentrated at the Fermi surface. Future studies should consider final-state effects.

Current state-of-the-art QMC algorithms are ready to aid synchrotron experiments in understanding the measured Compton profiles. It would be interesting to revisit the challenging problem that is the 3D reconstructing of the momentum distribution from directional Compton profiles [208, 211]. Momentum resolution has been increased by new techniques in both theory and experiment. Further, all-electron QMC for lithium is feasible for perfect crystals in supercells containing thousands of electrons. The comparison between lithium and sodium will be particularly interesting, because they have the same crystal structure but very different electron-ion interactions [206]. A detailed study of these systems can shed more light on the nature of electron-ion and perhaps the electron-phonon interactions in simple metals.

Finally, when sufficient accuracy has been achieved in both theory and experiment, one can study the difference between ground-state (QMC) and final-state (experimental) Compton profiles to extract information on the dynamic structure factor of the system.

Chapter 8

Finite-size correction to the fundamental gap of insulators

This chapter is based on the following article(s):

I. Yubo Yang, Vitaly Gorelov, Carlo Pierleoni, Markus Holzmann, and David Ceperley, "Electronic band gaps from quantum Monte Carlo methods," Phys. Rev. B **101**, 085115 (2020).

8.1 Introduction

Insulator and semiconductors are characterized by a non-vanishing *fundamental gap* [24], defined in terms of the ground state energies of a system of fixed ions as the number of electrons is varied:

$$\Delta_{N_e} = E_0(N_e + 1) + E_0(N_e - 1) - 2E_0(N_e) \tag{8.1}$$

where $E_0(N_e)$ is the ground-state energy of an N_e electron system.

Within density functional theory (DFT), it is common to interpret the eigenvalues of the Kohn-Sham equations as excitation energies, the gap being the minimum excitation energy. However, the resulting band gap within the local density approximation (LDA) is typically found to be too small [255]. This qualitative failure can be alleviated either by hybrid functionals or by adding corrections based on GW many-body perturbation theory, although the precise value depends on the underlying functional and approximation scheme involved [24]. In principle, the fundamental gap can be calculated from any method for ground-state energies based on the above formula. High-precision methods for correlation energies as, for example, provided by quantum Monte Carlo (QMC) [256–259] or coupled cluster methods [260, 261] can be used. In this work, we propose a method for accurate calculations of the fundamental gap within explicitly correlated methods and demonstrate its use with fixed-node diffusion Monte Carlo (DMC) benchmark studies on solid H_2, C, and Si.

Methods based on correlated many-body wave functions are usually applied to finite-sized systems, e.g., limited to supercells containing only few unit cells. QMC calculations of single-particle excitations for adding and removing electrons [2, 262–264] crucially rely on the imposed extrapolation law (e.g., finite-size error

$\propto 1/L$ in Ref. [2] opposed to $1/L^3$ in Ref. [264], where L denotes the linear extension of the supercell). This introduces considerable uncertainty in the results. Heuristically, single-particle excitations are expected to converge slowly for electronic systems, inversely proportional to L, due to the interaction of charges across the periodic boundaries [265, 266]. Extrapolations with respect to the size of the supercells are then essential to obtain reliable values of the gap in the thermodynamic limit.

Most of the QMC calculations [200, 267–275] have therefore addressed charge-neutral, particle-hole excitations, where faster convergence with respect to the size of the supercell is expected. Although the comparison with experiment is appealing [258], a later, more extended DMC study [276] of simple semiconductor materials with larger supercells observed a $1/L$ dependence of the gap on the size of the supercell for both charged single-particle and charge-neutral particle-hole excitations. In addition, fixed-node energy differences are not constrained to be upper bounds for particle-hole excitations [277] since orthogonality to the ground state cannot be strictly guaranteed. Furthermore, all QMC calculations so far have addressed excitations at selected symmetry points contained inside the supercell of the simulation. The fundamental gap was then estimated indirectly by introducing a "scissor operator" [278] which assumes a rigid shift of the underlying DFT band structure over the whole Brillouin zone.

In this work, we show that twisted boundary conditions within the grand canonical ensemble can be used to determine the fundamental gap from QMC without relying on the "scissor" approximation. We prove that to leading order, finite size effects due to two-body correlations are of order $1/L$, and are related to the dielectric constant of the material. Such effects can be understood and corrected for by using the long wavelength properties of the electronic structure factor. For that, we extend the approach described in Refs. [60, 62] which discusses the correction of finite size effects on the ground-state energy based on information contained in the static correlation functions of the finite system. Using the static structure factor from simulation, it is possible to obtain estimates of finite size corrections for the band gap, and its asymptotic functional form without the need for explicit studies at different sizes or referring to DFT or to experimental information external to the QMC calculation.

The chapter is organized as follows. In Sec. 8.2, we describe the main ideas behind our band-gap method based on the grand canonical ensemble. In Sec. 8.3, we derive finite size corrections to energy differences based on an explicit many-body wave function and exact diagrammatic relations. In Sec. 8.4, we describe the computational methods used to calculate the fundamental gap. In Sec. 8.5, we show results for H_2, C, and Si crystals and compare with available experimental values of the gap in Sec. 8.6. Finally in Sec. 8.7, we summarize general features of the method and outline possible extensions and applications.

8.2 Grand-Canonical twist-averaged boundary condition (GCTABC)

In the following, we consider N_e electrons in a perfect crystal, neglecting both zero-point and thermal motion of the ions. A uniform background charge (depending on N_e) is added to assure global charge neutrality when adding or subtracting electrons to a charge-neutral system. The background charge will introduce a rigid shift in the density of states. However, the fundamental gap, Eq. (8.1), is unaffected, because the background charge needed when adding an electron cancels against the one needed when removing an electron. Periodic boundary conditions of the charge densities are used to eliminate surface effects.

The energetic cost of adding an electron to the system at fixed volume, $V = L^3$, defines the chemical potential:

$$\mu^+_{N_e} = E_0(N_e + 1) - E_0(N_e). \tag{8.2}$$

A non-vanishing gap implies a discontinuity in the chemical potential from Eq. (8.1).

It is convenient to work in the grand-canonical ensemble. There, the chemical potential μ is treated as an independent variable and we minimize $E_0(N_e) - \mu N_e$ with respect to N_e at zero temperature and fixed volume. Insulators then represent an incompressible electronic state; for values of μ within the gap, $\partial N_e/\partial\mu = 0$.

To reduce finite size effects, we employ twisted boundary conditions on the many-body wave function. As an electron is moved across the supercell, e.g., by moving an electron a distance equal to the size of the box in the x direction,

$$\Psi(\mathbf{r}_1 + L_x\hat{x}) = e^{i\theta_x}\Psi(\mathbf{r}_1), \tag{8.3}$$

the phase of the many-body wave function changes by θ. The ground-state energy then depends on the twist angle, $E_0(N_e, \theta)$. Twist averaging can significantly accelerate convergence to the thermodynamic limit [72]. Within the grand-canonical ensemble [60, 62], the optimal number of electrons $\bar{N}_e(\theta)$ will depend on θ for given chemical potential μ. To fix nomenclature, we define the *mean electronic density*,

$$n_e(\mu) = (M_\theta V)^{-1} \sum_\theta \bar{N}_e(\theta), \tag{8.4}$$

and the *ground-state energy density*,

$$e_0(\mu) = (M_\theta V)^{-1} \sum_\theta E_0(\bar{N}_e(\theta), \theta). \tag{8.5}$$

n_e is determined by minimizing the free-energy density,

$$f = \frac{1}{M_\theta V} \sum_\theta \min_{N_e} \left[E_0(N_e, \theta) - \mu N_e \right], \tag{8.6}$$

where the sum is over a uniform grid containing M_θ twist angles. For any single-electron theory, the electronic density $n_e(\mu)$ and the ground-state energy density $e_0(\mu)$ coincide exactly with the corresponding thermodynamic limit values for a sufficiently large value of M_θ, e.g., when the sum over twists becomes an integral over the Brillouin zone. Size effects remaining after twist averaging are due to electron-electron correlations.

Figure 8.1(a) illustrates $e_0(\mu)$ and $n_e(\mu)$ for solid molecular hydrogen, computed from HSE functional and from QMC (see Sec. 8.4 for details). The value of the band gap can be directly extracted from the width of the incompressible region. Alternatively, if we eliminate μ in favor of n_e, and plot e_0 as a function of n_e [as in Fig. 8.1(b)], the fundamental gap is obtained by the discontinuity of the derivative, according to Eq. (8.1).

The definition of the fundamental gap can apply to different symmetry sectors. For a perfect crystal, the total momentum of the electrons modulo reciprocal lattice vectors, i.e., the crystal momentum, is conserved. By requiring the total crystal momentum of the electrons to be fixed, e.g., using Bloch-type orbitals in the Slater determinant, the full band structure in the Brillouin zone can be mapped out. For a spin-independent Hamiltonian, one can also impose the total spin to determine the fundamental gap in each spin sector. In practice, the charge gap in the spinless sector can be determined by adding or removing pairs of electrons. The extensions of our definitions and formulas to this case are straightforward, e.g., $\Delta_{N_e} = [E_0(N_e + 2) + E_0(N_e - 2) - 2E_0(N_e)]/2$. We follow this procedure of spin-neutral excitations in the remainder of this chapter.

8.3 Finite size effects

8.3.1 Potential energy

A key quantity in understanding size effects is the long wavelength behavior of the static structure factor, $S_{N_e}(\mathbf{k}) = \langle \rho_{-\mathbf{k}} \rho_{\mathbf{k}} \rangle / N_e$, where $\rho_{\mathbf{k}} = \sum_j e^{i\mathbf{k}\cdot\mathbf{r}_j}$ is the Fourier transform of the instantaneous electron density.

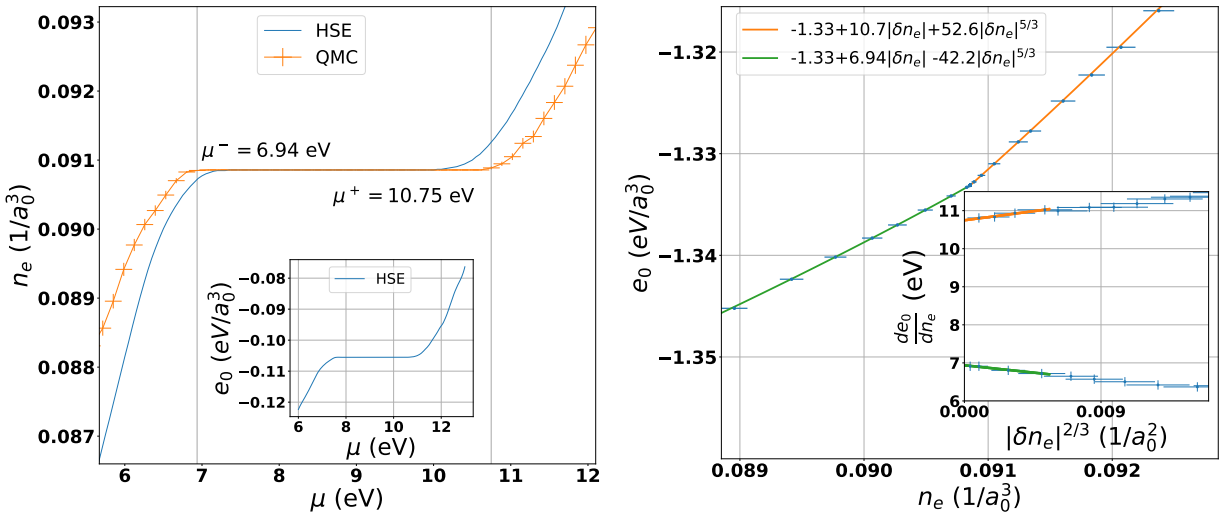

(a) (b)

Figure 8.1: GCTABC analyses of the C2/c-24 structure of solid hydrogen at $r_s = 1.38$ (234GPa). (a) The electron density, n_e, as a function of the chemical potential μ obtained from HSE functional in comparison to QMC; the inset illustrates the energy density, e_0, as a function of μ from HSE functional. (b) Energy density, e_0, as a function of n_e using QMC; the inset shows the derivative discontinuity where δn_e is the change of the electronic density with respect to the insulating state. Size corrections as discussed in the text are included.

The structure factor for a homogeneous system obeys the bound [24, 200],

$$S_{N_e}(k) \leq \frac{\hbar k^2}{2m\omega_p}\left(1 - \frac{1}{\epsilon_k}\right)^{1/2}, \tag{8.7}$$

where $\omega_p = 4\pi\hbar^2 e^2 n_e/m$ is the plasma frequency and ϵ_k the static dielectric constant for wavevector k (to simplify the notations, we will suppress the dependence on the wave vector in the following). This inequality is derived by applying the plasmon-pole approximation to the sum rules of the dynamic structure factor $S(k,\omega)$. It implies that the structure factor must vanish quadratically as $k \to 0$ [279]. Equality will be obtained if $S(k,\omega)$ reduces to a single delta function at small k. The $1/N_e$ finite-size corrections of the energy per electron is a direct consequence of this behavior of $S_{N_e}(k)$ [62]. However, these leading order corrections are not sufficient for excitation energies, since the energy gap is of the same order as finite-size corrections to the total energy.

As we will show below, the key to understanding size effects of energy differences is encoded in the change of $S_{N_e}(k)$ as electrons are added or removed. In particular, the limiting behavior of $S_{N_e\pm1}(k)$ as $k \to 0$ will provide the dominant finite-size correction.

For concreteness, we will assume a Slater-Jastrow form for the ground-state wave function $\Psi_0 \propto D\exp[-U]$. The determinant, D, is built out of Bloch orbitals, $\phi_{\mathbf{q}n}(\mathbf{r})$ with $\mathbf{q}$ inside the first Brillouin zone, n is the

band index, and U is a general, symmetric n-body correlation factor [30]. For simplicity, we assume it is two body: $U = \sum_{i<j} u(r_i, r_j)$. Let us consider the action of $e^{i\mathbf{k}\cdot\mathbf{r}_j}$ on a single-particle orbital $\phi_{\mathbf{q}n}(\mathbf{r}_j)$ in the Slater determinant of the ground state. In the limit of small $\mathbf{k}$, this can be approximately written as $\phi_{\mathbf{q}+\mathbf{k}n}(\mathbf{r}_j)$. Expanding the determinant in terms of its cofactors $\frac{\delta D}{\delta\phi_{\mathbf{q}n}(\mathbf{r}_j)}$ and making the excitation, we have

$$\rho_{\mathbf{k}}\Psi_0 \propto \sum_j \sum_{\mathbf{q},n} \frac{\delta D}{\delta\phi_{\mathbf{q}n}(\mathbf{r}_j)} e^{i\mathbf{k}\cdot\mathbf{r}_j}\phi_{\mathbf{q}n}(\mathbf{r}_j)e^{-U}. \tag{8.8}$$

and the resulting determinant after summation over j vanishes for small k if the Bloch orbital $(\mathbf{q}+\mathbf{k}, n)$ is already occupied in the ground-state determinant. Considering $N_e \pm 1$ electron wave functions, $\Psi_0(N_e \pm 1; \pm\mathbf{q}, m)$, where N_e corresponds to the insulating state with fully occupied bands in the Slater determinant, and $\mathbf{q}m$ denotes the additional particle/ hole orbital, we get

$$\lim_{k\to 0} \rho_{\mathbf{k}}\Psi_0(N_e \pm 1; \mathbf{q}, m) \sim \pm\Psi_0(N_e \pm 1; \mathbf{q}+\mathbf{k}, m) \tag{8.9}$$

for $k \neq 0$, where different signs for particle or hole excitations on the r.h.s. are chosen to match the most common sign convention, e.g., of Ref. [280]. The limit $k \to 0$ is discontinuous since $\rho_{\mathbf{k}=0}\Psi_0(N_e \pm 1; \mathbf{q}, m) \equiv (N_e \pm 1)\Psi_0(N_e \pm 1; \mathbf{q}, m)$.

Kohn [280, 281] has pointed out that in the insulating state, the matrix elements

$$\lim_{\mathbf{q}'\to\mathbf{q}} \langle\Psi_0(N_e \pm 1; \mathbf{q}, m)|\rho_{\mathbf{q}-\mathbf{q}'}|\Psi_0(N_e \pm 1; \mathbf{q}', m)\rangle = \pm\frac{1}{\epsilon} \tag{8.10}$$

approach the inverse dielectric constant, ϵ^{-1}, up to a sign.

Substituting Eq. (8.9) into Eq. (8.10), suggests the following finite-size behavior of the static structure factor of insulators

$$\lim_{k\to 0} S_k^{\pm} = \alpha_{\pm} + \mathcal{O}(k^2), \tag{8.11}$$

$$S_k^{\pm} \equiv (N_e \pm 1)S_{N_e\pm 1}(k) - N_e S_{N_e}(k), \tag{8.12}$$

where $\alpha_{\pm}$ is proportional to ϵ^{-1}. However, $\alpha_{\pm}$ in general differs from ϵ^{-1} unless Eq. (8.9) is an exact equality.

Figure 8.2 shows the behavior of $S_k^{\pm}$ for carbon and silicon crystals. Note that these functions extrapolate to a nonzero value as $k \to 0$.

The long wavelength behavior of the structure factor, Eq. (8.11), then gives rise to size corrections to

excitation energies through the potential energy term

$$\left[\int \frac{d^3k}{(2\pi)^3} - \frac{1}{V}\sum_{\mathbf{k}\neq 0}\right] \frac{v_k}{2} S_k^{\pm} \simeq \alpha_{\pm}\frac{|v_M|}{2}, \tag{8.13}$$

where we have defined the Madelung constant as

$$v_M = \left[\frac{1}{V}\sum_{\mathbf{k}\neq 0} - \int \frac{d^3k}{(2\pi)^3}\right] v_k \sim L^{-1} \sim N_e^{-1/3}. \tag{8.14}$$

For the Coulomb potential, v_M is proportional to L^{-1}, the inverse linear extension of the simulation cell. The negative proportionality constant depends on the boundary conditions, e.g., cell geometry, and can be calculated by the Ewald image technique [282].

8.3.2 Kinetic energy

Following Ref. [30], we now discuss the kinetic energy contribution $\hbar^2[\nabla U]^2/2m$ which arises from electron correlation. For a two-body Jastrow, $U = \sum_{\mathbf{k}} u_k \rho_{\mathbf{k}}\rho_{-\mathbf{k}}/2V$, and we are only interested in the long-wavelength limit, $k \to 0$, of the electron-electron correlation, with wave vectors smaller than the reciprocal lattice vectors of the crystal, $\mathbf{G}$. Isolating the singular contributions involving $\rho_{k=0} \equiv N_e$ in the spirit of the rotating (random) phase approximation (RPA) we have

$$\begin{aligned}\left\langle [\nabla U]^2 \right\rangle &= -\frac{1}{V^2}\sum_{\mathbf{k}\neq 0,\mathbf{k}'\neq 0} (\mathbf{k}\cdot\mathbf{k}') u_k u_{k'} \langle \rho_{\mathbf{k}+\mathbf{k}'}\rho_{-\mathbf{k}}\rho_{-\mathbf{k}'}\rangle \\ &\simeq \frac{1}{V^2}\sum_{\mathbf{k}\neq 0} N_e k^2 u_k^2 \langle \rho_{\mathbf{k}}\rho_{-\mathbf{k}}\rangle. \end{aligned} \tag{8.15}$$

Therefore, for systems with explicit long-range correlations $u_k \sim k^{-2}$, the kinetic energy will also contribute to the leading order size corrections with

$$\left[\int \frac{d^3k}{(2\pi)^3} - \frac{1}{V}\sum_{\mathbf{k}\neq 0}\right] \frac{n_e\hbar^2k^2u_k^2}{2m} S_k^{\pm} \simeq \alpha_{\pm} c\frac{|v_M|}{2}, \tag{8.16}$$

where $c = \lim_{k\to 0} n_e\hbar^2k^2u_k^2/(mv_k)$ is approximately given by the ratio of the $1/N_e$ finite-size corrections of the kinetic to potential energy of the ground state energy per particle due to two-body correlations [60].

8.3.3 Total gap corrections from Coulomb singularity

Up to now, we have shown how the long-range behavior of the structure factor and Jastrow factor can give rise to a $1/L$ correction to the excitation gap with a proportionality factor determined by the structure factor changes. In the following, we will further demonstrate that, given that the trial wave functions coincide with the exact ground-state wave function for N_e and $N_e \pm 1$ electrons, this proportionality factor is indeed given by the dielectric constant

$$\Delta_\infty - \Delta_V = \frac{|v_M|}{\epsilon} + \mathcal{O}\left(\frac{1}{V}\right), \tag{8.17}$$

as phenomenologically assumed in previous work [266, 276].

We prove this by an independent argument based on commutation relations. Let us denote the exact insulating ground state of the N_e electron system as $|\Psi_0^{N_e}\rangle$, its energy as $E_0^{N_e}$, and the exact excited state of the $N_e \pm 1$ electron system as $|\Psi_{\mathbf{k}}^{N_e \pm 1}\rangle$ with energy $E_{\mathbf{k}}^{N_e \pm 1}$; $\mathbf{k}$ indicates that the additional/subtracted electron adds/subtracts the crystal momentum $\mathbf{k}$. We have

$$E_{\mathbf{k}}^{N_e+1} - E_0^{N_e} = \frac{\langle \Psi_{\mathbf{k}}^{N_e+1} | \left[H, a_{\mathbf{k}}^\dagger\right] | \Psi_0^{N_e} \rangle}{\langle \Psi_{\mathbf{k}}^{N_e+1} | a_{\mathbf{k}}^\dagger | \Psi_0^{N_e} \rangle} \tag{8.18}$$

for particle and

$$E_{\mathbf{k}}^{N_e-1} - E_0^{N_e} = \frac{\langle \Psi_{\mathbf{k}}^{N_e-1} | \left[H, a_{\mathbf{k}}\right] | \Psi_0^{N_e} \rangle}{\langle \Psi_{\mathbf{k}}^{N_e-1} | a_{\mathbf{k}} | \Psi_0^{N_e} \rangle} \tag{8.19}$$

for hole excitations. In second quantization, the Hamiltonian, $H = T + V_{ee}$, is given by

$$T = \sum_{\mathbf{k}} \left[\frac{\hbar k^2}{2m} a_{\mathbf{k}}^\dagger a_{\mathbf{k}} + \sum_{\mathbf{G}} u(\mathbf{G}) a_{\mathbf{k}+\mathbf{G}}^\dagger a_{\mathbf{k}} \right], \tag{8.20}$$

$$V_{ee} = \frac{1}{2V} \sum_{\mathbf{q} \neq 0} v_q \left[\rho_{\mathbf{q}} \rho_{-\mathbf{q}} - N_e \right], \tag{8.21}$$

where $a_{\mathbf{k}}$ is the annihilation operator for plane-wave states of wave vector $\mathbf{k}$, $u(\mathbf{G})$ the periodic crystal potential, and v_q is the Coulomb potential between electrons, $\rho_{\mathbf{q}} = \sum_{\mathbf{k}} a_{\mathbf{k}+\mathbf{q}}^\dagger a_{\mathbf{k}}$, and $N_e = \sum_k a_{\mathbf{k}}^\dagger a_{\mathbf{k}}$.

The commutator involving the single-particle energy term is

$$\left[T, a_{\mathbf{k}}^\dagger\right] = \frac{\hbar^2 k^2}{2m} a_{\mathbf{k}}^\dagger + \sum_{\mathbf{G}} u(\mathbf{G}) a_{\mathbf{G}+\mathbf{k}}^\dagger. \tag{8.22}$$

There are corresponding terms for hole excitations, but none of these terms involve singular contributions

responsible for anomalous size effects, so these terms do not contribute at leading order. However,

$$\left[V_{ee}, a_{\mathbf{k}}^{\dagger}\right] = \frac{1}{V}\sum_{\mathbf{q}\neq 0} v_q \left[\rho_{\mathbf{q}} a_{\mathbf{k}-\mathbf{q}}^{\dagger} - 1\right] \tag{8.23}$$

and

$$\left[V_{ee}, a_{\mathbf{k}}\right] = -\frac{1}{V}\sum_{\mathbf{q}\neq 0} v_q \rho_{\mathbf{q}} a_{\mathbf{k}+\mathbf{q}} \tag{8.24}$$

involve terms approaching the Coulomb singularity, $v_q \sim q^{-2} \to \infty$ for $q \to 0$.

From these terms, we get the leading order size corrections by noting that

$$\lim_{\mathbf{k},\mathbf{q}\to 0} \frac{\langle \Psi_{\mathbf{k}}^{N_e+1} | \rho_{\mathbf{q}} a_{\mathbf{k}-\mathbf{q}}^{\dagger} | \Psi_0^{N_e}\rangle}{\langle \Psi_{\mathbf{k}}^{N_e+1} | a_{\mathbf{k}}^{\dagger} | \Psi_0^{N_e}\rangle} = \frac{1}{2}\left[\frac{1}{\epsilon} + 1\right] \tag{8.25}$$

and

$$\lim_{\mathbf{k},\mathbf{q}\to 0} \frac{\langle \Psi_{\mathbf{k}}^{N_e-1} | \rho_{\mathbf{q}} a_{\mathbf{k}+\mathbf{q}} | \Psi_0^{N_e}\rangle}{\langle \Psi_{\mathbf{k}}^{N_e-1} | a_{\mathbf{k}} | \Psi_0^{N_e}\rangle} = -\frac{1}{2}\left[1 + \frac{1}{\epsilon}\right]. \tag{8.26}$$

Both relations can be obtained[1] by extending Kohn's diagrammatic approach [280] (see Supplemental Materials[2]). Integrating around the v_q singularity for small q in Eq. (8.23), we obtain the leading order finite size corrections. As before, this involves the Madelung constant, Eq (8.14). In the particle channel, we get $\frac{|v_M|}{2}\left(\frac{1}{\epsilon} - 1\right)$ and in the hole channel, $\frac{|v_M|}{2}\left(\frac{1}{\epsilon} + 1\right)$. The corrections independent of ϵ correspond to the change in the background charge which cancel for the fundamental gap and we obtain Eq. (8.17).

Previous, heuristic approaches [276] have suggested that one can use experimental or DFT values of the dielectric constant for finite-size extrapolation. Our approach further suggests that this value can be determined from the QMC structure factor extrapolated to zero wave vector

$$\frac{2}{\epsilon} \equiv (1+c) \lim_{N_e\to\infty} \lim_{k\to 0} \left[S_k^{+} + S_k^{-}\right], \tag{8.27}$$

with the singular behavior of the Jastrow factor determining c. We emphasize that the order of the limits involved above is crucial.

An independent estimate is based on the inequality of Eq. (8.7). We can bound and estimate the value

[1] We can adapt the proof of Kohn [280] by noting that the extra particle (hole) propagator does not interact with the other particles before $t = 0$. The equivalent graphs of class I contribute with ± 1 for particle and hole excitations, the equivalent graphs of class IIA remain, contributing $\pm(1/\epsilon - 1)/2$, whereas graphs of class IIB are absent.

[2] See Supplemental Material at http://link.aps.org/supplemental/10.1103/PhysRevB.101.085115 for diagrammatic proof and QMC data.

of dielectric constant using the structure factor of the insulating ground state. By extrapolating $1-\Gamma_k^2$ vs. k to $k=0$ we obtain an upper bound to the inverse dielectric constant, where $\Gamma_k \equiv 2m\omega_p S_{N_e}(k)/\hbar k^2$. This involves only the extensive part of the density-density correlations, thus, it is less sensitive to noise and has much smaller statistical uncertainty. In Fig. 8.3, we show that for C and Si, this inequality gives accurate values of the dielectric constant.

8.3.4 Twist correction of two-particle correlations

The above size effects explain the leading order $1/L$ correction to the single-particle gap. However, as we will see in our results, the asymptotic region, where this law can be reliably applied, may still be difficult to reach for currently used system sizes and next-to-leading order effects are important. Here, we show that an important part can be corrected for, by further restoring the full symmetry properties in the contribution of the direct Coulomb interaction.

For inhomogeneous systems, it is convenient to separate the mean density from its fluctuating components in the static structure factor [30], i.e.,

$$S_{N_e}(\mathbf{k}) = \frac{1}{N_e}\langle\rho_{\mathbf{k}}\rangle\langle\rho_{-\mathbf{k}}\rangle + \delta S_{N_e}(\mathbf{k}), \tag{8.28}$$

$$\delta S_{N_e}(k) = \frac{1}{N_e}\left\langle\left(\rho_{\mathbf{k}} - \langle\rho_{\mathbf{k}}\rangle\right),\left(\rho_{-\mathbf{k}} - \langle\rho_{-\mathbf{k}}\rangle\right)\right\rangle. \tag{8.29}$$

For crystals with periodic density distributions, the Fourier components of the mean density, $\langle\rho_{\mathbf{k}}\rangle$, only contribute for reciprocal lattice vectors, $\mathbf{k}\in\mathbf{G}$. The long wavelength behavior of the structure factor is entirely due to the fluctuating part $\delta S_{N_e}(k)$, which therefore contains the leading order size effects [30]. However, the mean single particle density, $\langle\rho(\mathbf{r})\rangle = V^{-1}\sum_{\mathbf{k}}\langle\rho_{\mathbf{k}}\rangle e^{i\mathbf{k}\cdot\mathbf{r}}$, of the finite system may significantly differ from the infinite one, particularly in cases where the supercell is not compatible with the full symmetry group of the crystal.

Averaging over twisted boundary conditions is designed to restore the symmetry of the crystal, thus accelerate the convergence of single-particle densities to the thermodynamic limit. In the following, we denote the twist averaged expectation value by

$$\overline{\mathcal{O}} \equiv \frac{1}{M_\theta}\sum_\theta \langle\mathcal{O}\rangle_{N_e,\theta}, \tag{8.30}$$

where we have explicitly indicated the N_e and θ dependence on the expectation value on the r.h.s. For any single-particle theory, $\overline{\rho(\mathbf{r})}$ approaches its thermodynamic limit for calculations at fixed N_e by averaging

over a dense grid of twist angles ($M_\theta \to \infty$). Within many-body calculations, twist-averaging [72] takes over a large part of this property to any observable *linear* in the density. Here, we extend this approach to also correct the quadratic expression entering the two-body contributions of the total energy.

For the potential energy, this correction to the twist-converged QMC calculation is

$$\begin{aligned} \delta V^s_{N_e} &= \frac{1}{2V}\sum_{\mathbf{k}} v_k \delta C(\mathbf{k}), \\ & \delta C(\mathbf{k}) = \overline{\rho_{\mathbf{k}}}\,\overline{\rho_{-\mathbf{k}}} - \overline{\rho_{\mathbf{k}}\rho_{-\mathbf{k}}}. \end{aligned} \tag{8.31}$$

For the ground-state energies, this correction provides only a small improvement over our previous correction [30, 62].

For the gap, many terms entering Eqs. (8.31) cancel and the expression can be simplified. Let us consider the case of adding/removing one electron at twist ϕ to the insulating ground state, denoting $\Pi^\pm_{\mathbf{k}}$ the difference of the respective densities:

$$\Pi^\pm_{\mathbf{k}} \equiv \langle \rho_{\mathbf{k}} \rangle_{N_e \pm 1, \phi} - \langle \rho_{\mathbf{k}} \rangle_{N_e, \phi} \tag{8.32}$$

In the thermodynamic limit, the density of the ground-state system with N_e electrons coincides with the twist-averaged ground-state density $\overline{\rho_{\mathbf{k}}}$, whereas we obtain $\overline{\rho_{\mathbf{k}}} + \Pi^\pm_{\mathbf{k}}$ for the density of the $N_e \pm 1$ electron system. Inserting into Eqs. (8.31), we obtain the correction for the difference between the two states,

$$\delta V^s_{N_e \pm 1, \phi} - \delta V^s_{N_e} = \frac{1}{V}\sum_{\mathbf{k}\in\mathbf{G}} v_k \mathrm{Re}\left[(\overline{\rho}_{\mathbf{k}} - \langle \rho_{\mathbf{k}} \rangle_{N_e,\phi})\, \Pi^\pm_{-\mathbf{k}} \right], \tag{8.33}$$

where only wave vectors of the reciprocal crystal lattice contribute to the sum. The corresponding finite size correction for the gap, denoted by $\delta\Delta_s$ in the following, is order $1/N_e$ or smaller, mainly determined by the changes of the ground-state densities at the first Bragg-peaks due to twist averaging.

Equation (8.33) can be understood quite intuitively: It corrects the direct Coulomb interaction between the electron/hole in the excited state ($\Pi^\pm$) with the unexcited electrons. The density of those electrons is expected to change by $\overline{\rho}_{\mathbf{k}} - \langle \rho_{\mathbf{k}} \rangle_{N_e,\phi}$ in the thermodynamic limit.

Converged ground-state densities are naturally calculated within GCTABC. It is straightforward to apply the correction Eq. (8.33) to all excitation energies. Alternatively, the corresponding DFT densities may be used. This removes the stochastic error at the cost of introducing a small bias in the next-to-leading order size correction.

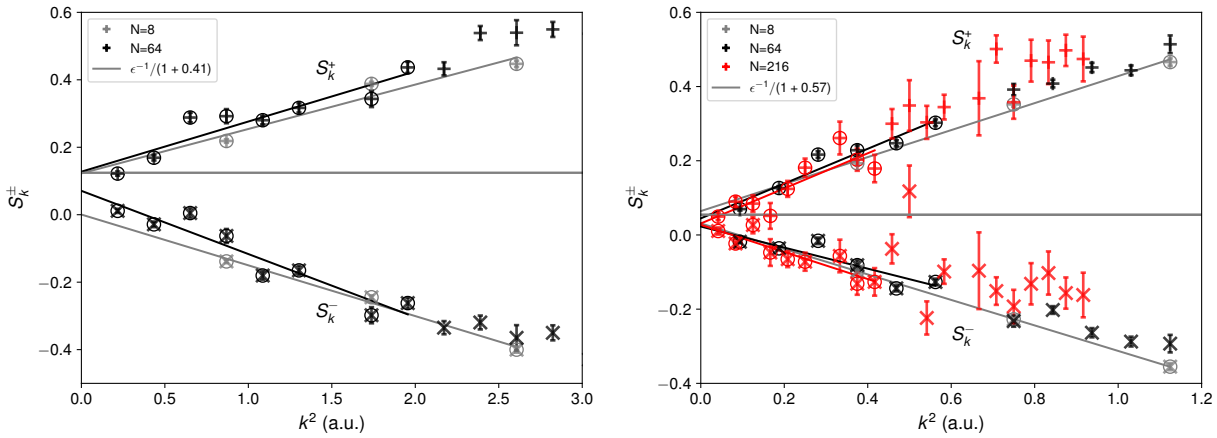

(a) carbon (b) silicon

Figure 8.2: Change in the static structure factor as an electron (upper curves) or a hole (lower curves) is added to the insulating system with N atoms. The lines are fits to the data points. The horizontal lines show the expected $k \to 0$ limit based on the experimental dielectric constants. We have used $c = 0.41$ for C and $c = 0.57$ for Si.

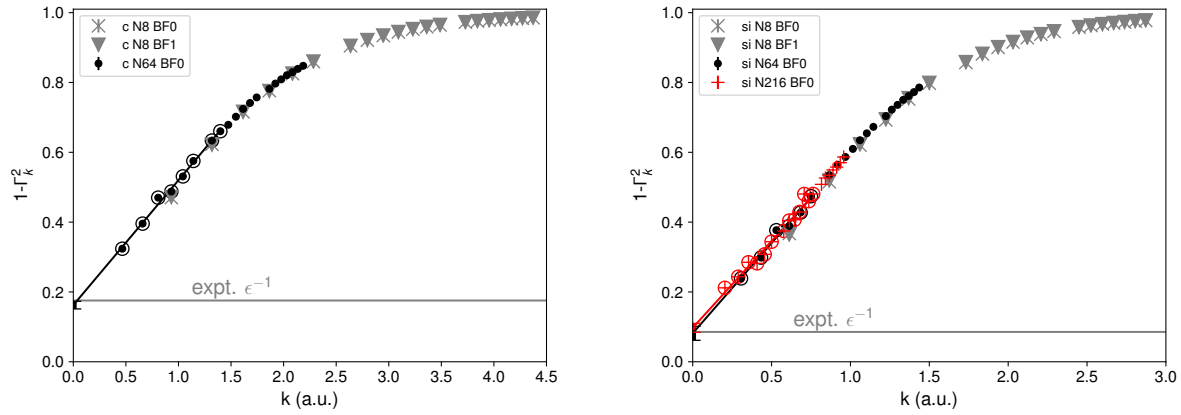

(a) carbon (b) silicon

Figure 8.3: Upper bound to the inverse dielectric constant Eq. (8.7), where $\Gamma_k \equiv \frac{2m\omega_p S_{N_e}(k)}{\hbar k^2}$. Lines are fits to the low-k data. The horizontal lines mark experimental inverse dielectric constants.

8.4 Computational methods

We have performed electronic QMC calculations on three insulating solids: molecular hydrogen at high pressure, and carbon and silicon in the diamond structure at zero pressure. Since we are interested in the spin-neutral charge gap, we used an equal number of spin-up and spin-down electrons. We used a Slater-Jastrow trial wave function with backflow (BF) corrections [10, 31]. The Jastrow and BF functions were fully optimized within variational Monte Carlo, including the long-range (reciprocal lattice) contributions. The orbitals in the Slater determinant were taken from DFT calculations using Quantum Espresso [241, 242]. The carbon and silicon orbitals were generated using the LDA functional, whereas the hydrogen orbitals were generated using the PBE functional, which has been shown to provide a good trial QMC wave function [283, 284].

Molecular hydrogen was placed in the C2/c-24 structure [168] at two different densities ($r_s = 1.38$ and $r_s = 1.34$), roughly corresponding to pressures of 234 GPa and 285 GPa, respectively. Energies and structure factors were obtained from reptation Quantum Monte Carlo calculations using the BOPIMC code [285]. For carbon and silicon, DMC calculations have been performed with the QMCPACK code [244] at the experimentally measured zero pressure valence densities, $r_s = 1.318$ and $r_s = 2.005$, respectively. The crystal structures were optimized by DFT using the vdW-DF1 functional. For hydrogen, the QMC calculations have been done with the bare Coulomb interaction. The PAW pseudo-potential has been used for the DFT results shown in Fig. 8.1. For carbon and silicon, pseudopotentials were used to remove the core electrons: carbon ions modeled by the Burkatzki-Filippi-Dolg pseudopotential [233], and silicon ions by the Trail-Needs pseudopotential [286]. These are considered good pseudo-potentials for correlated calculations, but their use within DFT calculations produces slightly different results from the literature even with the same functional. For hydrogen, we used a supercell with $2 \times 2 \times 1$ primitive cells so the supercell is nearly cubic and contained 96 protons. For carbon, we used two system sizes: the cubic cell containing 8 atoms and a $2 \times 2 \times 2$ supercell containing 64 atoms. For silicon, in addition to these systems, we used a $3 \times 3 \times 3$ supercell containing 216 atoms. For hydrogen, the twist convergence has been achieved using a $8 \times 8 \times 8$ twist grid. For C and Si, the twist grid density decreases with increasing system size. The Supplemental Material [2] contains the QMC calculated energies and variances of the insulating ground states of the various systems obtained after twist averaging and two-body finite size corrections.

8.5 Results

For any effective single-particle theory, such as Kohn-Sham DFT, the densities and energies, $n_e(\mu)$ and $e_0(\mu)$, are obtained by occupying all single-particle states below the chemical potential μ. By construction, the gap, as determined from the incompressible region of $n_e(\mu)$ or from the discontinuity in the derivative of de_0/dn_e (see Fig. 8.1), then coincides with the one obtained from the band structure.

The LDA band gaps of carbon and silicon in the diamond structure are indirect and lie along the ΓX direction where Γ is the origin of the Brillouin zone and X the Brillouin zone boundary in the (100) direction. By looking directly at the highest-occupied molecular orbital (HOMO) and lowest unoccupied molecular orbital (LUMO) states with LDA, it is found that the carbon gap is 3.89 eV and the silicon gap is 0.34 eV. The bands immediately above and below the gap can be fit to a quadratic form which implies $e_0(\mu) = \mu^{\pm} n_e(\mu) + b^{\pm} n_e(\mu)^{5/3}$. Therefore, the derivative $de_0/dn_e = \mu^{\pm} + \frac{5b^{\pm}}{3} n_e^{2/3}$ has a discontinuity at $n_e = 0$ and behaves as $n_e^{2/3}$ above and below the gap. Applying our GCTABC procedure to a single-particle theory, all states with energies below the chemical potential are occupied. Varying the chemical potential thus scans the underlying density of states. The band gap is then determined by locating the band edges, $\mu^{\pm}$, disregarding the location in the Brillouin zone[2]. Figure 8.5 illustrates the density of states obtained from GCTABC giving an LDA gap of 3.95 eV for the carbon gap and 0.38 eV for the silicon gap. The small differences (~ 0.05 eV) from the values obtained before are due to the finite resolution of the twist grid, and can be controlled by using denser grids.

As can be seen in the same figure, the effective band edge densities of states from GCTABC-DMC have a similar functional form, but with a larger gap than the DFT ones. The QMC computed gaps for the different sizes of the supercell are summarized in table 8.1. The results from different supercells clearly show the important bias on gap introduced by the finite size of the supercell. In Fig. 8.4, we show the bare gap, Δ_N, the Madelung-corrected one, $\Delta_N + |v_M|/\epsilon$, and our best correction, $\Delta_\infty = \Delta_N + |v_M|/\epsilon + \delta\Delta_s$, for both systems against the linear size of the supercell, where N is the number of atoms in the supercell and ϵ is the experimental value of the dielectric constant. We see that the next-to-leading-order corrections are comparable to the leading-order one, in particular for the 8-atom supercell of Si, whereas they rapidly decay for the larger sizes.

The finite-size corrected values, Δ_∞, of all different sizes C and Si supercells agree with each other within the statistical uncertainty, yielding the DMC-SJ values $\Delta_\infty = 6.8(1)$ and $\Delta_\infty = 1.8(1)$ for the C and Si gap, respectively. We further note, that these values also agree with a numerical $N^{-1/3}$ extrapolation of the gap

[2]The reciprocal space information is not lost. By keeping track of the Bloch momentum of the states we can determine the locations of the HOMO and LUMO, but that has not been done here.

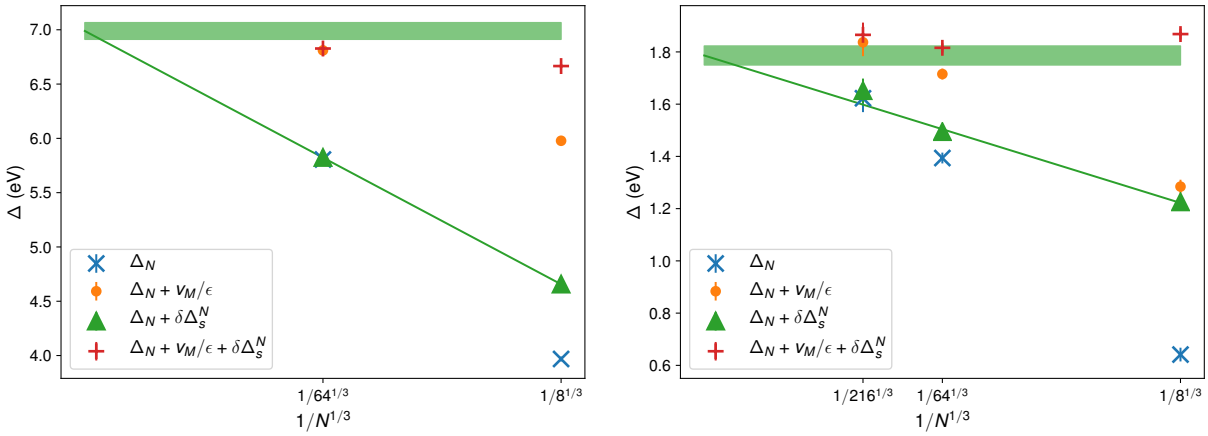

(a) carbon (b) silicon

Figure 8.4: Fundamental gap before and after finite-size corrections. Δ_N is the DMC gap from a simulation with N atoms in the supercell without any finite-size correction, v_M/ϵ is the leading-order Madelung correction using the experimental value of ϵ^{-1}, $\delta\Delta_s^N$ is the next-to-leading-order density correction, which is related to the static part of the structure factor. The line is a fit to $\Delta_N + \delta\Delta_s^N$.

values corrected by $\delta\Delta_s$. For any numerical $N^{-1/3}$ extrapolation, it is very important to reduce any bias due to higher order corrections as much as possible, since the outcome of a fit is sensitive to the smallest system sizes since they have the smallest statistical uncertainty. For Si, a $N^{-1/3}$ extrapolation of the bare Δ_N values yields an overestimation of 0.3 eV compared to Δ_∞.

Since our finite-size corrected gaps show size convergence for the smallest system size, it is now feasible to address the systematic error due to the fixed node approximation. To reduce this bias, we have added BF correlations in the Slater orbitals. Our BF correlations lower the SJ gap by 0.1 eV for both, C and Si. Previous BF calculations [276] on Si have reported a 0.2 eV lowering compared to SJ. The difference might be due to a different functional form or optimization procedure. A systematic study on the bias of the fixed-node approximation such as done with more general BF correlations [287, 288] or multi-determinant trial wave functions [289], possible for small supercells, could be done in the future.

So far, in our analysis of C and Si, we have imposed the experimentally known dielectric constant in the leading order Madelung correction. As described in Sec. 8.3, there is no need for any external knowledge to perform the size extrapolation as the value of the Madelung correction can be obtained from the behavior of the static structure factor, calculable within the same QMC run, see Figs. 8.2 and 8.3. However, since the extrapolation involved introduces an additional uncertainty, we have preferred to use the experimental values to benchmark our theory and better distinguish leading from next-to-leading order size effects.

Using the dielectric bound Eq. (8.7) on the ground-state structure factor to determine ϵ, we get $\epsilon_0 = 6.2 \pm 0.4$ for C and $\epsilon_0 = 10.3 \pm 1.3$ for Si, which are compatible with the experimental values of 5.7 and 11.7.

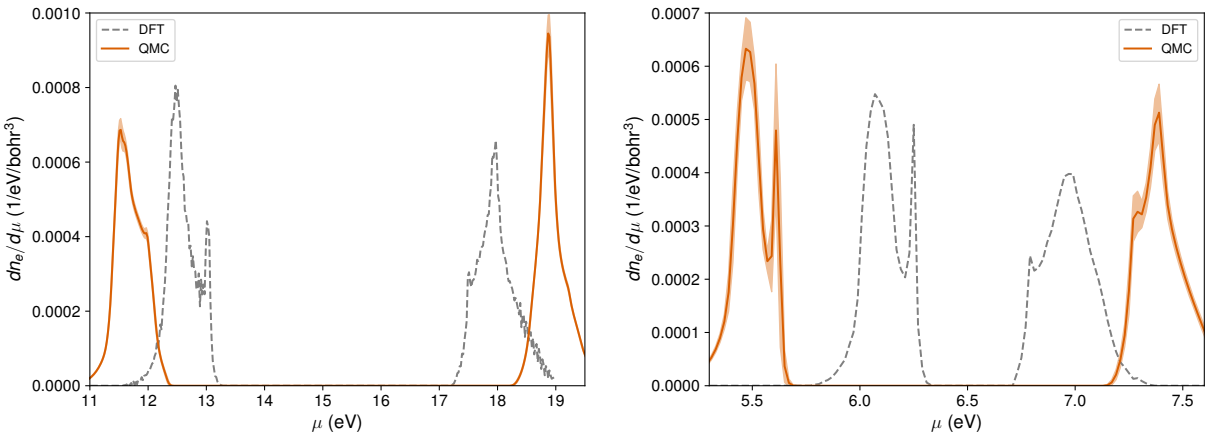

(a) carbon (a) silicon

Figure 8.5: Density of states for carbon and silicon near the band edge. Each plot shows the derivative of the mean electron density with respect to the chemical potential. This is the electronic density of states (DOS) in DFT, so the gap appears as a depleted region. The calculated DOS is only valid near the band edge because only the two bands closest to the gap are considered within DFT and QMC. The DFT bands (done in a primitive cell) have been folded into the Brillouin zone (BZ) of the 64-atom supercell to allow comparison with QMC.

The corresponding leading-order finite-size corrections on the gap of the 64-atom system are then 0.92 ± 0.06 eV for C and 0.36 ± 0.14 eV for Si using the *ab initio* ϵ^{-1}, as opposed to 1.00 eV for C and 0.32 eV for Si based on the experimental values of ϵ^{-1}.

As shown in Fig. 8.2, the asymptotic values of the finite-sized structure factors, $S_k^{\pm}$, are affected by a much larger uncertainty, introducing larger systematic bias when used for *ab-initio* size corrections. Still, already the extrapolation to a non-zero value fixes the leading order size corrections to decay as $1/L$. This information alone can be crucial as calculations for only two different supercell sizes will be sufficient to determine size effects, whereas more supercell sizes would be needed if the asymptotic form was not known.

We have also computed the band gap of solid hydrogen using GCTABC in BF-RQMC calculations for one of the possible molecular structures predicted for phase III: C2/c-24 at $r_s = 1.38$ and $r_s = 1.34$ (roughly corresponding to pressures of 234 and 285 GPa, respectively). The results, in Table 8.1, show that the gap and size effects decrease with increasing pressure. For these calculations, we use calculations for one supercell and use its structure factor to estimate the dielectric constant. From Fig. 8.1, we see that HSE DFT slightly underestimates the gap; however, the deviations from the plateau on both sides are quite similar.

Table 8.1: Energy gaps obtained from GCTAB QMC in eV. The bare gap, Δ_N, was calculated from Eq. (8.1) for a finite supercell containing N atoms. The leading-order finite-size corrections are given by the screened Madelung constants $|v_M|/\epsilon$, the next-to-leading order by the twist correction of two particle density correlations, $\delta\Delta_s$. We used the experimental value of ϵ for C and Si (5.7 and 11.7, respectively) and the value 18.8 for H_2 extracted from S(k). Finite-size corrections were also applied to the band edges, $\mu^{\pm}$. The estimate of the gap in the thermodynamic limit is $\Delta_\infty = \Delta_{N_e} + |v_M|/\epsilon + \delta\Delta_s$. From our LDA analysis, we estimate a systematic bias of ~ 0.1 eV from the finite twist grid. This bias is larger than the statistical error. SJ indicates Slater-Jastrow trial wave function, while BF indicates backflow. The lattice constants of carbon and silicon are 3.567 Å and 5.43 Å, respectively.

	r_s	N	Δ_N	$\lvert v_M\rvert/\epsilon$	$\delta\Delta_s$	μ^-_∞	μ^+_∞	Δ_∞
H_2 (BF)	1.38	96	3.3(1)	0.40	0.020	6.9(1)	10.7(1)	3.8(1)
	1.34	96	2.4(1)	0.20	0.018	8.6(1)	11.2(1)	2.6(1)
C (BF)	1.318	8	3.9(1)	2.01	0.69	11.5(1)	18.1(1)	6.6(1)
C (SJ)	1.318	8	4.0(1)	2.01	0.69	11.5(1)	18.2(1)	6.7(1)
		64	5.8(1)	1.00	0.02	11.9(1)	18.7(1)	6.8(1)
Si (BF)	2.005	8	0.6(1)	0.64	0.55	5.2(1)	6.9(1)	1.7(1)
Si (SJ)	2.005	8	0.6(1)	0.64	0.58	5.2(1)	7.0(1)	1.9(1)
		64	1.4(1)	0.32	0.08	5.5(1)	7.3(1)	1.8(1)
		216	1.6(1)	0.21	0.01	5.6(1)	7.4(1)	1.8(1)

8.6 Comparison with experiment

Our best values for the fundamental electronic gap (BF-DMC) significantly overestimate the experimentally measured values for C and Si by 1.1 and 0.5 eV, respectively as shown in Table 8.2. There are two main sources of systematic errors which need to be taken into account: the use of pseudo-potentials and the neglect of electron-phonon coupling.

The QMC values for C and Si presented above are based on pseudo-potentials to replace the core electrons of the atoms. Pseudo-potentials are usually designed for accurate prediction of static structural quantities. Excitation spectra, in particular, the single-particle excitation gap, may be less well described. This has been found in many-body perturbation theory calculations within the *GW* framework where all-electron calculations have been shown to lower the gap of C and Si by ~ -0.3 eV [290, 291] with respect to pseudo-potentials calculations. Although the actual pseudo-potentials of our QMC simulations differ from those used in the *GW* calculations, we expect that our QMC values will be shifted by a similar amount; we can roughly transfer the all-electron correction of *GW* to our QMC results.

For lighter atoms, electron-phonon coupling leads to a further reduction of the gap values, even at zero temperature, due to the presence of zero point motion of the ions in the crystal. For C, *GW* predicts a significant lowering of the gap by -0.6 eV [292], whereas a smaller shift between -60 meV [293] and -0.1 eV [294] is expected from DFT for Si. The effect of thermal expansion is to lower the gap by about 0.01 eV at room temperature for both carbon [293, 295] and silicon [169, 296], beyond the resolution of present

Table 8.2: Extrapolated band gap of Si and C from backflow DMC calculations, Δ_{BF} compared to the experimental values (exp). We tabulated two main corrections: the difference between the gap of an all-electron (AE) and the pseudo-potential (PP) calculation within GW calculations, and the neglect of electron-phonon coupling (e-ph).

	Δ_{BF}	AE - PP	e-ph	exp
C	6.6(2)	-0.26 (G_0W_0) [291]	-0.6 (GW) [292]	5.48 [299]
Si	1.7(1)	-0.25 (G_0W_0)[291]	-0.06 (DFT) [293]	1.17 [299]

calculations.

Considering both, the bias due to the pseudo-potential approximation and the neglect of electron-phonon coupling, our BF-DMC calculations for C and Si overestimate the gap by $\sim 0.1 - 0.2$ eV (see Table 8.2), larger than our statistical uncertainty. This remaining offset to experiment may either be due to residual bias of the fixed-node approximation, or due to effects in pseudo-potential and e-ph coupling beyond our simple estimations based on GW and DFT. They could be addressed by more accurate calculations in the future.

For hydrogen, we do not compare to experiment since electron-phonon coupling is expected to be very large, and the experimental results are not precise. If we do not make size corrections, our results are comparable to the Slater-Jastrow DMC calculations of Ref. [278] where the DFT band structure was corrected by a "scissor operator" based on QMC runs at the Γ point of the supercell. However, no size effects were observed within the statistical error in Ref. [278], so their extrapolated results differ from ours by $0.3 - 0.8$ eV (3.0 and 2.3 eV for 250 and 300 GPa). Comparison to GW values are also not conclusive: Whereas Ref. [297] provides smaller values of the gaps (1.8 and 1.0 eV for 250 and 300 GPa), the results of Ref. [2] (3.7 and 2.8 eV for 250 and 313 GPa) are close to our predictions. However, we note that the GW calculations were done with slightly different crystal structures. In Ref. [297], the PBE functional was used to optimize the lattice structure in contrast to the vdW-DF1 functional of Ref. [2], shown to be the most accurate functional at this density [298]. The smaller gap can then be seen as a consequence of a larger bond length as it was shown that structures optimized with PBE functional have a larger bond length than the ones with vdW-DF1 [2]. We have recently completed a more detailed analysis of the band gap of molecular hydrogen [18] using the method introduced here. This discusses extension to disorder coming from nuclear quantum and thermal effects.

8.7 Conclusions

We have introduced a method to calculate the fundamental gap of insulators and semi-conductors using QMC. Using grand-canonical twist averaging, the value of the gap can be determined at any point in the Brillouin zone whether the system has a direct or indirect gap. Although it is possible to map out the whole band structure, we have focused on the minimal, fundamental gap in this work. We have shown that for charged systems, finite size supercell calculations are necessarily biased by a finite size error decaying as $1/L$, where the prefactor is determined by the absolute value of the Madelung constant and the inverse dielectric constant. We have pointed out that the $1/L$ functional form is encoded in the long wavelength behavior of the finite size structure factor extrapolating to a non-vanishing value at the origin. Next-to-leading order effects can be corrected by proper use of twist-averaging in the two-particle part of the static Coulomb potential.

We have applied this procedure to determine the fundamental gap of molecular hydrogen at high pressure and carbon and silicon in the diamond structure at zero pressure. Our finite-size corrected gap values for carbon and silicon are larger than the experimental ones. We have argued that the bias may be due to the pseudo-potential approximation and the neglect of electron-phonon coupling.

We note that this procedure is not restricted to QMC calculations, but can be applied within any method which calculates the many-body wave functions and ground-state energies, e.g., for coupled cluster methods [261]. Our results for C and Si demonstrate that the bias due to the finite size supercell can be corrected for, so precise values in the thermodynamic limit can be obtained for small supercells without need for numerical extrapolation.

The procedure here has been developed for perfect crystals but can be generalized to systems with disorder, either due to thermal or quantum effects. Furthermore, the procedure provides a starting point to address optical, i. e., charge neutral excitations. Although neutral excitations are expected to be less sensitive to finite-size effects, recent calculations [275, 276] have observed the same slow $1/L$ decay for the optical gap. Since it is often not practical to perform calculations for more than two significantly different supercell sizes, our method suggests that the asymptotic behavior of the structure factor provides the needed insight to whether $1/L$ or $1/L^3$ should be used as a functional form for the size extrapolation.

Appendices

Appendix A

Nonadiabatic Coupling

The electron-ion problem can be made more tractable at the cost of a physically motivated Born-Oppenheimer approximation (BOA). I define the BOA at the end of this section, but first lay out the exact formulation in eq. (A.4) so that the content of the approximation is clear. Ions move much slower than electrons due to their heavy mass ($m_I \approx 10^3$ to $10^5 m_i$), so it is sensible to isolate the ionic degrees of freedom and consider the electronic part separately. The coupling between the ionic and electronic problems is presumably weak because of the separation of timescales.

$$\hat{H} = -\sum_I \frac{\hbar^2}{2m_I}\nabla_I^2 + \hat{\mathcal{H}}(\boldsymbol{R}; \boldsymbol{R}_I), \tag{A.1}$$

where $\hat{\mathcal{H}}$ is the clamped-ion or electronic hamiltonian, which typically defines the ultimate goal of an electronic structure method. The semicolon in $\hat{\mathcal{H}}(\boldsymbol{R}; \boldsymbol{R}_I)$ indicates that the electronic hamiltonian is only parametrically dependent on the ion positions $\boldsymbol{R}_I$. M. Born and R. Oppenheimer (BO) [300] first utilized this separation of timescales to study diatomic molecules in 1927. As explained around eq. (27) and (28) in Ref. [300], BO expressed the electronic hamiltonian as a Taylor expansion around the equilibrium positions of the ions. They discussed results using the first four leading order terms in the vibration amplitude of the ions. Thus, what we define as "the" BOA can be ambiguous. Here, I follow the interpretation by G. A. Worth and L. S. Cederbaum [9], which is equivalent to assuming a product ansatz eq. (A.7), but without a "diagonal correction".

If one can obtain the eigenstates of the electronic hamiltonian $\{\psi_k\}$ at any ion configuration $\boldsymbol{R}_I$

$$\hat{\mathcal{H}}(\boldsymbol{R}; \boldsymbol{R}_I)\psi_k(\boldsymbol{R}; \boldsymbol{R}_I) = E_k(\boldsymbol{R}_I)\psi_k(\boldsymbol{R}; \boldsymbol{R}_I), \tag{A.2}$$

then one can expand an eigenstate of the full hamiltonian $\hat{H}$ in the basis of electronic eigenstates

$$\Psi_l(\boldsymbol{R}, \boldsymbol{R}_I) = \sum_{k=0}^{\infty} \chi_{lk}(\boldsymbol{R}_I)\psi_k(\boldsymbol{R}; \boldsymbol{R}_I), \tag{A.3}$$

where the expansion coefficients $\chi_{lk}(\boldsymbol{R}_I)$ will later be identified with the ionic wave function in the Born-Oppenheimer approximation. l runs over the full electron-ion hamiltonian's eigenstates, which can have both ionic (vibrational) and electronic characters. The coefficient for one of these *vibronic* states cannot be determined separately for each electronic level k in general. To see this, substitute the $l = 0$ expansion eq. (A.3) into the time-dependent Schrödinger equation for the full electron-ion hamiltonian (drop l for simplicity)

$$
\begin{aligned}
\left(\hat{\mathcal{H}} - \sum_I \frac{\hbar^2}{2M_I}\nabla_I^2\right)\left(\sum_k \chi_k\psi_k\right) &= i\hbar\frac{d}{dt}\left(\sum_k \chi_k\psi_k\right) \Rightarrow \text{apply operators} \\
\sum_k E_k\chi_k\psi_k - \sum_I \frac{\hbar^2}{2M_I}\left(\nabla_I^2\chi_k\psi_k + 2\boldsymbol{\nabla}_I\chi_k\cdot\boldsymbol{\nabla}_I\psi_k + \chi_k\nabla_I^2\psi_k\right) &= \sum_k i\hbar\dot{\chi}_k\psi_k \Rightarrow \text{apply } \int\psi_j^* \\
\sum_k E_k\chi_k\delta_{jk} - \sum_I \frac{\hbar^2}{2M_I}\left(\nabla_I^2\chi_k\delta_{jk} + 2\boldsymbol{\nabla}_I\chi_k\cdot\boldsymbol{F}_{jk} + \chi_k G_{jk}\right) &= \sum_k i\hbar\dot{\chi}_k\delta_{jk} \Rightarrow \text{perform } \sum_k \\
\left(-\sum_I \frac{\hbar^2}{2M_I}\nabla_I^2 + E_j\right)\chi_j - \left(\sum_k\sum_I \frac{\hbar^2}{2M_I}\left(2\boldsymbol{F}_I^{jk}\cdot\boldsymbol{\nabla}_I + G_I^{jk}\right)\chi_k\right) &= i\hbar\dot{\chi}_j, \qquad \text{(A.4)}
\end{aligned}
$$

where the matrix elements for gradient (derivative-coupling terms) and laplacian (scalar-coupling terms) in the electronic eigenstates basis are

$$
\begin{cases}
\boldsymbol{F}_I^{jk} = \int d\boldsymbol{r}\psi_j^*(\boldsymbol{r};\boldsymbol{R})\boldsymbol{\nabla}_I\psi_k(\boldsymbol{r};\boldsymbol{R}) \\
G_I^{jk} = \int d\boldsymbol{r}\psi_j^*(\boldsymbol{r};\boldsymbol{R})\nabla_I^2\psi_k(\boldsymbol{r};\boldsymbol{R})
\end{cases}. \qquad \text{(A.5)}
$$

The matrix elements that couple different electronic states in eq. (A.4) are named *nonadibatic coupling operators* by Worth and Cederbaum [9]

$$
\Lambda_{jk} = \sum_I \frac{\hbar^2}{2M_I}\left(2\boldsymbol{F}_I^{jk}\cdot\boldsymbol{\nabla}_I + G_I^{jk}\right). \qquad \text{(A.6)}
$$

Every term in Λ_{jk} has an inverse ion mass prefactor $\frac{\hbar^2}{2M_I}$, so they are expected to be small in most cases. There are two common approximations of Λ_{kj}, the first is to set the entire matrix to zero, the second is to set only the off-diagonal terms to zero. Both approximations decouple (A.4), allowing the complete separation of electronic and ionic motions. Many different and sometimes conflicting names have been given to these two approximations including Born-Huang, Born-Oppenheimer and adiabatic approximation. To fix nomenclature, I will call the all-zero approximation, $\Lambda_{jk} = 0,\ \forall j,k$, the Born-Oppenheimer approximation (BOA). The diagonal terms Λ_{jj} are considered diagonal Born-Oppenheimer correction (DBOC). Non-zero off-diagonal elements are responsible for *nonadiabatic effects*.

The ground state in the BOA is a product of an ionic and an electronic component

$$\Psi_{lk}^{BO}(\boldsymbol{R}, \boldsymbol{R}_I) = \chi_{lk}(\boldsymbol{R}_I)\psi_k(\boldsymbol{R}; \boldsymbol{R}_I), \tag{A.7}$$

where a set of vibrational states labeled by l can be defined over a particular electronic state k. $\chi_l(\boldsymbol{R}_I)$ obeys its own Schrödinger equation on an effective potential energy surface provided by an eigenvalue of the electronic hamiltonian $E_k(\boldsymbol{R}_I) = \langle\psi_k|\hat{\mathcal{H}}|\psi_k\rangle$, a.k.a. the Born-Oppenheimer potential energy surface (BO-PES)

$$\left(-\sum_I \frac{\hbar^2}{2M_I}\nabla_I^2 + E_k\right)\chi_l = i\hbar\dot{\chi}_l. \tag{A.8}$$

Once the ionic eigenstates are obtained by diagonalizing eq. (A.8), the total energy of the electron-ion system is finally obtained as

$$E_{lk}^{BO} \equiv \langle\chi_l|E_k - \sum_I \frac{\hbar^2}{2M_I}\nabla_I^2|\chi_l\rangle\,. \tag{A.9}$$

E_{00}^{BO} differs in two ways from the electronic ground-state energy

$$E_0 \equiv \langle\psi_0|\hat{\mathcal{H}}|\psi_0\rangle\,(\boldsymbol{R}_I), \tag{A.10}$$

which is a function of the positions of the ions $\boldsymbol{R}_I$. First, in E_{00}^{BO} the electronic energy is averaged over a distribution of ion configurations $|\chi_0|^2(\boldsymbol{R}_I)$ rather than evaluated at one fixed configuration $\boldsymbol{R}_I$. This quantum delocalization effect raises the total energy from the bottom of the BO-PES $\boldsymbol{R}_I^e = \underset{\boldsymbol{R}_I}{\operatorname{argmin}}\, E_0(\boldsymbol{R}_I)$, which would have been the electron-ion ground state if the ions were classical. Second, the ions have kinetic energy even at absolute zero, which also contributes a positive term to the total energy. The difference between the electron-ion ground-state energy and the electronic one is the zero-point energy (ZPE). In the BOA, ZPE contains only two terms from delocalization and kinetic energy of the ions.

Within the BOA framework, solving the electron-ion problem for a particular combination of vibrational l and electronic state k involves finding the k^{th} eigenvalue of the clamped-ion electronic problem $\mathcal{H}(\boldsymbol{R}; \boldsymbol{R}_I)$ for many ion configuration $\boldsymbol{R}_I$. There are established first-principle molecular dynamics and Monte Carlo methods for achieving this, but they are not practical for even moderately sized system, e.g., O(1000) atoms, because the computational cost of electronic structure methods generally scale as N^3 or worse.

The main short-fall of the BOA is its lack of pathways for the ions to transfer energy to the electrons. This

is critical in the study of radiation damage, where a fast moving ion can transfer energy to both the electrons and the ions in a material. Further, for chemical reactions involving vibration-assisted bond breaking, the BOA reduces the number of pathways dissociation can happen, thereby resulting in an incomplete description. The BOA can also break down if the electrons interact with a particle much lighter than an atomic nucleus such as a positron or a muon. Finally, the nonadiabatic coupling terms can diverge when two electronic states cross, e.g., at a conical intersection. Thus, it is sometimes important to go beyond the BOA.

There are two small parameters that control the scale of nonadiabatic coupling eq. (A.6). One is clearly the inverse ionic mass $\frac{1}{M_I}$, while the other is the difference between electronic energy levels $\epsilon_j - \epsilon_k$. This can be seen from an explicit form of $\boldsymbol{F}_I^{jk} \equiv \langle\psi_j|\boldsymbol{\nabla}_I|\psi_k\rangle$ in the derivative-coupling term. Consider the effect of ion motion on the electronic problem, i.e., take $\boldsymbol{\nabla}_I$ of the time-independent electronic Schrödinger equation

$$\begin{aligned}
&\boldsymbol{\nabla}_I(\hat{\mathcal{H}}\psi_k) = \boldsymbol{\nabla}_I(\epsilon_k\psi_k) \Rightarrow \psi_k\boldsymbol{\nabla}_I\hat{\mathcal{H}} + \hat{\mathcal{H}}\boldsymbol{\nabla}_I\psi_k = \psi_k\boldsymbol{\nabla}_I\epsilon_k + \epsilon_k\boldsymbol{\nabla}_I\psi_k \Rightarrow \text{apply } \int \psi_j^* \\
&\left(\int \psi_j^*\psi_k\boldsymbol{\nabla}_I\hat{\mathcal{H}}\right) + \epsilon_j\boldsymbol{F}_I^{jk} = \boldsymbol{\nabla}_I\epsilon_k\delta_{jk} + \epsilon_k\boldsymbol{F}_I^{jk} \Rightarrow \text{solve for } \boldsymbol{F}_I^{jk} \\
&\boldsymbol{F}_I^{jk} = \frac{\langle\psi_j|\boldsymbol{\nabla}_I\hat{\mathcal{H}}|\psi_k\rangle + \boldsymbol{\nabla}_I\epsilon_k\delta_{jk}}{\epsilon_k - \epsilon_j}.
\end{aligned} \tag{A.11}$$

If the electronic eigenstates are defined to be orthonormal, then the real part of the derivative-coupling vectors vanish $(\boldsymbol{F}_I^{kj})^* + \boldsymbol{F}_I^{jk} = \boldsymbol{0} \Rightarrow \text{Re}[\boldsymbol{F}_I^{jk}] = 0$ as derived in eq. (A.12).

$$\begin{aligned}
&\begin{cases} \boldsymbol{F}_I^{jk} = \langle\psi_j|\boldsymbol{\nabla}_I\psi_k\rangle \\ \langle\psi_j|\psi_k\rangle = \delta_{jk} \end{cases} \Rightarrow \boldsymbol{\nabla}_I\langle\psi_j|\psi_k\rangle = \boldsymbol{0} \Rightarrow \\
&\langle\boldsymbol{\nabla}_I\psi_j|\psi_k\rangle + \langle\psi_j|\boldsymbol{\nabla}_I\psi_k\rangle = (\boldsymbol{F}_I^{kj})^* + \boldsymbol{F}_I^{jk} = \boldsymbol{0}.
\end{aligned} \tag{A.12}$$

$\boldsymbol{F}_I^{kj}$ can be interpreted as follows: the motion of the ions apply an imaginary "force" $\langle\psi_j|\boldsymbol{\nabla}_I|\psi_k\rangle$ that drives an electronic transition from state k to state j. This interpretation has led to surface hopping methods for classical and quantum ions [301, 302], which have been applied successfully to describe proton transfer and proton-coupled electron transfer reactions [303]. Further, this "force" is inversely proportional to the energy separation between the two eigenstates. The derivative-coupling term is considered more interesting than the scalar-coupling term due to its potential divergence as $\epsilon_k \to \epsilon_j$.

If the wave function is real, then there is no derivative coupling within the same electronic state $\boldsymbol{F}_I^{jj} = \langle\psi_j|\boldsymbol{\nabla}_I\psi_j\rangle = \langle\boldsymbol{\nabla}_I\psi_j|\psi_j\rangle = (\boldsymbol{F}_I^{jj})^* \Rightarrow \boldsymbol{F}_I^{jj} = \boldsymbol{0}$. In this case, the DBOC is simply the expectation value of

the ion kinetic operator in the electronic state

$$\Lambda_{jj} = \sum_I \frac{\hbar^2}{2M_I} G_I^{jj} = \int \psi_j^* \sum_I \frac{\hbar^2}{2M_I} \nabla_I^2 \psi_j = \langle \hat{T}_I \rangle_j \,. \tag{A.13}$$

The diagonal correction for the hydrogen molecule was studied extensively by Kolos and Wolniewicz [34, 304, 305]. For the atomization energy of H_2, the DBOC was found to be 4.947 cm^{-1}, which is only a 0.0129% correction of its clamped-ion value of 38292.7 cm^{-1}. The nonadiabatic contribution to ionization and atomization energies of a few atoms and small molecules are explored in Ref. [306] and references therein.

Appendix B

Minimum-basis H_2

To derive the Hartree-Fock equations, we use a Slater determinant to evaluate the total energy, then minimize it. Consider N spinless fermions, labeled using $i, j, k, \ldots$, in N orbitals $\chi_a, \chi_b, \ldots, \chi_N$. Given determinant wavefunction $|\Psi_0\rangle = |\chi_a \chi_b \ldots \chi_N\rangle$ and electronic Hamiltonian made up of only one- and two-electron terms $\mathcal{H} = \sum_{i=1}^{N} h(i) + \sum_{i=1}^{N} \sum_{j>i}^{N} v(i,j)$. The total energy is

$$E = \sum_{a=1}^{N} [a|h|a] + \frac{1}{2} \sum_{a,b=1}^{N} [aa|bb] - [ab|ba], \tag{B.1}$$

where $[a|h|a]$ denotes, and $[aa|bb]$ denotes [307].

Constraint minimization of eq. (B.1) with the extra requirement that each spin orbital is doubly occupied leads to the restricted Hartree-Fock (RHF) Fock operator. Its first $N/2$ eigenvectors are the spin orbitals in the lowest-energy Slater determinant. The lowest energy value can be obtained by a weighted sum of its eigenvalues according to the occupation of the spin orbitals.

Instead of starting with the tedious derivation of the Fock operator and its iterative numerical solver, I will first show a concrete application of RHF to minimum-basis hydrogen molecule (H_2). On p. 140 of A. Szabo and N. S. Ostlund, the restricted Fock operator in any basis $\{\phi_\mu\}$ is written as

$$F_{\mu\nu} = H_{\mu\nu}^{\text{core}} + \sum_{a=1}^{N/2} 2(\mu\nu|aa) - (\mu a|a\nu), \tag{B.2}$$

where a labels molecular orbitals, which are eigenstates of the Fock operator. We immediately note that the Fock operator is a peculiar one-electron operator that depends on its own eigenstates. A self-consistent solution to $F_{\mu\nu}$ typically involves guessing, checking and iterating.

$H_{\mu\nu}^{\text{core}}$ is the one-electron part of the Hamiltonian expressed in the given basis

$$H_{\mu\nu}^{\text{core}} = \int d\boldsymbol{r}_1 \phi_\mu^*(\boldsymbol{r}_1) \left(-\frac{1}{2}\nabla_1^2 - \sum_A \frac{Z_A}{|\boldsymbol{r}_1 - \boldsymbol{R}_A|} \right) \phi_\nu(\boldsymbol{r}_1). \tag{B.3}$$

The two-electron integral notation $(\mu\nu|\lambda\sigma)$ is defined by eq. (3.155) in Szabo

$$(\mu\nu|\lambda\sigma) = \iint d\boldsymbol{r}_1 d\boldsymbol{r}_2 \phi_\mu^*(\boldsymbol{r}_1)\phi_\nu(\boldsymbol{r}_1)\frac{1}{|\boldsymbol{r}_1 - \boldsymbol{r}_2|}\phi_\lambda^*(\boldsymbol{r}_2)\phi_\sigma(\boldsymbol{r}_2). \tag{B.4}$$

The first term in the sum of eq. (B.9)

$$J_{\mu\nu} \equiv (\mu\nu|aa) \tag{B.5}$$

is often called the Coulomb or direct operator, because it describes the Classical density-density interaction of charged particles having density distribution $\phi_a^*(\boldsymbol{r}_2)\phi_a(\boldsymbol{r}_2)$. The second term

$$K_{\mu\nu} \equiv (\mu a|\nu a) \tag{B.6}$$

is the exchange operator and has no classical interaction. The exchange-correlation contribution to the Fock matrix is sometimes called the Hartree-Fock effective potential operator

$$V_{\mu\nu}^{\text{eff}} \equiv 2J_{\mu\nu} - K_{\mu\nu}. \tag{B.7}$$

Suppose each molecular orbital a is written as a linear combination of the basis functions

$$\psi_a = \sum_{\mu=1}^{K} C_{\mu a}\phi_\mu, \tag{B.8}$$

then the Fock operator can be written as (from Roothaan equations)

$$F_{\mu\nu} = H_{\mu\nu}^{\text{core}} + \sum_{\lambda\sigma} P_{\lambda\sigma}\left[(\mu\nu|\sigma\lambda) - \frac{1}{2}(\mu\lambda|\sigma\nu)\right], \tag{B.9}$$

where $P_{\lambda\sigma} = 2\sum_{a=1}^{N/2} C_{\lambda a}C_{\sigma a}^*$ is the density matrix of the trial states.

Conceptually, the simplest approach would be to use the ground-state wavefunctions of the two hydrogen atoms as the basis for the hydrogen molecule. We can guess the ground-state wavefunction of the hydrogen molecule. First, the spins of the two electrons anti-align, so they are distinguishable particles. Second, due to symmetries imposed by the two protons, the ground state must be equal superposition of the two basis functions. Third, the lowest-energy solution has no node. Therefore, the ground state of H_2 in the minimum

basis is

$$\psi_1 = [2(1+S_{12})]^{-1/2}\,(\phi_1+\phi_2)\,, \tag{B.10}$$

where $S_{12} = \langle\phi_1|\phi_2\rangle$. That is $C_{11} = C_{21} = [2(1+S_{12})]^{-1/2}$

$$P_{\lambda\sigma} = [2(1+S_{12})]^{-1/2}\begin{pmatrix} 1 & 1 \\ 1 & 1 \end{pmatrix}. \tag{B.11}$$

This guess was obtained as early as 1927 by V. W. Heitler and F. London [308]. Unfortunately, the multi-center integrals eq. (B.3) and (B.4), needed to evaluate the total energy, have no analyical form in the basis of Slater type orbitals (STOs) (see thesis of Michał Lesiuk). Thus, Heitler-London used an upper bound to approximate the two-electron integral and obtain a bond length of 1.5 bohr and binding energy of 2.5 eV, noticeably different from the experimental values of 1.4 bohr and 4.5 eV.

In modern quantum chemistry, instead of directly approximating the integrals, we analytically evaluate the integrals by approximating each basis function as a sum of Gaussians. This reduces the multi-center integrals to single-center integrals, because a product of Gaussians centered on different atoms is also Gaussian but with a different center. The so-called STO-3g basis expresses a STO as a sum of 3 "primitive Gaussians" (see eq. (3.225) of Szabo). Using this basis, the bond length and binding energy become 1.35 bohr and 3.2 eV, having roughly half the discrepancy with experiment when compared to the Heitler-London values.

Figure B.1 shows the STO-3g basis compared to the exact STO it approximates

$$\chi(r) \equiv \left(\frac{\zeta^3}{\pi}\right)^{1/2} e^{-\zeta r} \approx \phi(\boldsymbol{r}) = \sum_{i=1}^{3} c_i \left(\frac{2\alpha_i}{\pi}\right)^{3/4} e^{-\alpha_i r^2}, \tag{B.12}$$

where the exponents $\boldsymbol{\alpha}$ and coefficients $\boldsymbol{c}$ are given below:

For H_2, the STO-3G basis consists of only two 1s functions, each centered around a nucleus.

$$\begin{cases} \phi_1(\boldsymbol{r}) = \sum\limits_{i=1}^{3} c_i \left(\dfrac{2\alpha_i}{\pi}\right)^{3/4} e^{-\alpha_i|\boldsymbol{r}-\boldsymbol{R}_1|^2} \\ \phi_2(\boldsymbol{r}) = \sum\limits_{i=1}^{3} c_i \left(\dfrac{2\alpha_i}{\pi}\right)^{3/4} e^{-\alpha_i|\boldsymbol{r}-\boldsymbol{R}_2|^2} \end{cases}, \tag{B.13}$$

where $\boldsymbol{R}_1 = \boldsymbol{0}$, and $\boldsymbol{R}_2 = 1.4\ \hat{\boldsymbol{z}}$ bohr near equilibrium. At 1.4 bohr separation, the kinetic and the electron-

α	c
3.42525091	0.15432897
0.62391373	0.53532814
0.16885540	0.44463454

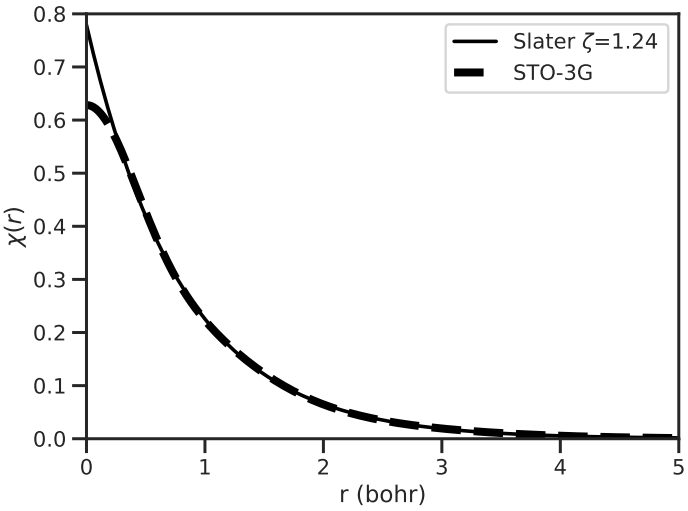

Figure B.1: STO-3G

ion interaction matrices evaluate to

$$T_{\mu\nu} \equiv \langle\phi_\mu| - \frac{1}{2}\nabla^2|\phi_\nu\rangle = \begin{pmatrix} 0.76003188 & 0.23645465 \\ 0.23645465 & 0.76003188 \end{pmatrix}, \tag{B.14}$$

$$V_{\mu\nu} \equiv \langle\phi_\mu| \sum_{i=1}^{2} \frac{1}{|\boldsymbol{r} - \boldsymbol{R}_i|} |\phi_\nu\rangle = \begin{pmatrix} -1.88044088 & -1.19483461 \\ -1.19483461 & -1.88044088 \end{pmatrix}, \tag{B.15}$$

which sum to the 1-electron hamiltonian $H_{\mu\nu}^{\text{core}}$ by eq. (B.3)

Eigenvectors of $H_{\mu\nu}^{\text{core}}$ are typically used to construct the initial density matrix to start a self-consist solution of the Hartree-Fock equations. However, in the case of H_2, these eigenvectors coincide with the final solution, so we obtain the converged density matrix with no iteration from eq. (B.11)

$$C_{\mu 1} = \begin{pmatrix} 0.70710678 \\ -0.70710678 \end{pmatrix}; \; P_{\mu\nu} = \begin{pmatrix} 0.60265716 & 0.60265716 \\ 0.60265716 & 0.60265716 \end{pmatrix}. \tag{B.16}$$

Finally, we can evaluate the so-called electron repulsion integrals (eris) and the Fock matrix eq. (B.9)

Table B.1: symmetry-inequivalent electron repulsion integrals for H_2 in STO-3G.

μ	ν	λ	σ	$(\mu\nu\|\lambda\sigma)$
1	1	1	1	0.774605930
1	1	1	2	0.444107650
1	1	2	2	0.569675915
1	2	1	2	0.297028535

$$J_{\mu\nu} = \begin{pmatrix} 0.67271523 & 0.44665109 \\ 0.44665109 & 0.67271523 \end{pmatrix}; \quad K_{\mu\nu} = \begin{pmatrix} 0.59055879 & 0.52880753 \\ 0.52880753 & 0.59055879 \end{pmatrix}; \tag{B.17}$$

$$F_{\mu\nu} = \begin{pmatrix} -0.36553735 & -0.59388537 \\ -0.59388537 & -0.36553735 \end{pmatrix}. \tag{B.18}$$

The total energy is -1.11671432 ha, while the electronic contribution is -1.831 ha, before adding the ion-ion repulsion $V_{ii} = 1/1.4$ ha. Interested reader should reproduce the Fock matrix for STO-3G H_2 at 1.4 bohr separation, i.e. eq. (B.18), to consolidate a practical understanding of RHF.

In the PZ formulation of KS-DFT, the only difference between the LDA and the RHF calculations lies in the "exchange" matrix

$$K'_{\mu\nu} = \begin{pmatrix} 0.38980073 & 0.25499926 \\ 0.25499926 & 0.38980073 \end{pmatrix}, \tag{B.19}$$

which now contains an approximation to both exchange and correlation effects rather than exact exchange in the case of HF. The Fock matrix is

$$F_{\mu\nu} = \begin{pmatrix} -0.16477935 & -0.32007715 \\ -0.32007715 & -0.16477935 \end{pmatrix}, \tag{B.20}$$

and the LDA electronic contribution is -1.73929592 ha.

Appendix C

Derivation of Higher-order Band Gap Correction

Total potential energy

$$V = \frac{N_e}{\Omega} \sum_{\boldsymbol{k}\neq\boldsymbol{0}} \frac{1}{2} v_k S_{\boldsymbol{k}}, \tag{C.1}$$

where $S_{\boldsymbol{k}} \equiv \frac{1}{N_e} \langle \rho_{\boldsymbol{k}} \rho_{-\boldsymbol{k}} \rangle$. $\rho_{\boldsymbol{k}} \equiv \sum_{j=1}^{N_e} e^{i\boldsymbol{k}\cdot\boldsymbol{r}_j}$ is the electronic density in reciprocal space. Ω is system volume. $\langle\rangle$ denotes average over walker ensemble. The potential energy V can be written as a sum of static (density) contribution and fluctuating contribution

$$V = \left(\frac{1}{\Omega} \sum_{\boldsymbol{k}\neq\boldsymbol{0}} \frac{1}{2} v_k \langle \rho_{\boldsymbol{k}} \rangle \langle \rho_{-\boldsymbol{k}} \rangle \right) + \left(\frac{1}{\Omega} \sum_{\boldsymbol{k}\neq\boldsymbol{0}} \frac{1}{2} v_k (\rho_{\boldsymbol{k}} - \langle \rho_{\boldsymbol{k}} \rangle)(\rho_{-\boldsymbol{k}} - \langle \rho_{-\boldsymbol{k}} \rangle) \right). \tag{C.2}$$

The fluctuating part can be used to calculate leading-order finite-size correction to the band gap, where the static part leads to the next-to-leading-order correction.

$$V_s \equiv \frac{1}{\Omega} \sum_{\boldsymbol{k}\neq\boldsymbol{0}} \frac{1}{2} v_k \langle \rho_{\boldsymbol{k}} \rangle \langle \rho_{-\boldsymbol{k}} \rangle . \tag{C.3}$$

The goal of this Appendix is to find the FSC formula for V_s. Assuming the finite-size error in the electron density can be fully recovered by twist-averaging, the infinite-system potential energy can be computed using the twist-averaged density $\overline{\langle \rho_{\boldsymbol{k}} \rangle}$, where twist average is denoted by overline

$$V_s^{N\to\infty} = \frac{1}{\Omega} \sum_{\boldsymbol{k}\neq\boldsymbol{0}} \frac{1}{2} v_k \overline{\langle \rho_{\boldsymbol{k}} \rangle} \ \ \overline{\langle \rho_{-\boldsymbol{k}} \rangle}. \tag{C.4}$$

Therefore, the FSC of V_s is

$$\delta V_s \equiv V_s^{N\to\infty} - V_s = \frac{1}{\Omega} \sum_{\boldsymbol{k}\neq\boldsymbol{0}} \frac{1}{2} v_k \left[\overline{\langle \rho_{\boldsymbol{k}} \rangle} \ \ \overline{\langle \rho_{-\boldsymbol{k}} \rangle} - \langle \rho_{\boldsymbol{k}} \rangle \langle \rho_{-\boldsymbol{k}} \rangle \right]. \tag{C.5}$$

$\langle \rho_{\boldsymbol{k}} \rangle$ differs from twist to twist, so there is one such correction for each twist. Define

$$C_{\boldsymbol{k}} \equiv \left[\overline{\langle \rho_{\boldsymbol{k}} \rangle} \;\; \overline{\langle \rho_{-\boldsymbol{k}} \rangle} - \langle \rho_{\boldsymbol{k}} \rangle \langle \rho_{-\boldsymbol{k}} \rangle \right], \tag{C.6}$$

then the FSC of the potential energy is

$$\delta V_s = \frac{2\pi}{\Omega} \sum_{\boldsymbol{k} \neq \boldsymbol{0}} C_{\boldsymbol{k}} / k^2. \tag{C.7}$$

In simulation, we assemble the $MN_e + 1$ system with varying density at each twist

$$\rho_{\boldsymbol{k}}^{MN_e \pm 1} = \sum_{\boldsymbol{\theta}} \left(\langle \rho_{\boldsymbol{k}} \rangle_{N_e \pm 1, \boldsymbol{\phi}} - \langle \rho_{\boldsymbol{k}} \rangle_{N_e, \boldsymbol{\phi}} \right) \delta_{\boldsymbol{\theta}, \boldsymbol{\phi}} + \langle \rho_{\boldsymbol{k}} \rangle_{N_e, \boldsymbol{\theta}} \,. \tag{C.8}$$

The GCTA corrected charge density varies only at the target twist $\boldsymbol{\phi}$

$$\overline{\rho_{\boldsymbol{k}}}^{MN_e \pm 1} = \sum_{\boldsymbol{\theta}} \left(\langle \rho_{\boldsymbol{k}} \rangle_{N_e \pm 1, \boldsymbol{\phi}} - \langle \rho_{\boldsymbol{k}} \rangle_{N_e, \boldsymbol{\phi}} \right) \delta_{\boldsymbol{\theta}, \boldsymbol{\phi}} + \overline{\rho_{\boldsymbol{k}}}^{N_e}. \tag{C.9}$$

The *neutral mean density* $\overline{\rho_{\boldsymbol{k}}}^{N_e}$ has no dependence on the twist $\boldsymbol{\theta}$

$$\overline{\rho_{\boldsymbol{k}}}^{N_e} \equiv \frac{1}{M_{\boldsymbol{\theta}}} \langle \rho \rangle_{N_e, \boldsymbol{\theta}} \,. \tag{C.10}$$

For simplicity, define the charge density of the particle/hole as

$$\Pi_{\boldsymbol{k}} \equiv \langle \rho_{\boldsymbol{k}} \rangle_{N_e \pm 1, \boldsymbol{\phi}} - \langle \rho_{\boldsymbol{k}} \rangle_{N_e, \boldsymbol{\phi}} \,. \tag{C.11}$$

Now, the GCTA correction can be clearly seen as the replacement of *neutral twist density* $\langle \rho_{\boldsymbol{k}} \rangle_{N_e, \boldsymbol{\theta}}$ with *neutral mean density* $\overline{\rho_{\boldsymbol{k}}}^{N_e}$

$$\begin{cases} \rho_{\boldsymbol{k}}^{MN_e \pm 1} \equiv & \sum\limits_{\boldsymbol{\theta}} \rho_{\boldsymbol{k}}^{N_e \pm 1}(\boldsymbol{\theta}) = & \sum\limits_{\boldsymbol{\theta}} \left(\Pi_{\boldsymbol{k}} \delta_{\boldsymbol{\theta}, \boldsymbol{\phi}} + \langle \rho_{\boldsymbol{k}} \rangle_{N_e, \boldsymbol{\theta}} \right) \\ \overline{\rho_{\boldsymbol{k}}}^{MN_e \pm 1} \equiv & \sum\limits_{\boldsymbol{\theta}} \overline{\rho_{\boldsymbol{k}}}^{N_e \pm 1}(\boldsymbol{\theta}) = & \sum\limits_{\boldsymbol{\theta}} \left(\Pi_{\boldsymbol{k}} \delta_{\boldsymbol{\theta}, \boldsymbol{\phi}} + \overline{\rho_{\boldsymbol{k}}}^{N_e} \right) \end{cases} . \tag{C.12}$$

The *charged twist density* $\rho_{\boldsymbol{k}}^{N_e \pm 1}(\boldsymbol{\theta})$ and the *charged mean density* $\overline{\rho_{\boldsymbol{k}}}^{N_e \pm 1}(\boldsymbol{\theta})$ are defined by the summand on each line. A likely cause of confusion here is that the charged mean density depends on the twist $\boldsymbol{\theta}$.

Further, it is not the mean of the charged twist density

$$\overline{\rho_{\boldsymbol{k}}}^{N_e\pm1}(\boldsymbol{\theta}')\neq\frac{1}{M_{\boldsymbol{\theta}}}\sum_{\boldsymbol{\theta}}\rho_{\boldsymbol{k}}^{N_e\pm1}(\boldsymbol{\theta}). \tag{C.13}$$

This correction does not affect properties linear in $\rho_{\boldsymbol{k}}$, but does change the potential energy, which is quadratic in $\rho_{\boldsymbol{k}}$. If the MN_e system is constructed from M independent simulations each containing N_e electrons, then the charge density is different at each twist. The Hartree contribution to the total potential energy is

$$V_s^{MN_e+1}=\frac{1}{\Omega}\sum_{\boldsymbol{\theta}}\sum_{\boldsymbol{k}\in G}\frac{1}{2}v_k\ \rho_{\boldsymbol{k}}^{N_e+1}(\boldsymbol{\theta})\rho_{-\boldsymbol{k}}^{N_e+1}(\boldsymbol{\theta}). \tag{C.14}$$

One can speed up the convergence of eq. (C.14) to the thermodynamic limit by replacing twist density with mean density

$$\lim_{N\to\infty}V_s^{MN_e+1}=\frac{1}{\Omega}\sum_{\boldsymbol{\theta}}\sum_{\boldsymbol{k}\in G}\frac{1}{2}v_k\ \overline{\rho_{\boldsymbol{k}}}^{N_e+1}(\boldsymbol{\theta})\overline{\rho_{-\boldsymbol{k}}}^{N_e+1}(\boldsymbol{\theta}). \tag{C.15}$$

Define the correction factor

$$C_{\boldsymbol{k}}^{N_e+1}(\boldsymbol{\theta})\equiv\overline{\rho}_{\boldsymbol{k}}^{N_e+1}(\boldsymbol{\theta})\overline{\rho}_{-\boldsymbol{k}}^{N_e+1}(\boldsymbol{\theta})-\rho_{\boldsymbol{k}}^{N_e+1}(\boldsymbol{\theta})\rho_{-\boldsymbol{k}}^{N_e+1}(\boldsymbol{\theta}), \tag{C.16}$$

then the GCTA finite-size correction to the Hartree contribution to the potential is

$$\delta V_s^{MN_e+1}=\frac{1}{\Omega}\sum_{\boldsymbol{k}\in G}\frac{1}{2}v_k\ \sum_{\boldsymbol{\theta}}C_{\boldsymbol{k}}^{N_e+1}(\boldsymbol{\theta}). \tag{C.17}$$

Eq. (C.16) can be much simplified when calculated relative to the neutral state

$$\begin{aligned}
C_{\boldsymbol{k}}^{N_e+1}(\boldsymbol{\theta})=&(\Pi_{\boldsymbol{k}}\delta_{\boldsymbol{\theta},\boldsymbol{\phi}}+\overline{\rho_{\boldsymbol{k}}}^{N_e})(\Pi_{\boldsymbol{k}}\delta_{\boldsymbol{\theta},\boldsymbol{\phi}}+\overline{\rho_{\boldsymbol{k}}}^{N_e})-(\Pi_{\boldsymbol{k}}\delta_{\boldsymbol{\theta},\boldsymbol{\phi}}+\langle\rho_{\boldsymbol{k}}\rangle_{N_e,\boldsymbol{\theta}})(\Pi_{\boldsymbol{k}}\delta_{\boldsymbol{\theta},\boldsymbol{\phi}}+\langle\rho_{\boldsymbol{k}}\rangle_{N_e,\boldsymbol{\theta}})\\
=&\Pi_{\boldsymbol{k}}\delta_{\boldsymbol{\theta},\boldsymbol{\phi}}(\overline{\rho_{-\boldsymbol{k}}}^{N_e}-\langle\rho_{-\boldsymbol{k}}\rangle_{N_e,\boldsymbol{\theta}})+(\overline{\rho_{\boldsymbol{k}}}^{N_e}-\langle\rho_{\boldsymbol{k}}\rangle_{N_e,\boldsymbol{\theta}})\Pi_{-\boldsymbol{k}}\delta_{\boldsymbol{\theta},\boldsymbol{\phi}}\\
&+\left[\overline{\rho_{\boldsymbol{k}}}^{N_e}\overline{\rho_{-\boldsymbol{k}}}^{N_e}-\langle\rho_{\boldsymbol{k}}\rangle_{N_e,\boldsymbol{\theta}}\langle\rho_{\boldsymbol{k}}\rangle_{N_e,\boldsymbol{\theta}}\right]\\
=&\Pi_{\boldsymbol{k}}\delta_{\boldsymbol{\theta},\boldsymbol{\phi}}(\overline{\rho_{-\boldsymbol{k}}}^{N_e}-\langle\rho_{-\boldsymbol{k}}\rangle_{N_e,\boldsymbol{\theta}})+(\overline{\rho_{\boldsymbol{k}}}^{N_e}-\langle\rho_{\boldsymbol{k}}\rangle_{N_e,\boldsymbol{\theta}})\Pi_{-\boldsymbol{k}}\delta_{\boldsymbol{\theta},\boldsymbol{\phi}}+C_{\boldsymbol{k}}^{N_e}(\boldsymbol{\theta}).
\end{aligned} \tag{C.18}$$

Therefore, the correction to electron addition energy is

$$\begin{aligned}\delta\mu_s^+ =&\frac{1}{\Omega}\sum_{\boldsymbol{k}\in G}\frac{1}{2}v_k\left[\sum_{\boldsymbol{\theta}}C_{\boldsymbol{k}}^{N_e+1}(\boldsymbol{\theta})-C_{\boldsymbol{k}}^{N_e}(\boldsymbol{\theta})\right]\\ =&\frac{1}{\Omega}\sum_{\boldsymbol{k}\in G}\frac{1}{2}v_k\left\{\left[\overline{\rho_{\boldsymbol{k}}}^{N_e}-\langle\rho_{\boldsymbol{k}}\rangle_{N_e,\boldsymbol{\phi}}\right]\Pi_{-\boldsymbol{k}}+\Pi_{\boldsymbol{k}}\left[\overline{\rho_{-\boldsymbol{k}}}^{N_e}-\langle\rho_{-\boldsymbol{k}}\rangle_{N_e,\boldsymbol{\phi}}\right]\right\}. \qquad \text{(C.19)}\end{aligned}$$

References

[1] Sam Azadi et al. "Dissociation of High-Pressure Solid Molecular Hydrogen: A Quantum Monte Carlo and Anharmonic Vibrational Study". In: *Phys. Rev. Lett.* 112.16 (2014), p. 165501. ISSN: 0031-9007. DOI: 10.1103/PhysRevLett.112.165501. URL: https://link.aps.org/doi/10.1103/PhysRevLett.112.165501.

[2] Jeremy McMinis et al. "Molecular to Atomic Phase Transition in Hydrogen under High Pressure". In: *Phys. Rev. Lett.* 114.10 (2015), pp. 1–6. ISSN: 10797114. DOI: 10.1103/PhysRevLett.114.105305.

[3] N. D. Drummond et al. "Quantum Monte Carlo study of the phase diagram of solid molecular hydrogen at extreme pressures". In: *Nat. Commun.* 6 (2015), p. 7794. ISSN: 2041-1723. DOI: 10.1038/ncomms8794. arXiv: arXiv:1508.02313v1. URL: http://www.nature.com/doifinder/10.1038/ncomms8794.

[4] Carlo Pierleoni et al. "Liquid–liquid phase transition in hydrogen by coupled electron–ion Monte Carlo simulations". In: *Proc. Natl. Acad. Sci.* 113.18 (2016), pp. 4953–4957. ISSN: 0027-8424. DOI: 10.1073/pnas.1603853113. URL: http://www.pnas.org/lookup/doi/10.1073/pnas.1603853113.

[5] Peter M Celliers et al. "Insulator-metal transition in dense fluid deuterium". In: *Science* 361.6403 (2018), pp. 677–682. ISSN: 0036-8075. DOI: 10.1126/science.aat0970. URL: https://www.sciencemag.org/lookup/doi/10.1126/science.aat0970.

[6] D.M. Ceperley and B.J. Alder. "The calculation of the properties of metallic hydrogen using Monte Carlo". In: *Phys. B+C* 108.1-3 (1981), pp. 875–876. ISSN: 03784363. DOI: 10.1016/0378-4363(81)90742-7. URL: https://linkinghub.elsevier.com/retrieve/pii/0378436381907427.

[7] Vincent Natoli, Richard M. Martin, and David Ceperley. "Crystal Structure of Molecular Hydrogen at High Pressure". In: *Phys. Rev. Lett.* 74.9 (1995), pp. 1601–1604. ISSN: 0031-9007. DOI: 10.1103/PhysRevLett.74.1601. URL: https://link.aps.org/doi/10.1103/PhysRevLett.74.1601.

[8] Yueqing Chang and Lucas K. Wagner. "Effective spin-orbit models using correlated first-principles wave functions". In: *Phys. Rev. Res.* 2.1 (2020), p. 013195. ISSN: 2643-1564. DOI: 10.1103/PhysRevResearch.2.013195. URL: https://link.aps.org/doi/10.1103/PhysRevResearch.2.013195.

[9] Graham A. Worth and Lorenz S. Cederbaum. "BEYOND BORN-OPPENHEIMER: Molecular Dynamics Through a Conical Intersection". In: *Annu. Rev. Phys. Chem.* 55.1 (2004), pp. 127–158. ISSN: 0066-426X. DOI: 10.1146/annurev.physchem.55.091602.094335. URL: http://www.annualreviews.org/doi/10.1146/annurev.physchem.55.091602.094335.

[10] M Holzmann et al. "Backflow correlations for the electron gas and metallic hydrogen." In: *Phys. Rev. E.* 68.4 Pt 2 (2003), p. 046707. ISSN: 1063-651X. DOI: 10.1103/PhysRevE.68.046707. arXiv: 0304165 [cond-mat].

[11] Burkhard Militzer. "Path Integral Monte Carlo Simulations of Hot Dense Hydrogen". PhD thesis. University of Illinois at Urbana-Champaign, 2000.

[12] W. B. Hubbard and B. Militzer. "A PRELIMINARY JUPITER MODEL". In: *Astrophys. J.* 820.1 (2016), p. 80. ISSN: 1538-4357. DOI: 10.3847/0004-637X/820/1/80. arXiv: 1602.05143. URL: http://dx.doi.org/10.3847/0004-637X/820/1/80http://stacks.iop.org/0004-637X/820/i=1/a=80?key=crossref.acea06e37f7f7dc99ca975ec8290c997.

[13] A. P. Drozdov et al. "Conventional superconductivity at 203 kelvin at high pressures in the sulfur hydride system". In: *Nature* 525.7567 (2015), pp. 73–76. ISSN: 0028-0836. DOI: 10.1038/nature14964. URL: http://www.nature.com/articles/nature14964.

[14] Ion Errea et al. "Quantum crystal structure in the 250-kelvin superconducting lanthanum hydride". In: *Nature* 578.7793 (2020), pp. 66–69. ISSN: 0028-0836. DOI: 10.1038/s41586-020-1955-z. URL: http://www.nature.com/articles/s41586-020-1955-z.

[15] E. Wigner and H. B. Huntington. "On the Possibility of a Metallic Modification of Hydrogen". In: *J. Chem. Phys.* 3.12 (1935), pp. 764–770. ISSN: 0021-9606. DOI: 10.1063/1.1749590. URL: http://aip.scitation.org/doi/10.1063/1.1749590.

[16] Ranga P Dias, Ori Noked, and Isaac F Silvera. "New Phases and Dissociation-Recombination of Hydrogen Deuteride to 3.4 Mbar". In: *Phys. Rev. Lett.* 116.14 (2016), p. 145501. ISSN: 10797114. DOI: 10.1103/PhysRevLett.116.145501. arXiv: 1510.05686. URL: https://link.aps.org/doi/10.1103/PhysRevLett.116.145501.

[17] Paul Loubeyre, Florent Occelli, and Paul Dumas. "Synchrotron infrared spectroscopic evidence of the probable transition to metal hydrogen". In: *Nature* 577.7792 (2020), pp. 631–635. ISSN: 0028-0836. DOI: 10.1038/s41586-019-1927-3. URL: http://dx.doi.org/10.1038/s41586-019-1927-3http://www.nature.com/articles/s41586-019-1927-3.

[18] Vitaly Gorelov et al. "Energy gap closure of crystalline molecular hydrogen with pressure". In: *Phys. Rev. Lett.* 124.11 (2019), p. 116401. ISSN: 1079-7114. DOI: 10.1103/PhysRevLett.124.116401. arXiv: 1911.06135. URL: http://arxiv.org/abs/1911.06135.

[19] Nicholas Metropolis et al. "Equation of State Calculations by Fast Computing Machines". In: *J. Chem. Phys.* 21.6 (1953), pp. 1087–1092. ISSN: 0021-9606. DOI: 10.1063/1.1699114. URL: http://aip.scitation.org/doi/10.1063/1.1699114.

[20] D. M. Ceperley. "Path integrals in the theory of condensed helium". In: *Rev. Mod. Phys.* 67.2 (1995), pp. 279–355. ISSN: 0034-6861. DOI: 10.1103/RevModPhys.67.279. URL: https://link.aps.org/doi/10.1103/RevModPhys.67.279.

[21] Carolyn Meldgin et al. "Probing the Bose glass–superfluid transition using quantum quenches of disorder". In: *Nat. Phys.* 12.7 (2016), pp. 646–649. ISSN: 1745-2473. DOI: 10.1038/nphys3695. arXiv: 1502.02333. URL: http://www.nature.com/articles/nphys3695.

[22] Stefano Baroni and Saverio Moroni. "Reptation Quantum Monte Carlo: A Method for Unbiased Ground-State Averages and Imaginary-Time Correlations". In: *Phys. Rev. Lett.* 82.24 (1999), pp. 4745–4748. ISSN: 0031-9007. DOI: 10.1103/PhysRevLett.82.4745. URL: https://link.aps.org/doi/10.1103/PhysRevLett.82.4745.

[23] Peter J. Reynolds et al. "Fixed-node quantum Monte Carlo for molecules a) b)". In: *J. Chem. Phys.* 77.11 (1982), pp. 5593–5603. ISSN: 0021-9606. DOI: 10.1063/1.443766. URL: http://aip.scitation.org/doi/10.1063/1.443766.

[24] R. M. Martin, Reining L., and Ceperley D. M. *Interacting Electrons : Theory and Computational Approaches*. Cambridge University Press, 2016.

[25] B. L. Hammond, W. A. Lester, and Reynolds P. J. *Monte Carlo Methods in Ab Initio Quantum Chemistry*. World Scientific Publishing Co., 1994.

[26] D. M. Ceperley. "Fermion nodes". In: *J. Stat. Phys.* 63.5-6 (1991), pp. 1237–1267. ISSN: 0022-4715. DOI: 10.1007/BF01030009. URL: http://link.springer.com/10.1007/BF01030009.

[27] D. M. Ceperley. "Path-integral calculations of normal liquid He_3". In: *Phys. Rev. Lett.* 69.2 (1992), pp. 331–334. ISSN: 0031-9007. DOI: 10.1103/PhysRevLett.69.331. URL: http://link.aps.org/doi/10.1103/PhysRevLett.69.331https://link.aps.org/doi/10.1103/PhysRevLett.69.331.

[28] D. M. Ceperley. "Path integral Monte Carlo methods for fermions". In: *Monte Carlo and Molecular Dynamics of Condensed Matter Systems*. Ed. by K. Binder and G. Ciccotti. Italy: Editrice Compository, 1996.

[29] D. M. Ceperley. "Ground state of the fermion one-component plasma: A Monte Carlo study in two and three dimensions". In: *Phys. Rev. B* 18.7 (1978), pp. 3126–3138. ISSN: 0163-1829. DOI: 10.1103/PhysRevB.18.3126. URL: https://link.aps.org/doi/10.1103/PhysRevB.18.3126.

[30] Markus Holzmann, Bernard Bernu, and D. M. Ceperley. "Many-body wavefunctions for normal liquid He_3". In: *Phys. Rev. B* 74.10 (2006), p. 104510. ISSN: 1098-0121. DOI: 10.1103/PhysRevB.74.104510. URL: https://link.aps.org/doi/10.1103/PhysRevB.74.104510.

[31] Carlo Pierleoni et al. "Trial wave functions for high-pressure metallic hydrogen". In: *Comput. Phys. Commun.* 179.1-3 (2008), pp. 89–97. ISSN: 00104655. DOI: 10.1016/j.cpc.2008.01.041. arXiv: 0712.0161. URL: http://www.sciencedirect.com/science/article/pii/S0010465508000210.

[32] G. F Giuliani and G. Vignale. *Quantum Theory of the Electron Liquid*. Cambridge University Press, 2005.

[33] T. Koopmans. "Über die Zuordnung von Wellenfunktionen und Eigenwerten zu den Einzelnen Elektronen Eines Atoms". In: *Physica* 1.1-6 (1934), pp. 104–113. ISSN: 00318914. DOI: 10.1016/S0031-8914(34)90011-2. URL: https://linkinghub.elsevier.com/retrieve/pii/S0031891434900112.

[34] W. Kolos and L. Wolniewicz. "Accurate Adiabatic Treatment of the Ground State of the Hydrogen Molecule". In: *J. Chem. Phys.* 41.12 (1964), pp. 3663–3673. ISSN: 0021-9606. DOI: 10.1063/1.1725796. URL: http://aip.scitation.org/doi/10.1063/1.1725796.

[35] Carlos L. Benavides-Riveros, Nektarios N. Lathiotakis, and Miguel A. L. Marques. "Towards a formal definition of static and dynamic electronic correlations". In: *Phys. Chem. Chem. Phys.* 19.20 (2017), pp. 12655–12664. ISSN: 1463-9076. DOI: 10.1039/C7CP01137G. arXiv: 1705.00238. URL: http://xlink.rsc.org/?DOI=C7CP01137G.

[36] Aron J. Cohen, P. Mori-Sanchez, and Weitao Yang. "Insights into Current Limitations of Density Functional Theory". In: *Science* 321.5890 (2008), pp. 792–794. ISSN: 0036-8075. DOI: 10.1126/science.1158722. URL: https://www.sciencemag.org/lookup/doi/10.1126/science.1158722.

[37] J. P. Perdew and Alex Zunger. "Self-interaction correction to density-functional approximations for many-electron systems". In: *Phys. Rev. B* 23.10 (1981), pp. 5048–5079. ISSN: 0163-1829. DOI: 10.1103/PhysRevB.23.5048. URL: https://link.aps.org/doi/10.1103/PhysRevB.23.5048.

[38] R. G. Parr and W. Yang. *Density-Functional Theory of Atoms and Molecules*. New York, NY: Oxford University Press, 1989.

[39] P. Hohenberg and W. Kohn. "Inhomogeneous Electron Gas". In: *Phys. Rev.* 136.3B (1964), B864–B871. ISSN: 0031-899X. DOI: 10.1103/PhysRev.136.B864. URL: https://link.aps.org/doi/10.1103/PhysRev.136.B864.

[40] Mel Levy. "Electron densities in search of Hamiltonians". In: *Phys. Rev. A* 26.3 (1982), pp. 1200–1208. ISSN: 0556-2791. DOI: 10.1103/PhysRevA.26.1200. URL: https://link.aps.org/doi/10.1103/PhysRevA.26.1200.

[41] Elliott H. Lieb. "Density functionals for coulomb systems". In: *Int. J. Quantum Chem.* 24.3 (1983), pp. 243–277. ISSN: 0020-7608. DOI: 10.1002/qua.560240302. URL: http://doi.wiley.com/10.1002/qua.560240302.

[42] M. Levy. "Universal variational functionals of electron densities, first-order density matrices, and natural spin-orbitals and solution of the v-representability problem". In: *Proc. Natl. Acad. Sci.* 76.12 (1979), pp. 6062–6065. ISSN: 0027-8424. DOI: 10.1073/pnas.76.12.6062. URL: http://www.pnas.org/cgi/doi/10.1073/pnas.76.12.6062.

[43] W. Kohn and L. J. Sham. "Self-Consistent Equations Including Exchange and Correlation Effects". In: *Phys. Rev.* 140.4A (1965), A1133–A1138. ISSN: 0031-899X. DOI: 10.1103/PhysRev.140.A1133. URL: https://link.aps.org/doi/10.1103/PhysRev.140.A1133.

[44] D. M. Ceperley and B. J. Alder. "Ground State of the Electron Gas by a Stochastic Method". In: *Phys. Rev. Lett.* 45.7 (1980), pp. 566–569. ISSN: 0031-9007. DOI: 10.1103/PhysRevLett.45.566. URL: https://link.aps.org/doi/10.1103/PhysRevLett.45.566.

[45] John P. Perdew, Kieron Burke, and Matthias Ernzerhof. "Generalized Gradient Approximation Made Simple". In: *Phys. Rev. Lett.* 77.18 (1996), pp. 3865–3868. ISSN: 0031-9007. DOI: 10.1103/PhysRevLett.77.3865. URL: https://link.aps.org/doi/10.1103/PhysRevLett.77.3865.

[46] Jochen Heyd, Gustavo E. Scuseria, and Matthias Ernzerhof. "Hybrid functionals based on a screened Coulomb potential". In: *J. Chem. Phys.* 118.18 (2003), pp. 8207–8215. ISSN: 0021-9606. DOI: 10.1063/1.1564060. URL: http://aip.scitation.org/doi/10.1063/1.1564060.

[47] D. M. Ceperley. "Understanding Electronic Wave Functions". In: *Electron Correlations and Materials Properties*. Ed. by A. Gonis, N. Kioussis, and M. Ciftan. Springer US, 1999, pp. 429–438.

[48] Paul Adrien Maurice Dirac and Ralph Howard Fowler. "Quantum mechanics of many-electron systems". In: *Proceedings of the Royal Society of London. Series A, Containing Papers of a Mathematical and Physical Character* 123.792 (1929), pp. 714–733. DOI: 10.1098/rspa.1929.0094. eprint: https://royalsocietypublishing.org/doi/pdf/10.1098/rspa.1929.0094. URL: https://royalsocietypublishing.org/doi/abs/10.1098/rspa.1929.0094.

[49] E. Wigner. "On the Interaction of Electrons in Metals". In: *Phys. Rev.* 46.11 (1934), pp. 1002–1011. ISSN: 0031-899X. DOI: 10.1103/PhysRev.46.1002. URL: https://link.aps.org/doi/10.1103/PhysRev.46.1002.

[50] A. Bijl. "The lowest wave function of the symmetrical many particles system". In: *Physica* 7.9 (1940), pp. 869–886. ISSN: 00318914. DOI: 10.1016/0031-8914(40)90166-5. URL: https://linkinghub.elsevier.com/retrieve/pii/0031891440901665.

[51] Giuseppe Carleo et al. "Unitary Dynamics of Strongly Interacting Bose Gases with the Time-Dependent Variational Monte Carlo Method in Continuous Space". In: *Phys. Rev. X* 7.3 (2017), p. 031026. ISSN: 2160-3308. DOI: 10.1103/PhysRevX.7.031026. URL: http://link.aps.org/doi/10.1103/PhysRevX.7.031026.

[52] R.B. Dingle. "LI. The zero-point energy of a system of particles". In: *London, Edinburgh, Dublin Philos. Mag. J. Sci.* 40.304 (1949), pp. 573–578. ISSN: 1941-5982. DOI: 10.1080/14786444908521743. URL: http://www.tandfonline.com/doi/abs/10.1080/14786444908521743.

[53] Robert Jastrow. "Many-Body Problem with Strong Forces". In: *Phys. Rev.* 98.5 (1955), pp. 1479–1484. ISSN: 0031-899X. DOI: 10.1103/PhysRev.98.1479. URL: https://link.aps.org/doi/10.1103/PhysRev.98.1479.

[54] R. P. Feynman and Michael Cohen. "Energy Spectrum of the Excitations in Liquid Helium". In: *Phys. Rev.* 102.5 (1956), pp. 1189–1204. ISSN: 0031-899X. DOI: 10.1103/PhysRev.102.1189. URL: https://link.aps.org/doi/10.1103/PhysRev.102.1189.

[55] R. P. Feynman. "Atomic Theory of the Two-Fluid Model of Liquid Helium". In: *Phys. Rev.* 94.2 (1954), pp. 262–277. ISSN: 0031-899X. DOI: 10.1103/PhysRev.94.262. URL: https://link.aps.org/doi/10.1103/PhysRev.94.262.

[56] Fa Yueh Wu and Eugene Feenberg. "Ground State of Liquid Helium (Mass 4)". In: *Phys. Rev.* 122.3 (1961), pp. 739–742. ISSN: 0031-899X. DOI: 10.1103/PhysRev.122.739. URL: https://link.aps.org/doi/10.1103/PhysRev.122.739.

[57] T Gaskell. "The Collective Treatment of a Fermi Gas: II". In: *Proc. Phys. Soc.* 77.6 (1961), pp. 1182–1192. ISSN: 0370-1328. DOI: 10.1088/0370-1328/77/6/312. URL: http://stacks.iop.org/0370-1328/72/i=5/a=301?key=crossref.a03e8e8c89696490a53671d5515ea8dahttp://stacks.iop.org/0370-1328/77/i=6/a=312?key=crossref.a131ff4ffa841443ea0142ac2f764057.

[58] Michele Taddei et al. "Iterative backflow renormalization procedure for many-body ground-state wave functions of strongly interacting normal Fermi liquids". In: *Phys. Rev. B* 91 (11 2015), p. 115106. DOI: 10.1103/PhysRevB.91.115106. URL: https://link.aps.org/doi/10.1103/PhysRevB.91.115106.

[59] Markus Holzmann et al. "Renormalization factor and effective mass of the two-dimensional electron gas". In: *Phys. Rev. B* 79.4 (2009), p. 041308. ISSN: 1098-0121. DOI: 10.1103/PhysRevB.79.041308. arXiv: 0810.2450. URL: https://link.aps.org/doi/10.1103/PhysRevB.79.041308.

[60] Markus Holzmann et al. "Theory of finite size effects for electronic quantum Monte Carlo calculations of liquids and solids". In: *Phys. Rev. B* 94.3 (2016), p. 035126. ISSN: 2469-9950. DOI: 10.1103/PhysRevB.94.035126. arXiv: 1603.03957. URL: http://arxiv.org/abs/1603.03957https://link.aps.org/doi/10.1103/PhysRevB.94.035126.

[61] Paola Gori-Giorgi, Francesco Sacchetti, and Giovanni Bachelet. "Analytic static structure factors and pair-correlation functions for the unpolarized homogeneous electron gas". In: *Phys. Rev. B* 61.11 (2000), pp. 7353–7363. DOI: 10.1063/1.1390176.

[62] Simone Chiesa et al. "Finite-Size Error in Many-Body Simulations with Long-Range Interactions". In: *Phys. Rev. Lett.* 97.7 (2006), p. 076404. ISSN: 0031-9007. DOI: 10.1103/PhysRevLett.97.076404. URL: https://link.aps.org/doi/10.1103/PhysRevLett.97.076404.

[63] N. D. Drummond et al. "Finite-size errors in continuum quantum Monte Carlo calculations". In: *Phys. Rev. B* 78.12 (2008), p. 125106. ISSN: 1098-0121. DOI: 10.1103/PhysRevB.78.125106. arXiv: 0806.0957. URL: https://link.aps.org/doi/10.1103/PhysRevB.78.125106.

[64] David Bohm and David Pines. "A Collective Description of Electron Interactions: III. Coulomb Interactions in a Degenerate Electron Gas". In: *Phys. Rev.* 92.3 (1953), pp. 609–625. ISSN: 0031-899X. DOI: 10.1103/PhysRev.92.609. URL: https://link.aps.org/doi/10.1103/PhysRev.92.609.

[65] Simone Chiesa et al. "Random phase approximation and the finite size errors in many body simulations". In: *AIP Conf. Proc.* Vol. 918. 2007. AIP, 2007, pp. 284–288. ISBN: 0735404283. DOI: 10.1063/1.2751996. URL: http://aip.scitation.org/doi/abs/10.1063/1.2751996.

[66] Paola Gori-Giorgi, Saverio Moroni, and Giovanni B. Bachelet. "Pair-distribution functions of the two-dimensional electron gas". In: *Phys. Rev. B* 70.11 (2004), pp. 1–12. ISSN: 01631829. DOI: 10.1103/PhysRevB.70.115102.

[67] Raymond C. Clay et al. "Benchmarking density functionals for hydrogen-helium mixtures with quantum Monte Carlo: Energetics, pressures, and forces". In: *Phys. Rev. B* 93.3 (2016), p. 035121. ISSN: 2469-9950. DOI: 10.1103/PhysRevB.93.035121. URL: https://link.aps.org/doi/10.1103/PhysRevB.93.035121.

[68] Yubo Yang et al. "Electronic band gaps from quantum Monte Carlo methods". In: *Phys. Rev. B* 101.8 (2020), p. 085115. ISSN: 2469-9950. DOI: 10.1103/PhysRevB.101.085115. arXiv: 1910.07531. URL: http://arxiv.org/abs/1910.07531https://link.aps.org/doi/10.1103/PhysRevB.101.085115.

[69] W.L.McMillan. "Ground State of Liquid He_4". In: *Phys. Rev.* 138.2 (1965).

[70] W. R. Magro and D. M. Ceperley. "Ground-State Properties of the Two-Dimensional Bose Coulomb Liquid". In: *Phys. Rev. Lett.* 73.6 (1994), pp. 826–829. ISSN: 0031-9007. DOI: 10.1103/PhysRevLett.73.826. URL: https://link.aps.org/doi/10.1103/PhysRevLett.73.826.

[71] Yubo Yang et al. "Quantum Monte Carlo Compton profiles of solid and liquid lithium". In: *Phys. Rev. B* 101.16 (2020), p. 165125. ISSN: 2469-9950. DOI: 10.1103/PhysRevB.101.165125. URL: https://link.aps.org/doi/10.1103/PhysRevB.101.165125.

[72] C Lin, F H Zong, and D M Ceperley. "Twist-averaged boundary conditions in continuum quantum Monte Carlo algorithms". In: *Phys. Rev. E* 64.1 (2001), p. 016702. ISSN: 1063-651X. DOI: 10.1103/PhysRevE.64.016702. arXiv: 0101339 [cond-mat]. URL: http://journals.aps.org/pre/abstract/10.1103/PhysRevE.64.016702https://link.aps.org/doi/10.1103/PhysRevE.64.016702.

[73] Norm M. Tubman et al. "Beyond the Born-Oppenheimer approximation with quantum Monte Carlo methods". In: *Phys. Rev. A* 90 (4 2014), p. 042507. DOI: 10.1103/PhysRevA.90.042507. URL: http://link.aps.org/doi/10.1103/PhysRevA.90.042507.

[74] Lorenz S. Cederbaum. "The exact molecular wavefunction as a product of an electronic and a nuclear wavefunction". In: *J. Chem. Phys.* 138.22, 224110 (2013). DOI: 10.1063/1.4807115. URL: http://scitation.aip.org/content/aip/journal/jcp/138/22/10.1063/1.4807115.

[75] Seung Kyu Min et al. "Is the Molecular Berry Phase an Artifact of the Born-Oppenheimer Approximation?" In: *Phys. Rev. Lett.* 113 (2014), p. 263004. DOI: 10.1103/PhysRevLett.113.263004. URL: http://link.aps.org/doi/10.1103/PhysRevLett.113.263004.

[76] PeterA. Bouvrie et al. "Entanglement and the Born-Oppenheimer approximation in an exactly solvable quantum many-body system". English. In: *The European Physical Journal D* 68.11, 346 (2014). ISSN: 1434-6060. URL: 10.1140/epjd/e2014-50349-2.

[77] Benjamin G. Levine and Todd J. Martínez. "Isomerization Through Conical Intersections". In: *Annu. Rev. Phys. Chem.* 58.1 (2007), pp. 613–634. DOI: 10.1146/annurev.physchem.57.032905.104612. URL: 10.1146/annurev.physchem.57.032905.104612.

[78] Lorenz S. Cederbaum. "Erratum: The exact molecular wavefunction as a product of an electronic and a nuclear wavefunction [J. Chem. Phys.138, 224110 (2013)]". In: *J. Chem. Phys.* 141.2, 029902 (2014). DOI: 10.1063/1.4890075. URL: http://scitation.aip.org/content/aip/journal/jcp/141/2/10.1063/1.4890075.

[79] Jim Mitroy et al. "Theory and application of explicitly correlated Gaussians". In: *Rev. Mod. Phys.* 85 (2 2013), pp. 693–749. DOI: 10.1103/RevModPhys.85.693. URL: http://link.aps.org/doi/10.1103/RevModPhys.85.693.

[80] Simon P. Webb, Tzvetelin Iordanov, and Sharon Hammes-Schiffer. "Multiconfigurational nuclear-electronic orbital approach: Incorporation of nuclear quantum effects in electronic structure calculations". In: *J. Chem. Phys.* 117.9 (2002), pp. 4106–4118. DOI: 10.1063/1.1494980. URL: http://scitation.aip.org/content/aip/journal/jcp/117/9/10.1063/1.1494980.

[81] Arindam Chakraborty, Michael V. Pak, and Sharon Hammes-Schiffer. "Inclusion of explicit electron-proton correlation in the nuclear-electronic orbital approach using Gaussian-type geminal functions". In: *J. Chem. Phys.* 129.1, 014101 (2008). DOI: 10.1063/1.2943144. URL: http://scitation.aip.org/content/aip/journal/jcp/129/1/10.1063/1.2943144.

[82] Andrew Sirjoosingh et al. "Reduced explicitly correlated Hartree-Fock approach within the nuclear-electronic orbital framework: Theoretical formulation". In: *J. Chem. Phys.* 139.3, 034102 (2013). DOI: 10.1063/1.4812257. URL: http://scitation.aip.org/content/aip/journal/jcp/139/3/10.1063/1.4812257.

[83] Chet Swalina et al. "Explicit Dynamical ElectronProton Correlation in the NuclearElectronic Orbital Framework". In: *J. Phys. Chem. A* 110.33 (2006), pp. 9983–9987. DOI: 10.1021/jp0634297. URL: 10.1021/jp0634297.

[84] Kurt R. Brorsen et al. "Nuclear-electronic orbital reduced explicitly correlated Hartree-Fock approach: Restricted basis sets and open-shell systems". In: *J. Chem. Phys.* 142.21, 214108 (2015). DOI: 10.1063/1.4921304. URL: http://scitation.aip.org/content/aip/journal/jcp/142/21/10.1063/1.4921304.

[85] Andrew Sirjoosingh et al. "Quantum treatment of protons with the reduced explicitly correlated Hartree-Fock approach". In: *J. Chem. Phys.* 142.21, 214107 (2015). DOI: 10.1063/1.4921303. URL: http://scitation.aip.org/content/aip/journal/jcp/142/21/10.1063/1.4921303.

[86] Arindam Chakraborty, Michael Pak, and Sharon Hammes-Schiffer. "Development of Electron-Proton Density Functionals for Multicomponent Density Functional Theory". In: *Phys. Rev. Lett.* 101 (15 2008), p. 153001. DOI: 10.1103/PhysRevLett.101.153001. URL: http://link.aps.org/doi/10.1103/PhysRevLett.101.153001.

[87] Andrew Sirjoosingh, Michael V. Pak, and Sharon Hammes-Schiffer. "Multicomponent density functional theory study of the interplay between electron-electron and electron-proton correlation". In: *J. Chem. Phys.* 136.17, 174114 (2012). DOI: 10.1063/1.4709609. URL: http://scitation.aip.org/content/aip/journal/jcp/136/17/10.1063/1.4709609.

[88] Andrew Sirjoosingh, Michael V. Pak, and Sharon Hammes-Schiffer. "Derivation of an ElectronProton Correlation Functional for Multicomponent Density Functional Theory within the NuclearElectronic Orbital Approach". In: *J. Chem. Theory Comput.* 7.9 (2011), pp. 2689–2693. DOI: 10.1021/ct200473r. URL: 10.1021/ct200473r.

[89] T. Kreibich and E. Gross. "Multicomponent Density-Functional Theory for Electrons and Nuclei". In: *Phys. Rev. Lett.* 86 (2001), pp. 2984–2987. DOI: 10.1103/PhysRevLett.86.2984. URL: http://link.aps.org/doi/10.1103/PhysRevLett.86.2984.

[90] Thomas Kreibich, Robert van Leeuwen, and E. Gross. "Multicomponent density-functional theory for electrons and nuclei". In: *Phys. Rev. A* 78 (2008), p. 022501. DOI: 10.1103/PhysRevA.78.022501. URL: http://link.aps.org/doi/10.1103/PhysRevA.78.022501.

[91] Ilkka Kylänpää, Tapio Rantala, and David Ceperley. "Few-body reference data for multicomponent formalisms: Light-nuclei molecules". In: *Phys. Rev. A* 86 (2012), p. 052506. DOI: 10.1103/PhysRevA.86.052506. URL: http://link.aps.org/doi/10.1103/PhysRevA.86.052506.

[92] Ilkka Kylänpää and Tapio T. Rantala. "First-principles simulation of molecular dissociationrecombination equilibrium". In: *J. Chem. Phys.* 135.10, 104310 (2011). DOI: 10.1063/1.3633516. URL: http://scitation.aip.org/content/aip/journal/jcp/135/10/10.1063/1.3633516.

[93] Ilkka Kylänpää and Tapio T. Rantala. "Finite temperature quantum statistics of H3+ molecular ion". In: *J. Chem. Phys.* 133.4, 044312 (2010). DOI: 10.1063/1.3464758. URL: http://scitation.aip.org/content/aip/journal/jcp/133/4/10.1063/1.3464758.

[94] James B. Anderson. "A randomwalk simulation of the Schrdinger equation: H_3^+". In: *J. Chem. Phys.* 63.4 (1975), pp. 1499–1503. DOI: 10.1063/1.431514. URL: http://scitation.aip.org/content/aip/journal/jcp/63/4/10.1063/1.431514.

[95] Brian L. Hammond, Peter J. Reynolds, and William A. Lester. *Monte Carlo Methods in Ab Initio Quantum Chemistry*. World Scientific, 1994.

[96] Stuart M. Rothstein. "A survey on pure sampling in quantum Monte Carlo methods". In: *Can. J. Chem.* 91.7 (2013), pp. 505–510. DOI: 10.1139/cjc-2012-0539. URL: 10.1139/cjc-2012-0539.

[97] R J Needs et al. "Continuum variational and diffusion quantum Monte Carlo calculations". In: *J. Phys-Condens. Mat.* 22.2 (2010), p. 023201. URL: http://stacks.iop.org/0953-8984/22/i=2/a=023201.

[98] R. J. Needs and M. D. Towler. "The Diffusion Quantum Monte Carlo Method: Designing Trial Wave Functions For NiO". In: *Int. J. Mod Phys B* 17.28 (2003), pp. 5425–5434. DOI: 10.1142/S0217979203020533. URL: http://www.worldscientific.com/doi/abs/10.1142/S0217979203020533.

[99] W. M. C. Foulkes et al. "Quantum Monte Carlo simulations of solids". In: *Rev. Mod. Phys.* 73 (2001), pp. 33–83. DOI: 10.1103/RevModPhys.73.33. URL: http://link.aps.org/doi/10.1103/RevModPhys.73.33.

[100] Jeffrey C. Grossman. "Benchmark quantum Monte Carlo calculations". In: *J. Chem. Phys.* 117.4 (2002), pp. 1434–1440. DOI: 10.1063/1.1487829. URL: http://scitation.aip.org/content/aip/journal/jcp/117/4/10.1063/1.1487829.

[101] D. Ceperley and B. Alder. "Ground state of solid hydrogen at high pressures". In: *Phys. Rev. B* 36 (4 1987), pp. 2092–2106. DOI: 10.1103/PhysRevB.36.2092. URL: http://link.aps.org/doi/10.1103/PhysRevB.36.2092.

[102] V. Natoli, Richard Martin, and D. Ceperley. "Crystal structure of atomic hydrogen". In: *Phys. Rev. Lett.* 70 (1993), pp. 1952–1955. DOI: 10.1103/PhysRevLett.70.1952. URL: http://link.aps.org/doi/10.1103/PhysRevLett.70.1952.

[103] Vincent Natoli, Richard Martin, and David Ceperley. "Crystal Structure of Molecular Hydrogen at High Pressure". In: *Phys. Rev. Lett.* 74 (1995), pp. 1601–1604. DOI: 10.1103/PhysRevLett.74.1601. URL: http://link.aps.org/doi/10.1103/PhysRevLett.74.1601.

[104] Bin Chen and James B. Anderson. "Improved quantum Monte Carlo calculation of the groundstate energy of the hydrogen molecule". In: *J. Chem. Phys.* 102.7 (1995), pp. 2802–2805. DOI: 10.1063/1.468656. URL: http://scitation.aip.org/content/aip/journal/jcp/102/7/10.1063/1.468656.

[105] S. A. Alexander and R. L. Coldwell. "Fully nonadiabatic properties of all H2 isotopomers". In: *J. Chem. Phys.* 129.11, 114306 (2008). DOI: 10.1063/1.2978172. URL: http://scitation.aip.org/content/aip/journal/jcp/129/11/10.1063/1.2978172.

[106] Luca Bertini et al. "Borromean binding in H_2 with Yukawa potential: A nonadiabatic quantum Monte Carlo study". In: *Phys. Rev. A* 69 (2004), p. 042504. DOI: 10.1103/PhysRevA.69.042504. URL: http://link.aps.org/doi/10.1103/PhysRevA.69.042504.

[107] Guglielmo Mazzola, Andrea Zen, and Sandro Sorella. "Finite-temperature electronic simulations without the Born-Oppenheimer constraint". In: *J. Chem. Phys.* 137.13, 134112 (2012). DOI: 10.1063/1.4755992. URL: http://scitation.aip.org/content/aip/journal/jcp/137/13/10.1063/1.4755992.

[108] C. J. Umrigar et al. "Alleviation of the Fermion-Sign Problem by Optimization of Many-Body Wave Functions". In: *Phys. Rev. Lett.* 98 (2007), p. 110201. DOI: 10.1103/PhysRevLett.98.110201. URL: http://link.aps.org/doi/10.1103/PhysRevLett.98.110201.

[109] Julien Toulouse and C. J. Umrigar. "Full optimization of JastrowSlater wave functions with application to the first-row atoms and homonuclear diatomic molecules". In: *J. Chem. Phys.* 128.17, 174101 (2008). DOI: 10.1063/1.2908237. URL: http://scitation.aip.org/content/aip/journal/jcp/128/17/10.1063/1.2908237.

[110] M. D. Brown et al. "Energies of the first row atoms from quantum Monte Carlo". In: *J. Chem. Phys.* 126.22, 224110 (2007). DOI: 10.1063/1.2743972. URL: http://scitation.aip.org/content/aip/journal/jcp/126/22/10.1063/1.2743972.

[111] P. Seth, P. López Ríos, and R. J. Needs. "Quantum Monte Carlo study of the first-row atoms and ions". In: *J. Chem. Phys.* 134.8, 084105 (2011). DOI: 10.1063/1.3554625. URL: http://scitation.aip.org/content/aip/journal/jcp/134/8/10.1063/1.3554625.

[112] M. Nightingale and Vilen Melik-Alaverdian. "Optimization of Ground- and Excited-State Wave Functions and van der Waals Clusters". In: *Phys. Rev. Lett.* 87 (2001), p. 043401. DOI: 10.1103/PhysRevLett.87.043401. URL: http://link.aps.org/doi/10.1103/PhysRevLett.87.043401.

[113] C. Umrigar and Claudia Filippi. "Energy and Variance Optimization of Many-Body Wave Functions". In: *Phys. Rev. Lett.* 94 (2005), p. 150201. DOI: 10.1103/PhysRevLett.94.150201. URL: http://link.aps.org/doi/10.1103/PhysRevLett.94.150201.

[114] Galina Chaban, Michael W. Schmidt, and Mark S. Gordon. "Approximate second order method for orbital optimization of SCF and MCSCF wavefunctions". English. In: *Theor. Chem. Acc.* 97.1-4 (1997), pp. 88–95. ISSN: 1432-881X. DOI: 10.1007/s002140050241. URL: http://dx.doi.org/10.1007/s002140050241.

[115] Attila Szabo and Neil S. Ostlund. *Modern Quantum Chemistry*. McGraw-Hill, Inc., 1989.

[116] Michael W. Schmidt et al. "General atomic and molecular electronic structure system". In: *J. Comput. Chem.* 14.11 (1993), pp. 1347–1363. ISSN: 1096-987X. DOI: 10.1002/jcc.540141112. URL: 10.1002/jcc.540141112.

[117] Ruben Pauncz. *Spin Eigenfunctions: Construction and Use*. 227 West 17th Street, New York, N.Y. 10011: Plenum Press, New York, 1979.

[118] Thom H. Dunning. "Gaussian basis sets for use in correlated molecular calculations. I. The atoms boron through neon and hydrogen". In: *J. Chem. Phys.* 90.2 (1989), pp. 1007–1023. DOI: 10.1063/1.456153. URL: http://scitation.aip.org/content/aip/journal/jcp/90/2/10.1063/1.456153.

[119] Per-Olof Widmark, Per-ke Malmqvist, and BjrnO. Roos. "Density matrix averaged atomic natural orbital (ANO) basis sets for correlated molecular wave functions". In: *Theoretica chimica acta* 77.5 (1990), pp. 291–306. ISSN: 0040-5744. DOI: 10.1007/BF01120130. URL: http://dx.doi.org/10.1007/BF01120130.

[120] A. Ma et al. "Scheme for adding electronnucleus cusps to Gaussian orbitals". In: *J. Chem. Phys.* 122.22, 224322 (2005). DOI: 10.1063/1.1940588. URL: http://scitation.aip.org/content/aip/journal/jcp/122/22/10.1063/1.1940588.

[121] Tosio Kato. "On the eigenfunctions of many-particle systems in quantum mechanics". In: *Commun. Pur. Appl. Math.* 10.2 (1957), pp. 151–177. ISSN: 1097-0312. DOI: 10.1002/cpa.3160100201. URL: 10.1002/cpa.3160100201.

[122] Jeongnim Kim et al. "Hybrid algorithms in quantum Monte Carlo". In: *J. Phys. Conf. Ser.* 402.1 (2012), p. 012008. URL: http://stacks.iop.org/1742-6596/402/i=1/a=012008.

[123] K.P. Esler et al. "Accelerating Quantum Monte Carlo Simulations of Real Materials on GPU Clusters". In: *Comput. Sci. Eng.* 14.1 (2012), pp. 40–51. ISSN: 1521-9615. DOI: 10.1109/MCSE.2010.122.

[124] In: (). NIST Computational Chemistry Comparison and Benchmark Database, NIST Standard Reference Database Number 101, Release 16a, August 2013. Editor: Russell D. Johnson III, http://cccbdb.nist.gov.

[125] Graham A. Worth and Lorenz S. Cederbaum. "BEYOND BORN-OPPENHEIMER: Molecular Dynamics Through a Conical Intersection". In: *Annu. Rev. Phys. Chem.* 55.1 (2004), pp. 127–158. DOI: 10.1146/annurev.physchem.55.091602.094335. URL: 10.1146/annurev.physchem.55.091602.094335.

[126] L. M. Wang et al. "Variational upper bounds for low-lying states of lithium". In: *Phys. Rev. A* 83 (2011), p. 034503. DOI: 10.1103/PhysRevA.83.034503. URL: http://link.aps.org/doi/10.1103/PhysRevA.83.034503.

[127] Monika Stanke et al. "Five lowest ^1S states of the Be atom calculated with a finite-nuclear-mass approach and with relativistic and QED corrections". In: *Phys. Rev. A* 80 (2009), p. 022514. DOI: 10.1103/PhysRevA.80.022514. URL: http://link.aps.org/doi/10.1103/PhysRevA.80.022514.

[128] Sergiy Bubin and Ludwik Adamowicz. "Correlated-Gaussian calculations of the ground and low-lying excited states of the boron atom". In: *Phys. Rev. A* 83 (2011), p. 022505. DOI: 10.1103/PhysRevA.83.022505. URL: http://link.aps.org/doi/10.1103/PhysRevA.83.022505.

[129] Subhas J. Chakravorty et al. "Ground-state correlation energies for atomic ions with 3 to 18 electrons". In: *Phys. Rev. A* 47 (1993), pp. 3649–3670. DOI: 10.1103/PhysRevA.47.3649. URL: http://link.aps.org/doi/10.1103/PhysRevA.47.3649.

[130] Monika Stanke et al. "Accuracy limits on the description of the lowest S excitation in the Li atom using explicitly correlated Gaussian basis functions". In: *Phys. Rev. A* 78 (2008), p. 052507. DOI: 10.1103/PhysRevA.78.052507. URL: http://link.aps.org/doi/10.1103/PhysRevA.78.052507.

[131] Sergiy Bubin and Ludwik Adamowicz. "Calculations of the ground states of BeH and BeH+ without the Born-Oppenheimer approximation". In: *J. Chem. Phys.* 126.21, 214305 (2007). DOI: 10.1063/1.2736699. URL: http://scitation.aip.org/content/aip/journal/jcp/126/21/10.1063/1.2736699.

[132] Sergiy Bubin et al. "Born-Oppenheimer and Non-Born-Oppenheimer, Atomic and Molecular Calculations with Explicitly Correlated Gaussians". In: *Chem. Rev.* 113.1 (2013), pp. 36–79. DOI: 10.1021/cr200419d. URL: 10.1021/cr200419d.

[133] Hiroyuki Nakashima and Hiroshi Nakatsuji. "Solving the Schrdinger equation for helium atom and its isoelectronic ions with the free iterative complement interaction (ICI) method". In: *J. Chem. Phys.* 127.22, 224104 (2007). DOI: 10.1063/1.2801981. URL: http://scitation.aip.org/content/aip/journal/jcp/127/22/10.1063/1.2801981.

[134] Mariusz Puchalski, and Krzysztof Pachucki. "Ground state of Li and Be^+ using explicitly correlated functions". In: *Phys. Rev. A* 80 (2009), p. 032521. DOI: 10.1103/PhysRevA.80.032521. URL: https://link.aps.org/doi/10.1103/PhysRevA.80.032521.

[135] Sergiy Bubin et al. "Isotope shifts of the three lowest S1 states of the B+ ion calculated with a finite-nuclear-mass approach and with relativistic and quantum electrodynamics corrections". In: *J. Chem. Phys.* 132.11, 114109 (2010), p. 032521. DOI: 10.1063/1.3358999. URL: http://scitation.aip.org/content/aip/journal/jcp/132/11/10.1063/1.3358999.

[136] Sergiy Bubin and Ludwik Adamowicz. "Accurate variational calculations of the ground 2Po(1s22s22p) and excited 2S(1s22s2p2) and 2Po(1s22s23p) states of singly ionized carbon atom". In: *J. Chem. Phys.* 135.21, 214104 (2011), p. 032521. DOI: 10.1063/1.3664900. URL: http://scitation.aip.org/content/aip/journal/jcp/135/21/10.1063/1.3664900.

[137] Wim Klopper et al. "Sub-meV accuracy in first-principles computations of the ionization potentials and electron affinities of the atoms H to Ne". In: *Phys. Rev. A* 81 (2010), p. 022503. DOI: 10.1103/PhysRevA.81.022503. URL: http://link.aps.org/doi/10.1103/PhysRevA.81.022503.

[138] J. E. Sansonetti and W. C. Martin. "Handbook of Basic Atomic Spectroscopic Data". In: *J. Phys. Chem. Ref. Data* 34.4 (2005), pp. 1559–2259. DOI: 10.1063/1.1800011. URL: http://scitation.aip.org/content/aip/journal/jpcrd/34/4/10.1063/1.1800011.

[139] Miguel A. Morales et al. "Multideterminant Wave Functions in Quantum Monte Carlo". In: *J. Chem. Theory Comput.* 8.7 (2012), pp. 2181–2188. DOI: 10.1021/ct3003404. URL: 10.1021/ct3003404.

[140] Myung Won Lee, Massimo Mella, and Andrew M. Rappe. "Electronic quantum Monte Carlo calculations of atomic forces, vibrations, and anharmonicities". In: *J. Chem. Phys.* 122.24, 244103 (2005), p. 032521. DOI: 10.1063/1.1924690. URL: http://scitation.aip.org/content/aip/journal/jcp/122/24/10.1063/1.1924690.

[141] Keeper L. Sharkey and Ludwik Adamowicz. "An algorithm for nonrelativistic quantum-mechanical finite-nuclear-mass variational calculations of nitrogen atom in L = 0, M = 0 states using all-electrons explicitly correlated Gaussian basis functions". In: *J. Chem. Phys.* 140.17, 174112 (2014), p. 032521.

DOI: 10.1063/1.4873916. URL: http://scitation.aip.org/content/aip/journal/jcp/140/17/10.1063/1.4873916.

[142] George H. Booth and Ali Alavi. "Approaching chemical accuracy using full configuration-interaction quantum Monte Carlo: A study of ionization potentials". In: *J. Chem. Phys.* 132.17, 174104 (2010), p. 032521. DOI: 10.1063/1.3407895. URL: http://scitation.aip.org/content/aip/journal/jcp/132/17/10.1063/1.3407895.

[143] Shiwei Zhang and Henry Krakauer. "Quantum Monte Carlo Method using Phase-Free Random Walks with Slater Determinants". In: *Phys. Rev. Lett.* 90 (13 2003), p. 136401. DOI: 10.1103/PhysRevLett.90.136401. URL: http://link.aps.org/doi/10.1103/PhysRevLett.90.136401.

[144] Norm M. Tubman et al. "Prospects for release-node quantum Monte Carlo". In: *J. Chem. Phys.* 135.18, 184109 (2011), p. 032521. DOI: 10.1063/1.3659143. URL: http://scitation.aip.org/content/aip/journal/jcp/135/18/10.1063/1.3659143.

[145] Norm M. Tubman, Jonathan L. DuBois, and Berni J. Alder. "Recent Results in the Exact Treatment of Fermions at Zero and Finite Temperature". In: *Advances in Quantum Monte Carlo*. Vol. 80. American Physical Society, 2009. Chap. 5, pp. 41–50. DOI: 10.1021/bk-2012-1094.ch004. URL: http://pubs.acs.org/doi/abs/10.1021/bk-2012-1094.ch004.

[146] Wojciech Cencek and Jacek Rychlewski. "Benchmark calculations for He2+ and LiH molecules using explicitly correlated Gaussian functions". In: *Chem. Phys. Lett.* 320.56 (2000), pp. 549 –552. ISSN: 0009-2614. DOI: 10.1016/S0009-2614(00)00303-1. URL: http://www.sciencedirect.com/science/article/pii/S0009261400003031.

[147] Michael E. Harding et al. "Parallel Calculation of CCSD and CCSD(T) Analytic First and Second Derivatives". In: *J. Chem. Theory Comput.* 4.1 (2008), pp. 64–74. DOI: 10.1021/ct700152c. URL: http://dx.doi.org/10.1021/ct700152c.

[148] Jinjun Liu et al. "Determination of the ionization and dissociation energies of the hydrogen molecule". In: *J. Chem. Phys.* 130.17, 174306 (2009), p. 032521. DOI: 10.1063/1.3120443. URL: http://scitation.aip.org/content/aip/journal/jcp/130/17/10.1063/1.3120443.

[149] Sergiy Bubin, Ludwik Adamowicz, and Marcin Molski. "An accurate non-BornOppenheimer calculation of the first purely vibrational transition in LiH molecule". In: *J. Chem. Phys.* 123.13, 134310 (2005), p. 032521. DOI: 10.1063/1.2047487. URL: http://scitation.aip.org/content/aip/journal/jcp/123/13/10.1063/1.2047487.

[150] Sergiy Bubin, Monika Stanke, and Ludwik Adamowicz. "Non-BornOppenheimer calculations of the BH molecule". In: *J. Chem. Phys.* 131.4, 044128 (2009), p. 032521. DOI: 10.1063/1.3195061. URL: http://scitation.aip.org/content/aip/journal/jcp/131/4/10.1063/1.3195061.

[151] K. P. Huber and G. Herzberg. *Molecular Spectra and Molecular Structure: Constants of Diatomic Molecules*. Vol. 80. Van Nostrand Reinhold, New York, 1979, 1979, p. 032521. DOI: 10.1103/PhysRevA.80.032521. URL: https://link.aps.org/doi/10.1103/PhysRevA.80.032521.

[152] Wei-Cheng Tung, Michele Pavanello, and Ludwik Adamowicz. "Very accurate potential energy curve of the LiH molecule". In: *J. Chem. Phys.* 134.6, 064117 (2011), p. 032521. DOI: 10.1063/1.3554211. URL: http://scitation.aip.org/content/aip/journal/jcp/134/6/10.1063/1.3554211.

[153] David Feller, Kirk A. Peterson, and David A. Dixon. "A survey of factors contributing to accurate theoretical predictions of atomization energies and molecular structures". In: *J. Chem. Phys.* 129.20, 204105 (2008), p. 032521. DOI: 10.1063/1.3008061. URL: http://scitation.aip.org/content/aip/journal/jcp/129/20/10.1063/1.3008061.

[154] Jacek Koput. "The ab initio ground-state potential energy function of beryllium monohydride, BeH". In: *J. Chem. Phys.* 135.24, 244308 (2011), p. 032521. DOI: 10.1063/1.3671610. URL: http://scitation.aip.org/content/aip/journal/jcp/135/24/10.1063/1.3671610.

[155] Evangelos Miliordos and Aristides Mavridis. "Ab initio investigation of the electronic structure and bonding of BH, BH, and HBBH molecules". In: *J. Chem. Phys.* 128.14, 144308 (2008), p. 032521. DOI: 10.1063/1.2902284. URL: http://scitation.aip.org/content/aip/journal/jcp/128/14/10.1063/1.2902284.

[156] Sergiy Bubin and Ludwik Adamowicz. "Nonrelativistic molecular quantum mechanics without approximations: Electron affinities of LiH and LiD". In: *J. Chem. Phys.* 121.13 (2004), pp. 6249–6253. DOI: http://dx.doi.org/10.1063/1.1786580. URL: http://scitation.aip.org/content/aip/journal/jcp/121/13/10.1063/1.1786580.

[157] S. M. Wahl et al. "Comparing Jupiter interior structure models to Juno gravity measurements and the role of a dilute core". In: *Geophys. Res. Lett.* 44.10 (2017), pp. 4649–4659. ISSN: 19448007. DOI: 10.1002/2017GL073160. arXiv: 1707.01997. URL: https://link.aps.org/doi/10.1103/PhysRevA.80.032521.

[158] Jeffrey M. McMahon and David M. Ceperley. "Ground-State Structures of Atomic Metallic Hydrogen". In: *Phys. Rev. Lett.* 106 (16 2011), p. 165302. DOI: 10.1103/PhysRevLett.106.165302. URL: https://link.aps.org/doi/10.1103/PhysRevLett.106.165302.

[159] Jeffrey M. McMahon and David M. Ceperley. "Erratum: High-temperature superconductivity in atomic metallic hydrogen [Phys. Rev. B 84 , 144515 (2011)]". In: *Phys. Rev. B* 85.21 (2012), p. 219902. ISSN: 1098-0121. DOI: 10.1103/PhysRevB.85.219902. arXiv: 0504077 [arXiv:cond-mat]. URL: https://link.aps.org/doi/10.1103/PhysRevB.85.219902.

[160] Mario Motta et al. "Towards the Solution of the Many-Electron Problem in Real Materials: Equation of State of the Hydrogen Chain with State-of-the-Art Many-Body Methods". In: *Phys. Rev. X* 7.3 (2017), p. 031059. ISSN: 2160-3308. DOI: 10.1103/PhysRevX.7.031059. arXiv: 1705.01608. URL: https://link.aps.org/doi/10.1103/PhysRevX.7.031059.

[161] Jeffrey M. McMahon et al. "The properties of hydrogen and helium under extreme conditions". In: *Rev. Mod. Phys.* 84 (2012), pp. 1607–1653. DOI: 10.1103/RevModPhys.84.1607. URL: https://link.aps.org/doi/10.1103/RevModPhys.84.1607.

[162] Ranga P. Dias and Isaac F. Silvera. "Observation of the Wigner-Huntington transition to metallic hydrogen". In: *Science* 355.6326 (2017), pp. 715–718. ISSN: 0036-8075. DOI: 10.1126/science.aal1579. arXiv: 1702.04246. URL: https://www.sciencemag.org/lookup/doi/10.1126/science.aal1579.

[163] Chang-Sheng Zha et al. "Raman measurements of phase transitions in dense solid hydrogen and deuterium to 325 GPa." In: *Proc. Natl. Acad. Sci. U. S. A.* 69.7 (2014), pp. 1129–1132. ISSN: 1091-6490. DOI: 10.1073/pnas.1402737111. URL: http://www.ncbi.nlm.nih.gov/pubmed/24639543.

[164] Yuichi Akahama et al. "Evidence from x-ray diffraction of orientational ordering in phase III of solid hydrogen at pressures up to 183 GPa". In: *Phys. Rev. B* 82.6 (2010), p. 060101. ISSN: 1098-0121. DOI: 10.1103/PhysRevB.82.060101. URL: https://link.aps.org/doi/10.1103/PhysRevB.82.060101.

[165] Cheng Ji et al. "Ultrahigh-pressure isostructural electronic transitions in hydrogen". In: *Nature* 573.7775 (2019), pp. 558–562. ISSN: 0028-0836. DOI: 10.1038/s41586-019-1565-9. URL: http://dx.doi.org/10.1038/s41586-019-1565-9http://www.nature.com/articles/s41586-019-1565-9.

[166] M. D. Knudson et al. "Principal Hugoniot, reverberating wave, and mechanical reshock measurements of liquid deuterium to 400 GPa using plate impact techniques". In: *Phys. Rev. B* 69.14 (2004), p. 144209. ISSN: 1098-0121. DOI: 10.1103/PhysRevB.69.144209. URL: https://link.aps.org/doi/10.1103/PhysRevB.69.144209.

[167] M. D. Knudson and M. P. Desjarlais. "High-Precision Shock Wave Measurements of Deuterium: Evaluation of Exchange-Correlation Functionals at the Molecular-to-Atomic Transition". In: *Phys. Rev. Lett.* 118.3 (2017), p. 035501. ISSN: 0031-9007. DOI: 10.1103/PhysRevLett.118.035501. URL: https://link.aps.org/doi/10.1103/PhysRevLett.118.035501.

[168] Chris J. Pickard and Richard J. Needs. "Structure of phase III of solid hydrogen". In: *Nat. Phys.* 3.7 (2007), pp. 473–476. ISSN: 1745-2473. DOI: 10.1038/nphys625. URL: http://www.nature.com/nphys/journal/v3/n7/abs/nphys625.htmlhttp://www.nature.com/articles/nphys625.

[169] Bartomeu Monserrat et al. "Hexagonal structure of phase III of solid hydrogen". In: *Phys. Rev. B* 94.13 (2016), p. 134101. ISSN: 2469-9950. DOI: 10.1103/PhysRevB.94.134101. arXiv: 1609.07486. URL: http://link.aps.org/doi/10.1103/PhysRevB.94.134101https://link.aps.org/doi/10.1103/PhysRevB.94.134101.

[170] Miguel A. Morales et al. "Nuclear quantum effects and nonlocal exchange-correlation functionals applied to liquid hydrogen at high pressure". In: *Phys. Rev. Lett.* 110.6 (2013), pp. 1–6. ISSN: 00319007. DOI: 10.1103/PhysRevLett.110.065702. arXiv: arXiv:1303.6671v1. URL: https://link.aps.org/doi/10.1103/PhysRevA.80.032521.

[171] Hector E. Lorenzana, Isaac F. Silvera, and Kenneth A. Goettel. "Orientational phase transitions in hydrogen at megabar pressures". In: *Phys. Rev. Lett.* 64.16 (1990), pp. 1939–1942. ISSN: 00319007. DOI: 10.1103/PhysRevLett.64.1939. URL: https://link.aps.org/doi/10.1103/PhysRevA.80.032521.

[172] Hector E. Lorenzana, Isaac F. Silvera, and Kenneth A. Goettel. "Evidence for a structural phase transition in solid hydrogen at megabar pressures". In: *Phys. Rev. Lett.* 63.19 (1989), pp. 2080–2083. ISSN: 0031-9007. DOI: 10.1103/PhysRevLett.63.2080. URL: https://link.aps.org/doi/10.1103/PhysRevLett.63.2080.

[173] Isaac F. Silvera and Rinke J. Wijngaarden. "New Low-Temperature Phase of Molecular Deuterium at Ultrahigh Pressure". In: *Phys. Rev. Lett.* 47.1 (1981), pp. 39–42. ISSN: 0031-9007. DOI: 10.1103/PhysRevLett.47.39. URL: https://link.aps.org/doi/10.1103/PhysRevLett.47.39.

[174] Akobuije Chijioke and Isaac F. Silvera. "Megabar-Pressure Infrared Study of Hydrogen Deuteride". In: *Phys. Rev. Lett.* 97.25 (2006), p. 255701. ISSN: 0031-9007. DOI: 10.1103/PhysRevLett.97.255701. URL: https://link.aps.org/doi/10.1103/PhysRevLett.97.255701.

[175] R. J. Hemley and H. K. Mao. "Phase Transition in Solid Molecular Hydrogen at Ultrahigh Pressures". In: *Phys. Rev. Lett.* 61.7 (1988), pp. 857–860. ISSN: 0031-9007. DOI: 10.1103/PhysRevLett.61.857. URL: https://link.aps.org/doi/10.1103/PhysRevLett.61.857.

[176] Lijing Cui et al. "Megabar pressure triple point in solid deuterium". In: *Phys. Rev. Lett.* 72.19 (1994), pp. 3048–3051. ISSN: 0031-9007. DOI: 10.1103/PhysRevLett.72.3048. URL: https://link.aps.org/doi/10.1103/PhysRevLett.72.3048.

[177] Alexander F. Goncharov et al. "New High-Pressure Excitations in Parahydrogen". In: *Phys. Rev. Lett.* 80.1 (1998), pp. 101–104. ISSN: 0031-9007. DOI: 10.1103/PhysRevLett.80.101. URL: https://link.aps.org/doi/10.1103/PhysRevLett.80.101.

[178] Ranga P. Dias, Ori Noked, and Isaac F. Silvera. "Quantum phase transition in solid hydrogen at high pressure". In: *Phys. Rev. B* 100.18 (2019), p. 184112. ISSN: 2469-9950. DOI: 10.1103/PhysRevB.100.184112. URL: https://link.aps.org/doi/10.1103/PhysRevB.100.184112.

[179] Chang-sheng Zha et al. "High-Pressure Measurements of Hydrogen Phase IV Using Synchrotron Infrared Spectroscopy". In: *Phys. Rev. Lett.* 110.21 (2013), p. 217402. ISSN: 0031-9007. DOI: 10.1103/PhysRevLett.110.217402. URL: https://link.aps.org/doi/10.1103/PhysRevLett.110.217402.

[180] M. I. Eremets et al. "Semimetallic molecular hydrogen at pressure above 350 GPa". In: *Nat. Phys.* 15.12 (2019), pp. 1246–1249. ISSN: 17452481. DOI: 10.1038/s41567-019-0646-x. arXiv: 1708.05217. URL: http://dx.doi.org/10.1038/s41567-019-0646-x.

[181] Isaac F. Silvera, Mohamed Zaghoo, and Ashkan Salamat. "Reply to Comment on Evidence of a first-order phase transition to metallic hydrogen' ". In: *Phys. Rev. B* 96.23 (2017), p. 237102. ISSN: 2469-9950. DOI: 10.1103/PhysRevB.96.237102. URL: https://link.aps.org/doi/10.1103/PhysRevB.96.237102.

[182] R. M. Hazen et al. "Single-crystal x-ray diffraction ofn-H2 at high pressure". In: *Phys. Rev. B* 36.7 (1987), pp. 3944–3947. ISSN: 0163-1829. DOI: 10.1103/PhysRevB.36.3944. URL: https://link.aps.org/doi/10.1103/PhysRevB.36.3944.

[183] H. K. MAao et al. "Synchrotron X-ray Diffraction Measurements of Single-Crystal Hydrogen to 26.5 Gigapascals". In: *Science* 239.4844 (1988), pp. 1131–1134. ISSN: 0036-8075. DOI: 10.1126/science.239.4844.1131. URL: https://www.sciencemag.org/lookup/doi/10.1126/science.239.4844.1131.

[184] P. Loubeyre et al. “X-ray diffraction and equation of state of hydrogen at megabar pressures”. In: *Nature* 383.6602 (1996), pp. 702–704. ISSN: 0028-0836. DOI: 10.1038/383702a0. URL: https://www.nature.com/articles/383702a0.pdfhttp://www.nature.com/articles/383702a0.

[185] H. Kawamura et al. “X-ray powder diffraction from solid deuterium”. In: *J. Phys. Condens. Matter* 14.44 (2002), pp. 10407–10410. ISSN: 0953-8984. DOI: 10.1088/0953-8984/14/44/301. URL: http://stacks.iop.org/0953-8984/14/i=44/a=301?key=crossref.f7ecb62bd6245af471fba020c86831b0.

[186] Igor Goncharenko and Paul Loubeyre. “Neutron and X-ray diffraction study of the broken symmetry phase transition in solid deuterium”. In: *Nature* 435.7046 (2005), pp. 1206–1209. ISSN: 0028-0836. DOI: 10.1038/nature03699. URL: http://www.nature.com/articles/nature03699.

[187] M. I. Eremets and I. A. Trojan. “Evidence of maximum in the melting curve of hydrogen at megabar pressures”. In: *JETP Lett.* 89.4 (2009), pp. 174–179. ISSN: 0021-3640. DOI: 10.1134/S0021364009040031. URL: http://link.springer.com/10.1134/S0021364009040031.

[188] Ross T. Howie et al. “Mixed Molecular and Atomic Phase of Dense Hydrogen”. In: *Phys. Rev. Lett.* 108.12 (2012), p. 125501. ISSN: 0031-9007. DOI: 10.1103/PhysRevLett.108.125501. URL: https://link.aps.org/doi/10.1103/PhysRevLett.108.125501.

[189] Susanne Raynor. “Novel ab initio self-consistent-field approach to molecular solids under pressure. II. Solid H_2 under high pressure”. In: *J. Chem. Phys.* 87.5 (1987), pp. 2795–2799. ISSN: 0021-9606. DOI: 10.1063/1.453067. URL: http://aip.scitation.org/doi/10.1063/1.453067.

[190] T. W. Barbee, Marvin L. Cohen, and José Luís Martins. “Theory of high-pressure phases of hydrogen”. In: *Phys. Rev. Lett.* 62.10 (1989), pp. 1150–1153. ISSN: 0031-9007. DOI: 10.1103/PhysRevLett.62.1150. URL: https://link.aps.org/doi/10.1103/PhysRevLett.62.1150.

[191] Efthimios Kaxiras, Jeremy Broughton, and R. J. Hemley. “Onset of metallization and related transitions in solid hydrogen”. In: *Phys. Rev. Lett.* 67.9 (1991), pp. 1138–1141. ISSN: 0031-9007. DOI: 10.1103/PhysRevLett.67.1138. URL: https://link.aps.org/doi/10.1103/PhysRevLett.67.1138.

[192] E. Kaxiras and J. Broughton. “Energetics of Ordered Structures in Molecular Hydrogen”. In: *Europhys. Lett.* 17.2 (1992), pp. 151–155. ISSN: 0295-5075. DOI: 10.1209/0295-5075/17/2/012. URL: https://iopscience.iop.org/article/10.1209/0295-5075/17/2/012.

[193] Hitose Nagara and Tuto Nakamura. “Stable phases of solid hydrogen at megabar pressures and at zero temperature”. In: *Phys. Rev. Lett.* 68.16 (1992), pp. 2468–2471. ISSN: 0031-9007. DOI: 10.1103/PhysRevLett.68.2468. URL: https://link.aps.org/doi/10.1103/PhysRevLett.68.2468.

[194] B. Edwards, N. W. Ashcroft, and T. Lenosky. "Layering transitions and the structure of dense hydrogen". In: *Europhys. Lett.* 34.7 (1996), pp. 519–524. ISSN: 0295-5075. DOI: 10.1209/epl/i1996-00489-5. URL: https://iopscience.iop.org/article/10.1209/epl/i1996-00489-5.

[195] Kurt A. Johnson and N. W. Ashcroft. "Structure and bandgap closure in dense hydrogen". In: *Nature* 403.6770 (2000), pp. 632–635. ISSN: 0028-0836. DOI: 10.1038/35001024. URL: http://www.ncbi.nlm.nih.gov/pubmed/10688193http://www.nature.com/articles/35001024.

[196] T. Cui, Y. Ma, and G. Zou. "Crystal structure of solid molecular hydrogen under high pressures". In: *J. Phys. Condens. Matter* 14.44 (2002), pp. 10901–10906. ISSN: 0953-8984. DOI: 10.1088/0953-8984/14/44/398. URL: https://iopscience.iop.org/article/10.1088/0953-8984/14/44/398.

[197] Sam Azadi and Thomas D. Kühne. "Unconventional phase III of high-pressure solid hydrogen". In: *Phys. Rev. B* 100.15 (2019), p. 155103. ISSN: 2469-9950. DOI: 10.1103/PhysRevB.100.155103. arXiv: 1906.10854. URL: https://link.aps.org/doi/10.1103/PhysRevB.100.155103.

[198] Ke Liao et al. "A comparative study using state-of-the-art electronic structure theories on solid hydrogen phases under high pressures". In: *npj Comput. Mater.* 5.1 (2019), p. 110. ISSN: 2057-3960. DOI: 10.1038/s41524-019-0243-7. URL: http://dx.doi.org/10.1038/s41524-019-0243-7http://www.nature.com/articles/s41524-019-0243-7.

[199] Jonathan H. Lloyd-Williams and Bartomeu Monserrat. "Lattice dynamics and electron-phonon coupling calculations using nondiagonal supercells". In: *Phys. Rev. B* 92.18 (2015), p. 184301. ISSN: 1098-0121. DOI: 10.1103/PhysRevB.92.184301. arXiv: 1510.04418. URL: https://link.aps.org/doi/10.1103/PhysRevB.92.184301.

[200] David M. Ceperley and B. J. Alder. "Ground state of solid hydrogen at high pressures". In: *Phys. Rev. B* 36.4 (1987), pp. 2092–2106. ISSN: 0163-1829. DOI: 10.1103/PhysRevB.36.2092. URL: http://link.aps.org/doi/10.1103/PhysRevB.36.2092.

[201] V Natoli, R M Martin, and D M Ceperley. "Crystal Structure of Atomic Hydrogen". In: *Phys. Rev. Lett.* 70.13 (1993), p. 1952. ISSN: 0031-9007. DOI: 10.1103/PhysRevLett.70.1952. URL: file:///home/jarajar/Desktop/papers/General{_}physics/MetallicHydrogen.pdf.

[202] L. Reatto. "Structure of the ground-state wave function of quantum fluids and "exact" numerical methods". In: *Phys. Rev. B* 26.1 (1982), pp. 130–137. ISSN: 0163-1829. DOI: 10.1103/PhysRevB.26.130. URL: https://link.aps.org/doi/10.1103/PhysRevB.26.130.

[203] N. D. Drummond et al. *Data for "Quantum Monte Carlo study of the phase diagram of solid molecular hydrogen at extreme pressures"*. July 8, 2015. DOI: 10.1103/PhysRevA.80.032521. URL: https://www.repository.cam.ac.uk/handle/1810/248864.

[204] Hendra Kwee, Shiwei Zhang, and Henry Krakauer. "Finite-Size Correction in Many-Body Electronic Structure Calculations". In: *Phys. Rev. Lett.* 100.12 (2008), p. 126404. ISSN: 0031-9007. DOI: 10.1103/PhysRevLett.100.126404. URL: https://link.aps.org/doi/10.1103/PhysRevLett.100.126404.

[205] P. Eisenberger and P. M. Platzman. "Compton Scattering of X-Rays from Bound Electrons". In: *Phys. Rev. A* 2 (2 1970), pp. 415–423. DOI: 10.1103/PhysRevA.2.415. URL: https://link.aps.org/doi/10.1103/PhysRevA.2.415.

[206] P. Eisenberger et al. "X-Ray Compton Profiles of Li and Na: Theory and Experiments". In: *Phys. Rev. B* 6 (10 1972), pp. 3671–3681. DOI: 10.1103/PhysRevB.6.3671. URL: https://link.aps.org/doi/10.1103/PhysRevB.6.3671.

[207] Y. Sakurai et al. "High-resolution Compton scattering study of Li: Asphericity of the Fermi surface and electron correlation effects". In: *Phys. Rev. Lett.* 74.12 (1995), pp. 2252–2255. ISSN: 00319007. DOI: 10.1103/PhysRevLett.74.2252. URL: https://link.aps.org/doi/10.1103/PhysRevA.80.032521.

[208] W. Schülke et al. "Electron momentum-space densities of Li metal: A high-resolution Compton-scattering study". In: *Phys. Rev. B* 54.20 (1996), pp. 14381–14395. ISSN: 1550235X. DOI: 10.1103/PhysRevB.54.14381. URL: https://link.aps.org/doi/10.1103/PhysRevA.80.032521.

[209] K. J. Chen et al. "Investigation of temperature dependence of Compton profiles in lithium". In: *Solid State Commun.* 110.7 (1999), pp. 357–361. ISSN: 00381098. DOI: 10.1016/S0038-1098(99)00094-0. URL: https://link.aps.org/doi/10.1103/PhysRevA.80.032521.

[210] C. Sternemann et al. "Temperature influence on the valence Compton profiles of aluminum and lithium". In: *Phys. Rev. B* 63 (9 2001), p. 094301. DOI: 10.1103/PhysRevB.63.094301. URL: https://link.aps.org/doi/10.1103/PhysRevB.63.094301.

[211] Yoshikazu Tanaka et al. "Reconstructed three-dimensional electron momentum density in lithium: A Compton scattering study". In: *Phys. Rev. B* 63 (4 2001), p. 045120. DOI: 10.1103/PhysRevB.63.045120. URL: https://link.aps.org/doi/10.1103/PhysRevB.63.045120.

[212] K. Hämäläinen et al. "High resolution Compton scattering study of Be". In: *Phys. Rev. B* 54 (8 1996), pp. 5453–5459. DOI: 10.1103/PhysRevB.54.5453. URL: https://link.aps.org/doi/10.1103/PhysRevB.54.5453.

[213] S. Huotari et al. “Energy dependence of experimental Be Compton profiles”. In: *Phys. Rev. B* 62.12 (2000), pp. 7956–7963. ISSN: 01631829. DOI: 10.1103/PhysRevB.62.7956. URL: https://link.aps.org/doi/10.1103/PhysRevA.80.032521.

[214] Simo Huotari et al. “Momentum Distribution and Renormalization Factor in Sodium and the Electron Gas”. In: *Phys. Rev. Lett.* 105 (8 2010), p. 086403. DOI: 10.1103/PhysRevLett.105.086403. URL: https://link.aps.org/doi/10.1103/PhysRevLett.105.086403.

[215] S.B. Dugdale and T. Jarlborg. “Thermal disorder versus correlation in Compton profiles from alkali metals”. In: *Solid State Commun.* 105.5 (1998), pp. 283 –287. ISSN: 0038-1098. DOI: https://doi.org/10.1016/S0038-1098(97)10112-0. URL: http://www.sciencedirect.com/science/article/pii/S0038109897101120.

[216] Tunna Baruah, Rajendra R. Zope, and Anjali Kshirsagar. “Full-potential LAPW calculation of electron momentum density and related properties of Li”. In: *Phys. Rev. B* 60 (15 1999), pp. 10770–10775. DOI: 10.1103/PhysRevB.60.10770. URL: https://link.aps.org/doi/10.1103/PhysRevB.60.10770.

[217] Helmut Bross. “Electronic structure of Li with emphasis on the momentum density and the Compton profile”. In: *Phys. Rev. B* 72 (11 2005), p. 115109. DOI: 10.1103/PhysRevB.72.115109. URL: https://link.aps.org/doi/10.1103/PhysRevB.72.115109.

[218] I. Makkonen, M. Hakala, and M. J. Puska. “Calculation of valence electron momentum densities using the projector augmented-wave method”. In: *J. Phys. Chem. Solids* 66.6 (2005), pp. 1128–1135. ISSN: 00223697. DOI: 10.1016/j.jpcs.2005.02.009. URL: https://link.aps.org/doi/10.1103/PhysRevA.80.032521.

[219] E. Klevak et al. “Finite-temperature calculations of the Compton profile of Be, Li, and Si”. In: *Phys. Rev. B* 94 (21 2016), p. 214201. DOI: 10.1103/PhysRevB.94.214201. URL: https://link.aps.org/doi/10.1103/PhysRevB.94.214201.

[220] Michael Sekania et al. “Scaling behavior of the Compton profile of alkali metals”. In: *Physica A* 489 (2018), pp. 18–27. ISSN: 03784371. DOI: 10.1016/j.physa.2017.07.018. URL: http://dx.doi.org/10.1016/j.physa.2017.07.018.

[221] Claudia Filippi and David M. Ceperley. “Quantum Monte Carlo calculation of Compton profiles of solid lithium”. In: *Phys. Rev. B* 59 (12 1999), pp. 7907–7916. DOI: 10.1103/PhysRevB.59.7907. URL: https://link.aps.org/doi/10.1103/PhysRevB.59.7907.

[222] Kubo Yasunori. "Effects of Electron Correlations on Compton Profiles of Li and Na in the GW Approximation". In: *J. Phys. Soc. Jpn.* 66 (1997), pp. 2236–2239. DOI: 10.1143/JPSJ.66.2236. URL: https://link.aps.org/doi/10.1103/PhysRevA.80.032521.

[223] W. Schülke. "Comment on "Effects of Electron Correlation...." by Y. Kubo, J. Phys. Soc. Jpn. 66 (1997) 2236". In: *J. Phys. Soc. Jpn.* 68 (1999), pp. 2470–2471. DOI: 10.1143/JPSJ.68.2470. URL: https://link.aps.org/doi/10.1103/PhysRevA.80.032521.

[224] A. G. Eguiluz, W. Ku, and J. M. Sullivan. "Dynamical response of correlated electrons in solids probed by inelastic scattering experiments: An ab initio theoretical perspective". In: *J. Phys. Chem. Solids* 61.3 (2000), pp. 383–390. ISSN: 00223697. DOI: 10.1016/S0022-3697(99)00322-4. URL: https://link.aps.org/doi/10.1103/PhysRevA.80.032521.

[225] Valerio Olevano et al. "Momentum distribution and Compton profile by the ab initio GW approximation". In: *Phys. Rev. B* 86 (19 2012), p. 195123. DOI: 10.1103/PhysRevB.86.195123. URL: https://link.aps.org/doi/10.1103/PhysRevB.86.195123.

[226] L. Lam and P. M. Platzman. "Momentum density and Compton profile of the inhomogeneous interacting electronic system. I. Formalism". In: *Phys. Rev. B* 9.12 (1974), pp. 5122–5127. ISSN: 01631829. DOI: 10.1103/PhysRevB.9.5122. URL: https://link.aps.org/doi/10.1103/PhysRevA.80.032521.

[227] W. Schülke et al. "Ultra-high Resolution Compton Scattering of Li Metal : Evaluation with Respect to the Correlation Corrected Occupation Number Density". In: *Z. Phys. Chem.* 215.11 (2001), pp. 1353–1366. DOI: 10.1524/zpch.2001.215.11.1353. URL: https://link.aps.org/doi/10.1103/PhysRevA.80.032521.

[228] C. Sternemann et al. "Final-state interaction in Compton scattering from electron liquids". In: *Phys. Rev. B* 62.12 (2000), R7687–R7690. ISSN: 01631829. DOI: 10.1103/PhysRevB.62.R7687. URL: https://link.aps.org/doi/10.1103/PhysRevA.80.032521.

[229] J. A. Soininen, K. Hämäläinen, and S. Manninen. "Final-state electron-electron interaction in Compton scattering". In: *Phys. Rev. B* 64 (12 2001), p. 125116. DOI: 10.1103/PhysRevB.64.125116. URL: https://link.aps.org/doi/10.1103/PhysRevB.64.125116.

[230] Markus Holzmann et al. "Momentum distribution of the homogeneous electron gas". In: *Phys. Rev. Lett.* 107.11 (2011), pp. 1–5. ISSN: 00319007. DOI: 10.1103/PhysRevLett.107.110402. arXiv: 1105.2338. URL: https://link.aps.org/doi/10.1103/PhysRevA.80.032521.

[231] N Hiraoka et al. "Direct observation of the momentum distribution and renormalization factor in lithium". In: *Phys. Rev. B* 101.16 (2020), p. 165124. ISSN: 2469-9950. DOI: 10.1103/PhysRevB.101.165124. URL: https://link.aps.org/doi/10.1103/PhysRevB.101.165124.

[232] N. D. Drummond, M. D. Towler, and R. J. Needs. "Jastrow correlation factor for atoms, molecules, and solids". In: *Phys. Rev. B* 70 (23 2004), p. 235119. DOI: 10.1103/PhysRevB.70.235119. URL: https://link.aps.org/doi/10.1103/PhysRevB.70.235119.

[233] M. Burkatzki, C. Filippi, and M. Dolg. "Energy-consistent pseudopotentials for quantum Monte Carlo calculations". In: *J. Chem. Phys.* 126.23 (2007), p. 032521. ISSN: 00219606. DOI: 10.1063/1.2741534. URL: https://link.aps.org/doi/10.1103/PhysRevA.80.032521.

[234] W. L. McMillan. "Ground State of Liquid He^4". In: *Phys. Rev.* 138 (2A 1965), A442–A451. DOI: 10.1103/PhysRev.138.A442. URL: https://link.aps.org/doi/10.1103/PhysRev.138.A442.

[235] G. Ortiz, D. M. Ceperley, and R. M. Martin. "New stochastic method for systems with broken time-reversal symmetry: 2D fermions in a magnetic field". In: *Phys. Rev. Lett.* 71 (17 1993), pp. 2777–2780. DOI: 10.1103/PhysRevLett.71.2777. URL: https://link.aps.org/doi/10.1103/PhysRevLett.71.2777.

[236] Simone Chiesa et al. "Finite-Size Error in Many-Body Simulations with Long-Range Interactions". In: *Phys. Rev. Lett.* 97 (7 2006), p. 076404. DOI: 10.1103/PhysRevLett.97.076404. URL: https://link.aps.org/doi/10.1103/PhysRevLett.97.076404.

[237] Yubo Yang et al. "Electronic band gaps from quantum Monte Carlo methods". In: *Phys. Rev. B* 101.8 (2020), p. 085115. ISSN: 2469-9950. DOI: 10.1103/PhysRevB.101.085115. arXiv: 1910.07531. URL: http://arxiv.org/abs/1910.07531https://link.aps.org/doi/10.1103/PhysRevB.101.085115.

[238] M. I. Baskes. "Modified embedded-atom potentials for cubic materials and impurities". In: *Phys. Rev. B* 46.5 (1992), pp. 2727–2742. ISSN: 0163-1829. DOI: 10.1103/PhysRevB.46.2727. URL: https://link.aps.org/doi/10.1103/PhysRevB.46.2727.

[239] Claudia Filippi and David M. Ceperley. "Path-integral Monte Carlo calculation of the kinetic energy of condensed lithium". In: *Phys. Rev. B* 57.1 (1998), pp. 252–257. ISSN: 1550235X. DOI: 10.1103/PhysRevB.57.252. URL: https://link.aps.org/doi/10.1103/PhysRevA.80.032521.

[240] Steve Plimpton. "Fast Parallel Algorithms for Short-Range Molecular Dynamics". In: *J. of Comp. Phys.* 117.1 (1995), pp. 1 –19. ISSN: 0021-9991. DOI: https://doi.org/10.1006/jcph.1995.1039. URL: http://www.sciencedirect.com/science/article/pii/S002199918571039X.

[241] Paolo Giannozzi et al. "QUANTUM ESPRESSO: A modular and open-source software project for quantum simulations of materials". In: *J. Phys. Condens. Matter* 21.39 (2009), p. 032521. ISSN: 09538984. DOI: 10.1088/0953-8984/21/39/395502. arXiv: 0906.2569. URL: https://link.aps.org/doi/10.1103/PhysRevA.80.032521.

[242] Paolo Giannozzi et al. "Advanced capabilities for materials modelling with QUANTUM ESPRESSO". In: *Journal of Physics: Condensed Matter* 29.46 (2017), p. 465901. DOI: 10.1103/PhysRevA.80.032521. URL: http://stacks.iop.org/0953-8984/29/i=46/a=465901.

[243] Qiming Sun et al. *PySCF: the Python-based simulations of chemistry framework*. 2017. DOI: 10.1002/wcms.1340. URL: https://onlinelibrary.wiley.com/doi/abs/10.1002/wcms.1340.

[244] Jeongnim Kim et al. "QMCPACK: An open source ab initio quantum Monte Carlo package for the electronic structure of atoms, molecules and solids". In: *J. Phys. Condens. Matter* 30.19 (2018), p. 032521. ISSN: 1361648X. DOI: 10.1088/1361-648X/aab9c3. arXiv: 1802.06922. URL: https://link.aps.org/doi/10.1103/PhysRevA.80.032521.

[245] Jaron T. Krogel. "Nexus: A modular workflow management system for quantum simulation codes". In: *Comput. Phys. Commun.* 198 (2016), pp. 154–168. ISSN: 00104655. DOI: 10.1016/j.cpc.2015.08.012. URL: http://dx.doi.org/10.1016/j.cpc.2015.08.012.

[246] Yoshio Waseda. "The structure of liquids, amorphous solids and solid fast ion conductors". In: *Progress in Materials Science* 26.1 (1981), pp. 1 –122. ISSN: 0079-6425. DOI: https://doi.org/10.1016/0079-6425(81)90003-7. URL: http://www.sciencedirect.com/science/article/pii/0079642581900037.

[247] A V Mokshin and B N Galimzyanov. "Self-consistent description of local density dynamics in simple liquids. The case of molten lithium". In: *Journal of Physics: Condensed Matter* 30.8 (2018), p. 085102. DOI: 10.1088/1361-648x/aaa7bc. URL: https://doi.org/10.1088%2F1361-648x%2Faaa7bc.

[248] K. M. Rasch and L. Mitas. "Fixed-node diffusion Monte Carlo method for lithium systems". In: *Phys. Rev. B* 92 (4 2015), p. 045122. DOI: 10.1103/PhysRevB.92.045122. URL: https://link.aps.org/doi/10.1103/PhysRevB.92.045122.

[249] H. Bross. "The local density approximation limit of the momentum density and the Compton profiles of Al". In: *J. Phys. Condens. Matter* 16.41 (2004), pp. 7363–7378. ISSN: 09538984. DOI: 10.1088/0953-8984/16/41/016. URL: https://link.aps.org/doi/10.1103/PhysRevA.80.032521.

[250] Helmut Bross. "LDA and GGA Investigations of Some Ground-State Properties and the Compton Profile of Copper with the All-Electron MAPW Method". In: *ISRN Mater. Sci.* 2012 (2012), pp. 1–13. ISSN: 2090-6099. DOI: 10.5402/2012/975897. URL: http://www.hindawi.com/journals/isrn/2012/975897/https://www.hindawi.com/archive/2012/975897/.

[251] M. B. Hunt, P. H. P. Reinders, and M. Springford. "A de Haas-van Alphen effect study of the Fermi surface of lithium". In: *Journal of Physics: Condensed Matter* 1.37 (1989), pp. 6589–6602. DOI: 10.1088/0953-8984/1/37/007. URL: https://doi.org/10.1088%2F0953-8984%2F1%2F37%2F007.

[252] A. H. MacDonald. "Density functional approximation for the quasiparticle properties of simple metals. II. Application to Li, Rb and Cs". In: *Journal of Physics F: Metal Physics* 10.8 (1980), pp. 1737–1751. DOI: 10.1088/0305-4608/10/8/011. URL: https://doi.org/10.1088%2F0305-4608%2F10%2F8%2F011.

[253] S. Engelsberg and J. R. Schrieffer. "Coupled Electron-Phonon System". In: *Phys. Rev.* 131 (3 1963), pp. 993–1008. DOI: 10.1103/PhysRev.131.993. URL: https://link.aps.org/doi/10.1103/PhysRev.131.993.

[254] S. Huotari et al. "Asymmetry of Compton profiles". In: *J. Phys. Chem. Solids* 62.12 (2001), pp. 2205–2213. ISSN: 00223697. DOI: 10.1016/S0022-3697(01)00179-2. URL: https://link.aps.org/doi/10.1103/PhysRevA.80.032521.

[255] John P. Perdew. "Density functional theory and the band gap problem". In: *Int. J. Quantum Chem.* 28.S19 (1985), pp. 497–523. ISSN: 00207608. DOI: 10.1002/qua.560280846. URL: http://doi.wiley.com/10.1002/qua.560280846.

[256] W. M C Foulkes et al. "Quantum Monte Carlo simulations of solids". In: *Rev. Mod. Phys.* 73.1 (2001), pp. 33–83. ISSN: 00346861. DOI: 10.1103/RevModPhys.73.33. URL: https://link.aps.org/doi/10.1103/PhysRevA.80.032521.

[257] Jindřich Kolorenč and Lubos Mitas. "Applications of quantum Monte Carlo methods in condensed systems". In: *Reports Prog. Phys.* 74.2 (2011), p. 026502. ISSN: 0034-4885. DOI: 10.1088/0034-4885/74/2/026502. arXiv: 1010.4992. URL: https://iopscience.iop.org/article/10.1088/0034-4885/74/2/026502.

[258] Lucas K. Wagner and David M. Ceperley. "Discovering correlated fermions using quantum Monte Carlo". In: *Reports Prog. Phys.* 79.9 (2016), p. 094501. ISSN: 0034-4885. DOI: 10.1088/0034-4885/79/9/094501. arXiv: 1602.01344. URL: http://arxiv.org/abs/1602.01344{\%}5Cnhttp://stacks.iop.org/0034-4885/79/i=9/a=094501?key=crossref.1f8ebfedf7db8e775e7179ded0e32d11.

[259] Michele Ruggeri, Pablo López Ríos, and Ali Alavi. "Correlation energies of the high-density spin-polarized electron gas to meV accuracy". In: *Phys. Rev. B* 98.16 (2018), p. 161105. ISSN: 2469-9950. DOI: 10.1103/PhysRevB.98.161105. arXiv: 1804.04938. URL: https://doi.org/10.1103/PhysRevB.98.161105https://link.aps.org/doi/10.1103/PhysRevB.98.161105.

[260] James J. Shepherd and Andreas Grüneis. "Many-Body Quantum Chemistry for the Electron Gas: Convergent Perturbative Theories". In: *Phys. Rev. Lett.* 110.22 (2013), p. 226401. ISSN: 0031-9007. DOI: 10.1103/PhysRevLett.110.226401. arXiv: 1310.6059. URL: https://link.aps.org/doi/10.1103/PhysRevLett.110.226401.

[261] Thomas Gruber et al. "Applying the Coupled-Cluster Ansatz to Solids and Surfaces in the Thermodynamic Limit". In: *Phys. Rev. X* 8.2 (2018), p. 021043. ISSN: 2160-3308. DOI: 10.1103/PhysRevX.8.021043. URL: https://doi.org/10.1103/PhysRevX.8.021043https://link.aps.org/doi/10.1103/PhysRevX.8.021043.

[262] P. R. C. Kent et al. "Quantum Monte Carlo calculations of the one-body density matrix and excitation energies of silicon". In: *Phys. Rev. B* 57.24 (1998), pp. 15293–15302. ISSN: 0163-1829. DOI: 10.1103/PhysRevB.57.15293. URL: https://link.aps.org/doi/10.1103/PhysRevB.57.15293.

[263] P. R. C. Kent et al. "Finite-size errors in quantum many-body simulations of extended systems". In: *Phys. Rev. B* 59.3 (1999), pp. 1917–1929. ISSN: 0163-1829. DOI: 10.1103/PhysRevB.59.1917. URL: https://link.aps.org/doi/10.1103/PhysRevB.59.1917.

[264] Chandrima Mitra et al. "Many-body ab initio diffusion quantum Monte Carlo applied to the strongly correlated oxide NiO". In: *J. Chem. Phys.* 143.16 (2015), p. 164710. ISSN: 0021-9606. DOI: 10.1063/1.4934262. URL: http://dx.doi.org/10.1063/1.4934262http://aip.scitation.org/doi/10.1063/1.4934262.

[265] G. Makov and M. C. Payne. "Periodic boundary conditions in ab initio calculations". In: *Phys. Rev. B* 51.7 (1995), pp. 4014–4022. ISSN: 0163-1829. DOI: 10.1103/PhysRevB.51.4014. URL: https://link.aps.org/doi/10.1103/PhysRevB.51.4014https://link.aps.org/doi/10.1103/PhysRevB.51.13538.

[266] G. E. Engel, Yongkyung Kwon, and Richard M. Martin. "Quasiparticle bands in a two-dimensional crystal found by GW and quantum Monte Carlo calculations". In: *Phys. Rev. B* 51.19 (1995), pp. 13538–13546. ISSN: 01631829. DOI: 10.1103/PhysRevB.51.13538. URL: https://link.aps.org/doi/10.1103/PhysRevA.80.032521.

[267] Luboš Mitáš and Richard M. Martin. "Quantum Monte Carlo of nitrogen: Atom, dimer, atomic, and molecular solids". In: *Phys. Rev. Lett.* 72.15 (1994), pp. 2438–2441. ISSN: 0031-9007. DOI: 10.1103/PhysRevLett.72.2438. URL: https://link.aps.org/doi/10.1103/PhysRevLett.72.2438.

[268] A. J. Williamson et al. "Diffusion quantum Monte Carlo calculations of the excited states of silicon". In: *Phys. Rev. B* 57.19 (1998), pp. 12140–12144. ISSN: 0163-1829. DOI: 10.1103/PhysRevB.57.12140. URL: https://link.aps.org/doi/10.1103/PhysRevB.57.12140.

[269] M. D. Towler, Randolph Q. Hood, and R. J. Needs. "Minimum principles and level splitting in quantum Monte Carlo excitation energies: Application to diamond". In: *Phys. Rev. B* 62.4 (2000), pp. 2330–2337. ISSN: 0163-1829. DOI: 10.1103/PhysRevB.62.2330. URL: https://www.cambridge.org/core/product/identifier/S0079497X00000487/type/journal{_}articlehttps://link.aps.org/doi/10.1103/PhysRevB.62.2330.

[270] Jindřich Kolorenč and Lubos Mitas. "Quantum Monte Carlo Calculations of Structural Properties of FeO Under Pressure". In: *Phys. Rev. Lett.* 101.18 (2008), p. 185502. ISSN: 0031-9007. DOI: 10.1103/PhysRevLett.101.185502. URL: https://link.aps.org/doi/10.1103/PhysRevLett.101.185502.

[271] Fengjie Ma, Shiwei Zhang, and Henry Krakauer. "Excited state calculations in solids by auxiliary-field quantum Monte Carlo". In: *New J. Phys.* 15.9 (2013), p. 093017. ISSN: 1367-2630. DOI: 10.1088/1367-2630/15/9/093017. arXiv: 1211.4635. URL: http://stacks.iop.org/1367-2630/15/i=9/a=093017?key=crossref.70e301a31ac3cf9ea3a531bbd27e6d6ehttps://iopscience.iop.org/article/10.1088/1367-2630/15/9/093017.

[272] Lucas K. Wagner and Peter Abbamonte. "Effect of electron correlation on the electronic structure and spin-lattice coupling of high-Tc cuprates: Quantum Monte Carlo calculations". In: *Phys. Rev. B* 90.12 (2014), p. 125129. ISSN: 1098-0121. DOI: 10.1103/PhysRevB.90.125129. arXiv: 1402.4680. URL: https://link.aps.org/doi/10.1103/PhysRevB.90.125129.

[273] Jaehyung Yu, Lucas K. Wagner, and Elif Ertekin. "Towards a systematic assessment of errors in diffusion Monte Carlo calculations of semiconductors: Case study of zinc selenide and zinc oxide". In: *J. Chem. Phys.* 143.22 (2015), p. 224707. ISSN: 0021-9606. DOI: 10.1063/1.4937421. arXiv: 1509.04114. URL: http://dx.doi.org/10.1063/1.4937421http://aip.scitation.org/doi/10.1063/1.4937421.

[274] Huihuo Zheng and Lucas K. Wagner. "Computation of the Correlated Metal-Insulator Transition in Vanadium Dioxide from First Principles". In: *Phys. Rev. Lett.* 114.17 (2015), p. 176401. ISSN: 0031-

9007. DOI: 10.1103/PhysRevLett.114.176401. arXiv: 1310.1066. URL: https://link.aps.org/doi/10.1103/PhysRevLett.114.176401.

[275] T. Frank et al. "Many-Body Quantum Monte Carlo Study of 2D Materials: Cohesion and Band Gap in Single-Layer Phosphorene". In: *Phys. Rev. X* 9.1 (2019), p. 011018. ISSN: 2160-3308. DOI: 10.1103/PhysRevX.9.011018. URL: https://link.aps.org/doi/10.1103/PhysRevX.9.011018.

[276] R. J. Hunt et al. "Quantum Monte Carlo calculations of energy gaps from first principles". In: *Phys. Rev. B* 98.7 (2018), p. 075122. ISSN: 2469-9950. DOI: 10.1103/PhysRevB.98.075122. URL: https://link.aps.org/doi/10.1103/PhysRevB.98.075122.

[277] W. M. C. Foulkes, Randolph Q. Hood, and R. J. Needs. "Symmetry constraints and variational principles in diffusion quantum Monte Carlo calculations of excited-state energies". In: *Phys. Rev. B* 60.7 (1999), pp. 4558–4570. ISSN: 0163-1829. DOI: 10.1103/PhysRevB.60.4558. URL: https://link.aps.org/doi/10.1103/PhysRevB.60.4558.

[278] Sam Azadi, N. D. Drummond, and W. M.C. Foulkes. "Nature of the metallization transition in solid hydrogen". In: *Phys. Rev. B* 95.3 (2017), pp. 1–11. ISSN: 24699969. DOI: 10.1103/PhysRevB.95.035142. URL: https://link.aps.org/doi/10.1103/PhysRevA.80.032521.

[279] D. Pine and P. Nozières. *The Theory of Quantum Liquids*. Vol. I. Redwood City, CA: Addison-Wesley, 1989, p. 032521. DOI: 10.1103/PhysRevA.80.032521. URL: https://link.aps.org/doi/10.1103/PhysRevA.80.032521.

[280] Walter Kohn. "Interaction of Charged Particles in a Dielectric". In: *Phys. Rev.* 110.4 (1958), pp. 857–864. ISSN: 0031-899X. DOI: 10.1103/PhysRev.110.857. URL: https://link.aps.org/doi/10.1103/PhysRev.110.857.

[281] W. Kohn. "Effective Mass Theory in Solids from a Many-Particle Standpoint". In: *Phys. Rev.* 105.2 (1957), pp. 509–516. ISSN: 0031-899X. DOI: 10.1103/PhysRev.105.509. URL: https://link.aps.org/doi/10.1103/PhysRev.105.509.

[282] P. P. Ewald. "Die Berechnung optischer und elektrostatischer Gitterpotentiale". In: *Ann. Phys.* 369.3 (1921), pp. 253–287. ISSN: 00033804. DOI: 10.1002/andp.19213690304. URL: http://doi.wiley.com/10.1002/andp.19213690304.

[283] Miguel Morales et al. "First Principles Methods: A Perspective from Quantum Monte Carlo". In: *Entropy* 16.1 (2014), pp. 287–321. ISSN: 1099-4300. DOI: 10.3390/e16010287. URL: http://www.mdpi.com/1099-4300/16/1/287/http://www.mdpi.com/1099-4300/16/1/287.

[284] Carlo Pierleoni et al. “Liquid–liquid phase transition in hydrogen by coupled electron–ion Monte Carlo simulations”. In: *Proc. Natl. Acad. Sci.* 113.18 (2016), pp. 4953–4957. ISSN: 0027-8424. DOI: 10.1073/pnas.1603853113. URL: http://www.pnas.org/lookup/doi/10.1073/pnas.1603853113.

[285] C. Pierleoni and D. M. Ceperley. “The Coupled Electron-Ion Monte Carlo Method. From Materials to Chemical Biology”. In: *Computer Simulations in Condensed Matter*. Ed. by M. Ferrario, G. Ciccotti, and Binder K. Vol. 1. Lecture Notes in Physics. Heielberg, Germany: Springer, 2006, pp. 641–683. ISBN: 978-3-540-35270-9. DOI: 10.1007/3-540-35273-218. URL: https://link.aps.org/doi/10.1103/PhysRevA.80.032521.

[286] J. R. Trail and R. J. Needs. “Smooth relativistic Hartree–Fock pseudopotentials for H to Ba and Lu to Hg”. In: *J. Chem. Phys.* 122.17 (2005), p. 174109. ISSN: 0021-9606. DOI: 10.1063/1.1888569. arXiv: 0909.5503. URL: http://aip.scitation.org/doi/10.1063/1.1888569.

[287] Michele Ruggeri, Saverio Moroni, and Markus Holzmann. “Nonlinear Network Description for Many-Body Quantum Systems in Continuous Space”. In: *Phys. Rev. Lett.* 120.20 (2018), p. 205302. ISSN: 0031-9007. DOI: 10.1103/PhysRevLett.120.205302. URL: https://doi.org/10.1103/PhysRevLett.120.205302https://link.aps.org/doi/10.1103/PhysRevLett.120.205302.

[288] Markus Holzmann and Saverio Moroni. “Orbital-dependent backflow wave functions for real-space quantum Monte Carlo”. In: *Phys. Rev. B* 99.8 (2019), p. 085121. ISSN: 2469-9950. DOI: 10.1103/PhysRevB.99.085121. URL: https://link.aps.org/doi/10.1103/PhysRevB.99.085121.

[289] Luning Zhao and Eric Neuscamman. “Supplemental Material : A Variational Approach to Optical Band Gaps Optical Gap (eV)”. In: *Phys. Rev. A* 164705.2015 (2019), p. 164705. DOI: 10.1103/PhysRevA.80.032521. URL: https://link.aps.org/doi/10.1103/PhysRevA.80.032521.

[290] Wei Ku and Adolfo G. Eguiluz. “Band-Gap Problem in Semiconductors Revisited: Effects of Core States and Many-Body Self-Consistency”. In: *Phys. Rev. Lett.* 89.12 (2002), p. 126401. ISSN: 0031-9007. DOI: 10.1103/PhysRevLett.89.126401. URL: https://link.aps.org/doi/10.1103/PhysRevLett.89.126401.

[291] Ricardo Gómez-Abal et al. “Influence of the Core-Valence Interaction and of the Pseudopotential Approximation on the Electron Self-Energy in Semiconductors”. In: *Phys. Rev. Lett.* 101.10 (2008), p. 106404. ISSN: 0031-9007. DOI: 10.1103/PhysRevLett.101.106404. URL: https://link.aps.org/doi/10.1103/PhysRevLett.101.106404.

[292] Feliciano Giustino, Steven G. Louie, and Marvin L. Cohen. "Electron-Phonon Renormalization of the Direct Band Gap of Diamond". In: *Phys. Rev. Lett.* 105.26 (2010), p. 265501. ISSN: 0031-9007. DOI: 10.1103/PhysRevLett.105.265501. URL: https://link.aps.org/doi/10.1103/PhysRevLett.105.265501.

[293] Bartomeu Monserrat, G. J. Conduit, and R. J. Needs. "Extracting semiconductor band gap zero-point corrections from experimental data". In: *Phys. Rev. B* 90.18 (2014), p. 184302. ISSN: 1098-0121. DOI: 10.1103/PhysRevB.90.184302. URL: https://link.aps.org/doi/10.1103/PhysRevB.90.184302.

[294] P. Lautenschlager, P. B. Allen, and M. Cardona. "Temperature dependence of band gaps in Si and Ge". In: *Phys. Rev. B* 31.4 (1985), pp. 2163–2171. ISSN: 0163-1829. DOI: 10.1103/PhysRevB.31.2163. URL: https://link.aps.org/doi/10.1103/PhysRevA.80.032521.

[295] C. D. Clark, P. J. Dean, and P. V. Harris. "Intrinsic edge absorption in diamond". In: *Proc. R. Soc. London. Ser. A. Math. Phys. Sci.* 277.1370 (1964), pp. 312–329. ISSN: 0080-4630. DOI: 10.1098/rspa.1964.0025. URL: http://www.royalsocietypublishing.org/doi/10.1098/rspa.1964.0025https://royalsocietypublishing.org/doi/10.1098/rspa.1964.0025.

[296] P. Lautenschlager et al. "Temperature dependence of the dielectric function and interband critical points in silicon". In: *Phys. Rev. B* 36.9 (1987), pp. 4821–4830. ISSN: 0163-1829. DOI: 10.1103/PhysRevB.36.4821. URL: https://link.aps.org/doi/10.1103/PhysRevB.33.1110https://link.aps.org/doi/10.1103/PhysRevB.31.2163https://link.aps.org/doi/10.1103/PhysRevB.36.4821.

[297] S. Lebegue et al. "Semimetallic dense hydrogen above 260 GPa". In: *Proc. Natl. Acad. Sci.* 109.25 (2012), pp. 9766–9769. ISSN: 0027-8424. DOI: 10.1073/pnas.1207065109. URL: http://www.pnas.org/cgi/doi/10.1073/pnas.1207065109.

[298] Raymond C. Clay et al. "Benchmarking exchange-correlation functionals for hydrogen at high pressures using quantum Monte Carlo". In: *Phys. Rev. B* 89.18 (2014), pp. 1–11. ISSN: 1550235X. DOI: 10.1103/PhysRevB.89.184106. URL: https://link.aps.org/doi/10.1103/PhysRevA.80.032521.

[299] O. Madelung, M. Schulz, and H. Weiss. *Intrinsic Properties of Group IV Elements and III-V, II-VI and I-VII Compounds, Landolt-Bŕnstein, NewSeries, Group III/22A*. Vol. 80. New York, 1987: Springer-Verlag, 2009, p. 032521. DOI: 10.1103/PhysRevA.80.032521. URL: https://link.aps.org/doi/10.1103/PhysRevA.80.032521.

[300] M. Born and R. Oppenheimer. "Zur Quantentheorie der Molekeln". In: *Ann. Phys.* 389.20 (1927), pp. 457–484. ISSN: 00033804. DOI: 10.1146/annurev.physchem.55.091602.094335. URL: http://doi.wiley.com/10.1002/andp.19273892002.

[301] Sharon Hammes-Schiffer and John C. Tully. "Vibrationally Enhanced Proton Transfer". In: *J. Phys. Chem.* 99.16 (1995), pp. 5793–5797. ISSN: 0022-3654. DOI: 10.1021/j100016a011. URL: https://pubs.acs.org/doi/abs/10.1021/j100016a011.

[302] David S. Sholl and John C. Tully. "A generalized surface hopping method". In: *J. Chem. Phys.* 109.18 (1998), pp. 7702–7710. ISSN: 0021-9606. DOI: 10.1063/1.477416. URL: http://aip.scitation.org/doi/10.1063/1.477416.

[303] Sharon Hammes-Schiffer. "Proton-Coupled Electron Transfer: Moving Together and Charging Forward". In: *J. Am. Chem. Soc.* 137.28 (2015), pp. 8860–8871. ISSN: 0002-7863. DOI: 10.1021/jacs.5b04087. URL: https://pubs.acs.org/doi/10.1021/jacs.5b04087.

[304] W. Kolos and L. Wolniewicz. "Improved Theoretical Ground-State Energy of the Hydrogen Molecule". In: *J. Chem. Phys.* 49.1 (1968), pp. 404–410. ISSN: 0021-9606. DOI: 10.1063/1.1669836. URL: http://aip.scitation.org/doi/10.1063/1.1669836.

[305] L. Wolniewicz. "The X 1Σ+g state vibration-rotational energies of the H2, HD, and D2 molecules". In: *The Journal of Chemical Physics* 78.10 (1983), p. 6173. ISSN: 00219606. DOI: 10.1063/1.444580. URL: http://link.aip.org/link/?JCP/78/6173/1{\&}Agg=doi.

[306] Yubo Yang et al. "How large are nonadiabatic effects in atomic and diatomic systems?" In: *Journal of Chemical Physics* 143.12 (2015), pp. 0–9. ISSN: 00219606. DOI: 10.1063/1.4931667. arXiv: 1507.05959. URL: http://dx.doi.org/10.1063/1.4931667.

[307] A. Szabo and N. S. Ostlund. *Modern quantum chemistry : introduction to advanced electronic structure theory*. Vol. 80. Minelola, N. Y.: Dover Publications, 1996, p. 032521. DOI: 10.1103/PhysRevA.80.032521. URL: https://link.aps.org/doi/10.1103/PhysRevA.80.032521.

[308] W. Heitler and F. London. "Wechselwirkung neutraler Atome und homopolare Bindung nach der Quantenmechanik". In: *Zeitschrift fur Phys.* 44.6-7 (1927), pp. 455–472. ISSN: 1434-6001. DOI: 10.1007/BF01397394. URL: http://link.springer.com/10.1007/BF01397394.